Fundamental Studies of Biomass Fluidization

by

Gbenga Olatunde

A dissertation submitted to the Biosystems Engineering of
Auburn University
in partial fulfillment of the
requirements for the Degree of
Doctor of Philosophy

Auburn, Alabama
December 12, 2015

Keyword: Biomass, loblolly pine, fluidization, particle size, particle shape, modeling

Approved by

Oladiran Fasina, Chair, Professor of Biosystems Engineering
Sushil Adhikari, Associate Professor of Biosystems Engineering
Timothy McDonald, Associate Professor of Biosystems Engineering
Steve Duke, Associate Professor of Chemical Engineering

Abstract

The world is presently at a point of making important decisions regarding how to minimize disasters such as super storm, super earthquakes, and landslides that are caused by global warming due to fossil fuel exploration and consumption. One route is to use varieties of renewable energy resources such as solar, wind, biomass etc. to replace some of the fossil fuels consumed. Biomass such as wood, energy plants (switchgrass, poplar, and willow) is the only renewable energy that can be converted into liquid fuel. However, in the process of converting biomass to fuel, there are numerous technical challenges that are encountered primarily due to assumptions made in measuring values of physical properties of biomass grinds (e.g. size, particle geometry, and voidage). These properties are utilized in the design and sizing of biomass conversion and processing equipment and facilities. For example, the use of average (mean) particle diameter in fluidization models and equation seems to imply that biomass ground particles are uniformly sized, thus neglecting the size distribution of biomass. In addition, as non-spherical particles, the use of a mean diameter is problematic because axis of measurement significantly influences the value of diameter. Some mean diameter that can be obtained from non-spherical particle include, the diameter of a sphere that has the same surface area to volume ratio as a particle, Martins, Ferret and Sauter mean diameter. At present comprehensive investigation on contribution of physical properties vis-a-vis particle size measurement scheme on predictability of loblolly pine wood grind minimum fluidization velocity and other parameters that are used in designing fluidized bed system is lacking in literature. Hence, this study

investigated how the physical properties of loblolly pine wood influence the ability to predict important design parameters and the behavior of biomass grinds during fluidization.

The result showed that loblolly pine wood grinds have mean particle density of 1460.6 ± 7 kg/m^3, bulk density of 311 ± 37 kg/m^3 and porosity of 0.787 ± 0.003. With regards to particle size, the Ferret diameter was found to be higher than surface-volume diameter, Martin's diameter and chord diameter by 18.3, 23.6, and 7.03% respectively. Also, the shape characteristic based on the sphericity value of biomass grinds ranges between 0.235 and 0.603, thus indicating that biomass grinds have flat shape. The minimum fluidization velocity of ground loblolly pine wood (unfractionated samples) was found to be 0.25 ± 0.04 m/s. For fractionated samples, the minimum fluidization velocity increased from 0.29 to 0.81 m/s as fractionating screen size increased from 0.15 to 1.70 mm. Predictions of minimum fluidization velocity obtained from selected equations were significantly different from the measured values. Moreover, increase in moisture content increased the bulk density, particle density, and porosity but the particle size coefficient of variation reduced from 90 at 8.46% MC to 42 at 27.02 % MC. Increase in moisture content also increased the minimum fluidization velocity of unfractionated grinds from 0.20 to 0.32 m/s as moisture was increased from 8.45 to 27.02 % wet basis respectively. In addition, the correlation developed predicted the experimental data for minimum fluidization velocity with mean deviation less than 10%. For the modified Ergun equation, the coefficients K_1 and K_2 were estimated to be 201 and 2.7 respectively. The overall mean relative deviation obtained between the predicted and experimental pressure drop using loblolly pine wood grind and the equation

developed in this study and the Ergun equation were -17.48 and 63.5 % respectively. Finally, an evaluation of the interface exchange drag law equations (Gidaspow, Syamlal-Obrien, Wen & Yu and non-spherical) showed that non-spherical drag law equation predicted the minimum fluidization velocity with mean relative deviation of 4.5%. It was also observed that bed entrainment occurred for all the drag law equation at 2 sec simulation time. The drag law equations under-predicted the bed pressure drop, and mass entrainment above 0.2 m/s superficial airflow velocity after bed material entrainment has begun. The incorporation of body force improved the predictability of the non-spherical drag law equation but exhibited little impact on the other drag law equations. Finally, this study has demonstrated the possibility of improving prediction of important parameters of fluidize bed system when particles with non-uniform and irregular geometry is used.

I will also like to acknowledge my fellow graduate students who have significantly contributed to my event-full years. I am deeply touched by your encouragement, support, and love. I can't but remember Anshu, Gurdeep, Jas, Omotolani, Tosin, Femi, Ujaain, Thomas, Dr. Abdoulmoumine, Ewurama, Charles, Yusuf, Aurelie, Narendra, Bangpin.

Let me appreciate some of my family members for their support, encouragement and even visitation to my humbly abode during this energy sapping degree: My father, Pastor Aderemi Augustus Olatunde, Samuel Olatunde, Kolade Olatunde and Folashade Olatunde. My mother in-law- Mrs. Ayoola, Prof. and Mrs Adeyemo. Dn. Dokun Olatunde, Mr. and Mrs Bamidele Falola, Mr. Dehinde Olatunde, Pastor and Mrs. Adelekan, Mr. and Mrs. Idowu, Mrs. Oladunmoye, Pastor and Mrs. Adedeji and Mr. and Mrs. Ajani. I will like to appreciate my families in Auburn- Mrs Popoola, Dr. Yewande Fasina, Dr. & Mrs Shodeke. I appreciate their supports, constant visits, and words of encouragements. Thank you and God bless you all.

I also want to appreciate the faculty staff of the department of Agricultural Engineering, Obafemi Awolowo University, Ile-Ife. Especially Prof. O.K Owolarafe and Dr. B.S. Ogunsina, who frequently called me and offer invaluable suggestions and advice on my work. Their words of encouragement and support was noted and appreciated.

Finally, to my wife, Adesola and my son, Oreofe, I am moved by your priceless sacrifices, sleepless nights, and support: spiritual and moral. I want to say you are indeed special to me and everything you did contributed immensely to the successful completion of this work.

Table of Contents

List of Tables

List of Figures

Chapter 1: Introduction

1.1   Fossil fuel consumption and impact

Currently, fossil fuels such as crude oil, coal, and natural gas represent the major energy source in U.S. (account for 90 Quadrillion BTU of energy per year) and in the world (account for 600 Quadrillion BTU of energy per year) (Arastoopour, 2001). In the United States, about 8.43 million barrels of crude oil is imported daily from countries such as Mexico, Venezuela, and Iraq where economic and political instability often lead to disruption in fuel supplies. These instabilities threaten energy security and price stability (Nair, 2002; Sawin, 2006; Siedlecki et al., 2010). In addition, the insatiable appetite for crude oil consumption in the US is being threatened by crude oil reserve depletion that has been forecasted to occur around 2050 and 2075 (Van Wachem et al., 2001). Furthermore, emission and greenhouse gases generated during exploration and consumption of fossil fuels are believed to have environmental impacts (global warming, pollution, acid rain, and smog) and contribute to the frequent occurrence of natural disasters such as super storm, super earthquakes, and landslides (Cherubini, 2010).

It is therefore important that we optimize alternative energy production using varieties of renewable energy resources (e.g. solar, wind, biomass) as a potential replacement for fossil fuels. Biomass such as wood, energy plants (switchgrass, poplar, and willow) combine CO_2 with water and sunlight to produce carbohydrates molecules and oxygen. The carbohydrate molecule stored in the plant cells can be extracted and processed into fuels, chemicals, and products, thus making biomass the only renewable resource of carbon (Climent et al., 2014).

 Biomass is a large and sustainable potential that can be grown and obtained locally. This local availability reduces the risk of dependency on other parts of the world for petroleum. In fact, Perlack et al. (2005) and Downing et al. (2011) reported that United States can produce 1.3

billion tons of dry biomass per year from forest and agricultural resources. This quantity of biomass resources is enough to produce 60 billion gallons of bio-ethanol representing about 30% of the current petroleum consumption. A large portion of this biomass resources is expected to come from the southern U.S. because the region supplies about 60 % (by volume) of the U.S. total timber harvest (Hanson et al., 2010). Loblolly pine wood is one of the predominant wood specie grown in this region.

Therefore, exploring various option for converting this woody species to biofuel and coproducts production would improve local economy and contribute toward achieving the renewable energy goal of 36 billion US gallons of biofuels annually by 2022 as stated in the Energy Independence and Security Act of 2007. In addition 16 billion of the 36 billion gallons is expected to come from cellulosic ethanol while 5 billion US gallons will be obtained from biomass-based diesel and other advanced biofuels (Sissine, 2007).

Biomass is converted to biofuels through two routes: thermo-chemical and bio-chemical conversion methods (Damartzis and Zabaniotou, 2011; Srirangan et al., 2012; Zhang et al., 2013). These two conversion methods are well known and established chemical processes but are not well adapted to handle the variability in properties of biomass feedstock. Some of the problems are evident in small biomass conversion pilot projects that have faced problems such as solid entrainments/ carry over, incomplete combustion of particles, temperature variation, feeding bottlenecks, and design inflexibility to feedstock moisture variation (James et al., 2013; San Miguel et al., 2012; Siedlecki et al., 2010; Verma et al., 2012; Wiltsee, 2000).

Thermochemical conversion method is the most preferred method because it is better suited for feedstocks with high variability in physical properties (Chen et al., 2012; Verma et al., 2012).

The most common thermochemical conversion methods are gasification and pyrolysis. Gasification convert biomass feedstock into syngas by exposing the material to controlled amount of oxygen and/ or steam at high temperatures (>700 °C). In pyrolysis, biomass is thermally decomposed at temperatures between 200-550 °C in the absence of oxygen (Mohan et al., 2006; Verma et al., 2012). In both conversion routes, a fluidized bed reactor is often used to change the state of granular material from solid-like state to a dynamic fluid-like state by suspending them in a gas stream (a process typically referred to as fluidization). Some of the advantages of fluidization includes high heat transfer rates between bed material and the feedstock, uniform temperature gradient across the bed, good bed temperature control, uniform particle mixing and adaptability to wide variety of feedstocks (Damartzis and Zabaniotou, 2011; M'Chirgui et al., 1997; Papadikis et al., 2010).

1.2 Research problem

In the process of fluidizing ground biomass, there are numerous technical challenges that are encountered primarily due to assumptions made in measuring the physical properties of biomass grinds (e.g. size, particle geometry, and voidage) that are used to design and size processing and conversion equipment and facilities. For example, the use of average (mean) particle diameter in fluidization models and equation (Abdullah et al., 2003; Abrahamsen and Geldart, 1980; Ergun, 1952; Leva, 1959; Miller and Logwinuk, 1951) seems to imply that biomass ground particles are uniformly sized thus neglecting the size distribution of biomass (Jiliang et al., 2013; Ray et al., 1987). Also, as non-spherical particles, the use of a mean diameter is problematic because axis of measurement significantly influence the value of diameter obtained. Mean diameters that are used to describe size of non-spherical particles include the diameter of a sphere that has the same surface area to volume ratio as a particle (Ortega-Rivas et al., 2006; Rhodes, 2008). Martins

3

diameter (Yang, 2007), Ferret diameter (Ortega-Rivas et al., 2006) and Sauter mean diameter (Abdullah et al., 2003; McMillan et al., 2007). At present comprehensive investigation on contribution of physical properties vis-a-vis particle size measurement method on predictability of loblolly pine wood grind minimum fluidization velocity and other parameters that are used in designing fluidized bed system is lacking in literature.

1.3   Hypothesis and objective

The main hypothesis of this project is that physical properties of biomass grinds affect its fluidization behavior. The overall objective was to investigate how the properties of ground biomass influence the behavior of particle in fluidization environment.

To achieve this main objective, the following specific objectives were pursued:

Objective 1:

Experimentally investigate the effect of physical properties (particle size, particle density, shape, and moisture content) fluidization behavior (bed expansion, pressure drop, minimum fluidization velocity) of biomass grinds.
Hypothesis: biomass grinds physical properties significantly affect fluidization behavior.

Objective 2:

Develop and validate a revised Ergun equation that predicts pressure drop across a bed of biomass grinds at different airflow velocities.
Hypothesis: biomass shape and size distribution influences porosity hence affect predicting equation.

Objective 3:

Develop a 3-D Computational Fluid Dynamics model for fluidization of biomass grinds using Discrete Element Method and Dense Discrete Phase Model in Fluent ANSYS software.

4

<u>Hypothesis:</u> associated drag laws for solid-gas modeling cannot be used for ground biomass unless they are modified.

1.4   Organization of dissertation

This dissertation is subtitled into seven chapters. A brief description of each chapters is as follows. Chapter 1 presents a brief introduction of biomass fluidization challenges and research problems that were addressed in this dissertation. The chapter also presents the statement of objectives and the relevant hypothesis. Chapter 2 includes comprehensive literature review of biomass as a feedstock for biofuels and coproducts production. In addition, the rationale for choice of feedstock used in this study was also discussed. Included also, is the challenges faced with fluidizing biomass grinds and physical properties of biomass that impede homogeneous fluidization, and a review of various fluidization models that have been used to predict important fluidization parameters. Finally, review of Computational Fluid Dynamics modeling using Fluent ANSYS software was presented in this chapter. Chapter 3 detailed the effect of diameters obtained from different measurement schemes on minimum fluidization velocity of loblolly pine wood grinds. In chapter 4, the effects of moisture content on fluidization behavior of loblolly pine wood grinds were detailed and empirical correlation used for predicting minimum fluidization velocity was developed and validated. Chapter 5 presents a new correlation for predicting pressure drop across a bed of loblolly pine wood grinds at varying fluid flow velocities. The correlation is an equation similar to Ergun's expression but included a new term for particle size distribution, void fraction correlation, and coefficients (K_1 and K_2). Chapter 6 presents a detailed fluidization behavior of ground biomass particle using Computational Fluid Dynamics, Dense Discrete Phase Model in Fluent ANSYS software. Finally, the overall conclusion and recommendation for future work based on the study were presented in Chapter 7.

Chapters 3 to 6 were presented using standard technical report format consisting of the Abstract, Introduction, Methodology, Result & discussion, Conclusion and References. Where necessary, additional data or analysis is referred to in the appendix, which is arranged on chapter basis. The American Society of Agricultural and Biological Engineering (ASABE) style guide was used for literature citing and for references listing.

1.5 References

Abdullah, M. Z., Z. Husain, and S. L. Yin Pong. 2003. Analysis of cold flow fluidization test results for various biomass fuels. *Biomass and Bioenergy* 24(6):487-494.

Abrahamsen, A., and D. Geldart. 1980. Behaviour of gas-fluidized beds of fine powders part I. Homogeneous expansion. *Powder Technology* 26(1):35-46.

Arastoopour, H. 2001. Numerical simulation and experimental analysis of gas/solid flow systems: 1999 Fluor-Daniel Plenary lecture. *Powder Technology* 119(2–3):59-67.

Chen, X., W. Zhong, X. Zhou, B. Jin, and B. Sun. 2012. CFD–DEM simulation of particle transport and deposition in pulmonary airway. *Powder Technology* 228(0):309-318.

Cherubini, F. 2010. The biorefinery concept: Using biomass instead of oil for producing energy and chemicals. *Energy Conversion and Management* 51(7):1412-1421.

Climent, M. J., A. Corma, and S. Iborra. 2014. Conversion of biomass platform molecules into fuel additives and liquid hydrocarbon fuels. *Green Chemistry* 16(2):516-547.

Damartzis, T., and A. Zabaniotou. 2011. Thermochemical conversion of biomass to second generation biofuels through integrated process design: A review. *Renewable and Sustainable Energy Reviews* 15(1):366-378.

Downing, M., L. M. Eaton, R. L. Graham, M. H. Langholtz, R. D. Perlack, A. F. Turhollow Jr, B. Stokes, and C. C. Brandt. 2011. US Billion-Ton Update: Biomass supply for a bioenergy and bioproducts industry. Oak Ridge National Laboratory (ORNL).

Ergun, S. 1952. Fluid flow through packed columns. *Chem. Eng. Prog.* 48:89-94.

Hanson, C., L. Yonavjak, C. Clarke, S. Minnemeyer, L. Biosrobert, A. Leach, and K. Schleeweis. 2010. Southern forests for the future. World Resources Institute. Washington, DC

James, A. K., R. W. Thring, P. M. Rutherford, and S. S. Helle. 2013. Characterization of biomass bottom ash from an industrial scale fixed-bed boiler by fractionation. *Energy and Environment Research* 3(2):21.

Jiliang, M., C. Xiaoping, and L. Daoyin. 2013. Minimum fluidization velocity of particles with wide size distribution at high temperatures. *Powder Technology* 235(0):271-278.

Leva, M. 1959. *Fluidization*. McGraw-Hill Chemical Engineering Series. McGraw-Hill, London

M'Chirgui, A., L. Tadrist, and J. Pantaloni. 1997. Influence of particle-size distribution on entrainment solid rate in fluidized bed. *AIChE Journal* 43(1):260-262.

McMillan, J., C. Briens, F. Berruti, and E. W. Chan. 2007. Study of High Velocity Attrition Nozzles in a Fluidized Bed. In *The 12th International Conference on Fluidization - New Horizons in Fluidization Engineering*. F. Berruti, X. Bi, and T. Pugsley, eds. Vancouver, Canada: Engineering Conferences International.

Miller, C. O., and A. Logwinuk. 1951. Fluidization studies of solid particles. *Industrial & Engineering Chemistry* 43(5):1220-1226.

Mohan, D., C. U. Pittman, and P. H. Steele. 2006. Pyrolysis of wood/biomass for bio-oil: A critical review. *Energy & Fuels* 20(3):848-889.

Nair, P. K. R. 2002. Our fragile world: Challenges and opportunities for sustainable development. Forerunner to the encyclopedia of life support systems (M. K. Tolba, Editor), Vols I and II. *Agroforestry Systems* 54(3):251-251.

Ortega-Rivas, Enrique, P. Juliano, and H. Yan. 2006. *Food powders: physical properties, processing, and functionality*. 1st ed. Springer, New York, Philadelphia.

Papadikis, K., S. Gu, and A. V. Bridgwater. 2010. Computational modelling of the impact of particle size to the heat transfer coefficient between biomass particles and a fluidised bed. *Fuel Processing Technology* 91(1):68-79.

Perlack, R. D., L.L. Wright, A.F. Turhollow, R.L. Graham, B.J. Stokes, and D. C. Erbach. 2005. Biomass as feedstocks for a bioenergy and bioproducts industry: The technical feasibility of a billion -ton annual supply. http://www1.eere.energy.gov/biomass/pdfs/final_billionton_vision_report2.pdf: U.S. Department of Energy. Available at: http://www1.eere.energy.gov/biomass/pdfs/final_billionton_vision_report2.pdf.

Ray, Y.-C., T.-S. Jiang, and C. Y. Wen. 1987. Particle attrition phenomena in a fluidized bed. *Powder Technology* 49(3):193-206.

Rhodes, M. 2008. *Particle size analysis*. Introduction to Particle Technology. 1 ed. John Wiley & Sons, Ltd, Hoboken, NJ.

San Miguel, G., M. P. Domínguez, M. Hernández, and F. Sanz-Pérez. 2012. Characterization and potential applications of solid particles produced at a biomass gasification plant. *Biomass and Bioenergy* 47(0):134-144.

Sawin, J. 2006. National policy instruments: Policy lessons for the advancement & diffusion of renewable energy technologies around the world. *Renewable Energy. A Global Review of Technologies, Policies and Markets.*

Siedlecki, M., W. De Jong, and A. H. M. Verkooijen. 2010. Fluidized bed gasification as a mature and reliable technology for the production of bio-syngas and applied in the production of liquid transportation fuels: A review. *Energies* 4(3):389-434.

Sissine, F. 2007. Energy Independence and Security Act of 2007: A summary of major provisions. DTIC Document.

Srirangan, K., L. Akawi, M. Moo-Young, and C. P. Chou. 2012. Towards sustainable production of clean energy carriers from biomass resources. *Applied Energy* 100(0):172-186.

Van Wachem, B., J. Schouten, C. Van den Bleek, R. Krishna, and J. Sinclair. 2001. CFD modeling of gas-fluidized beds with a bimodal particle mixture. *AIChE Journal* 47(6):1292-1302.

Verma, M., S. Godbout, S. Brar, O. Solomatnikova, S. Lemay, and J. Larouche. 2012. Biofuels production from biomass by thermochemical conversion technologies. *International Journal of Chemical Engineering* 2012(0):1-18.

Wiltsee, G. 2000. Lessons learned from existing biomass power plants. National Renewable Energy Lab., Golden, CO (US) NREL/SR-570-26946. Colorado US.

Yang, W.-C. 2007. Modification and re-interpretation of Geldart's classification of powders. *Powder Technology* 171(2):69-74.

Zhang, K., J. Chang, Y. Guan, H. Chen, Y. Yang, and J. Jiang. 2013. Lignocellulosic biomass gasification technology in China. *Renewable Energy* 49(0):175-184.

Chapter 2: Literature review

2.1   Biomass resources

Biomass are organic materials that are plant or animal based (ANSI/ASABE, 2011). Interest in utilization of biomass feedstock such as agricultural and forest residues and dedicated energy plants, as feedstock for fuel and products production is gaining attention of the general public. Researchers and policy makers are vigorously working on technologies that can convert non-food biomass feedstock sources to minimize the complicated ethical and moral issue of using food materials. This non-food sources also have limitless renewable potential and at the same time have less environmental impacts (Lu et al., 2015) during harvesting, processing, and consumption. At present, conversion of non-food sources to fuels, chemicals, and products appears as the best and most logical alternative. Figure 2.1 showed different sources of biomass resources from where fuel and products can be obtained.
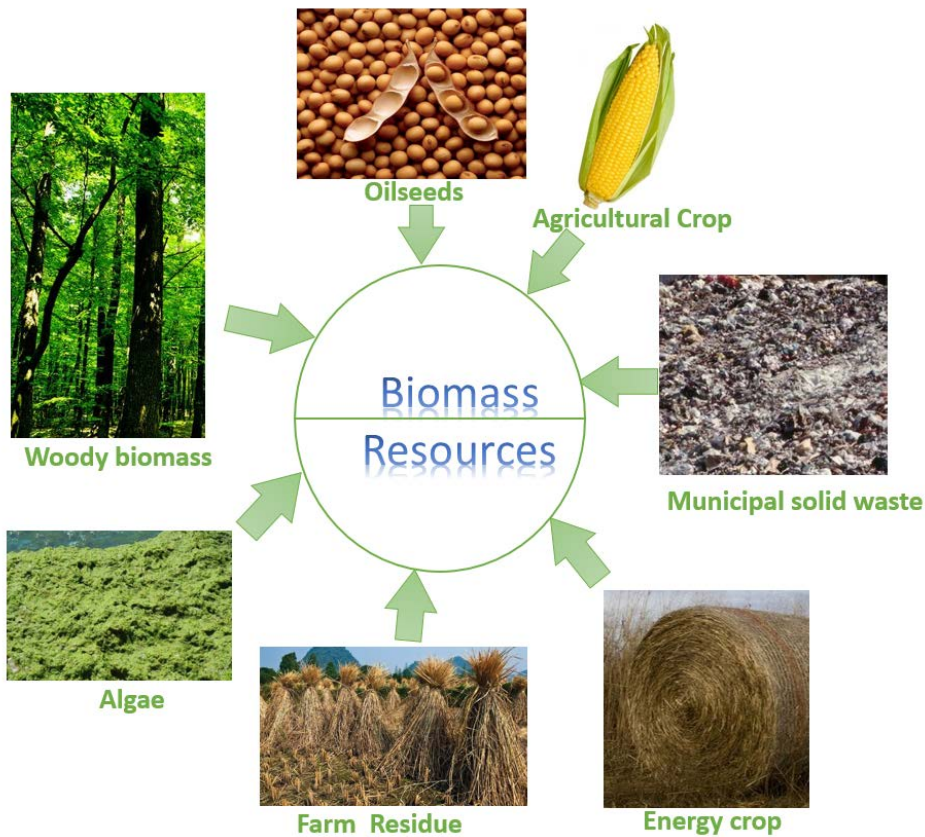
Figure 2.1: Biomass resources and sources

One of the advantages of biomass is its availability in most locations in the world. One form/type of biomass could be obtained in commercial quantities in virtually every country of the world. For example United States can produce 278 million dry tons biomass annually from forestlands and 194 million dry tons annually from croplands and about 254 million tons from municipal waste etc. (Perlack and Stokes, 2011). Obviously, this is a huge potential. In fact, gathering about a billion tons of biomass just from agriculture and forest resources in a sustainable manner was proved sufficient to be able to displace 30% or more of the country's present petroleum consumption by year 2030 (Downing et al., 2011). In order to optimally utilize the available billion-ton biomass and get a good return on investment, every available biomass must be carefully harvested and judiciously utilized.

In this study, our focus is on woody biomass specifically loblolly pine wood. The next paragraph will provide basic information on this specie and subsequent focus of this work would center on this biomass feedstock.

The forests of the South region account for 30 percent of the unreserved forest area of the United States and 27 percent of all forestland (Smith et al., 2009). Pine tree (Fig 2.2) - the most commonly available woody specie in this region was identified as a potential feedstock because it occupies about 55 million acres or nearly one-fourth of all southern forests and about 60% of the timber products manufactured in the United States. (Morris et al., 2010; NCSSF, 2005; Smith et al., 2009). Pine species are predominantly found in the southeast stretching from Virginia in the north to Florida in the south and to Oklahoma and Texas in the west (Allen et al., 1990; Munsell and Fox, 2010; Nelson et al., 2013). In addition over 95% of loblolly pine grown in the southern state are genetically modified hence lowering time to flowering and crossing from 8-10 years to 3-5 years and reducing selection age from 10-12 years to 4 – 5 years. This has resulted in gain in volume production of about 10% per generation over three generations (McKeand, 2014).

<center>(a)   (b)</center>

<center>Figure 2.2: Pine tree at early stage of life (a) and established plantation (b)</center>

2.2 Biomass conversion process

Figure 2.3 highlights four pathways that are used to convert biomass into fuels, products, and chemicals. Biochemical conversion method is used to produce ethanol and biogas by utilizing bacteria, microorganism, and enzymes through fermentation and anaerobic digestion pathways. Anaerobic digestion pathway produces methane, carbon dioxide, and hydrogen sulfide by breaking down biomass in absence of oxygen. Usually, animal waste, human waste and other waste with high moisture contents are preferred feedstock. Also agricultural crops such as sugarcane, cassava, sorghums corn etc. can be decomposed using bacterial and yeast to produce ethanol. The second pathway uses mechanical means to extract oil from oil-bearing kernels and then use trans-esterification chemical conversion process to obtain bio-diesel.
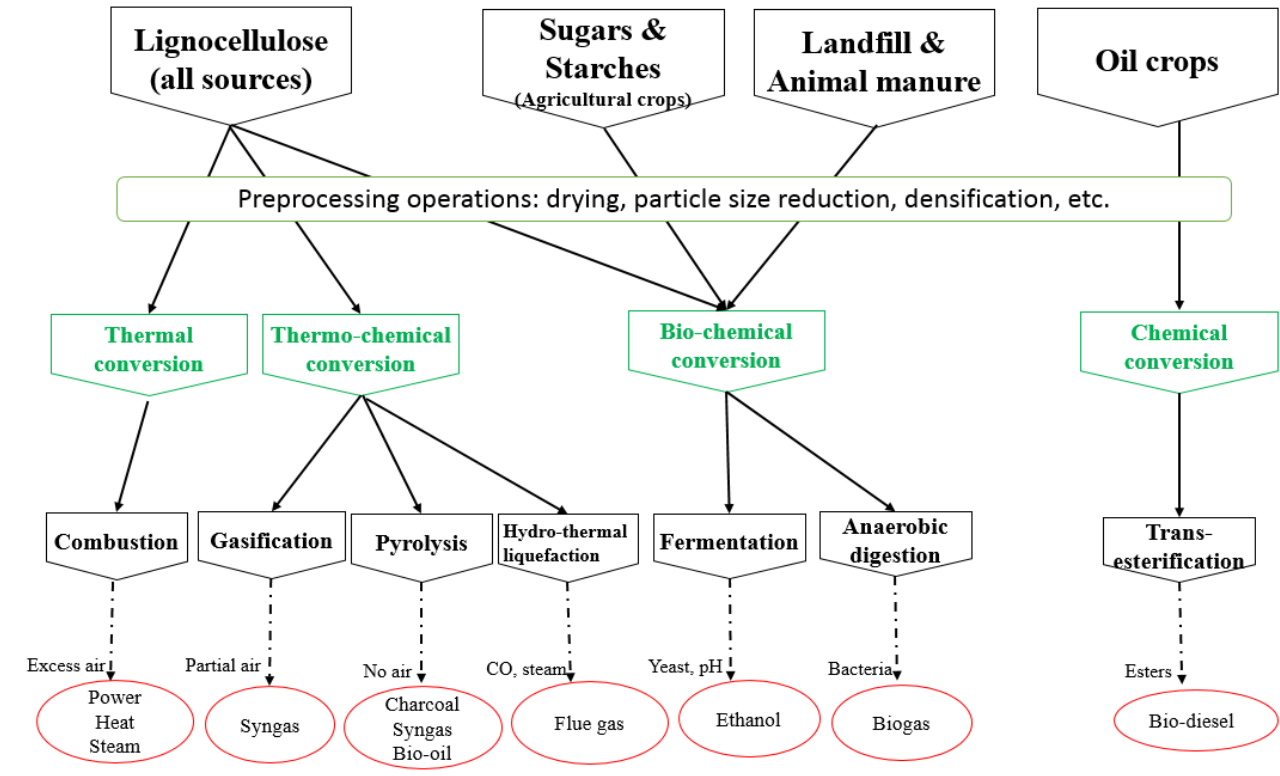
Figure 2.3: Flow chart for biomass conversion to energy paths.

In thermal conversion method (examples are presented in Table 2.1), biomass is directly burnt in the presence of excess air to convert the chemical energy stored in the biomass to produce heat (Clark and Deswarte, 2014). Direct combustion cannot be used to produce liquid fuel but can be used to generate heat, drive turbine for generation of electricity or other mechanical power etc. One of the disadvantages of direct combustion is that at surplus airflow rate (when air supplied is greater than the theoretically needed airflow for combustion), combustion temperature decreases, and thermal efficiency reduces (Bhaskar et al., 2011; Quaak et al., 1999).

Table 2.1: Different types of direct combustion system under thermal conversion method

Combustion method	Typical example	Features
Fixed bed	Spreader-stoker Under screw and through screw system Static and inclined grates	Air is supplied through the grate from below. Thus initial biomass combustion occurs with biomass closer to the grate. The biomass used in this system must be low in ash content. Because, the ash will simply block the airflow into the chamber. Typical combustion temperature ranges between 850 – 1400 ºC.
Moving bed	Forward and reverse moving grate Step grate	This was designed such that the biomass is fed from the top and moves downward during combustion and the ash is removed by dropping to the bottom. Material residence time is fixed with the rate at which the grate element moves. Typical combustion temperature ranges between 500 – 1200 ºC.

(Bhaskar et al., 2011; Christensen, 2011; Quaak et al., 1999)

Lastly, thermochemical conversion pathway includes hydrothermal liquefaction, combustion, pyrolysis, and gasification. Each of the pathways will be briefly described.

Hydrothermal liquefaction (HTL), also called hydrous pyrolysis, is a process for converting biomass into crude oil and other chemicals by mimicking the natural geological processes thought to be involved in the production of fossil fuels (Elliott et al., 2015). The process involves

processing the feedstock in a hot, pressurized liquid environment for sufficient time to break down the solid biopolymeric structure to mainly liquid components. Hydrothermal processing conditions is typically carried out at temperatures of 300–400 ℃ and pressures of 4 to 22 MPa (Brown et al., 2010; Elliott et al., 2015). This process is used to treat wet biomass because it access ionic reaction conditions by maintaining a liquid water processing medium (Elliott et al., 2015). HTL is an expensive process and the heavy oil obtained from the liquefaction process is a viscous tarry lump, which is sometimes difficult to handle (Demirbaş, 2000; Marcilla et al., 2013).

Pyrolysis is another thermo-chemical conversion method that thermally decompose biomass in the absence of oxygen at 400–500°C to produce liquid oils, char, and small amount of gases. Depending on the operating condition, pyrolysis can be classified into three main categories, conventional (slow), fast and flash pyrolysis. The operating condition based on the pyrolysis classification also influence relative distribution of products (Table 2.2). The most common form of pyrolysis is the slow or conventional method (heating rate of 2 -10 ℃/s min until 700 ℃ is attained) (Goyal et al., 2008). However, high residence time required for complete thermal decomposition of biomass adversely affect bio-oil yield and quality. In addition, long residence time demands extra energy input (Jahirul et al., 2012). Fast pyrolysis process is carried out at high heating rate (10 -300 ℃/s) (Luo et al., 2004) with very short residence time, rapid cooling of vapors and aerosol for high bio-oil yield and close control of reaction temperature. In flash pyrolysis, biomass is reacted at temperature ranged between 700 – 1100 ℃ and very short residence time of less than 1 second (Aguado et al., 2002; Gerçel, 2002). However, poor thermal stability, corrosiveness of the oil, and particulates/solids mixed with the oil are some of the drawback of the flash pyrolysis process (Jahirul et al., 2012).

Table 2.2: Typical operating parameters for pyrolysis process

Operating conditions	Pyrolysis types		
	Conventional	Fast	Flash
Pyrolysis temperature (^{o}C)	400 – 600	500 – 660	650 – 1000
Heating rate ($^{o}C/s$)	2 – 10	10 – 300	> 1000
Particle size (mm)	5–50	< 1	< 0.2
Solid residence time (s)	450–550	0.5–10	< 0.5

Source: (Demirbas and Arin, 2002; Jahirul et al., 2012)

In gasification method, biomass is converted into synthesis gas also known as syngas by reacting the biomass feedstock at high temperatures usually above 700°C with a controlled amount of oxygen and with or without steam. Syngas is composed mostly of H_2, CO, CO_2, CH_4, water vapor, and trace impurities (Damartzis and Zabaniotou, 2011; Skoulou et al., 2008). Gasification process can be divided into four steps namely drying, pyrolysis, combustion/oxidation, and reduction. The biomass moisture is evaporated in the drying section of the gasifier (temperature range of 100 to 150 ^{o} C). Pyrolysis step occur in the devolatilization zone (temperature range of 200 to 500 ^{o}C) where the volatiles are removed in form of light and long chain (tar) hydrocarbons, CO and CO_2. Damartzis and Zabaniotou (2011) reported that tar production depends on the properties of feedstock and operating conditions. In the combustion section (temperature range of 800 to 1200 ^{o}C), the char are further processes to produce more gaseous products. Finally, the reduction zone (temperature ranged between 650 and 900 ^{o}C), the material is decomposed into gas (syngas) and other products through a series of endothermic reactions.

Gasification reactors can be classified into three main categories; fluidized bed, fixed bed and entrained flow reactors base on solid movement and position in the bed during operation. Large-scale (industrial) applications usually employ entrained flow or fluidized bed gasifiers in which

solid material are consistently suspended in gas stream. More detail on fluidized bed would be presented in next section. Fixed bed gasifiers are used for small-scale gasification but solid suspension is not part of the requirement. Fixed bed can be either countercurrent or co-current based on the fuel and airflow direction into the bed (Fig 2.4). In both instances, the biomass enters the vessel from the top section. Air enters from the bottom and exits from the top side of the countercurrent bed while in concurrent bed, the air enters from the side close to the top of the gasifier and exits from the side close to the base of the bed. Due to the different mixing and flow conditions in each of these configurations, the final product may be greatly different in terms of temperature and composition, tar and particulates content and thermal efficiency (McKendry, 2002; Warnecke, 2000).
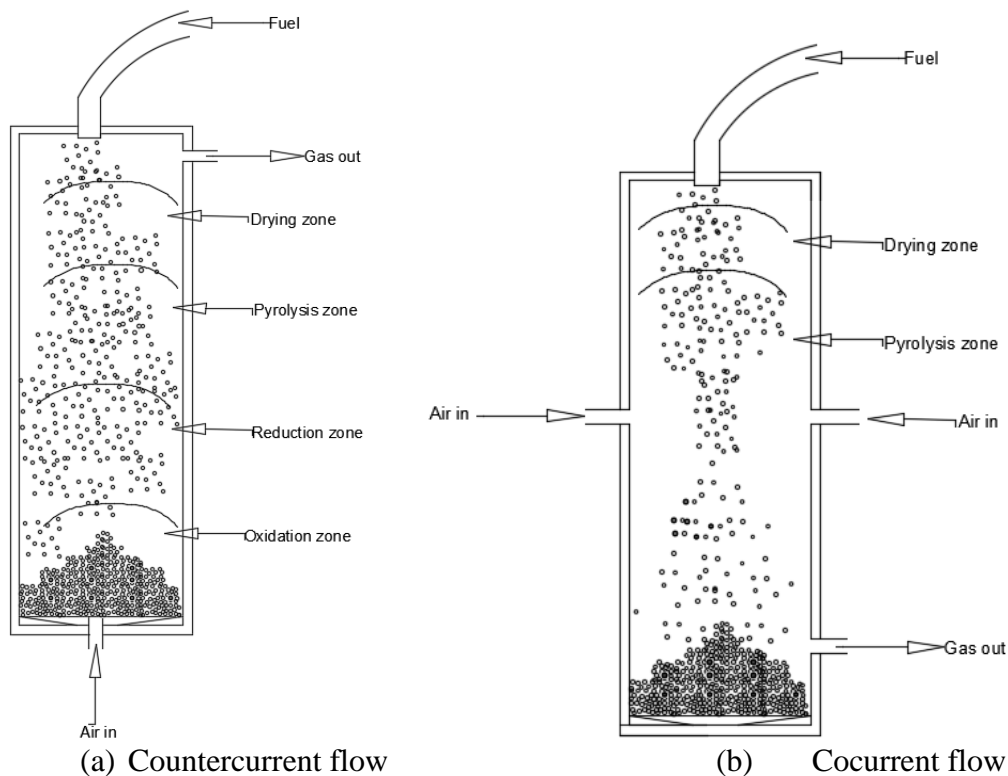
(a) Countercurrent flow   (b)   Cocurrent flow
Figure 2.4: Two different types of fixed bed reactors showing direction of flow of air and biomass into the bed.

In summary, biomass resources are huge. Lignocellulosic biomass such as wood and herbaceous plants are typically processed using gasification and pyrolysis conversion methods. The conversion occurs inside the gassifier through the concept of fluidization. Although the conversion methods are well-known thermo-chemical processes, but there are challenges in using biomass grinds as feedstock in this established processes. Before the biomass can be used in conversion process, the feedstock requires reconditioning/ preprocessing steps in order to obtain a particle size suitable for the reactor to handle and to ensure optimum conversion with good product quality. The size reduction however result in grinds properties that make homogeneous fluidization of biomass very difficult to achieve. The next section introduces the fluidized bed system and draws a parallel to how biomass feedstocks behave when compared to the conventional [1]feedstock.

2.3   Introduction to fluidized bed system

Fluidized beds reactors are piece of equipment /parts in a thermochemical conversion system where particulates materials are suspended in fluid streams in presence of heat with the aim of causing thermal degradation of the particulate material. Usually, the key component/section of fluidized bed includes a plenum, a distributor, bed region, and a freeboard region (Fig 2.5). The plenum is where the fluid enters the bed. The fluid then passes through the distributor plate, which uniformly redistribute the fluid flowing into the bed section. The particulate material to be fluidized is usually fed to the bed region supported by the distributor plate that is located on top of the plenum. Above the bed section is the freeboard where particles that have been entrained from the bed usually suspended. As fluid flow velocity through the bed increase, bed behavior could be classified into seven recognizable regimes, which are describe in section 2.5.

---

[1] Conventional feedstock here means materials with shapes that are nearly spherical and have normal size distribution
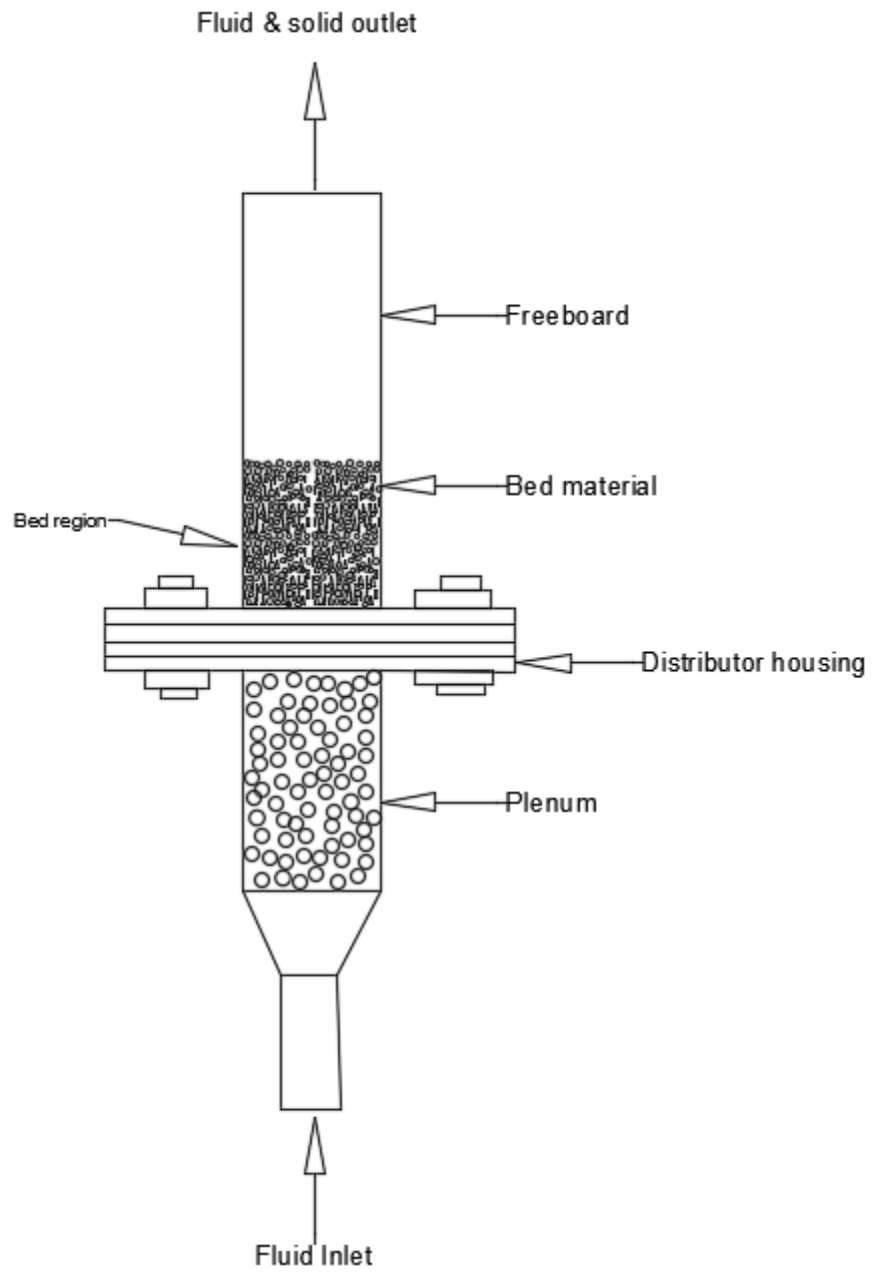
Figure 2.5: Schematic of a typical fluidized bed

2.4   Advantages and disadvantages of fluidized bed

Fluidized bed systems are particularly favored because of higher throughput than fixed bed gasification, improved heat and mass transfer, reduced char, and intense mixing of solids (fuel and bed material) that favors isothermal condition throughout the reactor. Some of the disadvantages of fluidized beds include, increase reactor vessel size to achieve complete fluidization, particle entrainment, increase-pumping requirement for gas flow, and uncontrollable pressure fluctuation that could lead to higher energy cost and bed instability. However, lack of complete understanding of particle behavior (especially those of biomass grinds) in the bed makes it difficult to predict and to calculate complex heat and mass flow within the bed (Simanjuntak and Zainal, 2015; Yates, 2013; Yin et al., 2012).

2.5   Fluidization phenomena and regimes

Raju (2011) reported that there are seven regimes of gas-solid fluidization. This include (a) fixed bed; (b) particulate fluidization; (c) bubbling fluidization; (d) slugging fluidization; (e) turbulent fluidization ; (f) fast fluidization; and (g) pneumatic conveyance. Fig. 2.6 shows the pictorial depiction of the bed condition at these fluidization regimes. When the gas flow rate is low, the fluids merely pass through the void spaces and the bed remains at its initial position (Fig 2.6a). This is called the fixed bed. As the fluid flow rate increases, the drag force between the fluid and particles becomes larger and the bed begins to expand in volume. Eventually a limit is reach when the drag force is in balance with the gravitational force and weight of particles resulting in suspension of the particle in the gas streams. At this point, the velocity is considered to be the minimum fluidization velocity and the bed is considered to be at the minimum fluidization state (Fig 2.6 b) (Davidson et al., 1977; Drake, 2011; Kunii and Levenspiel, 1991).

a	b	c	d	e	f	g
Fixed bed	Minimum fluidization	Bubbling bed	Slugging bed	Turbulent bed	Fast fluidization	Pneumatic transport
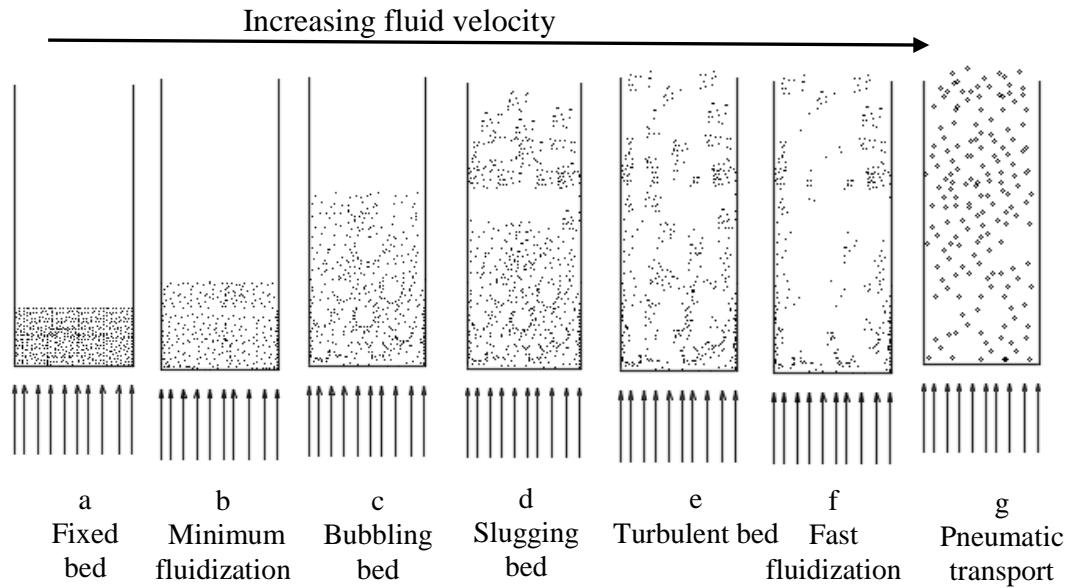
Figure 2.6: Different stages of gas –solid flow for spherical and uniformly sized particles.

When the fluid flow velocity is further increased, the excess gas starts to form bubbles within the bed (Fig. 2.6 c). The bubbles coalesce as they rise through the bed, increasing in their average diameter. As the bubble diameter expansion approaches the reactor diameter as a result of further increase in fluid flow velocity, a situation is reached when the bubbles can no longer grows, and slugging takes over (Constantineau et al., 2007). Thus slugging bed could be seen as a special case of bubbling where the bubble size is physically constrained by the wall of the fluidized bed system (Fig 2.6 d). Yang (2003) reported that slugging causes large pressure fluctuation, deteriorate bed mixing and gas-solid contact in fluidized bed. Turbulent fluidization occurs when the gas velocity is increased further still to a point where the bubbles and slugs breaks down and no longer appear distinct. Clusters and void with different sizes and shapes move about intensely. These movements limit the ability to distinguish between continuous and discontinuous phases in the bed (Fig 2.6 e). Velocity at this condition is called turbulent velocity. When the fluid velocity is further increased, the fast fluidization velocity is achieved. In the fast fluidization regime, solid particles are thrown outside of the bed as the materials are in dilute phase with the fluid. Further

21

increase in fluid velocity will result in the pneumatic transport of the particles – this fluid velocity is called pneumatic transport velocity. (Fig 2.6 g).

One of the areas of fluidization regimes studies attracting attention of researchers is the determination of the minimum fluidization velocity (U_{mf}). The U_{mf} is velocity at the point of transition between a fixed bed and bubbling fluidization regime. It is an important parameter because of its critical role in the design, operation, and characterization of fluidized beds (Ramos et al., 2002; Sánchez-Delgado et al., 2011; Suarez, 2003). Pressure drop at U_{mf} indicates the amount of drag force per unit area necessary to attain solid suspension in the gas phase. Also, U_{mf} is used as a reference for the evaluation of intensity of the fluidization regime (Yang, 2003). Therefore, in the next section discussions about how the U_{mf} is determined and the impact of biomass properties on U_{mf} are presented.

2.6   Determination of minimum fluidization velocity (U_{mf})

Usually, U_{mf} is obtained experimentally through the plots of pressure drop, bed voidage or the wall heat transfer coefficient against the superficial gas velocities (Gupta and Sathiyamoorthy, 1999). Fig. 2.7 shows the schematics describing different experimental methods for determining U_{mf} of a particulate material. On the y-axis are the bed pressure drop, voidage, or wall heat transfer coefficient, while, fluid flow velocity is on the x-axis. Using the bed pressure drop approach for U_{mf} determination, the velocity at which increasing bed pressure terminates and then reaches a constant pressure is the U_{mf} of the sample. This method is most widely used because the setup of the system to measure pressure drop and gas velocity can easily be carried out. In this research, this method was used to determine the U_{mf} of loblolly pine wood grinds. In the voidage method, the velocity at which the bed starts to expand as superficial gas velocity increases represents the U_{mf}. However, it is be difficult to measure and identify the point at

22

which expansion of bed of packed samples starts. In addition, the sophisticated instrumentation needed for experimental setup limits the usage of this method. Finally, in heat transfer method, the heat transfer coefficient of the wall with increase velocities is measured. The velocity where the heat transfer coefficient increases rapidly is regarded as the U_{mf}. However, this method requires expensive experimental setup and personnel in order to measure heat transfer data under transient state of fluidized bed.
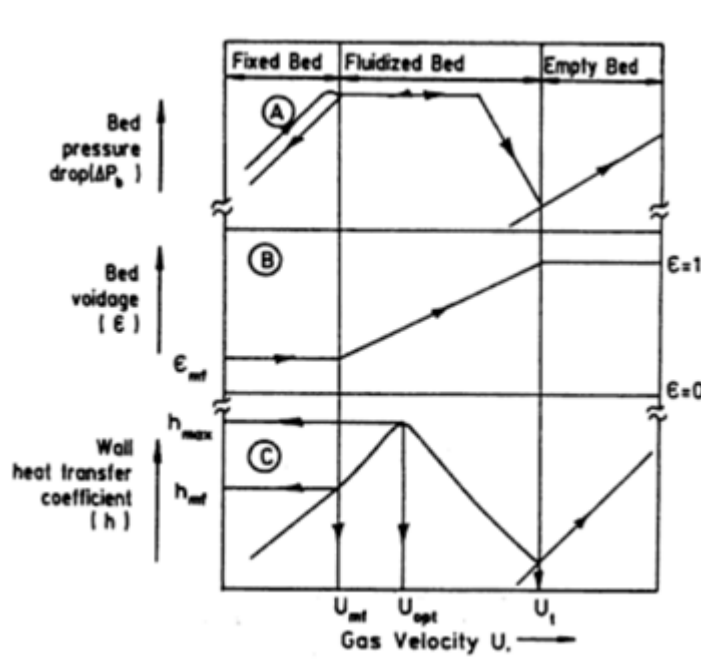
Figure 2.7: Various experimental methods to determine minimum fluidization velocity.
a) Pressure drop method; b) bed voidage variation; and c) heat transfer method (Gupta and Sathiyamoorthy, 1999)

2.7   Problem with determination of minimum fluidization velocity of biomass grinds

Earlier works on behavior of solid during the determination of U_{mf} of particle could be traced to several researcher among which is Geldart (1973) who examined the behavior of solids in a fluidized bed system and categorized them according to density differences (p_s - p_f) and mean particle sizes into four clearly recognizable groups. The key findings are presented in Fig 2.8. Geldart's classification requires that the average diameter of the material to be fluidized be known. For spherical materials, a single diameter value is obtained by measuring the size,

23

surface area or volume of the particle. This is not the case for non-spherical particles because the diameter measured depends strongly on the particle orientation during measurement (i.e. the measurement method or scheme used). In addition, Geldart's assumption underestimated the impact of multi-component beds material where the mean diameter may not be adequate in quantifying the size of all particles in the bed.
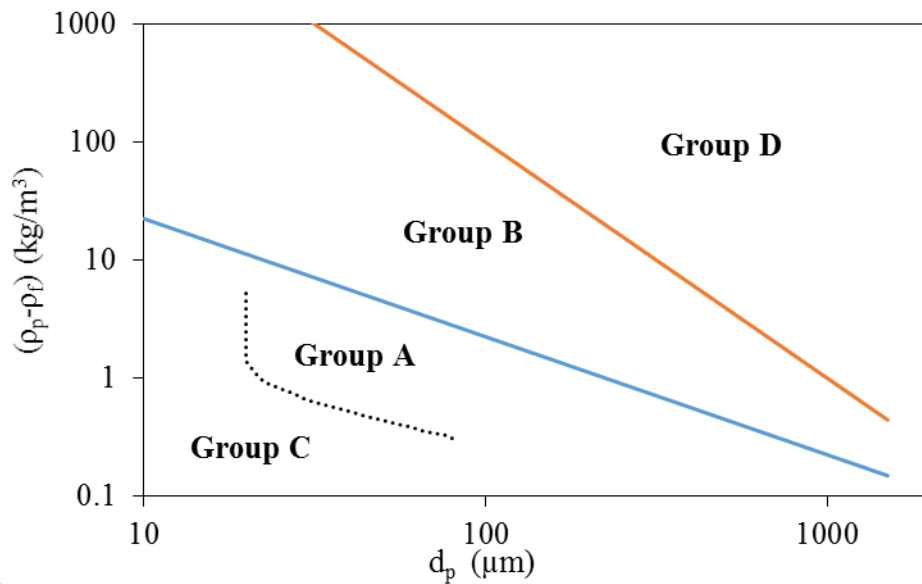
Figure 2.8: Geldart's classification (Geldart, 1973)

Similar notable authors have agreed that complete characterization of fluidized bed can never be captured with only mean particle diameter. They also expressed that the distribution of particle sizes about its mean also play a very important role on bed behaviors such as bed expansion, decreased incipient fluidization velocity and, increased minimum bubbling velocity (Gauthier et al., 1999; Grace and Sun, 1991; Jiliang et al., 2013; Khoe et al., 1991; Lv et al., 2004; Reddy and Mahapatra, 1999; Sun and Grace, 1992; Tanfara et al., 2002; Wang et al., 2007).

Furthermore, some other authors reported specific factors that affect the determination of minimum fluidization velocity (U_{mf}). For instance. Gunn and Hilal (1997) investigated fluidization of glass beads of 100 µm particle size using two different bed with internal diameter

(ID) of 0.09 and 0.29 m and obtained a U_{mf} of 0.025 and 0.017 m/s respectively. The author concluded that the wall effect is stronger in bed with 0.09 m ID and this was responsible for higher U_{mf}. Furthermore, the author adjusted the samples in the bed to different height (0.02 – 0.05) and found that the U_{mf} is independent of the bed height.

Ramos et al. (2002) also used glass beads with particle size:160–250, 250 – 400, 490–700 μm in a column made by Perspex sheets with dimension of $1.0\times0.2\times0.012$ m . The U_{mf} was determined by pressure drop method and found to be 0.05, 0.17 and 0.35 m/s respectively. The author also measured the U_{mf} for different bed heights (2, 4, 8, 16, 20, 40 and 60×10^{-2} m) as well as for different bed widths (6, 7, 9 and 12 m). The author found that U_{mf} depends on the particle diameter, and column width, and that the friction of the bed at the wall increases as bed height, and particle diameter increase, and the bed width decreases.

In summary, particle fluidization using a bed consisting of particle with uniform particle size and density may appear easy. But when the fluidizing bed is comprised of non-uniform and non-spherical particles as is typically the case for biomass grinds, the behavior of particle at the various fluidization regimes becomes difficult to determine because of the possibility of occurence of one or more regimes at a given airflow rate.

2.8   Biomass material properties that influence its fluidization

In order to understand and apply the established principle of fluidization to biomass grind fluidization, it is necessary to determine important factors affecting the fluidization of solids, particularly the point at which movement of particles is initiated. Table 2.3 showed some selected work on fluidization of biomass grinds and their key findings on influence of biomass material properties on fluidization.

Table 2.3: Selected work on solid-gas fluidization

Material/ properties	Diameter scheme	Fluidizing	U_{mf} (m/s)	Key finding	Reference	Issue identified
Coffee husk 1.6 mm 2.6 mm 2.0 mm	Sieve analysis; Sauter mean	Air	0.37 0.52 0.92	Particle size and U_{mf} has power relationship	Suarez (2003)	Particle size
Rice husk 0.93 0.66 0.40 Sawdust 0.66 0.40 Groundnut shell 0.93 0.66 0.4	Sauter mean	Air	0.54 0.50 0.48 0.54 0.48 0.62 0.48 0.54	Particle elutriate at velocity greater than 0.65 m/s Increase in fluidizing velocity resulted in less segregation Huge differences between predicted and observed values of U_{mf} using 7 different fluidization equations	Rao and Reddy (2010)	Size distribution Predicting equations Gas flow velocity
Walnut 856 µm Corn 1040 µm	Sauter mean	Air	0.55 0.61	Predicted values from selected fluidization equations underestimated actual data.	Paudel and Feng (2013)	Predicting equations
Bagasse Sieve screen 335 – 125 µm	Median / effective diameter	Air	0.10 – 0.15	Higher diameter ratio (inert/biomass) caused more pronounced bed segregation About 40% relative error between actual and predicted values	Oliveira et al. (2013)	Shape Predicting equations
Quart Sand	Sauter mean	Air		Ergun equation assumes that pressure drop occurs	Jiliang et al.	Temperature

0.5 mm Bottom Ash 1.29 mm			0.75	solely due to gas-particle drag force, neglecting the effects of inter-particle forces. U_{mf} reduced with increase in temperature. Wide size distribution lowers U_{mf} as a result of small particle infilling between bigger particles and in the process gives lubricate effect Correlations fail completely for giving unacceptably high errors (> 50%)	(2013)	Particle size distribution Predicting equations
Rice husk 1100 µm Bagasse 1250 µm Sawdust 530 µm	Mean	Air	0.155 0.153 0.145	Higher proportion of biomass in mixture with sand negatively affects fluidization. Predicted values from selected fluidization equations underestimated actual data	Karmakar et al. (2013)	Mix ratio Predicting equations
Tobacco stem 17.5 mm	Arithmetic mean size (Vernier caliper)	Air	0.22	TS particles could not be fluidized even at the highest superficial gas velocity of 1.48 m/s A good mixing behavior was maintained when the superficial gas velocity was less than five times of the U_{mf}	Zhang et al. (2012)	Shape Gas flow velocity
Olive pits: 1540 µm	Sauter mean	Air	0.66	Top and bottom fluidization due to difference in particle size and density	Formisani et al. (2014)	Density/size
Beech: 0.0134m Balsa: 0.0076 m	Equivalent spherical	Air	1.54 0.59	Partial segregation of wood with 20 – 50% floated at the bed surface. When the velocity was low (< 3 U_{mf}), the biomass particles tended to be more segregated than when the	Cluet et al. (2015)	Density Particle size

				velocity was higher than 3 U_{mf}		
Pine: 1 mm	Screen size	Air	0.48	The superficial velocity thus corresponds to 4–10 times of minimum fluidization velocity.	Jae et al. (2014)	Fluidizing velocity
River sands 282.5 µm 450.0 µm 900.0 µm 1425.0 µm 1800.0 µm	Sauter mean	Air	0.06 0.12 0.58 0.92 1.12	Bed transition from one fluidization regime to the other depends strongly on particle size distribution. Prediction of U_{mf} of 450.0 µm sample resulted in 50 % error deviation while others were below 50%. The author attributed the error to substantial difference in properties of the samples mixed in equal proportion.	Gauthier et al. (1999)	Size distribution Predicting equations
Sawdust 0.63 mm 82% MC 54% MC 45% MC 33% MC 26% MC 8% MC	Sauter mean		0.41 0.43 0.32 0.32 0.27 0.25	Sawdust by itself does not achieve adequate fluidization at moisture contents of 8–82 wt% on a dry basis	Clarke et al. (2005b)	Moisture content
Coal 104 µm	Martins	Air	0.06	Increase moisture causes inhomogeneous and sluggish formation of the fluidized bed over the entire velocity range	Merzsch et al. (2013)	Moisture content
Palm frond 1.83 mm	Arithmetic mean (Vernier caliper)	Air	0.7	An average percentage error calculated for all the 32 data points was more than 50%	Puspasari et al. (2013)	Predicting equations Shapes

28

In summary, particle size and distribution including diameter measurement scheme, particle shape, density, moisture content, and predicting equations are some of the major factors that are attracting attention in fluidization research. The next sections delve more on each factors and why they are important in biomass fluidization.

2.8.1   Particle size distribution

Lignocellulosic biomass requires size reduction before conversion process can commence because available technologies for converting biomass to biofuel cannot handle the harvest sizes of biomass feedstocks (Khanal, 2010; Mosier et al., 2005; Takara et al., 2010). Particle size is therefore one of the important parameters that influence the design and sizing of fluidized bed reactor and supporting facilities (Barakat et al., 2013; Schell and Harwood, 1994).

However, size reduction of biomass feedstock inevitably results in particles with non-uniform size distribution and non-spherical particle shapes. For instance, Fasina (2008), reported that the size range of peanut hull ground through 3.18 mm screen was between 0.10 and 3.40 mm nominal screen size. The size distribution was lognormal with geometric mean diameter (d_{gw}) and geometric standard deviation (s_{gw}) of 0.65 and 0.75 mm respectively. Fig 2.9 shows the size distribution profile of peanut grinds. This is similar to particle size distributions that have been reported for other biomass grinds (Chevanan et al., 2011; Gil et al., 2013; Vaezi et al., 2013). The plot has a tail toward the right hand side showing that certain portion within the sample has particle size greater than 3.0 mm while other particle size are less than 0.1 mm.

29
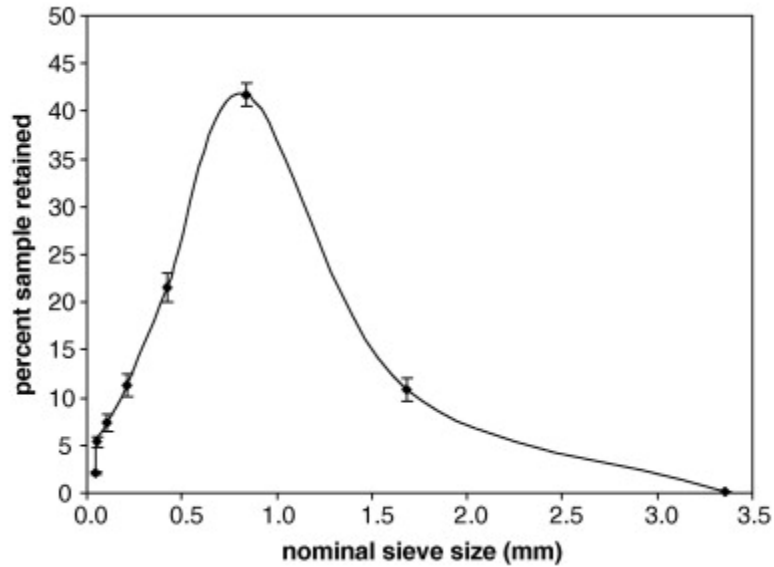
Figure 2.9 : Particle size distribution for peanut hull grind Fasina (2008).

In another study, Gil et al. (2013) used a hammer mill fitted with 2 mm screen size and obtained a d_{gw} and s_{gw} of 0.30 and 2.60 mm respectively for ground polar wood and 0.26 and 2.66 mm for ground cornstover. Fasina (2006) ground switchgrass through hammer mill fitted with 0.8, 1.6 or 3.2 mm screen sizes and obtained a lognormal particle size distribution with d_{gw} of 0.17, 0.23, 0.39 mm and s_{gw} of 0.15, 0.19 and 0.36 mm respectively. Also, using a hammer mill fitted with 2.4 and 4.6 mm screen size, Kaliyan and Morey (2009) ground switchgrass and obtained d_{gw} of 0.49 and 0.64 mm and s_{gw} 0.31 and 0.30 mm respectively. Similarly, Mani et al. (2004) obtained 0.25 and 0.43 mm for d_{gw} and s_{gw} respectively when switchgrass particle were ground through 0.8 mm screen size.

When particle size varied significantly, the question becomes how to determine the most appropriate mean particle size to represent the distribution since equipment design, facilities development, and modeling equation would require that the mean size be known. Fig. 2.10 showed comparisons of various types of mean diameter that can be

30

obtained from particles with lognormal size distribution. It can be seen that the estimated

mean diameter from the sample is dependent on how the mean diameter is computed.

This also implies that adoption of a particular mean value may over/under estimate the

sample parameters and result in error. It appears that most published articles that attempt

to predict the fluidization velocity used particle Sauter mean diameter (Paudel and Feng,

2013; Rao and Reddy, 2010). Loth et al. (2004) attributed the reasons for wide

acceptability of Sauter mean diameter in fluidization to its ability to better estimate the

average effect of net gravitational and drag force. Presently, there are no published works

on the comparisons of different mean estimates on biomass grinds process operation

prediction.
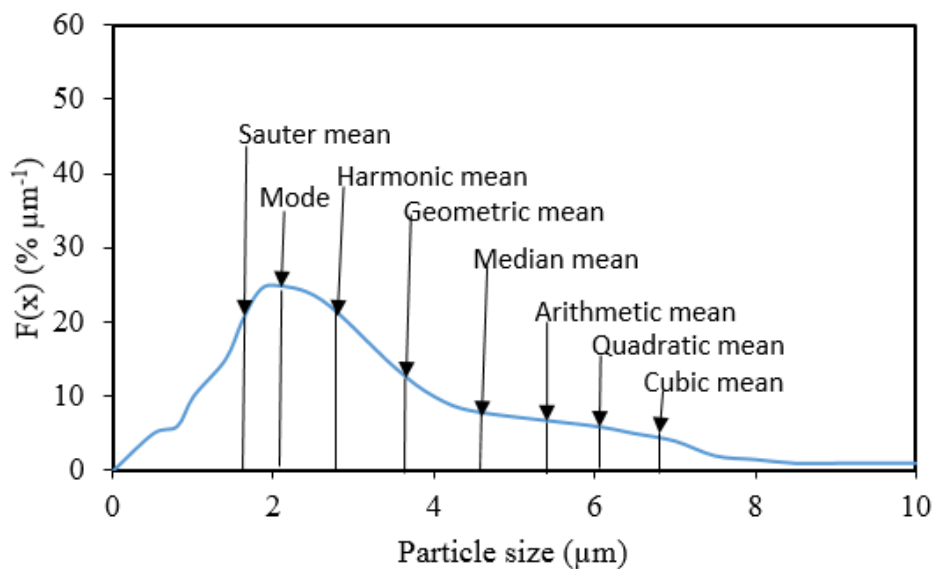
Figure 2.10: Comparisons between measures of central tendency

2.8.2 Particle size distribution measurement

2.8.2.1 **Particle size measurement using sieve analysis**

Sieve analysis uses set of nested sieves arranged with decreasing size of the screens of the sieves. The last sieve in the set/column is a round pan, called the receiver. Appendix 2.1 shows sieve classification for the US standard and Tyler series systems. In order to perform a sieve analysis, about 100 g of the sample is placed into the first sieve which is the largest screen size (ANSI/ASABE, 2012). The column is typically placed in a mechanical sieve shaker such as Tyler Ro-Tap[2]. The shaker shakes the column, usually for some 15 minutes. For hand-sieving, the nest of test sieves is inclined at an angle of about 20° with the point at which the sieve is held in the lower position, and the sieve (or nest) is tapped for approximately 120 times a minute with the other hand. After tapping, the sieve is returned to a horizontal position (90°) and tap until the mass on each sieve at 1-min intervals changes by 0.1% or less (ANSI/ASABE, 2012). After sieving operation, the mass fraction retained on each sieve is measured and midpoint of each interval chosen as the representative particle diameter. The process of obtaining sieve diameter is laborious and time consuming because of the time involved in selecting and weighing the sieves. Also, the choice of sieve set that is used may be subjective and may influence the calculated mean diameter (Mora et al., 1998).

In addition, one of the dimension of the particle passing through a sieve can be larger than the size of the aperture. Fig 2.11, shows that an elongated particle having its length greater than the aperture size can pass through the sieve without any difficulties.

---

[2] Registered trade name

Therefore, the sieve aperture size is a measure of the lateral dimensions of the particles only.
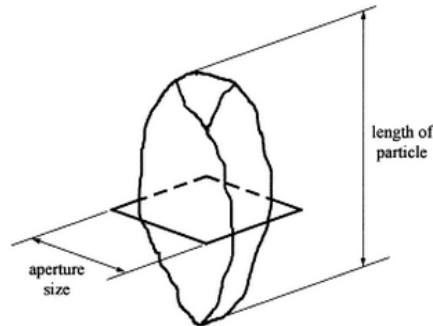
Figure 2.11 An elongated particle passing through a square sieve aperture (Mora et al., 1998).

To illustrate data obtained from sieve analysis, a plot of either the percentage of sample (on mass basis) retained on each sieve or a cumulative distribution of mass as a function of sieve size can be displayed. When the sieving result is plotted on a 3-cycle log paper, and a linear plot is obtained for the entire data range, then the material is characterized as a lognormal distribution. When the line is curved and consists of two or more linear segments, then the distribution is polymodal (Brittain, 2002).

Several mean diameter estimate could be obtained from sieve analysis result such as the surface /Sauter mean diameter (d_m) (Eqn. 2.1), mean volume diameter (Eqn. 2.2), geometric mean diameter (d_{gw}) (Eqn. 2.3), and median diameter (d_{50}). Depending on the intended use one mean value can have more significance to the analyst than another (Brittain, 2002). Table 2.4 shows the diameter schemes that can be obtained from sieving method and typical applications of each diameter scheme.

Table 2.4: Diameter type from sieve analysis and their field of application

Mean diameter	Field of application	Reference
Median	Atomization, mass transfer, agglomeration	Turchiuli et al. (2013)
Surface	Adsorption	Azzopardi (2011)
Volume	Evaporation, molecular diffusion	Liu (2012)
Sauter	Efficiency studies, mass transfer, reaction	Gelves et al. (2014)
Geometric	Statistical characterization	Hinds (2012)

$$d_m = \frac{1}{\sum {x_i}/{d_i}} \qquad (2.1)$$

$$d_v = \frac{1}{\sqrt[3]{\sum {x_i}/{d_i^3}}} \qquad (2.2)$$

where,

d_m = Sauter mean diameter or surface mean diameter (d_m) (mm)

d_i = arithmetic mean of the aperture (opening) of adjacent sieves (mm)

x_i = mass fraction on ith sieve

d_v = volume diameter (d_v) (mm)

$$d_{gw} = \log^{-1}\left[\frac{\sum_{i=1}^{n}\left(W_i \log \overline{d_i}\right)}{\sum_{i=1}^{n} W_i}\right] \qquad (2.3)$$

$$S_{\log} = \left[\frac{\sum_{i=1}^{n}\left(W_i \log \overline{d_i} - \log d_{wg}\right)^2}{\sum_{i=1}^{n} W_i}\right]^{1/2} = \log\left(\frac{d_{84}}{d_{50}}\right) = \log\left(\frac{d_{50}}{d16}\right) \qquad (2.4)$$

$$S_{gw} = \frac{1}{2}d_{gw}\left[\log^{-1} S_{\log} - \left(\log^{-1} S_{\log}\right)^{-1}\right] = \frac{1}{2}\left[d_{84} - d_{16}\right] \qquad (2.5)$$

where,

d_{gw} = geometric mean diameter or median size of particles by mass, (mm) or $\overline{d_i}$ =

$\sqrt{d_i \times d_{i+1}}$

d_i = nominal sieve aperture size of the ith sieve (mm)

d_{i+1} = nominal sieve aperture size in next larger than i^{th} sieve (just above in a set) (mm)

S_{log} = geometric standard deviation of log normal distribution by mass in ten-based logarithms, dimensionless.

S_{gw} = geometric standard deviation diameter of particles by mass, mm

W_i = mass on i^{th} sieve (g)

n = the number of sieves +1 (pan)

d_{84} = particle diameter at 84% probability (mm)

d_{50} = particle diameter at 54% probability = median diameter (mm)
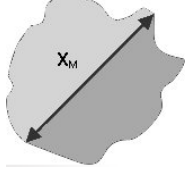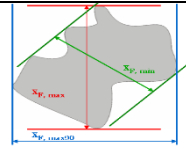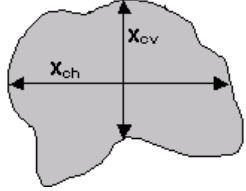
d_{16} = particle diameter at 16% probability (mm)

2.8.2.2 **Particle size measurement using image analysis**

Image analysis is the process of extracting size information from digitized image of particles by analyzing the pixel array (Nazar et al., 1996). Image measurement technique uses digital camera and image analysis software to acquire and analyze image. The characterization of particle using image analysis involves five procedures: image acquisition, preprocessing, segmentation, data extraction and representation (Nazar et al., 1996). This technique has been widely used in applications such as agriculture (Cardoso et al., 2013; Miller and Henderson, 2010), pharmaceutical (Heinicke and Schwartz, 2004), and combustion analysis (Mason et al., 2015).

The captured images are then further processed by computer software to extract useful information, which is then used to produce the size distribution, numbers of detected particles and the various mean particles diameters (Table 2.5). Some of the diameter schemes that are obtainable from software used to analyze images of non-spherical shaped particles include Martin, Ferret, chord, and projected area diameters. Furthermore, image analysis can provide detailed information on particle size distribution for each of these different diameter schemes (Figure 2.12). In addition, the diameter schemes that are obtained from sieve analysis method can also be obtained from image analysis methods (see Eqn. 2.1 -2.5).

Table 2.5: Definition of the diameter types from image analysis software.

Symbol	Diameter scheme	Formula and definition	Representation
X_{Ma}	Martins	Length of the chord through the centroid which bisects area of the particle into two equal halves.	GmbH (2011)
X_{Fe}	Ferret	Longest distance between parallel tangents touching opposite side of the object.	GmbH (2011)
X_c	Chord	The distance between two points on the contour, measured exactly across the center of gravity of the projection area. Chord length can be divided into minimum and maximum.	GmbH (2011)
Xarea	Area	Particle diameter calculated from the projected area (A) of particle $$X_{area} = \sqrt{\frac{4A}{\pi}}$$	
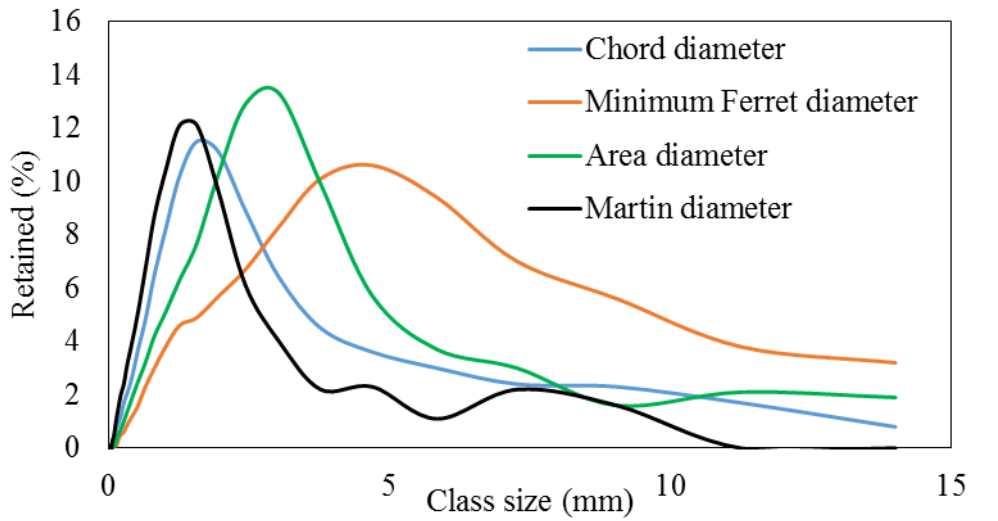
Figure 2:12: Particle size distribution from image analysis using different diameter type

Data obtained from the schemes used to measure the size of irregular-shape particles have been shown to be different and not in agreement (Trottier and Dhodapkar, 2014). Apart from imaging technologies, every other particle characterization technologies provide measurement of an equivalent spherical diameter as the particle pass through restricted volume or channels under the influence of gravity or centrifugal force field or interaction with some form of radiation or ultrasonic waves dynamic (Allen, 2003). For non-spherical particles, Trottier and Dhodapkar (2014), concluded that image analysis offered the best measurement in terms of accuracy, precision, resolution, capital cost, skill level and analysis time (Table 2.6). However, particle orientation in measurement field affect the result of image analysis as irregular particle can potentially present different cross section depending on orientation. Next section presents information on particle shape factor.

Table 2.6 : Advantages and limitation of particle size measurement techniques

Technique	Range, μm	Basis	Analysis Time	Precision	Accuracy	Resolution	Throughput	Capital Cost	Skill Level
Ensemble Techniques									
Laser Diffraction	0.04–2,000	Mass	Short	High	High	Low	High	High	Low
Dynamic Light Scattering	0.003–1	Intensity	Short	High	High	Low	High	Medium	Low
Ultrasonic Spectroscopy	0.01–1,000	Volume	Short	High	High	Low	High	High	Low
Fractionation Techniques									
Wet Sieving	>5	Mass	Medium	High	High	Low	Medium	Low	Low
Dry Sieving	>45	Mass	Medium	High	High	Low	Medium	Low	Low
Sedimentation	0.05–100	Mass	Medium	High	High	High	Medium	Medium	Medium
Field-Flow Fractionation	0.003–3	Mass	Medium	High	High	High	Medium	Medium	High
Hydrodynamic Chromatography (HDC) and Capillary HDC	0.02–1	Mass	Medium	High	High	High	Medium	Medium	High
Single-Particle Counting Techniques									
Dynamic Image Analysis	>5	Number	Short	High	High	High	High	Medium	Low
Optical Particle Counting	0.2–2,500	Number	Short	High	High	High	High	Medium	Medium
Electrozone Counter	0.4–1,200	Number	Short	High	High	High	High	Medium	Medium

Source (Trottier and Dhodapkar, 2014).

2.8.3 Particle shape factor

Shape factor is a dimensionless number used to characterize the shape of an object (Bouwman et al., 2004; Saad et al., 2011). Shape of a particle or geometry can be described by two or more shape factors namely form, roundness, irregularity aspect ratio and sphericity (Blott and Pye, 2008; Bouwman et al., 2004). Sneed and Folk (1958) used the term form to describe shape factor by finding the ratios of its three linear dimensions: length, breadth, and thickness. Blott and Pye (2008) defined roundness as angularity or sharpness of corners and edges of particles. Irregularity relates to the deviation of external expression of an object from that of a regular body due to indentations (Blott and Pye, 2008). In addition, the authors defined sphericity as a measure of the degree to which the shape of a particle approximates that of a true sphere and is dependent on both

39

form and roundness. Gantenbein et al. (2011) defined the aspect ratio (AR) of a particle as the proportional relationship between its width and its height.

Shape fof a non spherical particle has been widely repored using a scaled number from 0 to 1. For instance, Cui and Grace (2007) classified flatness of particles based on their sphericity. Sphericities of $\varphi < 0.5$ indicates an extremely flat particles, $\varphi > 0.5$ indicates flat particles and $\varphi > \sim 0.8$ is nearly spherical particles. Similarly, Lucas et al. (1986) also classified sphericity of particles into three categories namely, round ($0.8 \leq \varphi \leq 1$), sharp ($0.5 \leq \varphi \leq 0.8$) and others ($0.1 < \varphi < 0.5$). Recently, ISO 9276-6 defines the aspect ratio as the ratio of the Feret's minimum length to the Feret's maximum length. This is done to scale the aspect ratio such that the value is always in the range, $0 < AR \leq 1$ (Olson, 2011).

Sphericity (De Diego et al., 2002; Gil et al., 2014) and aspect ratio (Guo et al., 2012; Lu et al., 2010) are popularly used in characterizing the shape of biomass grinds. Since biomass grinds are not spherical, the effect of non-sphericity may cause discrepancies in estimating mean size results (Gil et al., 2014). For instance, Lees (1964) reported considerably deviation in average volume of particle retained on any sieve between spherical and non-spherical particle of the same material. This was also corroborated by Fernlund (1998) who used railroad aggregate with fraction ranged between 32 – 64 mm and concluded that the probability of particles passing through screens of a sieve depend strongly upon the shape of the particles. De Diego et al. (2002) studied devolatilization time of pine chips having particle size ranging from 7 to 37 mm with shape factor sphericity of 0.40 – 0.75, at temperature ranging from 650 and 950 ^{o}C. The author concluded that the models developed for spherical particles can be applied to particles of

different shapes by replacing the particle dimension in the model with the equivalent particle diameter multiplied by the shape factor.

When the particles are not spherical, the particles present more points of contact between each other and therefore make relative motion very difficult (Gil et al., 2013). In addition, as the point of contact within particles increased the friction between particles accordingly. If the bed consists of particles that are elongated, then the tendency of the particles in the bed to interlock is increased (Mattsson and Kofman, 2002; Paulrud et al., 2002).

In summary, a single measurement (mean diameter) may not be adequate to describe a typical non-spherical particle with particle size distributions. There are various definitions of size measurement schemes and standardized shape factors can provide additional descriptors to a particle population, which may be necessary to consider in particle characterization for model development and validation. These measurement schemes and shape factors can be measured using dynamic image analysis. However, like all measurement techniques, there are limitations and possible sources of error. These limitations can be minimized with a thorough understanding of the various diameter measurement scheme and shape factor definitions and how they can be used to improve the particle characterization and measurement.

2.8.4 Density of biomass grinds

2.8.4.1 **Bulk density**

Bulk density is the ratio of the mass of a bulk material to its bulk volume. Bulk density is an important parameter in material handling, storage, and transport, (Mani et al., 2006) and in designing and sizing of facilities for biomass conversion. For biological materials, the bulk density is affected by particle size, particle shape, moisture content, and specie/type of biomass. In fluidization, bulk density also influences the void spaces between particles, thus, affecting inter-particle movement and air penetration through the bed (Abdullah et al., 2003; Paudel and Feng, 2013).

Several studies have been conducted to quantify the bulk density of various biological material and its relationship with other properties of the material. Firstly, studies show that bulk density generally decreases with increase in particle size. This is because, void spaces within particle increases when bulk product particles do not fit together partly due to shape irregularity, size distribution, particle orientation, or packing arrangement (Klieger and Lamond, 1994). Hence, when particle size increase, void spaces increases and bulk density reduces. For instance, when the d_{gw} of wheat straw increased from 0.25 to 1.43 mm, the bulk density reduced from 115 to 77 kg/m^3 (Mani et al., 2004). Also, when the d_{gw} of switchgrass increase from 0.17 to 0.39 mm, bulk density reduced from 294 to 243 kg/m^3 (Fasina, 2006).

However, some studies have also showed that bulk density increases with increase in size up to a certain size limit. For instance, as the size of fluid cracking catalyst (FCC) increased from 6 to 25 µm, Abdullah and Geldart (1999) found that bulk density first increased from 400 to 700 kg/m^3 with increase in particle size up to 80 µm. The author

42

attributed this behavior to weakening of inter-particle force as particle size decreased for particle less than 25 µm resulting in less dense condition and decrease in bulk density. Also, Mani et al. (2004) reported similar behavior in which the bulk density of wheat straw grind increased from 104 to 115 kg/m^3 as size increase from 0.18 to 0.25 mm before reducing to 77 kg/m^3 when particle size were further increase to 1.43 mm. The author attributed higher density to the ability of fine particles to repel and create more void spaces. Chevanan et al. (2011) also reported that bulk density of corn stover, significantly increased ($p < 0.05$) by approximately 50% when particle size increased from 3.26 to 12.79 mm. This was attributed to packing effect of non-spherical shape of the grind in which at certain particle size, particles tend to repel, creating more void space (Mani et al., 2004).

Furthermore, moisture content of a feedstock has been reported to affect the bulk density. Generally, increase in moisture content results in decrease in bulk density. Increase in moisture increases the particle weight but the increment rate is lower compared with the resulting volumetric expansion of the bulk (Oginni, 2014). For instance, Littlefield et al. (2011) reported that the bulk density of pecan shells reduced from 460.3 to 396.7 kg/m^3 when moisture content increased from 4.4% to 24.7% wet basis. The author attributed this to moisture addition that increased the volume of the bulk pecan shells at a faster rate compared to the increase in mass of the pecan shells.

2.8.4.2 **Particle density**

Particle density is the ratio of the average mass to the average volume of particles that form the bulk solid. Particle density affects the state of dispersion and settling velocity of

particles (Onwulata, 2005). It is also important in understanding and determination of bulk solid structure (Ortega-Rivas et al., 2006).

Particle densities of several biological material has been reported in the literature, for example, Gil et al. (2013) reported that the particle density of ground poplar varied between 1293 and 1457 kg/m^3 as particle size reduced from 5 mm to 2 mm. Also, Hehar et al. (2014) classified loblolly pine ground wood into four groups namely unfractionated (< 420 μm), coarse (180–420 μm medium (90–180 μm) and fine (< 90 μm) and measured their particle densities to be 1437.9, 1423.6, 1448.3 and 1443.6 kg/m^3 respectively. Mani et al. (2004) also measured the particle density of wheat straw, barley straw, corn stover and switchgrass as 1030.0, 890.0, 1170.0 and 950.0 kg/m^3 respectively. The various studies on woody biomass grinds have shown that their particle densities tend to be higher than that of herbaceous straw biomass. Wang (2014) concluded that biomass with high particle density offer better flowability but low inner porosity that could limit gas-solid interaction during fluidization.

Particle density is an important parameter in fluidization studies because it is the main factor that causes segregation and defluidization (Zhang et al., 2009). When there are substantial variations in particle densities of bulk material to be fluidized, the less heavy particles are first fluidized while the heavier ones are still un- fluidized. Formisani et al. (2008) concluded that segregation constitutes a serious obstacle to predicting the state of mixing of the solids of the bed at a known regime of fluidization. Accordingly, potential advantages such as uniform thermal conditions and good product quality that are associated with proper regulation and control of mixing cannot be adequately exploited in fluidized bed system.

2.8.5   Moisture content

Moisture content (MC) is one of the major causes of the high variability in properties of biomass feedstock. This is because moisture influences flowablility, compressibility, cohesion and adhesion of particles as a result of formation of inter-particle bonds in biomass grinds (Fasina, 2008; Mani *et al.,* 2004; Probst *et al.,* 2013). For a bio-refinery plant, biomass feedstock may come from various sources with significant differences in time of harvest, specie of biomass and storage time. As a result biomass feedstock do not arrive at biorefinery plant at the same moisture content. Therefore, drying or rewetting may be necessary for preparing a material for conversion (Wright et al., 2006).

Impact of moisture content on fluidization processes has attracted attentions of several researchers. Some workers looked at the effect of moisture on the yield and products composition obtained from gasification /fluidization process. For instance Brammer and Bridgwater (2002) studied the influence of moisture before and after drying on the performance and cost of a fluidized bed gasifier engine for the combined generation of heat and electricity. They discovered that as moisture content increased from 45 to 100 % dry basis, overall efficiency reduced from 70 to 60% and cost of electricity increased from 10.5 to 12.0 c/kWh. This was attributed use of to heat/thermal energy to evaporate water contained in the biomass before actual conversion started.

Demirbas (2002) also investigated the relationship between heating value and lignin, moisture, ash and extractive content of biomass fuels. The author observed that heating value of biomass decreases with increase in moisture content. Similar result was also obtained by Antonopoulos et al. (2012) who reported that when moisture content of the

olive, miscanthus and cardoon increased by 40%, the lower heating value of the syngas obtained from a downdraft gasifier reduced by about 1 MJ/m^3.

Similarly, Plis and Wilk (2011) investigated the influence of moisture content (7.0 and 13.0 % wet basis) using wood pellet having cylindrical shape, with a diameter of 6 mm and a length of 10-30 mm on syngas production. The study found that the CO content in the syngas reduced from 27.47 to 16.44 % vol. dry basis as moisture content increased. Similar reductions were also obtained for the remaining combustible components in the syngas as moisture content increased (Fig 2.13).
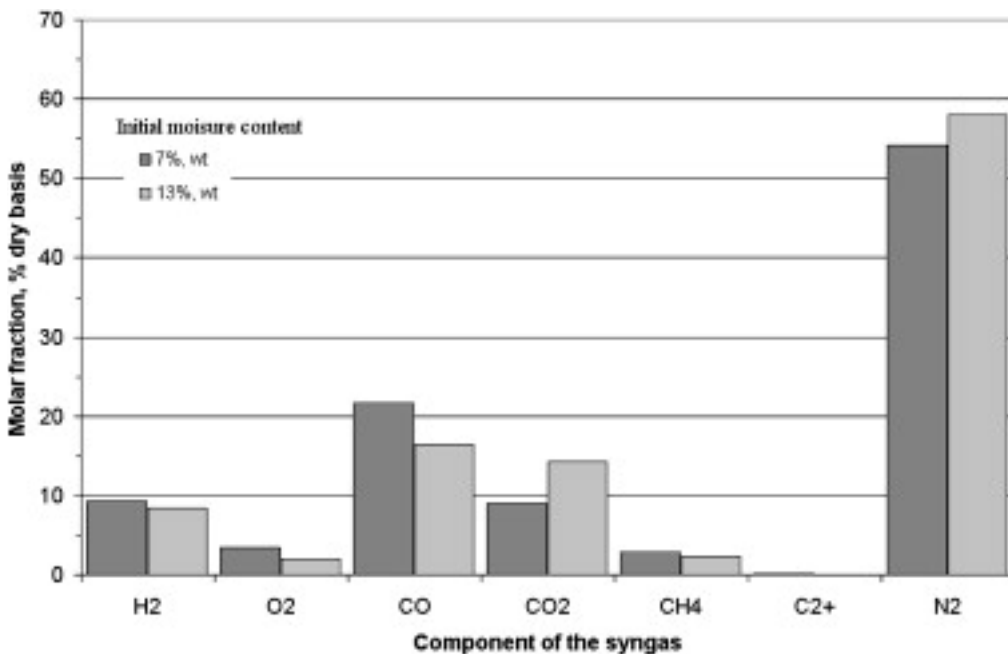
Figure 2:13: Comparison of the syngas composition in the case of dry and wet biomass gasification

Furthermore, some author have studied the impact of feedstock moisture on the fluidized bed hydrodynamics behavior. Clarke et al. (2005a) fluidized sawdust having 0.63 mm mean particle size. The sawdust moisture content was varied between 8 and 82 %-wet basis. The bed material used was glass sphere with particle size range 0.32 to 1.04 mm.

46

The U_{mf} was determined using pressure drop approach and was found to increase from 0.25 to 0.63 m/s as moisture content of the sawdust increased. They also observed that when moisture content exceeded 33 %, channeling became predominant in the bed and made determination of U_{mf} difficult to determine experimentally.

Wormsbecker and Pugsley (2008) linked poor fluidization states (channeling, entrainment, segregation) to feedstock moisture content. When particles are wet, a high fluid velocity is required to avoid segregation, defluidization and channeling due to dominant cohesive forces exerted by wetted surfaces and this could also cause top layer of the bed to be fully fluidized while the particles at the bottom were still stationary (Syahrul *et al.,* 2003).

Hartman et al. (2006) investigated the impediment to incipient fluidization in wet bed of porous ceramsite and lignite in a cold model fluidized bed. They found that as the moisture content in the bed increased from 15 to 30 % by mass, the limiting air velocity increased from 0.05 to 1.05 m/s. However, they observed that the equilibrium of the bed is affected by presence of free surface liquid that tends to hold the particles together. Gröger et al. (2003) explained this phenomenon as the inter-particle cohesion that enhanced the capillary forces arising from formation of liquid bridges between particles in contact.

In summary, because feedstock particles have extreme shapes, wide size distribution, non-uniform densities and significant moisture variations, estimation of parameters needed to develop facilities for fluidizing biomass feedstock pose technical challenge as to which properties is most important and must be given high priority. However,

conducting an experiment under certain operating conditions for fluidized bed system

may be difficult and require elaborate experimental setup and technical expertise. Hence,

it is usual to rely on equations and correlations earlier developed for other feedstock in

order to estimate the parameters. However, because those equations were developed

under certain condition, adapting them may require some modification. Next section

discusses some of the equations used in estimating fluidization parameter and basic

assumptions used in developing them.

2.9   Fluidization models/ predicting equations

In this section, the mathematical modeling studies related to prediction of minimum

fluidization velocity, and computational fluid dynamic models that has been used to

predict the state of bed during fluidization is reviewed and presented.

Predicting minimum fluidization velocity (U_{mf}) and the state of the bed has been

performed for decades using models that vary from simple equation of motion to highly

sophisticated three-dimensional unsteady models that utilize fluidization hydrodynamics

through coupling of fundamentals mass, momentum and energy balance equations. In

predicting U_{mf}, modeling approaches can be divided into the following categories: (1)

pressure drop approach, (2) empirical model approach, and (3) Computational Fluid

Dynamics (CFD) modeling approach. In the following section, each category will be

described and discussed.

2.9.1   Pressure drop approach

Pressure drop approach is the most widely used method of predicting minimum

fluidization velocity of a bed material. The pressure drop (ΔP) derived from a force

balance for the bed is related to the weight of the bed and the cross sectional area, (A).

Conceptually, when flow velocity is increased, the pressure drop increases until the

weight of material in the bed counter balance with the updraft created from the airflow.

At this point, the bed is supposed to be in fluidized state provided that (Yerushalmi et al.,

1976)

a) all solid particles are in densely packed,

b) clusters are spherical,

c) there are no walls or acceleration effects,

d) clusters have a voidage equal to that at minimum fluidization, and

e) clusters are discretely distributed in the bed.

The established correlation that is mostly used in the pressure-drop approach estimation

method is the Ergun (1952) equation (Eqn. 2.6):

$$\frac{\Delta P}{L} = 150\frac{(1-\varepsilon)^2}{\varepsilon^3}\frac{\mu_g U_m}{d_p^2} + 1.75\frac{1-\varepsilon}{\varepsilon^3}\frac{\rho_g U_m^2}{d_p} \tag{2.6}$$

Also using the pressure – weight per unit area balance, the pressure drop can be written

as:

$$\frac{\Delta P}{L} = (1-\varepsilon)(\rho_s - \rho_g)g \tag{2.7}$$

where,

ΔP	Pressure drop (Pa)
L	Bed length (m)
ε	Void fraction
μ_g	Viscosity of gas (Pa s)
U_m	Superficial gas velocity (m/s)

d_p	Particle mean diameter (m)
g	Gravitational force (m/s)
ρ_s	Solid density (kg/m^3)
ρ_g	Fluid density (kg/m^3)

However, the determination of U_{mf} from pressure drop approach required detailed knowledge of void fraction, which is difficult to determine in a real system. In addition, the equation assumes that the particles are spherical and therefore does not account for samples that contain numerous particle sizes (i.e. have significant size distribution) which is typically the case for biomass grinds (Cloete et al., 2015; Dolejs and Machac, 1995; Jing et al., 2000; Mawatari et al., 2003; Nemec et al., 2001).

2.9.2 Empirical model approach

Several, researchers have developed various correlations for predicting the U_{mf} of particles in fluidized bed systems. Correlations were developed in other to circumvent estimating those particle properties (especially, shape factor and porosity) that are difficult to determine. The empirical correlations rely on experimental data, particle size, particle and gas densities, and viscosity. However, because the correlations are specific to a system, they are valid under the conditions of the specific system (Shao et al., 2013). Table 2.7 shows various forms of correlations that have been developed for biomass fluidization.

Table 2.7: Various forms of correlations for predicting U_{mf}

Model	Equation	Material
Rao et al. (2001)	$U_{mf} = \dfrac{d_{eff}^2 \left(\rho_{eff} - \rho_g\right)g}{1650\mu_g}$	Rice husk, sawdust and groundnut shell powder
Abdullah et al. (2003)	$U_{mf} = \dfrac{0.0093 d_p^{1.83}\left(\rho_s - \rho_g\right)^{0.94}}{\rho_g^{0.06}\mu_g^{0.88}}$	Sawdust, Rice husk, peanut shell, coal
Shao et al. (2013)	$U_{mf} = 1.28\times10^{-3}\left[\dfrac{d_{eff}^2\left(\rho_{eff}-\rho_g\right)}{\mu_g}\left(\dfrac{\rho_{eff}}{\rho_g}\right)^{1.2}\right]^{0.356}$	Silica sand Rough rice Wood sticks
Zhong et al. (2008)	$U_{mf} = 1.45\times10^{-3}\left[\dfrac{d_{eff}^2\left(\rho_{eff}-\rho_g\right)}{\mu_g}\left(\dfrac{\rho_{eff}}{\rho_g}\right)^{1.2}\right]^{0.363}$	Wood chip, mung bean, millet, corn stalk, and cotton stalk
Abrahamsen and Geldart (1980)	$U_{mf} = 9\times10^{-4}d_p^{1.8}\left[\left(\rho_s - \rho_g\right)g\right]^{0.934}\rho_g^{-0.066}\mu_g^{-0.87}$	Literature data

where,

μ_g	Viscosity of gas (Pa.s)
U_{mf}	Minimum fluidization velocity (m/s)
d_p	Particle mean diameter (m)
g	Gravitational force (m/s)
ρ_s	Solid density (kg/m^3)
ρ_g	Fluid density (kg/m^3)
d_{eff}	Effective diameter (m)
ρ_{eff}	Effective density (kg/m^3)

It is obvious that these correlations can be divided into two generic forms as shown in

Eqns. 2.8 and 2.9. The categories of Eqn. 2.8 are generally used for all particles/ bed

materials irrespective of the properties, those in Eqn. 2.9 have been developed for

multicomponent bed material exclusively. At present, there are no documented evidence

in scientific literatures the use of equations of the form shown in Eqn. 2.9 to predict the

U_{mf} of biomass grinds. This is partly because, all the authors assumed biomass to be one

of the bed component (for instance sand and ground biomass is assumed to be two component bed). The properties of biomass that made it behave like a multicomponent material was clearly not factored into their assumptions.

$$U_{mf} = K \times d_s^m \frac{(\rho_s - \rho_g)^m}{\rho_g^x} \qquad (2.8)$$

$$U_{mf} = k \left[\frac{d_{eff}^2 (\rho_s - \rho_f) g}{\mu_g} \left(\frac{\rho_s}{\rho_g} \right)^{1.23} \right]^\alpha \qquad (2.9)$$

2.9.3   Computational Fluid Dynamics approach

Computational Fluid Dynamics (CFD) is a powerful tool used for modelling fluid-solid system. Depending on the simulation type, two or three dimensional partial conservation equations of mass, momentum, and energy can be combined and solved for a bed using drag laws over the defined domain. The domain is usually discretized, into numerous meshes using finite difference, finite volume, or finite element methods.

The CFD model has been applied for fluidized bed gasification of biomass grinds but due to properties of biomass, CFD model are still not optimally predicting non-spherical and complex behavior of particle especially in a fluidized bed system. For instance, Sun et al. (2010) experimentally and computationally pyrolysed ground rice husk and sawdust in an entrained flow reactor at different temperatures (700 -1000 ^oC). At 900 ^oC, the author reported 20% under-prediction of CO_2 yield at the first sampling point, while the yield of CH_4 was over-predicted for 21-28% at the early stage of pyrolysis. Backreedy et al. (2005) performed a simulation for comparing the burnout properties vis-à-vis drag coefficient of biomass and coal. The author found that the biomass remain (longer time)

in the combustion zone before it falls down into the ash hopper and he attributed this to the non-spherical shape of biomass particles that caused the drag to increase. Yin et al. (2004) also reported that the biomass particle experience increased dispersion due to lift forces imposed by the shape making them to heat up and combust faster than a spherical particle with same mass due to the larger surface area.

Despite CFD biomass gasification model challenges, it still predicted better the gasification behavior of biomass grinds when compared to other model approaches (Witt et al., 1997). The author observed that most reported predicted error falls within 20% of the experimental values whereas other models typically resulted in high prediction error. Zitney and Guenther (2005) said that using CFD model for gasification is better compared with other models because of its ability to predict syngas composition based on fluid flow, heat and mass transfer, and chemical reactions in the specified geometry and at the specified boundary/operating conditions. On the other hand, other models must be tuned by specifying temperature in the restricted equilibrium reactor models. However, the most significant drawback of the CFD model is because of its sophistication, computational time for 3D modelling are significantly longer and required special training before it can be effectively deployed.

Therefore, the prediction of minimum fluidization is mostly carried out with pressure drop and empirical models approaches. However, when the focus is to understand the conditions of bed at different flow condition, the CFD is the only available modelling tools that can be used to accomplish this goal. There are two different CFD approaches that can be used to model biomass fluidization behavior: the Eulerian – Eulerian (E-E) and Eulerian – Lagrangian (E-L) approach (Adamczyk et al., 2014a; FLUENT, 2012;

53

Huilin and Gidaspow, 2003; Rajeswari et al., 2011; Zhuang et al., 2014). The E-E model

is also referred to as the two-fluid model (TFM). This approach considers the solid and

fluid phases to be continuous and fully interpenetrating, and employs the Navier–Stokes

equations for solving the interacting continua. The kinetic theory of granular flow is used

to describe the gas–solid two-phase flow behavior, while the drag laws and constitutive

equations are used to account for the effect of particle interactions (Gao et al., 2012;

Sande and Ray, 2014).The E-E is most widely used in literature for gas-solid simulation

because it does not calculate the motion of individual particles resulting in less

computational time. The considerable reduction in computational time makes the E-E

approach the preferred CFD method for modelling fluidized bed (Chen et al., 2013; Gao

et al., 2012; Limayem and Ricke, 2012; Reddy and Yang, 2007; Zhuang et al., 2014).

E-E approach has been widely used use for modeling pilot scale and industrial scale

fluidized bed reactors (Gao et al., 2012; Shi et al., 2010; Zhuang et al., 2014). In such

cases, the particles is usually modeled using a single value for mean particle size, which

is clearly far from the reality of the typical biomass grinds in a biomass fluidization

reactor (Helland et al., 2000; Huilin and Gidaspow, 2003) and the system are sometimes

restricted to fewer particles (Brandani and Zhang, 2006; Jenkins and Savage, 1983).

When a non-uniform size distribution particle is modeled as a uniform distribution using

a single mean particle diameter, the reliability and the accuracy of these models are

doubtful (Wang et al., 2014). For instance Xue et al. (2012) performed both 2D and 3D

simulation using E-E model. For experimental validation, a ground red oak sieved

through screen size ranged of 250–400μm was used while for simulation, a single

diameter was used for simulation (Table 2.8). The author then used the result as a means

to validate the experimental setup and subsequently extracted several other simulation data. It was not surprising that the authors suggested that the bio-oil yield was under-predicted with high biomass loss and concluded that particle size distribution should be included in the model in order to improve the study.

Table 2.8: Product yields (wt.%) of a type of red oak pyrolysis from experiment and simulation.

Method	Bio-oil	Char	Temperature (°C)
Experiment	71.7	13.0	500
Simulation (dp = 250, 2D)	60.5	12.3	497
Simulation (dp = 325, 2D)	62.4	14.1	498
Simulation (dp = 325, 3D)	61.5	12.9	499
Simulation (dp = 400, 2D)	63.4	15.1	499

The Eulerian –Lagrangian (E-L) approach is therefore particularly favored for solving and determining motion for individual particles in a fluidizing system. The E-L scheme uses Newtonian equations of motion by taking into account the effects of particle collisions such as soft-sphere or hard-sphere models and forces acting on the particle by the gas (Garg et al., 2012; Li et al., 2012). In addition, the gas phase is treated as a continuum coupled to the motion of particles through an interphase exchange interaction terms for momentum, mass and energy. Since individual particle can be tracked, it is easy to assign a particular particle with its corresponding particle properties. However, due to computation time required for tracking individual particle, low volume fraction of solid phase is usually impose on the system,

However, for a system in which particle loading is high as typically the case for fluidized bed, low volume fraction restriction does not represent the reality. Hence, Dense Discrete Phase Model (DDPM) scheme in E-L approach is usually used. (Adamczyk et al., 2014a;

FLUENT, 2012). The DDPM is used to model the solid phase of the E-L model by accounting for the volume excluded by the particle in the gas phase by using conservation equations (FLUENT, 2012). Also, in DDPM model, a numerical particle is defined as a group of particles sharing the same properties so that density, shape, size. Particle-particle collision forces are simulated by means of a spatial gradient, using a particle stress model to describe particle collisions. Examples of published studies that have used DDPM models and their key findings are presented in Table 2.9.

Table 2.9: Some selected work that used Eulerian – Lagrangian with DDPM model

Material properties	Particle distribution	# of particle	Model type	Key finding	Reference
Sand: ρ_p = 2650 g/m³, d_p = 0.7mm alumina: ρ_p = 1350 kg/m³, d_p =1.2 mm, Gas velocity: u_g = 6.5 m/s	Mixture	7000	E-L	At 1.2 second simulation time all the injected large particles remain in the riser, whereas 16.1% of small particles flow out	Zhou et al. (2002)
Coarse glass beads ρ_p = 2500 kg/m³, d_{23} = 0.84 mm u_g= 18.5 m/s	Mono-disperse	n/a	E-L + DDPM model	DDPM performed better than other model (DEM, Granular and DP) because of the ability to capture part-particle and particle to wall collision	Pirker et al. (2010)
Mimic Geldart A particles ρ_p = 1500 g/m³, d_p = 100 μm u_g= 5 m/s.	Uniform distribution	10	E-L +DDPM, Two fluid model	Poor prediction obtained from using DDPM model without granular temperature transport	Cloete et al. (2012)
Coal ρ_p= 1300 kg/m³, d_p= 450 μm u_g=6.5 m/s	Rosin-Rammler	8	DDPM $_+$ Eddy Dissipation Mode	Simulation over predicted experimental data (Temperature)	Adamczyk et al. (2014b)

| Coal

ρ_p= not specified,
d_p= 1.19 mm
u_g=288 kg/h	Rosin-Rammler distribution	N/a	DDPM	It has been also observed that the applied time step led to wrong prediction of carbon conversion.	Klimanek et al. (2015)
Carbon capture system
ρ_p= 1300 kg/m^3,
d_p= 450 µm
u_g = (5.5- 12.6) cm/s. | Not specified | N/a | DDPM | The Wen-Yu drag model as the optimal model input parameters and values. | Lane et al. (2014) |
| Spherical glass bead
ρ_p= 2500 kg/m^3
d_p= 275 µm
u_g= 0.025–0.51m/s | Size vary between 250 and 300 mm diameter | | DDPM, compare Fluent and MFIX software simulation | Prediction obtained from E-L using DDPM, with Syamlal and Gidaspow drag law predicted experimental data | Herzog et al. (2012) |

2.10 Summary

In this chapter, the importance of biomass as a feedstock and replacement option for fossil fuel production/ consumption was discussed. The rationale for the choice of loblolly pine wood as feedstock in this work was also explained. Lignocellulosic biomass can be converted to fuels and products through thermochemical conversion. Gasification has been most favored due to advantages highlighted in the review. Furthermore, the reactor inside the gasifier houses the fluidized bed where the fluidization and actual reaction occurs. Inside the fluidized bed, the feedstock is suspended in a gas stream for optimal exposure to thermal decomposition into intermediate products and gases. Before biomass can be used as a feedstock in fluidized bed system, the size must be reduced to a range that the fluidized bed can effectively process. But size reduction inevitable result in non-uniform size distribution having non-spherical particle shapes and non-uniform densities. Properties variations therefore create a problem in determining important parameter needed to design the fluidized bed and auxiliary facilities. For a non-spherical particle, the axis and choice of a particular diameter scheme over another must be carefully evaluated for specific operation.

Thus, utilizing equations for predicting parameter needed for fluidization seems to provide an easy route. But majority of the available equation are developed with assumption specifically for material that has properties and fluidizing behavior clearly different from ground biomass. In this review, the three types of approaches to predict fluidization properties and behavior of grind were identified as pressure-drop, empirical and computational fluid dynamics approach. Pressure drop approaches based on the first principle are widely used for varying material. The empirical equations are however,

material specific and unless the conditions are similar to which the equation was developed, a wrong prediction would be obtain if applied to a different material and under different condition. The most sophisticated of the approaches is the CFD approach. For fluidized bed CFD simulation, Eulerian - Eulerian approach is popular and used widely because of less computational time. However, with inability to track individual particle the results obtained from E-E are doubtful, hence, the application of Dense Discrete Phase Model using Eulerian –Lagrangian framework to fluidized beds. However, since this model is new, it must be carefully evaluated for fluidized bed application especially for fluidized beds that contains biomass grinds.

2.11 References

Abdullah, E. C., and D. Geldart. 1999. The use of bulk density measurements as flowability indicators. *Powder Technology* 102(2):151-165.

Abdullah, M. Z., Z. Husain, and S. L. Yin Pong. 2003. Analysis of cold flow fluidization test results for various biomass fuels. *Biomass and Bioenergy* 24(6):487-494.

Abrahamsen, A., and D. Geldart. 1980. Behaviour of gas-fluidized beds of fine powders part I. Homogeneous expansion. *Powder Technology* 26(1):35-46.

Adamczyk, W. P., A. Klimanek, R. A. Białecki, G. Węcel, P. Kozołub, and T. Czakiert. 2014a. Comparison of the standard Euler–Euler and hybrid Euler–Lagrange approaches for modeling particle transport in a pilot-scale circulating fluidized bed. *Particuology* 15(0):129-137.

Adamczyk, W. P., P. Kozołub, G. Węcel, A. Klimanek, R. A. Białecki, and T. Czakiert. 2014b. Modeling oxy-fuel combustion in a 3D circulating fluidized bed using the hybrid Euler–Lagrange approach. *Applied Thermal Engineering* 71(1):266-275.

Aguado, R., M. Olazar, B. Gaisán, R. Prieto, and J. Bilbao. 2002. Kinetic study of polyolefin pyrolysis in a conical spouted bed reactor. *Industrial & engineering chemistry research* 41(18):4559-4566.

Allen, H., P. Dougherty, and R. Campbell. 1990. Manipulation of water and nutrients— practice and opportunity in southern US pine forests. *Forest Ecology and Management* 30(1):437-453.

Allen, T. 2003. 2 - Data presentation and interpretation. In *Powder Sampling and Particle Size Determination*, 56-141. T. Allen, ed. Amsterdam: Elsevier.

ANSI/ASABE.2011.S593.1: Terminology and Definitions for Biomass Production, Harvesting and Collection, Storage, Processing, Conversion and Utilization. St. Joseph, MI 49085-9659, USA: American Society of Agricultural and Biological Engineers.

ANSI/ASABE.2012.S319.4: Method of Determining and Expressing Fineness of Feed Materials by Sieving. Ml 49085-9659, USA,: American Society of Agricultural and Biological Engineers.

Antonopoulos, I. S., A. Karagiannidis, A. Gkouletsos, and G. Perkoulidis. 2012. Modelling of a downdraft gasifier fed by agricultural residues. *Waste Management* 32(4):710-718.

Azzopardi, B. J. 2011. Dropsize measurement: Sauter mean diameter. *Thermopedia TM. DOI* 10.

Backreedy, R., L. Fletcher, J. Jones, L. Ma, M. Pourkashanian, and A. Williams. 2005. Co-firing pulverised coal and biomass: a modeling approach. *Proceedings of the Combustion Institute* 30(2):2955-2964.

Barakat, A., H. de Vries, and X. Rouau. 2013. Dry fractionation process as an important step in current and future lignocellulose biorefineries: A review. *Bioresource Technology* 134(0):362-273.

Bhaskar, T., B. Bhavya, R. Singh, D. V. Naik, A. Kumar, and H. B. Goyal. 2011. Thermochemical conversion of biomass to biofuels. *Biofuels. Academic Press, Burlington*:51-77.

Blott, S. J., and K. Pye. 2008. Particle shape: a review and new methods of characterization and classification. *Sedimentology* 55(1):31-63.

Bouwman, A. M., J. C. Bosma, P. Vonk, J. A. Wesselingh, and H. W. Frijlink. 2004. Which shape factor(s) best describe granules? *Powder Technology* 146(1–2):66-72.

Brammer, J. G., and A. V. Bridgwater. 2002. The influence of feedstock drying on the performance and economics of a biomass gasifier engine CHP system. *Biomass and Bioenergy* 22(4):271-281.

Brandani, S., and K. Zhang. 2006. A new model for the prediction of the behaviour of fluidized beds. *Powder Technology* 163(1):80-87.

Brittain, H. G. 2002. Particle-size distribution, part III: determination by analytical sieving. *Pharmaceutical technology* 26(12):56-64.

Brown, T. M., P. Duan, and P. E. Savage. 2010. Hydrothermal liquefaction and gasification of Nannochloropsis sp. *Energy & Fuels* 24(6):3639-3646.

Cardoso, C. R., T. J. P. Oliveira, J. A. Santana Junior, and C. H. Ataíde. 2013. Physical characterization of sweet sorghum bagasse, tobacco residue, soy hull and fiber sorghum bagasse particles: Density, particle size and shape distributions. *Powder Technology* 245(0):105-114.

Chen, X., J. Wang, and J. Li. 2013. Coarse grid simulation of heterogeneous gas–solid flow in a CFB riser with polydisperse particles. *Chemical Engineering Journal* 234:173-183.

Chevanan, N., A. Womac, V. Bitra, and S. Sokhansanj. 2011. Effect of Particle Size Distribution on Loose-Filled and Tapped Densities of Selected Biomass after Knife Mill Size Reduction. *Applied Engineering in Agriculture* 27(4):631-644.

Christensen, T. H. 2011. *Solid waste technology & management*. Wiley West Sussex, UK.

Clark, J. H., and F. Deswarte. 2014. *Introduction to chemicals from biomass*. 1 ed. John Wiley & Sons, Wiley West Sussex, UK.

Clarke, K. L., T. Pugsley, and G. A. Hill. 2005a. Fluidization of moist sawdust in binary particle systems in a gas–solid fluidized bed. *Chemical Engineering Science* 60(24):6909-6918.

Clarke, K. L., T. Pugsley, and G. A. Hill. 2005b. Fluidization of moist sawdust in binary particle systems in a gas solid fluidized bed. *Chemical Engineering Science* 60(24):6909-6918.

Cloete, S., S. T. Johansen, and S. Amini. 2012. Performance evaluation of a complete Lagrangian KTGF approach for dilute granular flow modelling. *Powder Technology* 226(0):43-52.

Cloete, S., S. T. Johansen, and S. Amini. 2015. Grid independence behaviour of fluidized bed reactor simulations using the Two Fluid Model: Effect of particle size. *Powder Technology* 269(0):153-165.

Cluet, B., G. Mauviel, Y. Rogaume, O. Authier, and A. Delebarre. 2015. Segregation of wood particles in a bubbling fluidized bed. *Fuel Processing Technology* 133(0):80-88.

Constantineau, J. P., J. R. Grace, C. J. Lim, and G. G. Richards. 2007. Generalized bubbling–slugging fluidized bed reactor model. *Chemical engineering science* 62(1–2):70-81.

Cui, H., and J. R. Grace. 2007. Fluidization of biomass particles: A review of experimental multiphase flow aspects. *Chemical Engineering Science* 62(1):45-55.

Damartzis, T., and A. Zabaniotou. 2011. Thermochemical conversion of biomass to second generation biofuels through integrated process design—A review. *Renewable and Sustainable Energy Reviews* 15(1):366-378.

Davidson, J. F., D. Harrison, and J. Carvalho. 1977. On the liquidlike behavior of fluidized beds. *Annual Review of Fluid Mechanics* 9(1):55-86.

De Diego, L., F. Garcıa-Labiano, A. Abad, P. Gayan, and J. Adanez. 2002. Coupled drying and devolatilisation of non-spherical wet pine wood particles in fluidised beds. *Journal of Analytical and Applied Pyrolysis* 65(2):173-184.

Demirbas, A. 2002. Relationships Between Heating Value and Lignin, Moisture, Ash and Extractive Contents of Biomass Fuels. *Energy, Exploration & Exploitation* 20(1):105-111.

Demirbaş, A. 2000. Mechanisms of liquefaction and pyrolysis reactions of biomass. *Energy Conversion and Management* 41(6):633-646.

Demirbas, A., and G. Arin. 2002. An overview of biomass pyrolysis. *Energy Sources* 24(5):471-482.

Dolejs, V., and I. Machac. 1995. Pressure drop during the flow of a Newtonian fluid through a fixed bed of particles. *Chemical Engineering and Processing: Process Intensification* 34(1):1-8.

Downing, M., L. M. Eaton, R. L. Graham, M. H. Langholtz, R. D. Perlack, A. F. Turhollow Jr, B. Stokes, and C. C. Brandt. 2011. US Billion-Ton Update: Biomass supply for a bioenergy and bioproducts industry. Oak Ridge National Laboratory (ORNL).

Drake, J. B. a. H., Theodore J. 2011. The repeatability and uniformity of 3D fluidized beds. *Powder Technology* 213(13):148-154.

Elliott, D. C., P. Biller, A. B. Ross, A. J. Schmidt, and S. B. Jones. 2015. Hydrothermal liquefaction of biomass: Developments from batch to continuous process. *Bioresource Technology* 178(0):147-156.

Ergun, S. 1952. Fluid flow through packed columns. *Chem. Eng. Prog.* 48:89-94.

Fasina, O. 2006. Flow and physical properties of switchgrass, peanut hull, and poultry litter. *Transactions of the ASABE* 49(3):721-728.

Fasina, O. O. 2008. Physical properties of peanut hull pellets. *Bioresource Technology* 99(5):1259-1266.

Fernlund, J. M. R. 1998. The effect of particle form on sieve analysis: a test by image analysis. *Engineering Geology* 50(1–2):111-124.

FLUENT, M. 2012. ANSYS Release Version 14.5, ANSYS Inc. Documentation.

Formisani, B., R. Girimonte, and T. Longo. 2008. The fluidization process of binary mixtures of solids: Development of the approach based on the fluidization velocity interval. *Powder Technology* 185(2):97-108.

Formisani, B., R. Girimonte, and V. Vivacqua. 2014. The interaction between mixture components in the mechanism of binary fluidization. *Powder Technology* 266(0):228-235.

Gantenbein, D., J. Schoelkopf, G. P. Matthews, and P. A. C. Gane. 2011. Determining the size distribution-defined aspect ratio of rod-like particles. *Applied Clay Science* 53(4):538-543.

Gao, X., C. Wu, Y.-w. Cheng, L.-j. Wang, and X. Li. 2012. Experimental and numerical investigation of solid behavior in a gas–solid turbulent fluidized bed. *Powder Technology* 228(0):1-13.

Garg, R., J. Galvin, T. Li, and S. Pannala. 2012. Open-source MFIX-DEM software for gas–solids flows: Part I—Verification studies. *Powder Technology* 220:122-137.

Gauthier, D., S. Zerguerras, and G. Flamant. 1999. Influence of the particle size distribution of powders on the velocities of minimum and complete fluidization. *Chemical Engineering Journal* 74(3):181-196.

Geldart, D. 1973. Types of gas fluidization. *Powder Technology* 7(5):285-292.

Gelves, R., A. Dietrich, and R. Takors. 2014. Modeling of gas–liquid mass transfer in a stirred tank bioreactor agitated by a Rushton turbine or a new pitched blade impeller. *Bioprocess and biosystems engineering* 37(3):365-375.

Gerçel, H. F. 2002. Production and characterization of pyrolysis liquids from sunflower-pressed bagasse. *Bioresource Technology* 85(2):113-117.

Gil, M., D. Schott, I. Arauzo, and E. Teruel. 2013. Handling behavior of two milled biomass: SRF poplar and corn stover. *Fuel Processing Technology* 112(0):76-85.

Gil, M., E. Teruel, and I. Arauzo. 2014. Analysis of standard sieving method for milled biomass through image processing. Effects of particle shape and size for poplar and corn stover. *Fuel* 116(0):328-340.

Goyal, H. B., D. Seal, and R. C. Saxena. 2008. Bio-fuels from thermochemical conversion of renewable resources: A review. *Renewable and Sustainable Energy Reviews* 12(2):504-517.

Grace, J. R., and G. Sun. 1991. Influence of particle size distribution on the performance of fluidized bed reactors. *The Canadian Journal of Chemical Engineering* 69(5):1126-1134.

Gröger, T., U. Tüzün, and D. M. Heyes. 2003. Modelling and measuring of cohesion in wet granular materials. *Powder Technology* 133(1–3):203-215.

Gunn, D. J., and N. Hilal. 1997. The expansion of gas-fluidised beds in bubbling fluidisation. *Chemical Engineering Science* 52(16):2811-2822.

Guo, Q., X. Chen, and H. Liu. 2012. Experimental research on shape and size distribution of biomass particle. *Fuel* 94(0):551-555.

Gupta, C. K., and D. Sathiyamoorthy. 1999. *Fluid bed technology in materials processing*. CRC Press, Boca Raton, Fla.

Hartman, M., O. Trnka, and K. Svoboda. 2006. Impediment to incipient fluidization in wet beds of porous nonspherical particles. *Chemical Engineering Communications* 193(1):100-115.

Hehar, G., O. Fasina, S. Adhikari, and J. Fulton. 2014. Ignition and volatilization behavior of dust from loblolly pine wood. *Fuel Processing Technology* 127(0):117-123.

Heinicke, G., and J. B. Schwartz. 2004. Particle size distributions of inert spheres and pelletized pharmaceutical products by image analysis. *Pharmaceutical development and technology* 9(4):359-367.

Helland, E., R. Occelli, and L. Tadrist. 2000. Numerical study of cluster formation in a gas–particle circulating fluidized bed. *Powder Technology* 110(3):210-221.

Herzog, N., M. Schreiber, C. Egbers, and H. J. Krautz. 2012. A comparative study of different CFD-codes for numerical simulation of gas–solid fluidized bed hydrodynamics. *Computers & Chemical Engineering* 39(0):41-46.

Hinds, W. C. 2012. *Aerosol technology: properties, behavior, and measurement of airborne particles*. John Wiley & Sons, Wiley West Sussex, UK.

Huilin, L., and D. Gidaspow. 2003. Hydrodynamics of binary fluidization in a riser: CFD simulation using two granular temperatures. *Chemical Engineering Science* 58(16):3777-3792.

Jae, J., R. Coolman, T. J. Mountziaris, and G. W. Huber. 2014. Catalytic fast pyrolysis of lignocellulosic biomass in a process development unit with continual catalyst addition and removal. *Chemical Engineering Science* 108(0):33-46.

Jahirul, M. I., M. G. Rasul, A. A. Chowdhury, and N. Ashwath. 2012. Biofuels production through biomass pyrolysis—a technological review. *Energies* 5(12):4952-5001.

Jenkins, J., and S. Savage. 1983. A theory for the rapid flow of identical, smooth, nearly elastic, spherical particles. *Journal of Fluid Mechanics* 130:187-202.

Jiliang, M., C. Xiaoping, and L. Daoyin. 2013. Minimum fluidization velocity of particles with wide size distribution at high temperatures. *Powder Technology* 235(0):271-278.

Jing, S., Q. Hu, J. Wang, and Y. Jin. 2000. Fluidization of coarse particles in gas–solid conical beds. *Chemical Engineering and Processing: Process Intensification* 39(4):379-387.

Kaliyan, N., and R. Morey. 2009. Densification characteristics of corn stover and switchgrass. *Transactions of the ASABE* 52(3):907-920.

Karmakar, M. K., S. Haldar, and P. K. Chatterjee. 2013. Studies on fluidization behaviour of sand and biomass mixtures. *Int. J. Emerg. Technol. Adv. Eng.* 3.

Khanal, S. K. 2010. *Bioenergy and biofuel from biowastes and biomass*. ASCE Publications, Reston Virginia.

Khoe, G. K., T. L. Ip, and J. R. Grace. 1991. Rheological and fluidization behaviour of powders of different particle size distribution. *Powder Technology* 66(2):127-141.

Klieger, P., and J. F. Lamond. 1994. *Significance of tests and properties of concrete and concrete-making materials*. ASTM International.

Klimanek, A., W. Adamczyk, A. Katelbach-Woźniak, G. Węcel, and A. Szlęk. 2015. Towards a hybrid Eulerian–Lagrangian CFD modeling of coal gasification in a circulating fluidized bed reactor. *Fuel* 152(0):131-137.

Kunii, D., and O. Levenspiel. 1991. *Fluidization engineering*. Butterworth-Heinemann Boston.

Lane, W. A., C. B. Storlie, C. J. Montgomery, and E. M. Ryan. 2014. Numerical modeling and uncertainty quantification of a bubbling fluidized bed with immersed horizontal tubes. *Powder Technology* 253(0):733-743.

Lees, G. 1964. *The measurement of particle shape and its influence in engineering materials*. British Granite and Whinstone Federation.

Li, T., P. Gopalakrishnan, R. Garg, and M. Shahnam. 2012. CFD–DEM study of effect of bed thickness for bubbling fluidized beds. *Particuology* 10(5):532-541.

Limayem, A., and S. C. Ricke. 2012. Lignocellulosic biomass for bioethanol production: current perspectives, potential issues and future prospects. *Progress in Energy and Combustion Science* 38(4):449-467.

Littlefield, B., O. O. Fasina, J. Shaw, S. Adhikari, and B. Via. 2011. Physical and flow properties of pecan shells—Particle size and moisture effects. *Powder Technology* 212(1):173-180.

Liu, B. Y. 2012. *Fine particles: Aerosol generation, measurement, sampling, and analysis*. Elsevier.

Loth, E., T. O'Brien, M. Syamlal, and M. Cantero. 2004. Effective diameter for group motion of polydisperse particle mixtures. *Powder Technology* 142(2–3):209-218.

Lu, H., E. Ip, J. Scott, P. Foster, M. Vickers, and L. L. Baxter. 2010. Effects of particle shape and size on devolatilization of biomass particle. *Fuel* 89(5):1156-1168.

Lu, X., M. R. Withers, N. Seifkar, R. P. Field, S. R. H. Barrett, and H. J. Herzog. 2015. Biomass logistics analysis for large scale biofuel production: Case study of loblolly pine and switchgrass. *Bioresource Technology* 183(0):1-9.

Lucas, A., J. Arnaldos, J. Casal, and L. Puigjaner. 1986. Improved equation for the calculation of minimum fluidization velocity. *Industrial & Engineering Chemistry Process Design and Development* 25(2):426-429.

Luo, Z., S. Wang, Y. Liao, J. Zhou, Y. Gu, and K. Cen. 2004. Research on biomass fast pyrolysis for liquid fuel. *Biomass and Bioenergy* 26(5):455-462.

Lv, P. M., Z. H. Xiong, J. Chang, C. Z. Wu, Y. Chen, and J. X. Zhu. 2004. An experimental study on biomass air-steam gasification in a fluidized bed. *Bioresource Technology* 95(1):95-101.

Mani, S., L. G. Tabil, and S. Sokhansanj. 2004. Grinding performance and physical properties of wheat and barley straws, corn stover and switchgrass. *Biomass and Bioenergy* 27(4):339-352.

Mani, S., L. G. Tabil, and S. Sokhansanj. 2006. Effects of compressive force, particle size and moisture content on mechanical properties of biomass pellets from grasses. *Biomass and Bioenergy* 30(7):648-654.

Marcilla, A., L. Catalá, J. C. García-Quesada, F. J. Valdés, and M. R. Hernández. 2013. A review of thermochemical conversion of microalgae. *Renewable and Sustainable Energy Reviews* 27(0):11-19.

Mason, P. E., L. I. Darvell, J. M. Jones, M. Pourkashanian, and A. Williams. 2015. Single particle flame-combustion studies on solid biomass fuels. *Fuel* 151:21-30.

Mattsson, J. E., and P. D. Kofman. 2002. Method and apparatus for measuring the tendency of solid biofuels to bridge over openings. *Biomass and Bioenergy* 22(3):179-185.

Mawatari, Y., Y. Tatemoto, and K. Noda. 2003. Prediction of minimum fluidization velocity for vibrated fluidized bed. *Powder Technology* 131(1):66-70.

McKeand, S. 2014. The Success of Tree Breeding in the Southern US. *BioResources* 10(1):1-2.

McKendry, P. 2002. Energy production from biomass (part 1): overview of biomass. *Bioresource Technology* 83(1):37-46.

Merzsch, M., S. Lechner, and H. J. Krautz. 2013. Heat-transfer from single horizontal tubes in fluidized beds: Influence of tube diameter, moisture and diameter-definition by Geldart C fines content. *Powder Technology* 235(0):1038-1046.

Miller, N., and J. Henderson. 2010. Quantifying sand particle shape complexity using a dynamic, digital imaging technique. *Agronomy journal* 102(5):1407-1414.

Mora, C. F., A. K. H. Kwan, and H. C. Chan. 1998. Particle size distribution analysis of coarse aggregate using digital image processing. *Cement and Concrete Research* 28(6):921-932.

Morris, A. D., D. A. Miller, and M. C. Kalcounis-Rueppell. 2010. Use of Forest Edges by Bats in a Managed Pine Forest Landscape. *The Journal of Wildlife Management* 74(1):26-34.

Mosier, N., C. Wyman, B. Dale, R. Elander, Y. Y. Lee, M. Holtzapple, and M. Ladisch. 2005. Features of promising technologies for pretreatment of lignocellulosic biomass. *Bioresource Technology* 96(6):673-686.

Munsell, J. F., and T. R. Fox. 2010. An analysis of the feasibility for increasing woody biomass production from pine plantations in the southern United States. *Biomass and Bioenergy* 34(12):1631-1642.

Nazar, A. M., F. A. Silva, and J. J. Ammann. 1996. Image processing for particle characterization. *Materials Characterization* 36(4–5):165-173.

NCSSF. 2005. Global Markets Forum. Summary report of the National Commission on Science for Sustainable Forestry. Washington, D.C., USA.: National Commission on Science for Sustainable Forestry.

Nelson, C. D., G. F. Peter, S. E. McKeand, E. J. Jokela, R. B. Rummer, L. H. Groom, and K. H. Johnsen. 2013. 20 Pines.

Nemec, D., G. Berčič, and J. Levec. 2001. The hydrodynamics of trickling flow in packed beds operating at high pressures. The relative permeability concept. *Chemical Engineering Science* 56(21–22):5955-5962.

Oginni, O. J. 2014. Contribution of particle size and moisture content to flowability of fractionated ground loblolly pine. M.S thesis. Auburn University, Biosystems Engineering Department, Auburn Alabama.

Oliveira, T. J. P., C. R. Cardoso, and C. H. Ataíde. 2013. Bubbling fluidization of biomass and sand binary mixtures: Minimum fluidization velocity and particle segregation. *Chemical Engineering and Processing: Process Intensification* 72(0):113-121.

Olson, E. 2011. Particle Shape Factors and Their Use in Image Analysis Part 1: Theory. *Journal of GXP Compliance* 15(3):85.

Onwulata, C. 2005. *Encapsulated and powdered foods*. . ed. CRC Press, Boca Raton.

Ortega-Rivas, Enrique, P. Juliano, and H. Yan. 2006. *Food powders: physical properties, processing, and functionality*. 1st ed. Springer, New York, Philadelphia.

Paudel, B., and Z.-G. Feng. 2013. Prediction of minimum fluidization velocity for binary mixtures of biomass and inert particles. *Powder Technology* 237(0):134-140.

Paulrud, S., J. E. Mattsson, and C. Nilsson. 2002. Particle and handling characteristics of wood fuel powder: effects of different mills. *Fuel Processing Technology* 76(1):23-39.

Perlack, R. D. a., and B. J. Stokes. 2011. U.S. Billion-Ton Update: Biomass Supply for a Bioenergy and Bioproducts Industry. Department of Energy Oak Ridge, TN: Oak Ridge National Laboratory.

Pirker, S., D. Kahrimanovic, C. Kloss, B. Popoff, and M. Braun. 2010. Simulating coarse particle conveying by a set of Eulerian, Lagrangian and hybrid particle models. *Powder Technology* 204(2–3):203-213.

Plis, P., and R. K. Wilk. 2011. Theoretical and experimental investigation of biomass gasification process in a fixed bed gasifier. *Energy* 36(6):3838-3845.

Probst, K., A. Kingsly, R. Pinto, R. Bali, P. Krishnakumar, and K. Ileleji. 2013. The effect of moisture content on the grinding performance of corn and corncobs by hammermilling. *Transactions of the ASABE* 56(3):10251-11033.

Puspasari, I., M. Z. M. Talib, W. R. W. Daud, and S. M. Tasirin. 2013. Fluidization characteristics of oil palm frond particles in agitated bed. *Chemical Engineering Research and Design* 91(3):497-507.

Quaak, P., H. Knoef, and H. E. Stassen. 1999. *Energy from biomass: a review of combustion and gasification technologies*. World Bank Publications.

Rajeswari, M. S. R., K. Azizli, S. Hashim, M. Abdullah, M. A. Mujeebu, and M. Abdullah. 2011. CFD simulation and experimental analysis of flow dynamics and grinding performance of opposed fluidized bed air jet mill. *International Journal of Mineral Processing* 98(1):94-105.

Raju, K. 2011. *Fluid mechanics, Heat transfer, and Mass transfer: Chemical Engineering Practice*. 1 ed. John Wiley & Sons, Hoboken, New Jersey.

Ramos, C. G., M. García Ruiz, J. J. Prieto Marqués, and J. Guardiola Soler. 2002. Minimum fluidization velocities for gas–solid 2D beds. *Chemical Engineering and Processing: Process Intensification* 41(9):761-764.

Rao, K., and G. Reddy. 2010. Cold flow studies of rice husk, saw dust, and groundnut shell fuels in a fluidized bed. *Energy Sources, Part A: Recovery, Utilization, and Environmental Effects* 32(18):1701-1711.

Rao, R., T. Ram, and J. V. Bheemarasetti. 2001. Minimum fluidization velocities of mixtures of biomass and sands. *Energy* 26(6):633-644.

Reddy, G. V., and S. K. Mahapatra. 1999. Effect of coal particle size distribution on agglomerate formation in a fluidized bed combustor (FBC). *Energy Conversion and Management* 40(4):447-458.

Reddy, N., and Y. Yang. 2007. Natural cellulose fibers from switchgrass with tensile properties similar to cotton and linen. *Biotechnology and Bioengineering* 97(5):1021-1027.

Saad, M., A. Sadoudi, E. Rondet, and B. Cuq. 2011. Morphological characterization of wheat powders, how to characterize the shape of particles? *Journal of Food Engineering* 102(4):293-301.

Sánchez-Delgado, S., J. A. Almendros-Ibáñez, N. García-Hernando, and D. Santana. 2011. On the minimum fluidization velocity in 2D fluidized beds. *Powder Technology* 207(1–3):145-153.

Sande, P., and S. Ray. 2014. Mesh size effect on CFD simulation of gas-fluidized Geldart A particles. *Powder Technology* 264:43-53.

Schell, D., and C. Harwood. 1994. Milling of lignocellulosic biomass. *Applied biochemistry and biotechnology* 45-46(1):159-168.

Shao, Y., B. Ren, B. Jin, W. Zhong, H. Hu, X. Chen, and C. Sha. 2013. Experimental flow behaviors of irregular particles with silica sand in solid waste fluidized bed. *Powder Technology* 234(0):67-75.

Shi, D.-P., Z.-H. Luo, and A.-Y. Guo. 2010. Numerical simulation of the gas− solid flow in fluidized-bed polymerization reactors. *Industrial & engineering chemistry research* 49(9):4070-4079.

Simanjuntak, J. P., and Z. A. Zainal. 2015. Experimental study and characterization of a two-compartment cylindrical internally circulating fluidized bed gasifier. *Biomass and Bioenergy* 77(0):147-154.

Skoulou, V., A. Zabaniotou, G. Stavropoulos, and G. Sakelaropoulos. 2008. Syngas production from olive tree cuttings and olive kernels in a downdraft fixed-bed gasifier. *International Journal of Hydrogen Energy* 33(4):1185-1194.

Smith, W. B., P. D. Miles, C. H. Perry, and S. A. Pugh. 2009. Forest resources of the United States, 2007: a technical document supporting the forest service 2010 RPA Assessment. *General Technical Report-USDA Forest Service*(WO-78).

Sneed, E. D., and R. L. Folk. 1958. Pebbles in the lower Colorado River, Texas a study in particle morphogenesis. *The Journal of Geology* 66(2): 114-150.

Suarez, J. A. 2003. Physical Properties of Cuban Coffee Husk for Use as an Energy Source. *Energy Sources* 25(10):953-959.

Sun, G., and J. R. Grace. 1992. Effect of particle size distribution in different fluidization regimes. *AIChE Journal* 38(5): 716-722.

Sun, S., H. Tian, Y. Zhao, R. Sun, and H. Zhou. 2010. Experimental and numerical study of biomass flash pyrolysis in an entrained flow reactor. *Bioresource Technology* 101(10):3678-3684.
Syahrul, S., I. Dincer, and F. Hamdullahpur. 2003. Thermodynamic modeling of fluidized bed drying of moist particles. *International Journal of Thermal Sciences* 42(7):691-701.

Takara, D., P. Shrestha, and S. K. Khanal. 2010. Lignocellulosic biomass pretreatment. *Biofuel and bioenergy from biowastes and lignocellulosic biomass. American Society of Civil Engineers, Reston.*

Tanfara, H., T. Pugsley, and C. Winters. 2002. Effect of particle size distribution on local voidage in a bench-scale conical fluidized bed dryer. *Drying Technology* 20(6):1273.

Trottier, R., and S. Dhodapkar. 2014. A Guide to Characterizing Particle Size and Shape. *Chemical Engineering Progress* 110(7):36-46.

Turchiuli, C., R. Smail, and E. Dumoulin. 2013. Fluidized bed agglomeration of skim milk powder: analysis of sampling for the follow-up of agglomerate growth. *Powder Technology* 238:161-168.

Vaezi, M., V. Pandey, A. Kumar, and S. Bhattacharyya. 2013. Lignocellulosic biomass particle shape and size distribution analysis using digital image processing for pipeline hydro-transportation. *Biosystems Engineering* 114(2):97-112.

Wang, L. 2014. *Sustainable bioenergy production*. CRC Press.

Wang, Q., T. Niemi, J. Peltola, S. Kallio, H. Yang, J. Lu, and L. Wei. 2014. Particle size distribution in CPFD modeling of gas–solid flows in a CFB riser. *Particuology*(0).

Wang, Y., Y. Cheng, Y. Jin, and H. T. Bi. 2007. On impacts of solid properties and operating conditions on the performance of gas-solid fluidization systems. *Powder Technology* 172(3):167-176.

Warnecke, R. 2000. Gasification of biomass: comparison of fixed bed and fluidized bed gasifier. *Biomass and Bioenergy* 18(6):489-497.

Witt, P., H. Perry, and M. Schwartz. 1997. Application of CFD to fluidised bed systems. In *Proceedings of International conference on CFD in Minerals and Metals Processing and Power Generation*. CSIRO Minerals Melbourne, Australia.

Wormsbecker, M., and T. Pugsley. 2008. The influence of moisture on the fluidization behaviour of porous pharmaceutical granule. *Chemical Engineering Science* 63(16):4063-4069.

Wright, C. T., P. A. Pryfogle, N. A. Stevens, J. R. Hess, and C. W. Radtke. 2006. *Value of distributed preprocessing of biomass feedstocks to a bioenergy industry*. Idaho National Laboratory.

Xue, Q., D. Dalluge, T. J. Heindel, R. O. Fox, and R. C. Brown. 2012. Experimental validation and CFD modeling study of biomass fast pyrolysis in fluidized-bed reactors. *Fuel* 97(0):757-769.

Yang, W. 2003. *Handbook of Fluidization and Fluid-particle Systems*. CRC Press.

Yates, J. 2013. *Fundamentals of Fluidized-Bed Chemical Processes: Butterworths Monographs in Chemical Engineering*. Butterworth-Heinemann.

Yerushalmi, J., N. T. Cankurt, D. Geldart, and B. Liss. 1976. *Flow regimes in vertical gas-solid contact systems*.

Yin, C., L. Rosendahl, S. K. Kær, and T. J. Condra. 2004. Use of numerical modeling in design for co-firing biomass in wall-fired burners. *Chemical Engineering Science* 59(16):3281-3292.

Yin, R., R. Liu, J. Wu, X. Wu, C. Sun, and C. Wu. 2012. Influence of particle size on performance of a pilot-scale fixed-bed gasification system. *Bioresource technology* 119(0):15-21.

Zhang, K., B. Yu, J. Chang, G. Wu, T. Wang, and D. Wen. 2012. Hydrodynamics of a fluidized bed co-combustor for tobacco waste and coal. *Bioresource Technology* 119(0):339-348.

Zhang, Y., B. Jin, and W. Zhong. 2009. Experimental investigation on mixing and segregation behavior of biomass particle in fluidized bed. *Chemical Engineering and Processing: Process Intensification* 48(3):745-754.

Zhong, W., B. Jin, Y. Zhang, X. Wang, and R. Xiao. 2008. Fluidization of Biomass Particles in a Gas−Solid Fluidized Bed. *Energy & Fuels* 22(6):4170-4176.

Zhou, H., G. Flamant, D. Gauthier, and J. Lu. 2002. Lagrangian approach for simulating the gas-particle flow structure in a circulating fluidized bed riser. *International Journal of Multiphase Flow* 28(11):1801-1821.

Zhuang, Y.-Q., X.-M. Chen, Z.-H. Luo, and J. Xiao. 2014. CFD–DEM modeling of gas–solid flow and catalytic MTO reaction in a fluidized bed reactor. *Computers & Chemical Engineering* 60(0):1-16.

Zitney, S. E., and C. Guenther. 2005. Gasification CFD modeling for advanced power plant simulations. National Energy Technology Laboratory (NETL), Pittsburgh, PA, Morgantown, WV, and Albany, OR.

Chapter 3: Effect of Size on Physical Properties and Fluidization Behavior of Loblolly Pine Grinds

3.1 Abstract

This study investigated the effect of particle size on physical properties and fluidization behavior of loblolly pine wood grinds and the effect of size distribution on its fluidization properties. Wood chips was ground through 1/8 inch screen size (3.18 mm) and were fractionated using seven standard sieves that ranged between 0.053 - 3.2 mm. Particle density, bulk density, sphericities and particle size diameters of each fraction were measured. Effect of particle size distribution on minimum fluidization velocities (U_{mf}) was investigated by measuring bed-pressure drops as a function of superficial air velocity for each of the fraction in a cold flow fluidization bed chamber. The results of the experiment were compared with the predicted values obtained from some selected equations for predicting minimum fluidization velocities. The result showed that the loblolly pine wood grinds have mean particle density of 1460.6 ± 7 kg/m^3, bulk density of 311 ± 37 kg/m^3 and porosity of 0.787 ± 0.003. With regards to particle size, the Ferret diameter was found to be higher than surface-volume diameter, Martin's diameter and chord diameter by 18.3, 23.6, and 7.03% respectively. Also, the shape characteristic based on the sphericity value of biomass grinds ranges between 0.235 and 0.603, an indication that they have a flat shape. The minimum fluidization velocity of ground loblolly pine wood (unfractionated samples) was found to be 0.25 $\pm$0.04 m/s. For fractionated samples, the minimum fluidization velocity increased from 0.29 to 0.81 m/s as fractionating screen size increased from 0.15 to 1.7 mm. Predictions of minimum fluidization velocity from selected equations were significantly different from experimentally measured minimum fluidization velocity values.

3.2   Introduction

Lignocellulosic biomass feedstock such as woody biomass require size reduction before they can be converted because the available technology for converting biomass to fuels, products and chemicals cannot handle feedstock in the form they are harvested (Khanal, 2010; Mosier et al., 2005; Takara et al., 2010). In addition, the physical and chemical structures of the biomass need to be adjusted so as to influence parameters such as particle surface area, pore size, and rates of heat and mass transfer between the bed material so as to achieve optimum conversion efficiencies (Zhu et al., 2009). Furthermore, particle size is an important design parameter in fluidized bed reactor sizing and in estimating residence time in gasification systems (Barakat et al., 2013; Schell and Harwood, 1994).

However, size reduction of biomass material inevitably results in samples that are composed of several sizes of particles with non-spherical shapes. Fasina (2008), reported that the size range of peanut hull ground through 3.18 mm screen was between 0.10 and 3.40 mm nominal sieve size. The size distribution was log normal with geometric mean diameter (d_{gw}) and geometric standard deviation (s_{gw}) of 0.65 and 0.75 mm respectively. Also, Gil et al. (2013) used a hammer mill fitted with 2.0 mm screen size and obtained a d_{gw} and s_{gw} of 0.30 and 2.60 mm respectively for ground polar wood. Mani et al. (2004) reported that using hammer mill fitted with screen sizes that ranged between 0.8 and 3.2 mm, the particle density of wheat straw grinds varied between 1030 and 1340 kg/ m^3, barley straw grinds varied between 890 and 1250 kg/m^3, corn stover grinds varied between 1170 and 1340 kg/m^3 and switchgrass grinds varied between 950 and 1170

76

kg/m^3. Also, Adapa et al. (2009) measured the particle densities of ground wheat straw and ground canola straw to be between 1631 and 1539 kg/m^3, and 1504 and 1589 kg/m^3 respectively.

The non-uniformity in size, geometry, and density of ground biomass impedes homogeneous mixing of bed during fluidization. Phenomena such as channeling, segregations, and plug flow that have been attributed to multicomponent nature of ground biomass and the differences in the properties of the fractions that constitute the multicomponent are prevalent. For instance, Wang et al. (2014) fluidized sawdust with different size ranges (0–0.25, 0.25–0.36, 0.36–0.43, 0.43–0.50, 0.50–0.60, 0.60–0.71, and 0.71–0.85 mm). The author found that samples from 0–0.25 mm and 0.71–0.85 mm could not be properly fluidized because of channeling and slugging. Liu et al. (2008b) observed that glass ballotini (particle diameter: 0.57 – 0.24 mm and particle density: 2510 – 8750 kg/m^3) and coal (particle diameter: 2–40 mm and mean density: 1340 kg/m^3) segregate during fluidization because of substantial differences in the density of particles and distribution of particle size within the bulk material. Also, Sharma et al. (2013) reported that channelization caused ineffective fluidization when gasifier residue (0.080 ± 0.03 mm), sand (0.35 ± 0.02 mm) and switchgrass grinds (0.10 ± 0.02 mm) were combined in a cold flow fluidization system (ratio of 95% total bed weight for both sand and residues and the remaining 5% for switchgrass).

Owing to this heterogeneous nature of ground biomass, it is important to study the appropriateness of the models and equations used for describing fluidization behavior of biomass grinds. One of the earlier researchers who studied the behavior of particulate materials as influenced by fluidizing medium and the mean particle size (d_p), of a sample

during fluidization is Geldart (1973). His key findings are presented in Table 3.1.

However, these classification groupings require that the average diameter of the material

to be fluidized be known. For spherical materials, a single diameter value is obtained by

measuring the size, surface area, or volume of the particle. This is not the case for non-

spherical particles such as biomass grinds. Examples of the size measurement scheme

that can be measured from non-spherical particles are listed in Table 3.2. The method

used to measure the size of a particle is dependent on the process/unit operation the

material will be subjected. For example, the diameter of a sphere that has the same

surface area to volume ratio as a particle is used in grain chemical reaction kinetics

calculations (Ortega-Rivas et al., 2006; Rhodes, 2008). Chord, Martins diameter and

Ferret diameter (Ortega-Rivas et al., 2006; Yang, 2007)   are used as statistical diameter

for particle characterization and modeling while Sauter mean diameter (Abdullah et al.,

2003; McMillan et al., 2007) are used in combustion systems and fluidization models.

Although the Sauter mean diameter is typically used in fluidization studies, there has not

been a study conducted on the effectiveness of Sauter mean diameter and other diameter

types in predicting fluidization behavior of biomass grinds.

Furthermore, the equations that are commonly used for predicting fluidization velocity

(Abdullah et al., 2003; Abrahamsen and Geldart, 1980; Ergun, 1952; Leva, 1959; Miller

and Logwinuk, 1951) are based on average values of material properties such as density,

sphericity and particle diameter. These equations were developed with the underlying

principle that mono-component bed having uniformly sized particles is being fluidized.

Several studies in the literature have documented that this assumption is responsible for

the significant deviation of experimental from predicted fluidization velocity when these
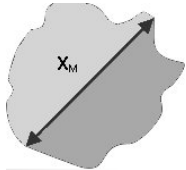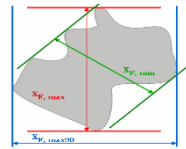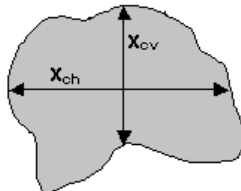
equations are applied to biological materials. For instance, using sand (particle size varies between 0.26 and 0.36 mm), and sawdust (particle size varies between 0.8 and 10 mm), Rao et al. (2001) obtained a relative percent error of 48% between experimental and predicted value. A relative error of up 88% was also obtained when Aznar et al. (1992) correlation was used to predict the fluidization velocity of sand (varies between 0.13 and 0.20 mm) and sawdust. One of the reasons why these correlations failed was because the author neglected the impact of multi-component nature of biomass grinds in formulating the predicting equations.

Therefore, the ability of commonly used equations and models to predict fluidization velocity must be re-examined. In this study, the particle properties (particle & bulk density, porosity, shape, and size distribution) of loblolly pine wood grind were thoroughly investigated. The particle sizes of the grind were quantified using different diameter measurement schemes for fractionated and unfractionated loblolly pine grind. Finally, the measured properties were plugged into some selected fluidization equations to predict the U_{mf} of loblolly pine wood grinds that were earlier determined experimentally using a bench scale fluidized bed system. The impact of particle size fraction on channel, plug flow, de-fluidization and minimum fluidization velocity prediction were also investigated.

Table 3.1: Properties of powders in Geldart's classification Geldart (1973)

| Geldart's Grouping | Properties and behavior of particles during fluidization | | | |
	Particle size (µm)	Particle density (kg/m^3)	Bed expansion behavior	Bubbling formation
A	20 and 100	< 1400	Bed expands considerably before bubbling commences and collapse slowly at the rate of 0.3 – 0.6 cm/s when gas supply is suddenly cut off.	In freely bubbling beds, the velocity of small bubbles (< 4 cm) appears to be about 30 – 40 cm/s regardless of bubble size.
B	$40 < dp < 500$	1400 – 4000	Small bed expansion and rapid collapse of bed when gas supply is cut off.	Bubble size increases linearly with both bed height and excess gas velocity (U - Uo).
C	$dp < 20$	200 – 1200	Powder lifts as a plug in a small diameter tube or formation of channel extending from distributor to the bed surface. Bed collapses slowly when gas supply is cut off.	Inter-particle forces are generally higher than forces exerted by fluid on the particle due to small particle size, strong electrostatic charges and or wet or sticky material, making bubbling formation difficult.
D	$dp > 1000$	> 400	Bed expansion is low and it is characterized by combination of steady slug motion and intense irregular particles motion. Bed collapse rapidly when gas supply is cut off.	Instead of bubbling, spouted bed can easily form

Table 3.2: Schematic representation of selected size measuring schemes for non-spherical particles.

Symbol	Diameter scheme	Formula and definition	Representation
X_{Ma}	Martins	Length of the chord through the centroid which bisects area of the particle into two equal halves.	\n\nGmbH (2011)
X_{Fe}	Ferret	Longest distance between parallel tangents touching opposite side of the object.	\n\nGmbH (2011)
X_c	Chord	The distance between two points on the contour, measured exactly across the center of gravity of the projection area. Chord length can be divided into minimum and maximum.	\n\nGmbH (2011)

3.3 Material and Methods

3.3.1 Sample preparation

Loblolly pine wood chips were obtained from a forest plantation in Alabama, U.S. The

chips were ground using a hammer mill (Model 358, New Holland, Pa.) fitted with 3.18

mm diameter round holes screen (Fig. 3.1). After grinding, the moisture content of the

sample was determined using ASTM standard E871-82 ASTM (2007) procedure. This

involves placing about 10 g sample in a convective oven at $105 \pm 2\ ^{o}C$ for 24 hrs. The

mass loss of the sample was used to calculate the sample moisture content in wet basis.

Figure 3.1: Hammer mill used for size reduction process

The ground samples were divided into two groups: whole (i.e. un-fractionated sample A)

and fractionated sample (B). Whole sample serves as the control sample. About 100 g of

group B sample was weighed and fractionated into seven fractions by screening through

the following sieves (US) # 12 (1.7 mm), # 14 (1.4 mm), # 18 (1 mm), # 30 (600 µm), #

50 (300 µm), #100 (150 µm), # 270 (53 µm). A sieve shaker (model Rx 29, Tyler, Inc.,

Mentor, Ohio) was used for fractionating the samples for 15 minutes (Fig 3.2). Particles

retained on each sieve were collected for subsequent test (see Table 3.3 for particle

groupings and identification). The fractionation process was repeated until an average of

1.5 kg samples were obtained for each of the fractions.

Figure 3.2: Sieve shaker used for fractionating the samples

Table 3.3: Sample preparation, groupings and identification based on sieve class

US sieve #		
Pass through	Retained on	Sample nomenclature
-	12 (1.7 mm)	B1
12	14 (1.4 mm)	B2
14	18 (1.0 mm)	B3
18	30 (600 µm)	B4
30	50 (300 µm)	B5
50	100 (150 µm)	B6
100	270 (53 µm)	B7

3.3.2   Particle size analysis

3.3.2.1 Whole sample (unfractionated sample A)

Particle size analysis was carried out on sample A by placing 100 g of sample on the

volume based image analysis (Camsizer®, Retsch Technology, Haan, Germany)

following the method described in the section 3.3.3. The distribution data obtained from

the software of the instrument was used to determine the geometric mean diameter (d_{gw})

of the particles as outlined in ASABE S319.3 standard procedure (ASABE, 2006).

3.3.2.2 Fractionated sample (sample B)

Eqn. 3.1 was used to determine the geometric mean diameters (d_{gw}) of all the sample

(ASABE, 2006) using the data obtained from the volume based image analysis (describe

in the next section).

$$d_{gw} = \log^{-1}\left[\frac{\sum\limits_{i=1}^{n}\left(W_i \log \overline{d_i}\right)}{\sum\limits_{i=1}^{n} W_i}\right] \tag{3.1}$$

$$S_{\log} = \left[\frac{\sum_{i=1}^{n} \left(W_i \log \overline{d_i} - \log d_{wg} \right)^2}{\sum_{i=1}^{n} W_i} \right]^{1/2} \qquad (3.2)$$

where,

d_i = nominal aperture size of the ith sieve, mm

$\overline{d_i} = \sqrt{d_i \times d_{i+1}}$

W_i = mass on i^{th} sieve, g

n = the number of sieves +1 (pan)

d_{gw} = geometric mean diameter by mass, mm

$S_{\log}$ = geometric standard deviation of log normal distribution by mass in ten-based logarithms, dimensionless

3.3.3   Particle size

An image analysis system (Camsizer®, Retsch Technology, Haan, Germany) was used to measure the Martin, chord and minimum Ferret diameters of all the samples. In addition, the software provided by the image analysis system was used to obtain the average specific surface area (S_{ssa}) and mean sphericity (φ) values of these samples. S_{ssa} was then used to calculate the surface to volume equivalent sphere diameter d_{sv} (Eqn. 3.3) (Rhodes, 2008). It is also important to state that chord diameter is the default diameter scheme on the Camsizer instrument. Hence, particle size distribution data were reported based on chord diameter unless stated otherwise.

$$d_{sv} = \frac{6}{S_{ssa}} \qquad (3.3)$$

3.3.4 Particle density

A gas pycnometer (Accupyc 1330, Micromeritics Instrument Corp., Norcross, Ga.) was used to measure the particle densities of all the samples. The gas pycnometer, uses helium to estimate the pressure difference between a reference cell and a cell containing the sample. The pressure difference was used by the pycnometer to estimate the volume of a known mass of sample.

The particle density was computed using Eqn. (3.4)

$$\rho_p = \frac{m_p}{v_p} \tag{3.4}$$

where, ρ_p is particle density (kg/m^3), m_p is sample mass (kg) of particle, and v_p is sample volume (m^3) of particle.

3.3.5 Bulk density

Bulk densities of all the samples were determined using an apparatus that consists of a funnel through which the sample freely falls onto 1137 mm^3 cup. Bulk density was estimated as the ratio of the mass of the sample in the container to the volume of the container.

3.3.6 Porosity

The inter – granular porosity (ε) of the ground wood sample was calculated from the measured values of bulk density and particle density as follows;

$$\varepsilon = 1 - \frac{\rho_b}{\rho_p} \tag{3.5}$$

where ρ_b is bulk density (kg/m^3) and ρ_p is particle density (kg/m^3).

3.3.7 Fluidized bed system and fluidization test

Fig. 3.3 shows a schematic diagram of the fluidized bed system that was used to measure the minimum fluidization velocity of all the samples. The bed is composed of an acrylic cylindrical pipe with internal diameter of 101.6 mm and a height of 1000 mm. The system is also fitted with a distributor that has 100 µm uniformly distributed perforations (Purolator, Model UNS 530403, Sacramento, CA 95828). The distributor supported the samples to be fluidized. Fluidized gas (air) was supplied by a blower (Black and Decker, Model LH5000, Antioch, CA). Air speed was regulated by a fan speed controller (Lutron electronic, MFG part S2-LFSQH-WH Monroe, NJ) and measured by a vane anemometer (FM Metal Vane anemometer, model 407113, Nashua, NH 03063) (see appendix 3 for equipment specification) located at 0.7 m from the blower and was connected to a computer through a RS-232 PC interface was used to transmit the recording on the computer monitor. The software (Vane anemometer data logger, model 47001, version 4.0) provided by the manufacturer was used to measure the airflow rate and display the result on the computer monitor. Pressure drop across the bed was measured by connecting a U-tube manometer into the upper (800 mm above the distributor) and lower (200 mm below the distributor) pressure taps. In order to quantify the pressure drop across the distributor at no load conditions, the pressure drop (ΔP_{empty}) across the bed and the corresponding air velocity were respectively measured and recorded with the manometer and vane anemometer (Fig 3.3). The flow patterns and bed mixing behavior at different operating conditions with time were studied from recordings made using a digital camera (Nikon, Model S3100 Melville, NY 11747-3064) that was installed at the front of the fluidized bed.
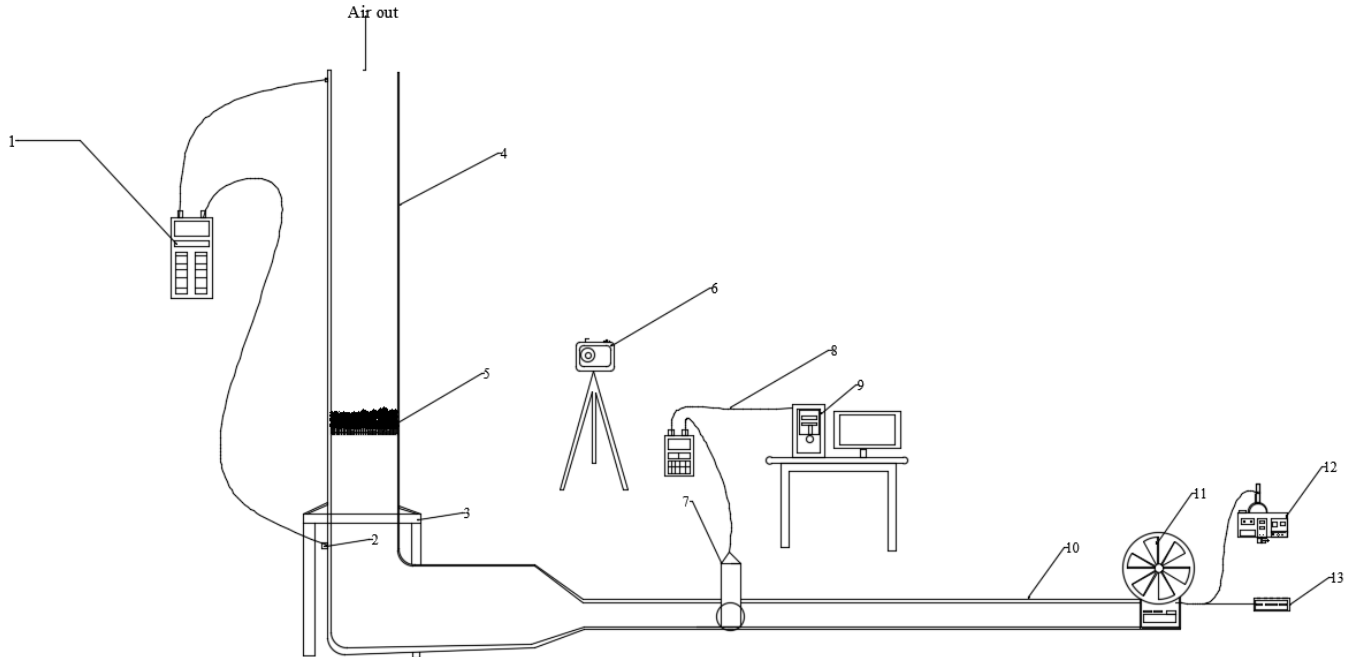
(1)- manometer, (2)- lower pressure tap, (3) bed support , (4) – fluidization test chamber having 4 inches diameter pipe, (5) – bed material on distributor plate, (6)- Nikon Digital camera (7) – flow rate probe, (8)- RS232 cable, (9)- computer system, (10) – 2 inches (D) PVC pipe, (11) – air blower, (12) air blower controller, (13) power source

Figure 3.3: Schematic diagram of the system used for fluidization.

To obtain the fluidization data for a sample, a weighed sample (120 g) was poured on the distributor of the fluidization system. The velocity of air into the bed was increased gradually. At any air velocity, the pressure drop (ΔP_{Total}), and the airflow reading were allowed to stabilize for 60 seconds before they were recorded. Minimum fluidization velocity was identified as the velocity at which increasing trend in bed pressure of the packed bed terminates when pressure drop was plotted against the air flow rate (Gupta and Sathiyamoorthy, 1998; Kunii and Levenspiel, 1991). To verify accuracy of the readings (pressure and airflow rate) obtained from this study, the fluidization system was used to measure the minimum fluidization velocity of sand.

3.3.8 Statistical analysis

All experiments were conducted in triplicates. The results were presented in relevant section as mean values and standard deviation. The effect of sample size obtained from the different size measurement scheme on bulk density, particle density and particle size diameter were analyzed using a generalized linear model from SAS statistical software (SAS, 2011). In addition, a pairwise t-test using least squares means procedure with tukey multiple comparison test was computed for each effect and their interactions. All the test were considered to be statistical significant when $p \leq 0.05$. The difference between predicted (minimum fluidization velocity based on equations and diameter types) and observed (minimum fluidization velocity obtained from laboratory experiment) were evaluated by determining the mean relative deviation (MRD) following the method used by (Nemec and Levec, 2005).

$$MRD(\%) = \frac{1}{N}100\sum_{i=1}^{N}\frac{\left|\lambda_{1.calc} - \lambda_{i.\exp}\right|}{\lambda_{i.\exp}} \qquad (3.6)$$

where

$\lambda_{1.calc}$ is calculated U_{mf} from predicting equation (m/s)
$\lambda_{i.\exp}$ is experimentally obtained U_{mf} (m/s)
N is the numbers of data points

3.4 Result and Discussion

3.4.1 Physical properties of ground loblolly pine wood (Sample A and B)

3.4.1.1 Particle size

Particle size distributions of the unfractionated and the seven fractionated ground loblolly pine wood samples obtained from the particle size imaging system are shown in Fig 3.4. There was skewness in the distributions of the ground sample, which is typical of ground biological materials. The skewness however reduces with increase in class size. For instance, particle retained on nominal screen size of 1.7 mm was almost normally distributed around 1.7 mm particle size. While particle retained on 0.15 mm had a long tail positive skewness. The estimated geometric mean diameters for the samples are given in Table 3.4.
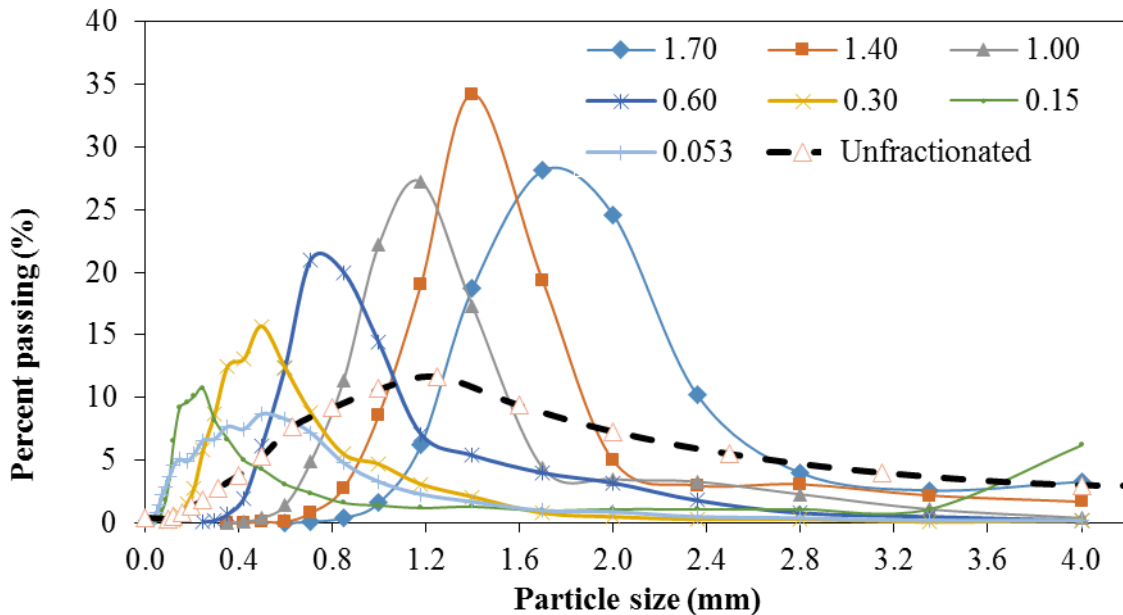
*Numbers in the legend are the nominal diameters (mm) of the screen used for fractionation.

Figure 3.4: Particle size distribution of fractionated and unfractionated loblolly pine wood.

90

The measured diameter using the different measurement schemes is shown in Table 3.4.

For sample A, the measured diameters varied between 0.58 and 1.07 mm. The highest

value was obtained from the minimum Ferret diameter (84.4% higher than the lowest

measured diameter – Sauter mean diameter). Similarly, for Group B samples, particle

size based on Ferret's diameter was the highest (Table 3.4). For instance, sample B3, the

value of minimum Ferret diameter was higher than the surface-volume diameter, the

Martin diameter, and the chord diameter by 18.3%, 23.6%, and 7.03% respectively.

These highest values of Ferret diameter is because the measurement scheme is based on

the longest distance between parallel tangents (Table 3.2). Furthermore, Fig. 3.4 shows

that the group B samples retained their lognormal size distribution profile even after

fractionation. This confirmed that the lognormal size distribution property is an inherent

property of biomass grinds. Statistical analysis affirmed that particle sizes of samples in

group B were significantly ($p <0.05$) affected by the choice of the diameter measurement

scheme.

Table 3.4: Effect of measurement scheme on diameter of fractionated and unfractionated loblolly pine wood grinds.

		Sieve number						
		4-12	12-14	14-18	18-30	30-50	50-100	100-270
		Fractionated samples						
Diameter schemes	A	B1	B2	B3	B4	B5	B6	B7
Geometric mean+ (mm)	0.83	$2.12^{A,2}$	$1.89^{B,1}$	$1.54^{C,1}$	$1.12^{D,1}$	$0.73^{E,1}$	$0.35^{F\,2,1}$	$0.17^{G,3}$
	(0.32) *	(1.73) *	(1.53) *	(1.35) *	(0.39) *	(0.34) *	(0.83) *	(0.88) *
Chord (mm)	1.002	$2.11^{A,\,2}$	$1.68^{B,\,2}$	$1.39^{C,\,2}$	$1.04^{D,\,2}$	$0.63^{E,\,3}$	$0.55^{F,\,2,1}$	$0.51^{F,\,1}$
	(0.05)	(0.03)	(0.01)	(0.01)	(0.02)	(0.02)	(0.26)	(0.10)
Min. Ferret (mm)	1.07	$2.24^{A,\,1}$	$1.80^{B,\,2,1}$	$1.49^{C,\,1}$	$1.13^{D,\,1}$	$0.69^{E,\,2,1}$	$0.59^{E,1}$	$0.54^{E,\,1}$
	(0.05)	(0.04)	(0.01)	(0.01)	(0.03)	(0.03)	(0.27)	(0.10)
Martins (mm)	0.83	$1.83^{A,\,3}$	$1.42^{B,\,3}$	$1.10^{C,\,4}$	$0.80^{D,\,3}$	$0.45^{E,F,\,4}$	$0.52^{E,\,2,1}$	$0.36^{F,\,2}$
	(0.04)	(0.02)	(0.01)	(0.06)	(0.01)	(0.01)	(0.13)	(0.09)
Surface-volume (mm)	0.79	$1.83^{A,\,3}$	$1.47^{B,\,3}$	$1.19^{C,\,3}$	$0.84^{D,\,4}$	$0.45^{E,\,4}$	$0.24^{F,\,2}$	$0.27^{F\,2,3}$
	(0.04)	(0.02)	(0.01)	(0.03)	(0.01)	(0.01)	(0.01)	(0.04)

 Values are means of triplicates and numbers in parentheses are standard deviation
Means with the different superscript (alphabet) in a row are significantly different (p<0.05)
Means with the different superscript (numeric) in a column are significantly different (p<0.05)
[+] Values are obtained from ASABE S319.3 analysis method.
*Geometric mean standard deviation obtained from Eqn. 3.2
A acronym for Unfractionated samples

3.4.1.2 Bulk, particle density and porosity

The particle density of whole sample obtained in this study was 1469.5 kg/m^3 and the

result was comparable to the value of 1440.0 kg/m^3 obtained by Hehar et al. (2014) for

loblolly pine wood grinds. In addition, there were no visible trends between particle

densities and particle size of fractionated samples (Table 3.5). This suggests that voids

within individual particle were not affected by the grinding (ground through 3.12 mm

screen size) process and by particle size. The bulk densities of group B samples however

decreased from 278 kg/m^3 to 166 kg/m^3 as nominal screen reduced from 1.7 mm (sieve

number 12) to 0.15 mm (sieve number 100) with the bulk densities of samples B1, B2,

B3, B4 and B5 being significantly different (p <0.05) from bulk densities obtained for B6

and B7. The reduction in bulk density with reduction in size could be attributed to

biomass grinds collected after fractionation exhibit different packing because of particles

having similar sizes as compared to the unfractionated biomass grinds which comprises

of different particle size range. Similar result was obtained by Oginni (2014) using

loblolly pine wood grinds and Liu et al. (2008a) using unlubricated ibuprofen size

fraction. Statistical analysis also revealed that the bulk densities were significantly

affected by particle size (p < 0.05).

Table 3.5: Physical properties of unfractionated and fractionated loblolly ground wood.

Properties	A	Sieve #						
		4-12	12-14	14-18	18-30	30-50	50-100	100-270
		Fractionated samples						
		B1	B2	B3	B4	B5	B6	B7
Bulk density (kg/m^3)	311.1 [A] (7.9)	278.0 [C] (1.0)	277.7 [C] (2.1)	320.7 [A] (2.1)	290.3 [B] (7.6)	234.3 [D] (1.5)	169.3 [E] (2.5)	166.3 [E] (1.2)
Particle Density (kg/m^3)	1469.0 [C] (7.0)	1471.6 [B] (0.8)	1466.1 [C,B] (7.4)	1470.7 [B] (12.3)	1468.2 [C,B] (6.7)	1486.9 [B] (11.5)	1512.7 [A] (17.7)	1524.3 [A] (19.4)
Porosity	0.79 [E] (0.01)	0.92 [C] (0.01)	0.81 [C] (0.01)	0.78 [E] (0.01)	0.79 [D] (0.01)	0.84 [B] (0.01)	0.89 [A] 0.01)	0.89 [A] (0.01)
Sphericity	0.52 [D] (0.02)	0.60 [A] (0.01)	0.57 [B,A] (0.01)	0.55 [B,C] (0.03)	0.51 [C,D] (0.01)	0.41 [E] 0.01)	0.23 [F] (0.01)	0.43 [E] (0.03)

Values are means of triplicates and numbers in parentheses are standard deviation
Means with the different superscript (alphabet) in a row are significantly different (p<0.05)
A acronym for Unfractionated samples

Table 3.5 also shows that the void spaces within the fractionated samples were high

(0.78-0.91). Other authors have reported similarly high porosity values for biomass

feedstock. Lam et al. (2008) found that the porosity of switchgrass decreased from 0.87

to 0.82 as particle size increased from 0.10 mm to 2.00 mm. Naimi et al. (2007) reported

that the porosity of switchgrass decreased with increase in particle size from 0.71 to 2.80

mm. Manickam and Suresh (2011) measured the porosity of coir pith to vary between

0.62 to 0.86 within the particle size range of 0.075 to 3.00 mm. Fasina (2006) concluded

that it will be difficult to justify the transportation of biomass grinds because the porosity

of switchgrass, peanut hull, and poultry litter varies between 0.62 to 0.83. Although high

void fraction should enhance easy fluid penetration through the packed bed, they can also aid in formation of channeling as airflow under pressure entrain smaller particles, create bigger holes as bed structure rearranges, and ultimately cause particle segregation during fluidization.

3.4.1.3   Particle shape

The sphericity (φ) of the samples varied from 0.24 to 0.60 and generally decreased ($P < 0.05$) with reduction in particle size (Table 3.5). Cui and Grace (2007) classified flatness of particles based on their sphericity. Sphericities of $\varphi < 0.5$ indicates an extremely flat particles, $\varphi > 0.5$ indicates flat particles and $\varphi > \sim 0.8$ is nearly spherical particles. Similarly, Lucas et al. (1986) also classified sphericity of particles into three categories namely, round ($0.8 \leq \varphi \leq 1$), sharp ($0.5 \leq \varphi \leq 0.8$) and others ($0.1 < \varphi < 0.5$). Therefore, based on these classifications, the sphericities of ground loblolly pine wood is flat and sharp.

3.4.2   Geldart's classification

Table 3.6 shows the effect of diameter measurement scheme on Geldart's classification of unfractionated and fractionated loblolly pine wood grinds. Owing to the influence of diameter measurement scheme on measured size, the Geldart's classifications of unfractionated grinds was either Group B or Group D. Group B and D particles in Geldart classification (Table 3.1) have distinct and opposite behavior. Therefore, the method used for size measurement can potentially affect the interpretation of how biomass grinds and similar non-spherical particles will respond in fluidization. In addition, prediction of minimum fluidization velocity and other design parameters such as equipment selection for fluidizing biomass material that require the size of the fluidizing biomass be known,

95

would be significantly affected by particle measurement method. For fractionated

loblolly pine grinds, fractions B1, B2, and B3 had similar classification (Group D), while

B4, B5, and B6 varied between Groups D, B, and A. This confirms that the wide range in

size of particles in biomass grind sample is partly responsible for the unpredictable

fluidization behavior of biomass grinds. Therefore, Geldart classification should be

applied with caution for sample with multi-component and multi-sized particles such as

ground biomass.

Table 3.6: Geldart's classification of unfractionated and fractionated loblolly pine wood
grinds as affected by diameter measurement schemes.

		Sieve #						
		4-12	12-14	14-18	18-30	30-50	50-100	100-270
Diameter		Fractionated samples						
Scheme	Unfractionated	B1	B2	B3	B4	B5	B6	B7
Chord	D	D	D	D	D	B	B	B
Ferret	D	D	D	D	D	B	B	B
Martins	B	D	D	D	B	B	B	A
Sur.-vol.	B	D	D	D	B	B	A	A

The mean diameter value used for the classification is presented in Table 3.4.
The particle density for each data is presented in Table 3.5
Geldart plot used for the classification is in Appendix 2
Unfractionated sample was previously referred to as sample A

3.4.3   Fluidization behavior of ground loblolly pine wood

3.4.3.1 Validation of fluidization system

Based on the plot of pressure drop across the bed of sand particles against the air

velocity as shown in Fig. 3.5. The minimum fluidization velocity of sand was measured

to be 0.28 ± 0.002 (m/s). The minimum fluidization velocity was identified as the

intersection between the rising and constant bed pressure drop (Gupta and

Sathiyamoorthy, 1998). It can be seen from the figure that duplicate runs for the sample

are essentially the same. This result is comparable to values of 0.35 m/s and 0.34 m/s

obtained for minimum fluidization velocity of sand as reported by Sánchez-Delgadoa et al. (2011) and Patil et al. (2005) respectively. This validates the pressure drop – velocity data obtained from the fluidization setup of Fig. 3.3.
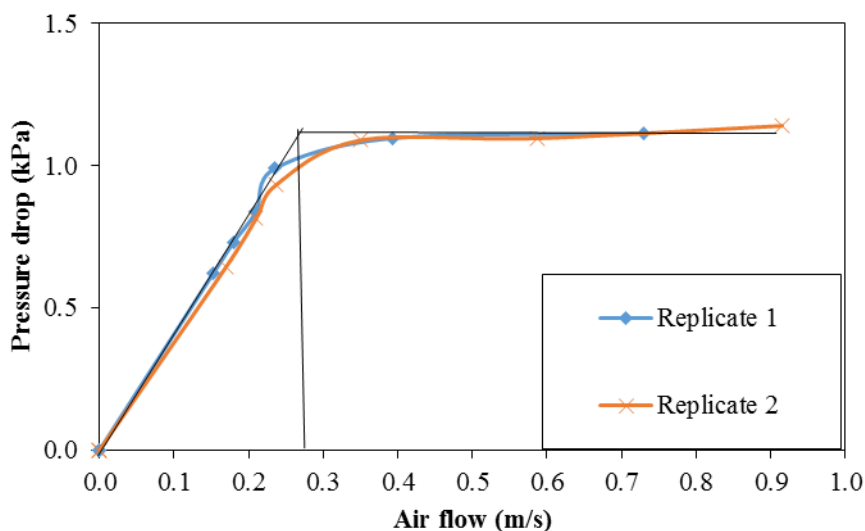
Figure 3.5: Plot of pressure drop versus air velocity for sand particles

3.4.3.2 Fluidization behavior of unfractionated biomass grinds (Sample A)

Figs. 3.6 and 3.7 show some of the behaviors that were observed when Sample A (whole sample) was fluidized. Plug-flow, channeling, top fluidization, and de-fluidization were observed before fluidization was eventually achieved. When air flow through the bed reached a velocity at which the updraft created from the air flow was sufficient to lift the bed entirely (suggesting the U_{mf} was attained at 0.16 to 0.30 m/s, smaller particles entrained in the air stream were either deposited in another location in the bed or carried out of the bed. This rearrangement caused the airflow to concentrate in a particular region (region that offered least resistance to airflow) thus causing channels of various sizes which can vary from multiple small channels (less than 0.01m diameter) to a channel with diameter that is almost half of the bed (0.05 m) (Fig 3.6).

97

Figure 3.6: Channeling during fluidization of ground biomass (unfractionated, sample A) impeded fluidization processes.

Further increase in air velocity resulted in bigger particles settling at the base in an interlock position. In between the interlocked particles (mostly bigger particles) are smaller particles that made air penetration through the bed difficult. All of these rearrangements of particle resulted in the bed rising in a plug (Fig 3.7).

Figure 3.7: Plugged flow during fluidization of ground biomass (unfractionated, sample A) because of particle interlocking.

The plug was disentangled by increasing the airflow rate. It is also important to mention that after the bed collapse due to plug flow breakage, smaller particles trapped within the bigger particle network escape thereby creating another stage for channeling and entrainment. Defluidization was another phenomenon that was observed after complete fluidization velocity of bed was achieved. Defluidization occurs after significant entrainment of smaller particles from the bed resulting in a situation where the remaining large particles require higher flow rate to fluidize. At this particular condition, a multicomponent bed was turned into almost mono-component bed. This suggests that the fluidization state of a bed that is composed of non-uniform and non-spherical particles is constantly evolving.

3.4.3.3   Fluidization behavior of fractionated biomass grinds (Sample B)

Figs. 3.8 and 3.9 showed some of the behaviors that were observed when group B samples (fractionated samples) were fluidized. The behavior observed can be categorized into two based on the class size. For sample B1, B2 and B3, channelings were seen more often before fluidization state was achieved. The channeling formation could be attributed to networks of void spaces that simply grew with increase in airflow into bigger channels. However, the channel breaks up once the updraft is sufficient to lift the bed entirely. In addition, particle entrainment out of the bed were minimal or not observed until the whole bed were in intensive mixing and at this stage, the minimum fluidization velocity has been achieved. Since bed channeling were rampant, bed expansion were not uniform too (Figure 3.8).

Figure 3.8: Typical channeling behavior observed for B1, B2 and B3 samples during fluidization processes (the snapshot was that of B1 sample).

The second category of behavior were obtained from B4, B5, and B6 samples. As airflow increased, channelings were observed but sometimes the channeling disperse quickly. However, at B5 samples, the cohesive force between particles causes channels to evolve into different shapes (Fig 3.9). Unless the bed mixes intensely, entrainment out of the bed was limited.

Figure 3.9: Typical channeling behavior observed for B4, B5 and B6 samples during fluidization processes (the snapshot was that of B5 sample).

In summary, there were notable differences in behavior of fractionated and unfractionated samples to airflow. For instance, the plug flow in fractionated samples could be problematic to break up while the unfractionated sample disentangled with relative ease as airflow increase. The difference in behavior is principally due to wide particle size distribution in unfractionated sample compared with fractionated samples.

3.4.3.4 Experimental determination of minimum fluidization velocity of samples A and B

Fig 3.10 shows the stages of fluidization during the experimental determination of the minimum fluidization velocity. At stage 1, which is the initial state, about 120 g sample is weighed and poured on the distributor in the bed chamber. The air velocity was increased slowly, and the corresponding pressure drop across the bed was recorded at each flow increment. Eventually a limit was reach after which three or four consecutive increase in airflow did not result in appreciable increase in pressure drop (stage 2). Then at this point, the velocity was considered to be the minimum fluidization velocity and the bed was considered to be at minimum fluidization state (Fig 3.8 b) (Davidson et al., 1977; Drake, 2011; Kunii and Levenspiel, 1991). Further increase in the superficial gas velocity to about $4 \times U_{mf}$ resulted in complete fluidization of the bed (stage 3).

Several measures were taken to prevent data collection from been compromised by poor fluidization behavior as previously discussed. For instance, plug flow were stopped by gently knocking on the wall or increase the airflow velocity and but in few cases that the plug refused to break, the airflow velocity would be cutoff and the experiment restarted with a new set of sample. For channeling, the air velocity was reduced so that particle can fall into their natural position. Afterward the velocity was ramped up again and when

channel persisted, the flow velocity is increased by ~50% of the last flow velocity. As previously stated, the channel usually disintegrated. However, at some occasions, we notice recalcitrant channels that refuse to break with increase in airflow (B6 samples). In such a situation, the airflow is stopped and the bed material is evacuated for fresh sample. It is also important to add that when bed entrainment increased because of increase in airflow velocity, the corresponding pressure drop data could be compromised (lower) because of reduction in bed inventory. When this occurred before minimum fluidization state were achieved, then the experiment is discarded and restarted.

| (a) Stage 1 | (b) Stage 2 | (c) stage 3 |
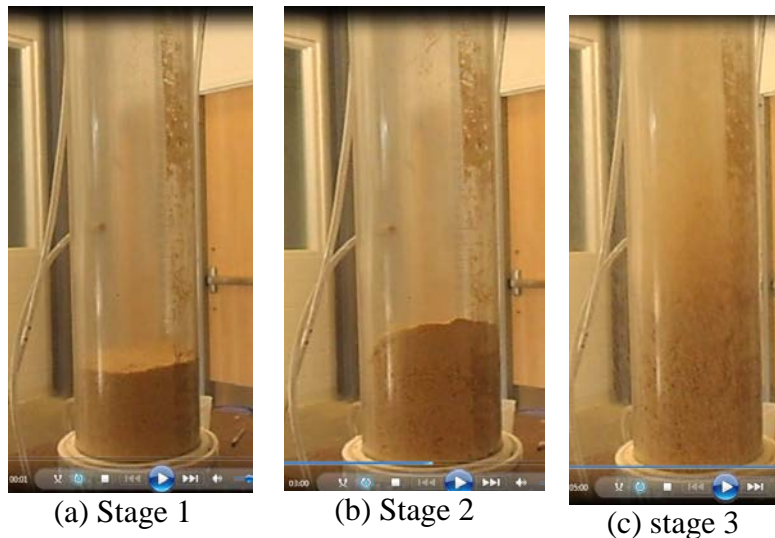
Figure 3.10: Typical behavior of loblolly pine wood grinds during fluidization.
First test from left side is the initial states (a) initial stage, (b) fluidization stage, (c) complete fluidization.

The plot of pressure drop against air velocity for sample A (unfractionated) and samples from group B fractionated (sample B) is shown in Fig. 3.11. The minimum fluidization velocity of sample A (un-fractionated ground loblolly pine wood) was measured to be 0.25±0.04 m/s. The nature of the pressure drop curve with increase in the superficial gas velocity showed a deviation from that of Fig. 3.5. The wobbling line where constant pressure line is expected could be attributed to the non-uniformity in size, shape and size

distribution of grinds (Woodcock and Mason, 2013). However, it can also be seen that the instability in the line of constant pressure gradually reduced with narrower size distribution group (Sample B).
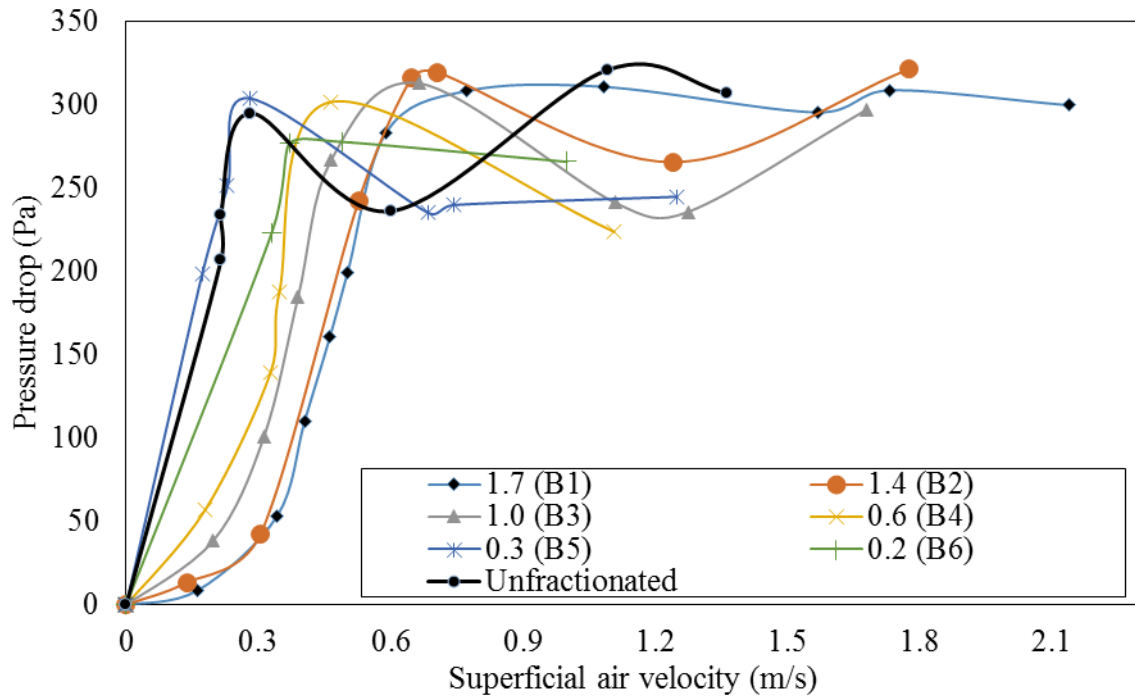
*Numbers in the legend are the nominal diameters (mm) of the screen used for fractionation.
Figure 3.11: Variation in pressure drop with superficial gas velocity for unfractionated sample and Sample B (fractionated sample).

All of the 'B' samples have U_{mf} greater than 0.25 m/s (the minimum fluidization velocity of unfractionated sample) with the minimum fluidization of larger particles being about 3 times of the smaller particles (Table 3.7). This explains the fundamental reason why large particles in ground samples remain un-fluidized whereas smaller particles are fluidized and often ejected out of fluidization chamber. Similar observation was made by Liu et al. (2008b) when a raw steam coal (a kind of bituminite usually used in industrial chain grate boilers) between > 2 mm to 40 mm was fluidized. They found that about half of the coal mass was blown out of the bed; some were entrained at the top section while the

remainder was at the bottom section of the bed after applying air at superficial gas velocity of 3.0 m/s for 10 min. This variation in the U_{mf} of multi-component materials such as biomass grinds will affect their optimal performance during fluidization. The same view was also expressed by Gauthier et al. (1999), Khoe et al. (1991) and Reina et al. (2000) when they determined the minimum fluidization velocity of river sand, spent fluid catalytic cracking catalyst (FCC) and scrap-wood particles respectively.

Table 3.7: Experimentally determined minimum fluidization velocities of ground loblolly pine wood fractions

Sample Tag	US sieve #		Minimum fluidization velocity (m/s)
	Pass through	Retained on	
B1	-	12	0.81±0.007
B2	12	14	0.63±0.035
B3	14	18	0.53±0.11
B4	18	30	0.40±0.07
B5	30	50	0.27±0.02
B6	50	100	0.29±0.01

The experimentally determined minimum fluidization velocities of the sample were compared with predicted velocities that were obtained from four commonly used fluidization equations (listed in Table 3.8). All of these equations only require measurement of physical properties of the material to be fluidized and the gas to be used for fluidization. Microsoft Excel® goal seek function was used to estimate the minimum fluidization velocity in equation 3.7 after substituting the appropriate values of the properties (Table 3.5). It is important to point out that the Eqn. 3.7 has a sphericity term and is different from the original Ergun equation in eqn. 2.6. The U_{mf} obtained from Eqns 3.8 -10 were obtained by direct substitution of physical properties of a fraction on

the right side of the equations. Physical properties of each fraction used in the equations

were obtained from Table 3.5. All of the diameters (Martins, chord, geometric mean,

minimum Ferret, and surface-volume diameter) were used in the equations to predict U_{mf}.

Table 3.8: Selected fluidization equation used for predicting the experimental U_{mf} of ground wood

Equation	Eqn. #	Label	Reference
$$\frac{\Delta P}{L} = 150 \frac{(1-\varepsilon)^2}{\varepsilon^3} \frac{\mu_g U}{(\phi_s d_p)^2} + 1.74 \frac{(1-\varepsilon)}{\varepsilon^3} \frac{\rho_g U^2}{(\phi_s d_p)}$$	3.7	Mod-Ergun	Ergun (1952)
$$U_{mf} = \frac{0.0093 d_m^{1.82} (\rho_p - \rho_g)^{0.94}}{\mu_g^{0.88} \rho_g^{0.06}}$$	3.8	Leva	Leva (1959)
$$U_{mf} = 1.25 \times 10^{-3} \left(\frac{d_p^2 (\rho_s - \rho_g)^{0.9} \rho_g^{1.1} g}{\mu_g} \right)$$	3.9	Miller	Miller and Logwinuk (1951)
$$U_{mf} = 9 \times 10^{-4} d_p^{1.8} [(\rho_s - \rho_g) g]^{0.934} \rho_g^{-0.066} \mu_g^{-0.87}$$	3.10	Geldart	Abrahamsen and Geldart (1980)

*Mod-Ergun has sphericity term while Original Ergun equation does not
where,

U_{mf}	=	Minimum fluidization velocity (m/s)
d_m	=	Sauter mean diameter (m)
U	=	Superficial velocity (m/s)
ρ_s	=	Density of particle (kg/m^3)
ρ_g	=	Density of gas (kg/m^3)
μ_g	=	Dynamic viscosity of fluidization gas (Pa s)
d_p	=	Surface volume mean diameter of particle (m)
ε	=	Void fraction of bed
φ_s	=	Sphericity of particle
ΔP	=	Pressure drop (Pa)
L	=	Length (m)
g	=	Acceleration due to gravity (m/s^2)

3.4.4 Effect of diameter measurement scheme on predicted values

Table 3.9 shows the effect of diameter measurement scheme on the predicted U_{mf} from the four equations listed in Table 3.8. The actual predicted values are shown in Appendix 2. For the unfractionated sample (A), when the mean diameter used in the equations was changed from surface-volume (least) diameter, to minimum Ferret diameter (highest), the predicted value obtained changed by 16.4%, 72.6 %, 73.7 %, 16.5 % and 83.4 % for Ergun, Geldart, Leva, Mod-Ergun, and Miller equations respectively. Although there were differences in the actual predicted values obtained when Ergun and Mod-Ergun were used, the difference resulted in the same percent change in predicted value. The least percent change in predicted values was obtained using Ergun equation. This could be could be attributed to the structure and the underlying assumption made during computation/ development of Ergun's equation. Firstly, Ergun and Mod-Ergun equations required more parameter than all other equation before U_{mf} can be estimated. For instance, Ergun has correlation for void fraction – a parameter that influence air movement /penetration through the bed. Particles are expected to have a voidage equal to the voidage at minimum fluidization (Ergun assumptions, see section 2.9.1). This is not the case for biomass grinds because the minimum fluidization velocity iof the particles that comprise the biomass grinds are different. Larachi et al. (1999) also made similar observation by attributing poor prediction between experimental and predicted data to the mathematical structure of the correlations and also alluded that the equation could not embrace the high variability inherent in the properties of the material. Secondly, the minimum fluidization velocities were estimated by balancing the pressure drop parameter between fixed beds and fluidize bed state. Therefore, in order to obtain a velocity value, Ergun equation essentially is computed from the bed weight/unit area.

Table 3.9: Effect of size measurement method and popular fluidization equation on
          predicted minimum fluidization velocity.

	Measurement scheme		Size (% change)*	Percent change in predicted value				
Sample	Maximum	Minimum		Ergun	Geldart[+]	Leva[+]	Mod-Ergun[+]	Miller[+]
A	Ferret	Sur-vol.	35.4	16.4	72.6	73.7	16.5	83.4
B1	Ferret	Martins	22.4	10.6	43.9	44.5	10.6	49.8
B2	Geometric	Martins	33.1	15.4	67.3	68.3	15.4	77.2
B3	Geometric	Martins	40.0	18.3	83.2	84.5	18.4	96.0
B4	Ferret	Martins	41.3	18.9	86.2	87.5	18.9	99.5
B5	Geometric	Martins	62.2	27.5	138.9	141.2	27.7	163.2
B6	Ferret	Sur-vol.	145.8	57.1	404.8	414.0	59.9	504.3
B7	Ferret	Sur-vol.	100.0	41.7	248.2	253.1	41.9	300.0

*% change obtained by the ratio of change in maximum and minimum diameter value to minimum
diameter value.
[+]Nomenclatures referred to Table 3.8.
ǀErgun obtained from original Ergun equation expressed in Eqn. 2.9 having no sphericity factor.

For fractionated samples, percent change in the predicted value increased with decrease

in size. This could be attributed to the sensitivity of smaller particle to measurement

method because smaller particle has the least shape factor (sphericity of 0.4 from Table

3.5). In general, both Ergun and Mod-Ergun equation prediction gave a consistent lower

percent change in predicted value between highest and least diameter. Therefore, we can

safely conclude that measurement scheme has significant influence on measured

parameters and eventually the predicted values. However, it appears that Ergun equation

offer the best fluidization equation that can handle the changes in size due to

measurement scheme used.

3.4.5   Comparison between predicted and experimental values

The mean relative deviations (MRD) between experimental and predicted U_{mf} values

using the fluidization equations (Eqn. 3.7 -10) are shown in Table 3.10. For

unfractionated sample, Miller had the least mean deviation irrespective of the

measurement scheme. In overall, prediction obtained using Ergun equations (Ergun and Mod-Ergun) are significantly different from other equations. For instance, using surface to volume diameter, the MRD obtained from Ergun and Mod-Ergun was 142.9 and 217.8 % respectively while Leva, Geldart, and Miller equation was 6.9, 24.8 and -3.85 % respectively. Geldart, Leva and Miller equation were developed through experimental correlations and have similar structure as depicted in Eqn. 3.11.

$$U_{mf} = \frac{K d_m^l \left(\rho_p - \rho_g\right)^x}{\mu_g^n \rho g^y}$$ (3.11)

Where k, l, x, n and, y represent different coefficient obtained from the fitting process.

Ergun equation required more material specific parameter (e.g. porosity and sphericity), that probably increased the error obtained. For instance, a constant porosity value was assumed in estimating U_{mf} even though several authors and observation from this study show that bed porosity changes with velocity (Vejahati et al., 2009).

For fractionated samples, the deviation between predicted, and the experimental data reduced with reduction in size for all the equation considered. When the sample size was greater than 1.00 mm, Miller equation produced the least MRD with values of -25.4, -6.11, 0.57, and -2.83 % for B1, B2, B3 and B4 using Martins diameter. However, for sample below 1.00 mm, Leva gave the least MRD. Reduction in prediction in MRD with size could be attributed to the fact that size distribution reduced with reduction in size (see Table 3.4, for geometric mean and geometric standard deviation of particles).

Significant prediction difference between Ergun and Mod-Ergun equation could be attributed to the fact that Ergun equation derivation did not include sphericity factor. If

this factor is to be added so as to improve Ergun predictions, than Ergun equation has to be refitted with sphericity factor. In addition, prediction obtained when Martins and surface to volume mean diameter was used in the fluidization equation resulted in the least MRD between predicted and actual value for sample B1,B2, B3, and B4 for all equations used. Martins diameter is difficult to determine in a laboratory unless through image analysis. Several procedure has been established and statistically verified for surface- volume diameter. In fact, surface-volume mean diameter is liberally used in fluidization equation. However, for sample B5, B6 and B7, the MRD were less than 15% for all diameter schemes used with Leva, Geldart and Miller equation. This suggests that reduction in size to certain diameter may neutralize the effect of non-sphericity on predictive equation. Finally, the result also revealed that the effect of size distribution is presently not captured in the equations, hence the high MRD obtained in unfractionated sample. However, since in a real preprocessing plant, average properties of unfractionated sample is typically used (not fractionated sample properties) then surface to volume diameter offers the best diameter scheme with least MRD.

Table 3.10: Predictability of fluidization model for unfractionated woood grinds and effect of diameter measurement scheme.

Sample id	Diameter types/ dp (mm)		Ergun	Mod-Ergun	Leva	Geldart	Miller
					MRD (%)		
	Martins	0.83	147.7	224.5	12.2	32.6	0.4
Sample A	Chord	1.01	168.2	252.8	38.9	72.3	21.8
	Ferret	1.07	174.6	261.7	48.8	87.2	29.6
	Surf-vol.	0.79	142.9	217.8	6.9	24.8	-3.8
	Geometric	0.83	147.7	224.5	12.2	32.6	0.4
	Martins	1.83	-76.7	-110.7	-41.9	-85.2	-25.3
Sample B1	Chord	2.11	-85.3	-121.9	-66.2	-126.4	-44.4
	Ferret	2.24	-89.2	-126.8	-78.4	-147.6	-54.0
	Surf-vol.	1.83	-76.7	-110.7	-41.9	-85.2	-25.3
	Geometric	2.12	-85.6	-122.2	-67.1	-128.0	-45.1
	Martins	1.42	-64.2	-96.5	-16.2	-39.8	-6.1
Sample B2	Chord	1.68	-72.9	-108.0	-34.6	-69.7	-20.6
	Ferret	1.80	-76.7	-113.0	-43.9	-85.2	-27.9
	Surf-vol.	1.47	-66.1	-98.8	-19.0	-45.2	-8.7
	Geometric	1.89	-79.5	-116.7	-51.2	-97.6	-33.7
Sample B3	Martins	1.1	-48.5	-75.9	-1.6	-14.2	4.4
	Chord	1.39	-58.3	-89.1	-18.5	-40.6	-8.9
	Ferret	1.49	-61.4	-93.3	-25.0	-51.1	-14.1
	Surf-vol.	1.19	-51.7	-80.2	-6.5	-21.7	0.6
	Geometric	1.54	-62.9	-95.4	-28.4	-56.6	-16.8
	Martins	0.8	-39.0	-62.7	2.4	-3.1	5.7
Sample B4	Chord	1.04	-47.3	-74.3	-8.2	-19.1	-2.8
	Ferret	1.13	-50.2	-78.3	-12.9	-26.1	-6.5
	Surf-vol.	0.84	-40.4	-64.7	0.8	-5.5	4.4
	Geometric	1.12	-49.8	-77.9	-12.3	-25.0	-6.0

Table 3.10 Continued: Statistical evaluation of the effect of diameter type on predictive ability of different models of unfractionated sample

Sample id	Diameter types		Ergun	Mod-Ergun	Leva	Geldart	Miller
	dp (mm)			MRD (%)			
	Martins	0.45	-23.3	-45.0	8.8	7.6	9.9
Sample B5	Chord	0.63	-30.4	-56.1	3.6	0.6	5.7
	Ferret	0.69	-32.5	-59.4	1.5	-2.2	4.0
	Surf-vol.	0.45	-23.3	-45.0	8.8	7.6	9.9
	Geometric	0.73	-33.9	-61.5	0.1	-4.3	2.9
	Martins	0.52	-17.5	-53.3	7.0	5.2	8.4
Sample B6	Chord	0.55	-18.4	-55.2	6.1	4.0	7.7
	Ferret	0.59	-19.6	-57.7	4.9	2.4	6.7
	Surf-vol.	0.24	-6.6	-31.3	13.0	12.9	13.3
	Geometric	0.35	-11.4	-41.0	11.1	10.5	11.7
	Martins	0.36	-31.7	-46.9	5.8	5.3	6.6
Sample B7	Chord	0.51	-39.7	-57.8	2.2	0.5	3.6
	Ferret	0.54	-41.2	-59.8	1.4	-0.5	2.9
	Surf-vol.	0.27	-26.0	-39.2	7.5	7.3	7.9
	Geometric	0.37	-32.3	-47.7	5.6	5.0	6.4

3.5   Conclusion

In this chapter, the results of an experimental study on the physical and fluidization properties of ground loblolly pine wood relevant to fluidized bed system were measured. The result showed that a ground loblolly pine wood sample has mean particle density of 1460.6 ± 7 kg/m^3, bulk density of 311 ± 37 kg/m^3 and porosity of 0.787 ± 0.003. The Ferret diameter was found to be higher than surface-volume diameter, Martin's diameter and chord diameter by 18.3, 23.6, and 7.03% respectively. Also, the shape characteristic based on the sphericity value showed that the particle is flat and ranges between 0.23

and 0.60. The minimum fluidization velocity of loblolly pine wood grinds

(unfractionated sample ground through 3.175 hammer mill screen) was found to be 0.25

$\pm$0.04 m/s. However, fractionated samples had their minimum fluidization velocity

higher than 0.25 m/s –the velocity of un-fractionated sample. Prediction error were

found to be significant ($p<0.05$) and increase with increase in particle size. The use of

different diameter types in fluidization equation had a significant effect on prediction

(U_{mf}) obtained. Generally, Ergun equation (with or without sphericity factor) gave the

highest MRD. Although, change in diameter measurement scheme has little effect on

prediction of experimental minimum fluidization velocity. Other predicting equation

resulted in lower MRD but change of diameter scheme significantly influences the

predictability of those equations. Even though Martins diameter generally exhibited the

least MRD values, surface to volume diameter appeared to be the most practical in the

equation since standard experimental procedure has been established when image

analysis is not available.

3.6 Reference

Abdullah, M. Z., Z. Husain, and S. L. Yin Pong. 2003. Analysis of cold flow fluidization test results for various biomass fuels. *Biomass and Bioenergy* 24(6):487-494.

Abrahamsen, A., and D. Geldart. 1980. Behaviour of gas-fluidized beds of fine powders part I. Homogeneous expansion. *Powder Technology* 26(1):35-46.

Adapa, P., L. Tabil, and G. Schoenau. 2009. Compaction characteristics of barley, canola, oat and wheat straw. *Biosystems Engineering* 104(3):335-344.

ASABE. 2006. ASAE S319. 3—method of determining and expressing fineness of feed materials by sieving, ASABE Standards, 602–605, American Society of Agricultural and Biological Engineers, St. *Joseph, MI*.

ASTM. 2007. Standard test methods for direct moisture content measurement of wood and wood-base materials. American Society for Testing Materials. ASTM International West Conshohocken, PA.

Aznar, M. P., F. A. Gracia-Gorria, and J. Corella. 1992. Minimum and maximum velocities for fluidization for mixtures of agricultural and forest residues with a second fluidized solid. II. Experimental results for different mixtures. *International chemical engineering* 32(1):103-113.

Barakat, A., H. de Vries, and X. Rouau. 2013. Dry fractionation process as an important step in current and future lignocellulose biorefineries: A review. *Bioresource Technology* 134(0):362-273.

Cui, H., and J. R. Grace. 2007. Fluidization of biomass particles: A review of experimental multiphase flow aspects. *Chemical Engineering Science* 62(1):45-55.

Davidson, J. F., D. Harrison, and J. Carvalho. 1977. On the liquidlike behavior of fluidized beds. *Annual Review of Fluid Mechanics* 9(1):55-86.

Drake, J. B. a. H., Theodore J. 2011. The repeatability and uniformity of 3D fluidized beds. *Powder Technology* 213(13):148-154.

Ergun, S. 1952. Fluid flow through packed columns. *Chem. Eng. Prog.* 48:89-94.

Fasina, O. 2006. Flow and physical properties of switchgrass, peanut hull, and poultry litter. *Transactions of the ASABE* 49(3):721-728.

Fasina, O. O. 2008. Physical properties of peanut hull pellets. *Bioresource Technology* 99(5):1259-1266.

Gauthier, D., S. Zerguerras, and G. Flamant. 1999. Influence of the particle size distribution of powders on the velocities of minimum and complete fluidization. *Chemical Engineering Journal* 74(3):181-196.

Geldart, D. 1973. Types of gas fluidization. *Powder Technology* 7(5):285-292.

Gil, M., D. Schott, I. Arauzo, and E. Teruel. 2013. Handling behavior of two milled biomass: SRF poplar and corn stover. *Fuel Processing Technology* 112(0):76-85.

GmbH, S. 2011. Particle shape. Clausthal-Zellerfeld, Germany: Am Pulverhaus Available at: http://www.sympatec.com/EN/Science/Characterisation/05_ParticleShape.html.

Gupta, C. K., and D. Sathiyamoorthy. 1998. *Fluid bed technology in materials processing*. CRC.

Hehar, G., O. Fasina, S. Adhikari, and J. Fulton. 2014. Ignition and volatilization behavior of dust from loblolly pine wood. *Fuel Processing Technology* 127(0):117-123.

Khanal, S. K. 2010. *Bioenergy and biofuel from biowastes and biomass*. ASCE Publications, Reston Virginia.

Khoe, G. K., T. L. Ip, and J. R. Grace. 1991. Rheological and fluidization behaviour of powders of different particle size distribution. *Powder Technology* 66(2):127-141.

Kunii, D., and O. Levenspiel. 1991. *Fluidization engineering*. Butterworth-Heinemann Boston.

Lam, P., S. Sokhansanj, X. Bi, C. Lim, T. JayaShankar, G. Rezaie, and L. Naimi. 2008. The Effect of Particle Size and Shape on Physical Properties of Biomass Grinds. In *An ASABE Meeting Presentation. Paper.*

Larachi, F., I. Iliuta, O. Rival, and B. P. A. Grandjean. 1999. Prediction of Minimum Fluidization Velocity in Three-Phase Fluidized-Bed Reactors. *Industrial & engineering chemistry research* 39(2):563-572.

Leva, M. 1959. *Fluidization*. McGraw-Hill Chemical Engineering Series. McGraw-Hill, London

Liu, L. X., I. Marziano, A. C. Bentham, J. D. Litster, E.T.White, and T. Howes. 2008a. Effect of particle properties on the flowability of ibuprofen powders. *International Journal of Pharmaceutics* 362(1–2):109-117.

Liu, X., G. Xu, and S. Gao. 2008b. Fluidization of extremely large and widely sized coal particles as well as its application in an advanced chain grate boiler. *Powder Technology* 188(1):23-29.

Lucas, A., J. Arnaldos, J. Casal, and L. Puigjaner. 1986. Improved equation for the calculation of minimum fluidization velocity. *Industrial & Engineering Chemistry Process Design and Development* 25(2):426-429.

Mani, S., L. G. Tabil, and S. Sokhansanj. 2004. Grinding performance and physical properties of wheat and barley straws, corn stover and switchgrass. *Biomass and Bioenergy* 27(4):339-352.

Manickam, I. N., and S. Suresh. 2011. Effect of moisture content and particle size on bulk density, porosity, particle density and coefficient of friction of coir pith. *International Journal of Engineering Science* 3.

McMillan, J., C. Briens, F. Berruti, and E. W. Chan. 2007. Study of High Velocity Attrition Nozzles in a Fluidized Bed. In *The 12th International Conference on Fluidization - New Horizons in Fluidization Engineering*. F. Berruti, X. Bi, and T. Pugsley, eds. Vancouver, Canada: Engineering Conferences International.

Miller, C. O., and A. Logwinuk. 1951. Fluidization studies of solid particles. *Industrial & Engineering Chemistry* 43(5):1220-1226.

Mosier, N., C. Wyman, B. Dale, R. Elander, Y. Y. Lee, M. Holtzapple, and M. Ladisch. 2005. Features of promising technologies for pretreatment of lignocellulosic biomass. *Bioresource Technology* 96(6):673-686.

Naimi, L., S. Sokhansanj, X. Bi, C. Lim, S. Mani, M. Hoque, P. Lam, and A. Womac. 2007. Modeling and Characterization of Biomass Size Reduction. In *ASAE Annual Meeting*.

Nemec, D., and J. Levec. 2005. Flow through packed bed reactors: 1. Single-phase flow. *Chemical Engineering Science* 60(24):6947-6957.

Oginni, O. J. 2014. Contribution of particle size and moisture content to flowability of fractionated ground loblolly pine. M. S thesis. Auburn University, M. S thesis, Bisoystems Engineering Department, Auburn Alabama

Ortega-Rivas, Enrique, P. Juliano, and H. Yan. 2006. *Food powders: physical properties, processing, and functionality*. 1st ed. Springer, New York, Philadelphia.

Patil, K., T. Bowser, D. Bellmer, and R. Huhnke. 2005. Fluidization characteristics of sand and chopped switchgrass-sand mixtures. *International Commission of Agricultural Engineering* 7.

Rao, R., T. Ram, and J. V. Bheemarasetti. 2001. Minimum fluidization velocities of mixtures of biomass and sands. *Energy* 26(6):633-644.

Reina, J., E. Velo, and L. Puigjaner. 2000. Predicting the minimum fluidization velocity of polydisperse mixtures of scrap-wood particles. *Powder Technology* 111(3):245-251.

Rhodes, M. 2008. *Introduction to particle technology*. Wiley.

Sánchez-Delgadoa, S., J. A. Almendros-Ibáñez, N. García-Hernando, and C. Santana. 2011. On the minimum fluidization velocity in 2D fluidized beds. *Powder Technology* 207(1-3):145-153.

SAS. 2011. *The SAS system for Windows*. Ver. Release 9.2. Cary, NC.: SAS Institute.

Schell, D., and C. Harwood. 1994. Milling of lignocellulosic biomass. *Applied biochemistry and biotechnology* 45-46(1):159-168.

Sharma, A. M., A. Kumar, K. N. Patil, and R. L. Huhnke. 2013. Fluidization characteristics of a mixture of gasifier solid residues, switchgrass and inert material. *Powder Technology* 235(0):661-668.

Takara, D., P. Shrestha, and S. K. Khanal. 2010. Lignocellulosic biomass pretreatment. *Biofuel and bioenergy from biowastes and lignocellulosic biomass. American Society of Civil Engineers, Reston*.

Vejahati, F., N. Mahinpey, N. Ellis, and M. B. Nikoo. 2009. CFD simulation of gas–solid bubbling fluidized bed: A new method for adjusting drag law. *The Canadian Journal of Chemical Engineering* 87(1):19-30.

Wang, Q., T. Niemi, J. Peltola, S. Kallio, H. Yang, J. Lu, and L. Wei. 2014. Particle size distribution in CPFD modeling of gas–solid flows in a CFB riser. *Particuology*(0).

Woodcock, C., and J. Mason. 2013. *Bulk solids handling: an introduction to the practice and technology*. Springer Science & Business Media.

Yang, W.-C. 2007. Modification and re-interpretation of Geldart's classification of powders. *Powder Technology* 171(2):69-74.

Zhu, J., X. Pan, G. Wang, and R. Gleisner. 2009. Sulfite pretreatment (SPORL) for robust enzymatic saccharification of spruce and red pine. *Bioresource Technology* 100(8):2411-2418.

Chapter 4: Moisture Effect on Fluidization Behavior of Loblolly Pine Wood Grinds

4.1 Abstract

The objective of this study was to quantify the effect of moisture contents on minimum fluidization velocity of ground loblolly pine wood. Loblolly pine wood chips were ground and screened through a 1/8-inch screen. Samples were adjusted to four moisture contents that varied between 8 and 25 wt. % wet basis. Each of the samples was divided into two groups (unfractionated and fractionated that consisted seven fractions). The particle distribution parameter, particle size, bulk, and particle densities of the samples were determined while their minimum fluidization velocities were determined from the plot of pressure drop across the bed versus air velocity through the bed. Physical properties results show that the bulk density, particle density, and porosity of grinds increased with increase in moisture content. However, with an increase in moisture content, the variations in sizes of particle within a sample reduced with coefficient of variation value that ranged from 90 at 8.45% MC to 40 at 27.02% MC. Generally, as moisture content increased the minimum fluidization velocity values increased. The minimum fluidization velocity (U_{mf}) was found to be 0.2 m/s for 8% MC, 0.24 m/s at 14.86% MC, 0.28 m/s at 19.86 % MC and 0.32 m/s for 27.02% MC. The correlation developed predicted the experimental data with mean relative deviation that was less than 10%.

4.2 Introduction

The United States has the potential to produce more than one billion tons of biomass that can be processed to replace 30% of current petroleum consumption by year 2030 (Downing *et al.,* 2011). About 33% (330 million) of these vast quantity of biomass is expected to come from forest and forest residues. This strategically positions the southern region of the U.S. as a key stakeholder to achieving the 2030 biofuel goal because it currently supplies about 60% of the U.S. total timber harvest by volume (Wear and Gries, 2011). With the U.S. pulp and paper manufacturing industry increasingly moving overseas, a significant amount of woody biomass resource is now available for conversion into fuels and products (Wilkinson, 1995). Loblolly pine is the most abundant wood species - accounting for 83% of all woody species in the southern region of the U.S (Smith et al., 2009).

Biomass conversion to fuels, chemical and products can be achieved through a biochemical or a thermochemical platform. Biochemical conversion involves the use of bacteria, microorganisms and enzymes to breakdown biomass into gaseous or liquid fuels (e.g. biogas and ethanol). Thermochemical platform uses heat and chemical processes to convert biomass to fuels, chemicals, and power via pyrolysis, gasification, and/or combustion processes. Interest in thermochemical platform continues including optimizing the fluidized bed system (FBS) that is typically used for this conversion method. Among the reasons why FBS is gaining attention is the vigorous mixing of feedstock and gasifying fluids (typically air) such that hotspots in the gassifier are minimized and the likelihood of uniform temperature distribution in the bed is high (Oliveira *et al.,* 2013; Rousset *et al.,* 2012).

FBS has been successfully used for various applications (drying, combusting, coating, and coagulating) in the coal and pharmaceutical industries. After harvest, biomass must be pre-processed before it can be fed into a fluidized bed system (Khanal, 2010). The preprocessing steps however result in feedstock properties that create technical and operational challenges during fluidization. Some of the properties include, bulk density, particle density, particle porosity, and particle size and distribution. Since there are numerous types of biomass that are harvested at different season of the year, and that the harvested biomasses are stored at different conditions, biomass moisture content varies tremendously. Moisture content (MC) also affect affects biomass properties thus worsening the variability in biomass feedstock properties (Wright *et al.,* 2006).

Moisture influence on the flow-ability, compressibility, cohesion, and adhesion of particles is mostly due to enhancement of inter-particle bonds of the particles of biomass grinds (Fasina, 2008; Mani *et al.,* 2004; Probst *et al.,* 2013). This causes operational challenges during fluidization process. In fact, Wormsbecker and Pugsley (2008) linked poor fluidization conditions (channeling, entrainment, segregation) to moisture content in pharmaceutical granules. When the particles are wet, high fluid velocity is required to prevent segregation, defluidization and channeling due to dominant cohesive forces of the wetted surfaces (Mujumdar, 2006). But increasing velocity can be problematic for reaction kinetic, and excessive air flow rate can lead to particle entrainment, channeling and segregation (Clarke et al., 2005). In addition, cycle efficiency and net power output from a biomass gasifier was shown to reduce with feedstock having MC above 30% (wet basis) in a fluidized bed gassifier that was operated between 850°C - 1000 °C (Hughes and Larson, 1997). Similarly, Kenney et al. (2013) reported that processes and facilities

that use feedstock with high variation in biomass properties barely achieve 40 % of their capacity in the first year due to handling difficulties.

Based on the aforementioned, it is obvious that moisture content strongly affects the properties of biomass grinds, hence its fluidization behavior, conversion, and product yields. At present, there are no information on effect of moisture on the fluidization properties of loblolly pine wood grinds. If loblolly pine wood is to be commercially utilized for biofuel and bioproducts production, it is important to investigate how moisture content of loblolly pine wood grinds contributes to its fluidization properties. Firstly, physical properties such as size, shape, densities, and porosities of loblolly pine grinds at different moisture contents must be quantified. In addition, the appropriateness of the schemes used to measure the size of non-spherical particles such as biomass grinds must be determined (Oliveira *et al.,* 2013).

Therefore, the focus of this study was to investigate whether moisture content affects the appropriateness of the scheme used to measure the shape and size of loblolly pine wood grinds. The study also investigated the contribution of fractions and the moisture content of the fraction on the fluidization behavior (bed expansion, channeling, and minimum fluidization velocity) of loblolly pine grinds.

4.3 Material and methods

4.3.1 Material preparation

Clean loblolly pine wood chips with initial moisture content of 55 % wet basis were obtained from a forest plantation in the southern part of the state of Alabama, U.S. The wood chips were dried at room temperature to a moisture content of 8 % wet basis. About 200 kg of the wood chips were ground using a hammer mill (Arthur H. Thomas Co., Philadelphia, PA) that was fitted with a 3.175 mm screen. The ground samples were divided into four subsamples. The moisture content of the first subsample was not adjusted while the other remaining subsamples were adjusted to 15, 20 and 25 % wet basis. Moisture adjustment following the method used by Rhén et al. (2005). This process involves spraying of a sample (having initial moisture content of 8.40 % wet basis) with calculated volume of water (to increase the moisture content of samples). The adjusted moisture samples were then kept in a refrigerator at temperature of about 4 ^{0}C for at least 7 days for moisture equilibration. The sample to be used for experiment was removed 24 h before experimentation to allow for equilibration at room temperature. Moisture content of the sample were determined before use and found to be 14.86, 19.80 and 27.02 % (w.b.) using ASTM (2006) E871-82 standard procedure. When a sample of a particular moisture content was selected, a portion was reserved for the control study experiment and the remaining quantity was fractionated into six fractions using the method described below.

4.3.2   Particle size fractionation

Fractionation were carried out by repeatedly using a sieve shaker (model Rx 29, Tyler, Inc., Mentor, Ohio) to fractionate about 100 g of a sample on a set of US standard sieves with US number #12 (1.7 mm), #14 (1.4 mm), #18 (1 mm), #30 (600 µm), #50 (300 µm) and #100 (150 µm) for 10 minutes. After the sieving operation, the materials retained on each sieve were collected and separately kept in clearly marked polyethylene bags. The fractionation process was stopped when at least 800 g of each fractionated samples was obtained. The moisture content of the fractionation samples were determined following the method described earlier. The result of moisture content of loblolly pine wood is presented in Table 4.1. It can be seen that the moisture content of the adjusted unfractionated samples were very close to the targeted value. However, as fractionating screen size reduced, the moisture content achieved gradually increase and increasingly higher than the targeted values. This showed that the smaller particles hold more moisture than the bigger particle.

Table 4.1: Moisture content of loblolly pine wood grinds after fractionation

Target	Achieved						
	Unfractionated	#12 (1.7 mm)	#14 (1.4 mm)	#18 (1 mm)	#30 (600 µm)	#50 300 µm)	#100 (150 µm)
	8.4 (1.2)	8.5 (0.6)	8.4 (0.8)	8.3 (0.6)	8.4 (0.4)	8.3 (0.3)	8.9 (0.2)
15.0	14.9 (2.2)	14.7 (0.1)	14.6 (0.3)	14.9 (0.4)	15.2 (0.2)	15.6 (1.2)	15.6 (1.2)
20.0	19.8 (1.4)	19.7 (0.3)	19.9 (0.6)	21.0 (0.2)	20.9 (0.1)	21.2 (0.7)	21.4 (0.2)
25.0	27.0 (2.0)	27.1 (1.3)	27.3 (0.9)	28.1 (0.9)	28.2(1.2)	29.6 (0.5)	29.8 (0.3)

4.3.3 Particle size measurement

An image analysis system (Camsizer, Retsch Technology GmbH, 42781 Haan, Germany) was used for particle size measurement. About 100 g (~ 1 million particles) of a sample was placed in the hopper of the equipment and was then transported to the measurement field through a feeder controlled by the amplitude of vibration of the feeder. As the particles fall through the measurement field which is located between a light source and two full-frame digital cameras, the first camera measures the parameter of the bigger particles (300 µm-30 mm), while the parameters of smaller particles are measured by the smaller camera (30µm–3mm). Table 4.2 shows the list of particle properties obtained from the Camsizer software.

Table 4.2: Properties of particles extracted from the software of the Camsizer

	Parameters	Definition	
Particle distribution	d_{50}	Particle diameter at 50% probability	
	d_{84}	Particle diameter at 84% probability	Allen (1997)
	d_{16}	Particle diameter at 16% probability	Based on chord length (mm)
	% retained and passing		
	Coefficient of variation (COV)	$COV = \dfrac{d_{84} - d_{16}}{d_{50}} \times 50$	
Diameter scheme	Ferret	Two tangents are perpendicularly to the direction of measurement of a convex particle.	
	Martins	The length of a bisector determined by dividing the projected area of the particle into two equal parts.	
	Chord	The shortest length of a bisector that passes through the centroid of the convex particle.	
	Area equivalent	$\sqrt{\dfrac{4A}{\pi}}$ A is area of particle projection	
	Surface to volume	$d_{sv} = \dfrac{6}{S_{ssa}}$	Rhodes (2008)Rhodes (2008)
	Geometric mean	From distribution plot	S319.4 (ASABE, 2006).
Particle properties	Specific surface	$S_{ssa} = \dfrac{surface}{Volume}$	Rhodes (2008)
	Aspect ratio	$ASP = \dfrac{b}{l} = \dfrac{Chord_{min\,imum}}{Feret_{max\,imum}}$	
	Sphericity	$SPHT = \dfrac{4\pi A}{P^2}$ P – measured perimeter/circumference of a particle projection A – measured area covered by a particle projection	

4.3.4 Bulk density

The bulk densities of each sample were determined using a bulk density measuring apparatus. This involved allowing the sample to freely fall through a funnel onto a standard cup (volume of 1137 mm^3). The material was then leveled across the surface of the container and weighed using a digital balance with a 0.001g precision (Model AR3130, Ohaus Corp, Pinebrook, NJ). The bulk density was then estimated as the ratio of the mass of the sample in the container to the volume of the container.

4.3.5 Particle density and porosity

The particle densities of each of the samples were measured using a gas pycnometer (Accupyc 1330, Micromeritics Instrument Corp., Norcross, Ga.). This involves measuring the pressure difference between a reference cell and a cell containing the measured sample. The pressure was generated by allowing helium to flow from the reference cell into the cell containing the sample. The pycnometer then calculates the volume of the material in the sample cell using equations that are based on ideal gas law. The particle density was computed from the ratio of the sample mass to the measured particle volume. The bulk and particle density values were used to calculate the theoretical inter – granular porosity (ε) of the wood grinds (Eqn. 4.1)

$$Porosity = 1 - \frac{\rho_b}{\rho_p} \qquad (4.1)$$

where ρ_b is bulk density (kg/m^3) and ρ_p is particle density (kg/m^3).

4.3.6   Fluidization test

4.3.6.1 Experimental device

A description of this experimental setup can be found in section 3.3.6.

4.3.6.2 Fluidization test procedure

Fluidization experiments were conducted using a 4×7 factorial experimental design (with 3 replicates). The factors considered were moisture content (8.40, 14.86, 19.80, and 27.02 % wet basis) and particle size (six fractionated and one unfractionated samples). For a particular fluidization test, about 200 g of sample was measured, poured onto the distribution plate of the fluidization chamber. The blower was then turned on and the fan speed controller was used to gradually increase the airflow rate through the bed. At each airflow velocity, 60 seconds was allowed for stabilization before recording the pressure drop across the chamber and the corresponding air velocity through the bed was recorded. The pressure drop across the chamber was determined for each superficial gas velocity starting from fixed bed condition until turbulent regime of fluidization was achieved. The flow patterns and bed mixing behavior at different operating conditions with time were studied from a recording made using a digital camera (Nikon, Model S3100 Melville, NY 11747-3064) located in front of the fluidized bed.

4.3.7   Statistical analysis

All experiments were conducted in triplicates. The results were presented in relevant section as mean values and standard deviation. Graphs were plotted using Microsoft Excel®, version 2013. Test of significance of the variables (diameter type, bulk density,

particle porosity, sphericity, aspect ratio and coefficient of variation) were conducted

using the analysis of variance (ANOVA) procedures performed through SAS statistical

software (SAS, 2011). A pairwise t-test using least squares means procedure with Tukey

multiple comparison test was computed for each effect and their interactions. All the test

were considered to be statistical significant when $p \leq 0.05$. The difference between

predicted (minimum fluidization velocity based on equations and diameter types) and

observed (minimum fluidization velocity obtained from laboratory experiment) were

evaluated by determining the mean relative deviation (MRD) following the method used

by (Nemec and Levec, 2005).

$$MRD\left(\%\right) = \frac{1}{N}100\sum_{i=1}^{N}\frac{\left|\lambda_{1.calc} - \lambda_{i.\exp}\right|}{\lambda_{i.\exp}}$$
(4.2)

where

$\lambda_{1.calc}$ is calculated U_{mf} from predicting equation (m/s)
$\lambda_{i.\exp}$ is experimentally obtained U_{mf} (m/s)
N is the numbers of data points

4.4   Results and discussion

4.4.1   Particle size

4.4.1.1 Effect of moisture content on the coefficient of variation of unfractionated (sample A)

The COV of sample using chord diameter measurement reduced as moisture content

increased. At 8.40, 14.86, 19.80, and 27.02 % wet basis, the COV obtained were 90, 65,

58, and 42% respectively –a reduction of 52 % when moisture content increased from

8.40 to 27.02 % (w.b.). (Appendix 4 showed particle size distribution at different

moisture content using different diameter measurement scheme). It can be seen that

irrespective of the diameter measurement scheme used, the particle distributions are log-

normal and different from one another. We suspect that the reduction in COV with

increase in moisture content could be attributed to increase in cohesiveness between fine

particles making them to stick together and form bigger particle and in essence reduce

size variability. The substantial variation in particle distribution in COV of samples

confirm the problems such as excessive dust generation, clogging of filters and

pneumatic transfer lines that are encountered during the processing and handling of

biomass grinds (Kenney et al., 2013).

4.4.1.2 Effect of measurement scheme on measured size

Figs. 4.1 - 4.4 shows the particle distribution profile of samples using the various

diameter measurement schemes at each of the four moisture content levels. Irrespective

of the moisture content and the diameter measurement scheme, the distribution is

positively skewed with the tail towards the right hand size. This is a log-normal

distribution that is typical of ground biological materials (Fasina, 2006). The profile

obtained using Ferret diameter was the farthest from the chord, area, and Martins

diameter measurement schemes irrespective of the moisture content. However, at 14.86

% and 19.80 % MC (Fig 4.2 and 4.2 respectively) the variation between Martins and

chord diameter reduced significantly to such a point that the percent retained profile

nearly overlay but Ferret and area diameter type were noticeably separated. Reduction in

variation between distribution profiles obtained from using Martins and chord diameter

could be attributed to the bisector line drawn by the camsizer software tending toward the

same value (Table 3.2). While the bisector drawn must pass through the centroid in chord diameter, this line has to pass through the centerline in which the particle is divided into two equal halves in Martins. Thus, at certain particle size, the bisector drawn by the digital image software tends to be equal and hence responsible for the tendency of Martins and chord diameters particle size distribution profile to overlay.
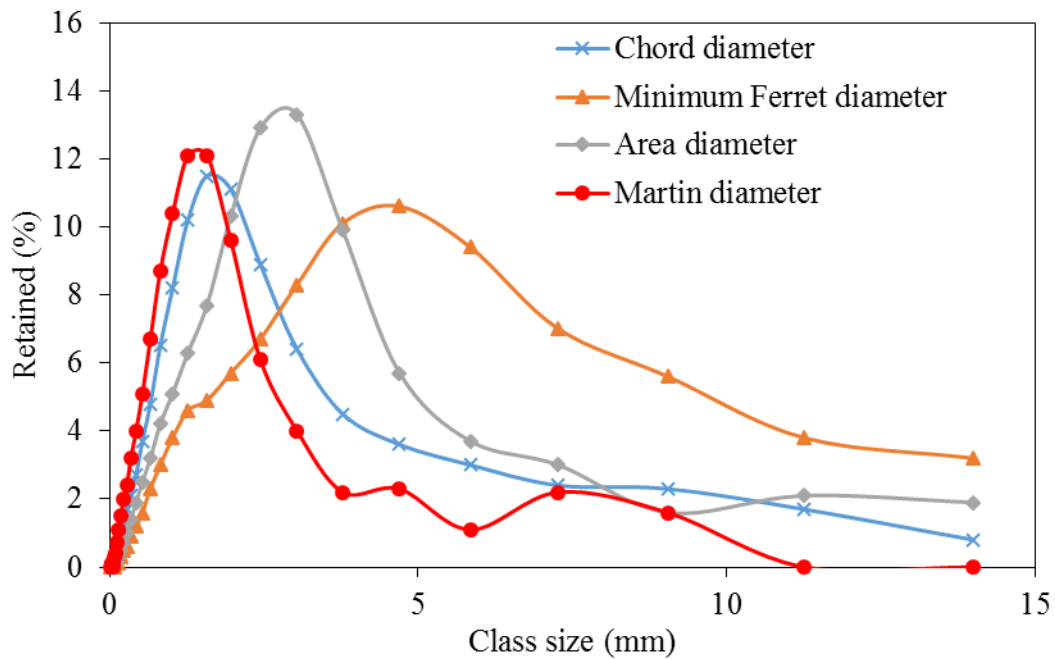
Figure 4.1: Differences in size distributions obtained from using different diameter measurement schemes for loblolly pine wood grinds (8.40% MC wet basis).
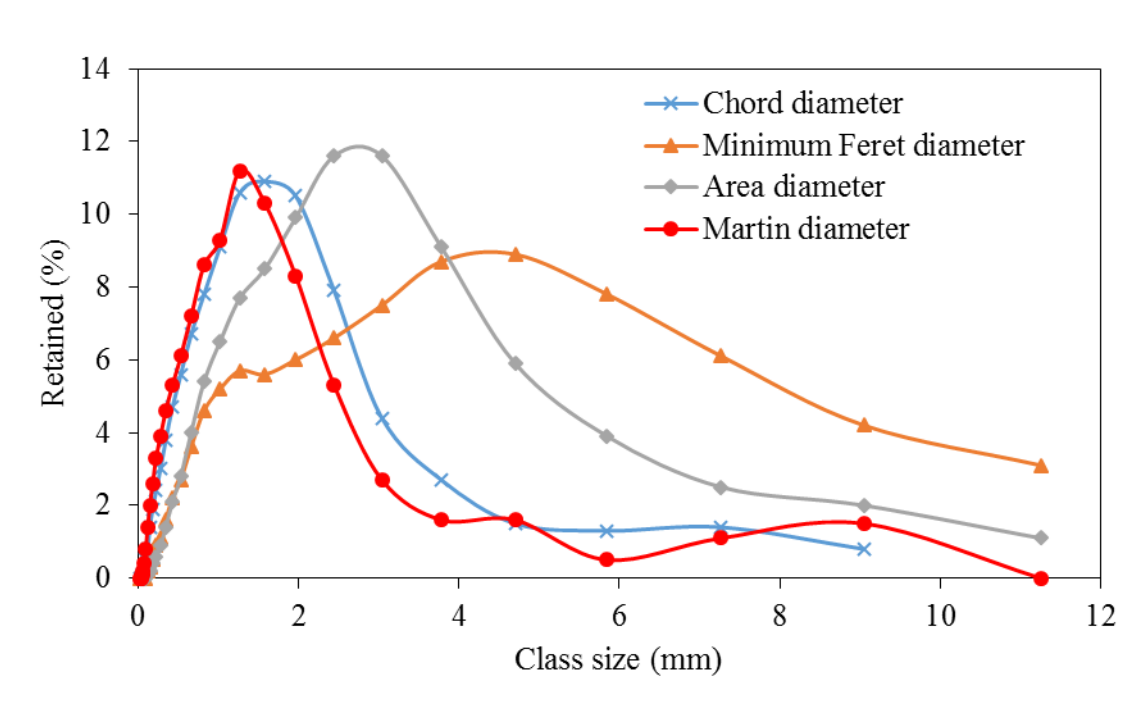
Figure 4.2: Differences in size distributions obtained from using different diameter measurement schemes for loblolly pine wood grinds (14.86% MC wet basis).
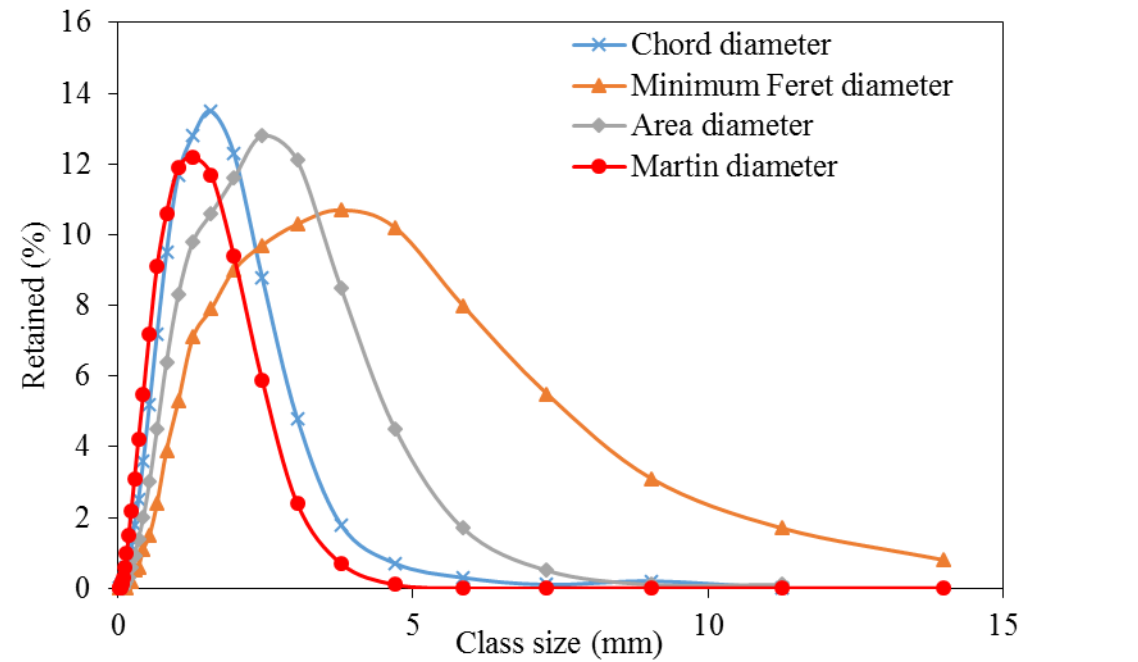
Figure 4.3: Differences in size distributions obtained from using different diameter measurement schemes for loblolly pine wood grinds (19.80% MC wet basis).
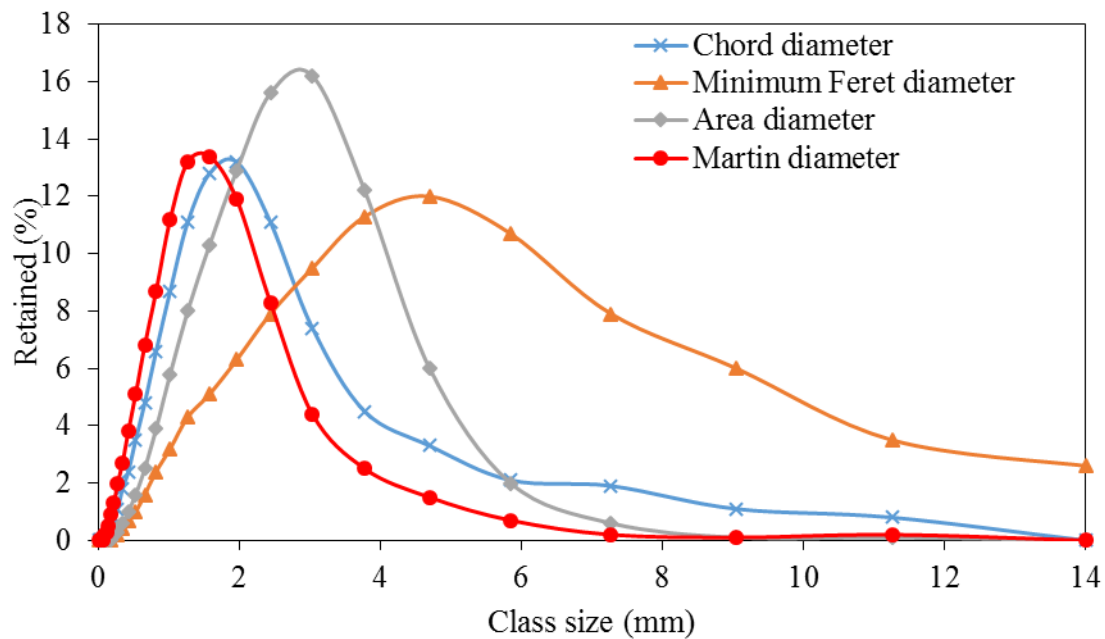
Figure 4.4: Differences in size distributions obtained from using different diameter measurement schemes for loblolly pine wood grinds (27.02 % MC wet basis).

In addition, the different diameter measurement schemes produced significantly ($p < 0.05$) different measured size because of change of measurement orientation or axis (Table 4.3). This suggest that the particles are not spherical and the decision to adopt a particular diameter measurement scheme has to be made in relation to the effectiveness of the measured axis (used in determining the diameter) to the unit operation of interest.

Table 4.3: Effect of moisture content and diameter measurement scheme on the measured size of loblolly pine wood grinds.

Screen Size (#)	MC (% w.b)	Diameter types (mm)				
		Area	Chord	Ferret	Martin	Surface-vol.
Un-fractionated	8.40	2.87 [a, 2](0.41)	1.01 [a,2 3](0.36)	4.90 [a,1](0.76)	1.59 [a, 3,4](0.30)	0.82 [b,4](0.04)
	14.86	2.42 [a, 2](0.12)	1.43 [b c,3](0.26)	4.18 [a, 1](0.11)	1.18 [c b,4](0.01)	0.57 [c, 4](0.03)
	19.80	1.89 [b, 2](0.03)	1.30 [c, 3](0.03)	3.10 [b, 1](0.06)	1.03 [c, 4](0.02)	0.71 [b c, 5](0.02
	27.02	2.48 [a, 2](0.27)	1.83 [b a, 3](0.26)	4.11 [a, 1](0.48)	1.37 [b, 2](0.15)	1.05 [a, 4](0.19)
12	8.40	3.53 [b, 2](0.1)	2.17 [b, 3](0.10)	6.15[b, 1](0.24)	1.83 [a, 5](0.03)	1.86 [b, 4](0.01)
	14.86	3.75[b, 2](0.1)	2.31 [a, 3](0.10)	6.72 [a, 1](0.04)	1.88 [a, 5](0.16)	1.92 [a, 4](0.02)
	19.80	3.54 [a, 2](0.1)	2.16 [b, 3](0.04)	6.09 [c, 1](0.15)	1.89 [a, 5](0.02)	1.89 [b, 4](0.01)
	27.02	3.37 [c, 2](0.1)	2.1 [b, 3](0.01)	5.72 [d, 1](0.04)	1.88 [a, 4](0.01)	1.83 [c, 5](0.01)
12 - 14	8.40	2.75 [a, 2](0.03)	1.75 [b,3](0.02)	4.87 [b, 1](0.10)	1.37 [a, 5](0.01)	1.46 [a, 4](0.01)
	14.86	2.8 [a,2](0.01)	1.79 [a, 3](0.02)	5.07 [a, 1](0.03)	1.37 [a, 5](0.15)	1.44[b a, 4](0.03)
	19.80	2.63 [b, 2](0.01)	1.61 [c, 3](0.01)	4.53 [c, 1](0.10)	1.36 [a, 4](0.01)	1.42 [b, 4](0.01)
	27.02	2.42[c, 2](0.02)	1.48[d, 3](0.02)	4.22[d, 1](0.04)	1.28 [b, 4](0.01)	1.31 [c, 4](0.01)
14 - 18	8.40	2.63 [a, 2](0.25)	1.54 [a, 3](0.05)	4.13 [b, 1](0.14)	1.13[a, 4](0.02)	1.18 [a, 4](0.01)
	14.86	2.25 [b, 2](0.07)	1.48 [a, 3](0.04)	4.09 [a, 1](0.01)	1.09 [b, 4](0.02)	1.14 [b a, 4](0.01
	19.80	2.06 [b, 2](0.01)	1.29 [b, 3](0.01)	3.65 [c, 1](0.02)	1.05[b, 5](0.01)	1.11[b, 4](0.04)
	27.02	1.8[c, 2](0.03)	1.19 [c, 3](0.03)	3.17 [d, 1](0.10)	0.94 [b, 4](0.01)	0.96 [c, 4](0.01)
18 - 30	8.40	1.91[b, 2](0.38)	1.20 [b, 3](0.02)	3.41[b, 1](0.68)	0.9 [2, 3c](0.20)	0.84 [b, 3](0.01)
	14.86	1.57[b c, 2](0.02)	1.10 [b c, 3](0.02)	2.77 [c, 1](0.45)	1.03 [b, 3](0.03)	0.79 [c, 3](0.02)
	19.80	1.34 [c, 2](0.01)	0.89 [d, 3](0.01)	2.3 [c, 1](0.03)	0.69 [c, 4](0.01)	0.71[d, 4](0.01)
	27.02	2.99 [a, 2](0.02)	2.59 [a, 3](0.02)	4.69 [a, 1](0.02)	1.89 [a, 4](0.03)	1.35 [a, 5](0.01)
30 - 50	8.40	1.36 [a, 2](0.94)	1.38 [a, 2](0.47)	2.96 [a, 1](1.03)	0.88 [b, 2](0.32)	0.53 [a, 2](0.04)
	14.86	1.10[b, 2](0.10)	0.85[b, 3](0.06)	1.87[b,1](0.05)	0.55[a, 3](0.11)	0.47 [b, 4](0.01)
	19.80	0.71[b, 2](0.01)	0.51[b, 3](0.02)	1.16 [b, 1](0.01)	0.36 [c, 5](0.02)	0.36 [c, 4](0.02)
	27.02	n/a	n/a	n/a	n/a	n/a
50 - 100	8.40	2.84 [a, 1](0.02)	2.25[a, 2 1](0.03)	2.31[a, 2 1](0.10)	1.56 [a, 2.3](0.23)	0.93 [a, 3](0.22)
	14.86	1.52 [a, 2](0.02)	1.25 [a, 3](0.02)	2.25 [a, 1](0.01)	2.25 [a, 1](0.01)	0.66 [a, 4](0.06)
	19.80	2.00 [a, 1](0.08)	1.62 [a, 1](0.89)	2.77[a, 1](0.02)	1.11[a, 1](0.61)	0.64[a, 1](0.21)
	27.02	n/a	n/a	n/a	n/a	n/a

N/a result not available from measurement equipment due to stickiness of the particle

132

Values are means of triplicates and numbers in parentheses are geometric standard deviation calculated from Eqn. 2.5
Means with the different superscript (alphabet) in a row at a particular screen range are significantly different (p<0.05)
Means with the different superscript (numeric) in a column at a particular screen range are significantly different (p<0.05)

Furthermore, the geometric mean diameter (d_{gw}) is shown in Table 4.4. The values inside parenthesis are the geometric mean standard deviations (S_{gw}) which gives indication on the distribution of the particles size. As moisture content increased, S_{wg} also reduced. This showed that the variability in particle size reduced with an increase in moisture content.

Table 4.4: Effect of moisture on geometric mean size of ground loblolly pine wood grinds

US sieve #		Moisture content (% w.b)			
Pass through	Retained on	8.40	14.86	19.80	27.02
	Unfractionated	0.64[a] (0.63)	0.54 [a] (0.89)	0.75 [a] (0.74)	1.09[b] (0.97)
-	12	2.25 [b] (0.71)	2.78 [a] (0.74)	2.32 [b] (0.59)	2.24 [b] (0.59)
12	14	1.75 [ab] (0.54)	2.00[a] (0.67)	1.76 [a,b] (0.36)	1.63 [b] (0.35)
14	18	0.76 [b] (0.67)	1.37 [a] (0.66)	1.36 [a] (0.37)	1.38 [a] (0.41)
18	30	0.73 [b] (0.68)	0.94 [b] (0.49)	0.89 [b] (0.31)	1.54 [a] (1.64)
30	50	0.39 [b] (0.40)	0.63 [a] (0.51)	0.43 [b] (0.25)	N/a
50	100	0.37 [b] (0.20)	0.67 [a] (0.47)	0.65 [a] (0.96)	N/a

N/a result not available from measurement equipment due to stickiness of the particle
Values are means of triplicates and numbers in parentheses are geometric standard deviation calculated from Eqn. 2.5
Means with the different superscript (alphabet) in a row are significantly different (p<0.05)

133

4.4.1.3 Effect of moisture content on particle shape of loblolly pine wood grinds

Table 4.5 shows the sphericity of ground loblolly pine wood (unfractionated and fractionated) at different moisture content levels. As moisture content increased, the sphericity first increased from 0.37 to 0.47 before decreasing to 0.42. Deshpande et al. (1993) also found that the sphericity of soybeans increased linearly with moisture content up to 20%. Beyond 20% MC, we suspect that the volumetric expansion resulted in uneven expansion thus sphericity reduced. Furthermore, it can be seen from Table 4.5 that the mean sphericity reduced as the particle size reduced. The effects of moisture and particle size are significant on sphericity value ($p < 0.05$).

Table 4.5: Effect of moisture on sphericity of loblolly pine wood grinds at different moisture content.

Screen size (#)		Moisture content (% w.b)			
Pass through	Retained on	8.40	14.86	19.80	27.02
	Unfractionated	0.37 [B,3] (0.02)	0.45 [D,12] (0.01)	0.47 [D,1] (0.01)	0.42 [C,2] (0.03)
-	12	0.57 [A,2] (0.01)	0.54 [A,3] (0.01)	0.58 [A,12] (0.01)	0.59 [A,1] (0.01)
12	14	0.53 [A,2] (0.01)	0.51 [B,3] (0.01)	0.56 [B,1] (0.01)	0.56 [BA,1] (0.01)
14	18	0.49 [A,2] (0.01)	0.49 [CB,2] (0.02)	0.54 [C,1] (0.01)	0.53 [B,1] (0.01)
18	30	0.46 [BA,3] (0.01)	0.48 [C,2] (0.02)	0.54 [C,1] (0.01)	n/a
30	50	0.28 [C,3] (0.1)	0.33 [E,2] (0.1)	0.4 [E,1] (0.01)	n/a
50	100	n/a	0.43 (0.01)	0.34 (0.05)	n/a

N/a result not available from measurement equipment due to stickiness of the particle
Values are means of triplicates and numbers in parentheses are standard deviation,
Means with the different superscript (numeric) in a row are significantly different ($p<0.05$)
Means with the different superscript (alphabet) in a column are significantly different ($p<0.05$)

Based on Cui and Grace (2007) classification, ($\varphi < 0.5$ indicates an extremely flat particles, $\varphi > 0.5$ indicates flat particles and $\varphi > \sim 0.8$ is nearly spherical particles). Particles varied from flat to extremely flat in shape. The flatness of the particles in the ground samples was confirmed in the result of aspect ratio (Table 4.6). The aspect ratio

was uniformly distributed between 0.38 and 0.52. We observed that aspect ratio of

particles retained between screen # 50 increased. We suspect that this is due to increase in

inter-particle cohesion at small particle size (Oginni, 2014)

In summary, when particle shapes are not spherical but pin-like, the tendency for particle

bridging during fluidization is increased (Mattsson and Kofman, 2002) and when

sphericity shape factor is between 0.1 and 0.5, particles will be difficult to fluidize (Yu

and Standish, 1993).

Table 4.6: Effect of moisture on aspect ratio of loblolly pine wood grinds at different
moisture content

Screen size (#)		Moisture content (% w.b)			
Pass through	Retained on	8.40	14.86	19.80	27.02
	Unfractionated	0.48 [1B] (0.01)	0.43 [2,B] (0.01)	0.47 [1,B] (0.01)	0.48 [1,A] (0.01)
	12	0.39 [1,D] (0.01)	0.38 [2,D C] (0.02)	0.40 [1,D] (0.01)	0.40 [1,CB] (0.01)
12	14	0.39 [1,D] (0.02)	0.43 [2 D] (0.1)	0.39 [12,E] (0.01)	0.38 [12,B] (0.01)
14	18	0.39 [2,D] (0.01)	0.39 [2,C] (0.02)	0.39 [2,E] (0.01)	0.41 [1,B] (0.01)
18	30	0.43 [1C] (0.01)	0.44 [2,B] (0.02)	0.45 [3,C] (0.01)	n/a
30	50	0.50 [2,A] (0.01)	0.49 [1,A] (0.01)	0.52 [3,A] (0.01)	n/a
50	100	n/a	0.59 (0.01)	0.58 (0.01)	n/a

N/a result not available from measurement equipment due to stickiness of the particle
Values are means of triplicates and numbers in parentheses are standard deviation,
Means with the different superscript (alphabet) in a row are significantly different (p<0.05)
Means with the different superscript (numeric) in a column are significantly different (p<0.05)

4.4.2 Bulk and particle density

The bulk density of the grinds at different moisture content is presented in Table 4.7.

Bulk density varied from 135.14 to 278.91 kg/m^3 (p < 0.05) and decreased as moisture

content increased from 8.40 % to 27.02 % wet basis. Lower bulk density at high moisture

content could be attributed to particle swelling as moisture content increased (Table 4.3).

The effect of moisture content on bulk density is similar to other biological material reported in literature such as wheat straw, barley straw, corn stover and switchgrass by Mani et al. (2004), and corn stover by Zhou et al. (2008). Furthermore, bulk density increased with increase in particle size. For example, at 8.40 % moisture content, bulk density increased from 152.70 to 278.91 kg/m^3 for particle retained on screen size numbers 100 and 12 respectively. When particle of similar sizes are poured into a given container, the particle shape and orientation of particles affect inter-granular spaces. However, when particle consisting of wide distribution is poured into similar container, smaller particle occupy spaces between bigger particles hence improve packing density. Therefore, increase in bulk density as fractionating screen size increase could be attributed to similarity in size that affects packing density, increase porosity and lowered bulk density. It is also important to point out that in this study, clean loblolly pine wood was used whereas the sample used in Chapter 3 was dirty loblolly pine chips (i.e. clean chip with bark attached) Hence, a careful look at the result of bulk density in Table 4.7 showed that a lower bulk density compared with Table 3.5. For a bed consisting of wide particle sizes, air penetration through the bed become very difficult because, the voids needed for easy penetration of air is blocked by the small particle size. Hence, a problem in fluidization of biomass grinds.

Table 4.7: Effect of moisture content on bulk densities of loblolly pine wood grinds (unfractionated and fractionated).

US sieve #		Moisture content (% wet basis)			
Pass through	Retained on	8.40	14.86	19.80	27.02
Unfractionated		253.96 [c, 1] (3.2)	233.22 [b, 2] (1.6)	214.00 [b,3] (2.1)	208.31 [b, 4] (3.9)
-	12	278.91 [a, 1] (3.7)	242.95 [a, 2] (6.5)	225.55 [a, 3] (6.0)	226.19 [a, 3] (10.48)
12	14	272.65 [b, 1] (4.5)	229.36 [c, 2] (2.5)	215.67 [b, 3] (1.7)	210.70 [b, 3] (2.5)
14	18	266.85 [b, 1] (2.0)	214.31 [d 2] (0.9)	196.39 [c, 3] (1.1)	185.37 [c, 4] (4.04)
18	30	231.92 [d, 1] (4.8)	185.31 [e, 2] (0.2)	167.32 [d, 3] (1.8)	150.57 [d, 4] (0.2)
30	50	183.06 [e, 1] (2.9)	160.79 [f, 2] (0.1)	143.06 [e, 3] (1.1)	138.46 [e, 4] (1.3)
50	100	152.70 [f, 1] (1.8)	139.28 [g, 2] (0.5)	135.14 [f, 3] (0.3)	N/a

N/a result not available from measurement equipment due to stickiness of the particle
Values are means of triplicates and numbers in parentheses are standard deviation,
Means with the different superscript (alphabet) in a row are significantly different (p<0.05)
Means with the different superscript (numeric) in a column are significantly different (p<0.05)

The particle densities at various moisture levels are presented in Table 4.8. Particle density reduced as moisture content increased up to 20% moisture level. Further increase in moisture content appears to increase the particle density. Manickam and Suresh (2011) reported an increase in particle density of coir pith as moisture content increased from 10.0 to 60.2 % wt. wet basis. Similarly result was reported by Raigar and Mishra (2015) using Bengal flour with moisture varied between 3.2 and 13.06 % wet basis. Sudden increase in particle density at 20% moisture level (p <0.05) could be attributed to apparent point of fiber saturation of woody biomass that has been identified to occur between 17.5 – 22.5 % moisture content wet basis (Huntinton, 1924).When sample moisture is at fiber saturation point, all the moisture are in the cell but as moisture

increases, the cell wall becomes flooded and causes increase in particle weight per unit

volume.

Table 4.8: Effect of moisture content on particle densities ground loblolly pine wood
(unfractionated and fractionated).

US sieve #		Moisture content (% wet basis)			
Pass through	Retained on	8.40	14.86	19.80	27.02
Unfractionated		1453.1 [a,1] (5.4)	1409.2 [a,2] (6.15)	1404 [bc,2] (5.6)	1360.3 [ba,3] (6.2)
50	100	1437.5 [a,1] (1.3)	1415.1 [a,1] (3.2)	1454.7 [c1] (2.6)	n/a
30	50	1439.3 [a,1] (1.1)	1431.7 [a,1] (6.9)	1392.9 [c,1] (5.2)	1447.3 [a,1] (3.45)
18	30	1434.0 [a,1] (8.1)	1421.6 [a,12] (7.3)	1388.3 [c,3] (7.1)	1408.2 [ab,23] (6.3)
14	18	1469.7 [a,1] (7.7)	1428.1 [a,2] (11.4)	1392.6 [c,3] (9.6)	1394.5 [ab,3] (8.6)
12	14	1441.1 [a,1] (8.4)	1405.4 [a,2] (3.9)	1409.8 [bc,2] (0.5)	1371.6 [ab,3] (5.1)
-	12	1427.0 [a,1] (0.6)	1434.5 [a,1] (0.5)	1420.4 [b,1] (7.9)	1338.93 [b,2] (5.5)

N/a result not available from measurement equipment due to stickiness of the particle
Values are means of triplicates and numbers in parentheses are standard deviation,
Means with the different superscript (alphabet) in a row are significantly different (p<0.05)
Means with the different superscript (numeric) in a column are significantly different (p<0.05)

The porosity values computed from bulk and particle densities of unfractionated

sample is shown in Table 4.9. The porosity values slightly increased with increase in

moisture content and fractionation screen size. At low moisture content, inter-particle

force and electrostatic force within bulk material increased bulk density and in essence

increased the void fraction. In addition, presence of moisture causes smaller particle to

cluster and form bigger particle thus increasing the voids spaces. While normal spherical

particle has porosity value of about 0.4 (Woodcock and Mason, 1988), non-spherical

particle void space are expected to increase. The result of the void fraction confirmed that

loblolly pine wood grind are highly irregular in shape (see Table 4.5). The result of high

porosity was similar to other published work from Oginni (2014) on loblolly pine wood

grinds and Lam et al. (2008) on switchgrass grinds.

Table 4.9: Porosity of loblolly pine wood grinds at different moisture content level for both unfractionated and fractionated sample

US sieve #		Moisture content (% wet basis)			
Pass through	Retained on	8.4	14.86	19.8	27.02
Unfractionated		0.83 [C 4] (0.002)	0.83 [B 6] (0.001)	0.85 [A, 6] (0.001)	0.85 [A,4] (0.004)
50	100	0.89 [C 1] (0.0001)	0.90 [B 1] (0.0001)	0.90 [A 1] (0.0001)	na
30	50	0.87 [C 2] (0.001)	0.89 [B 2] (0.001)	0.89 [A 2] (0.001)	0.90 [A,1] (0.001)
18	30	0.84 [D 3] (0.002)	0.86 [C 3] (0.0004)	0.88 [B 3] (0.001)	0.89 [A,2] (0.001)
14	18	0.82 [D 5] (0.002)	0.85 [C 4] (0.001)	0.86 [B 4] (0.001)	0.87 [A 3] (0.0002)
12	14	0.81 [C 6] (0.003)	0.84 [B 5] (0.002)	0.85 [A 5] (0.001)	0.85 [A 4] (0.002)
-	12	0.81 [C 7] (0.003)	0.83 [B 7] (0.001)	0.84 [A 7] (0.002)	0.83 [B,5] (0.001)

N/a result not available from measurement equipment due to stickiness of the particle
Values are means of triplicates and numbers in parentheses are standard deviation,
Means with the different superscript (alphabet) in a row are significantly different (p<0.05)
Means with the different superscript (numeric) in a column are significantly different (p<0.05)

4.4.3   Fluidization studies

4.4.3.1 Minimum fluidization velocity

The plots of pressure drop across the sample bed against the airflow velocity of loblolly

pine wood at 8.4 % moisture content are shown in Fig 4.5. The intersection of increasing

pressure drop (representing fixed bed) and constant pressure drop (representing fluidized

bed) was used to estimate the minimum fluidization velocity (U_{mf}). The minimum

fluidization was obtained by computing W/A (the pressure drop) and finding the air

velocity that correspond to the calculated W/A (0.24 kPa) values. The value of U_{mf} from

the graph is 0.2 (0.01) m/s. The U_{mf} obtained is lower but comparable with the result obtained in Chapter 3. Similarly, Abdullah et al. (2003) determined the U_{mf} of sawdust with mean particle size of 0.8 mm to be 0.22 m/s . However, it can be seen that the pressure drop exceeded the expected W/A (0.24 kPa). This suggests that other forces such as particle – particle cohesive force and particle- wall interactions contributed to the increase in pressure (Srivastava and Sundaresan, 2002; Tsinontides and Jackson, 1993).
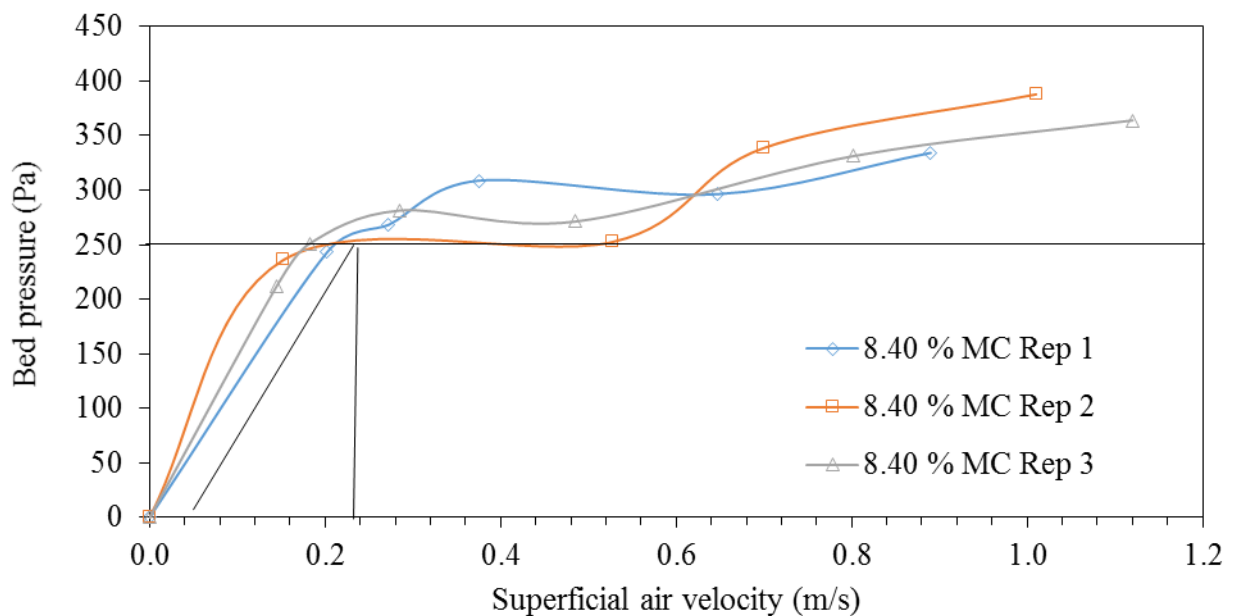
Figure 4.5: Pressure drop against superficial gas velocity for unfractionated sample at 8.40 % MC.

Plots of minimum fluidization velocity against the sample various moisture content is shown in Fig. 4.6. The plot showed a linear relationship (R^2 =0.99) exists between the U_{mf} and moisture content of loblolly pine wood. As moisture increased particle inter-particles cohesiveness increase, hence higher air velocity would be needed to fluidize the material.
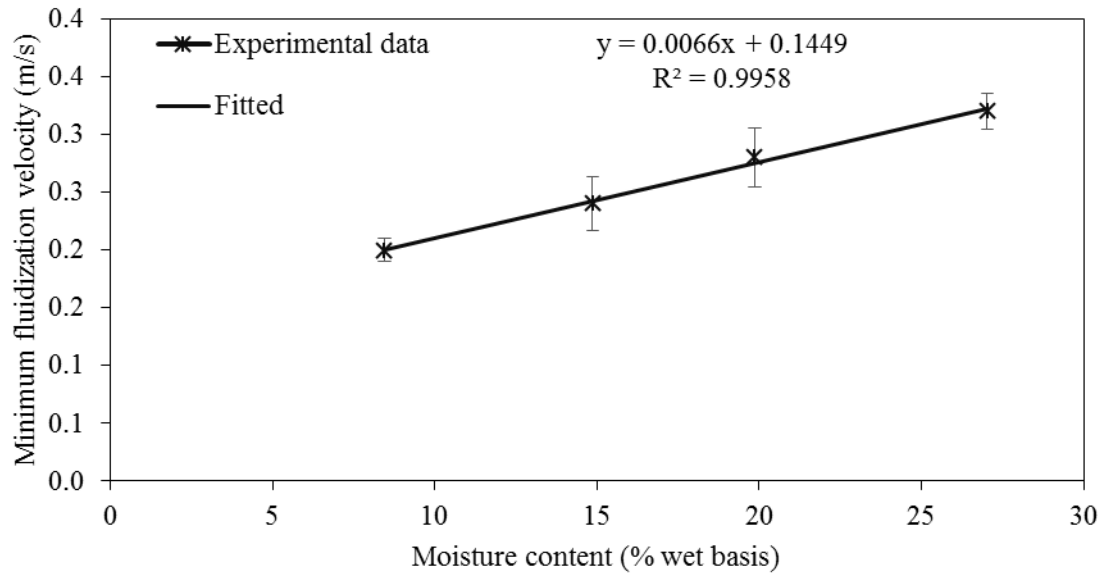
Figure 4.6: Effect of moisture content on fluidization velocity of unfractionated loblolly pine wood

For the fractionated samples, the U_{mf}, for a bed height of 0.106 m (200g sample) is presented in Table 4.10. At 8% MC, the U_{mf} of particles retained on 1.7 mm screen (#12) was 60% higher than that required to fluidize particle retained on 300µm (#50) sieves. Similarly, the differences for grinds at moisture contents at 14.86 and 19.86 % MC were 42 % and 70% respectively. This shows that particles that constitute biomass grinds have varying fluidization velocity. When there are substantial variations in U_{mf} of particles in the bed, this result in a situation where smaller particle are entrained when the bigger particles are yet to fluidize.

Table 4.10: Minimum fluidization velocity of fractionated loblolly pine wood as affected by moisture content.

Pass through (US sieve #)	Retained on (US sieve #)	Moisture content (% wet basis)			
		8.40	14.86	19.80	27.02
30	50	0.25 (0.06)	0.38 (0.18)	0.2 (0.06)	N/A*
18	30	0.43 (0.01)	0.45 (0.09)	0.39 (0.04)	0.26 - 0.6*
14	18	0.68 (0.16)	0.56 (0.07)	0.56 (0.11)	0.52 (0.09)
12	14	0.89 (0.07)	0.58 (0.04)	0.72 (0.06)	0.62 (0.02)
-	12	0.59 (0.02)	0.65 (0.10)	0.78 (0.02)	0.76 (0.28)

*Cohesive nature of sample (high moisture and fine particle size) impede accurate determination of U_{mf}

4.4.3.2 Fluidization behavior of loblolly pine wood grinds

The condition of bed of 8.4% MC of loblolly pine wood grinds (unfractionated) at minimum fluidization condition is shown in Fig 4.7 a –d. The U_{mf} was estimated to be 0.20 m/s and it correspond to bed behavior between Figs. 4.7 a and b. Although the bed slightly expanded (Fig 4.7 b) by 11 % of initial bed height, the figure shows a crack across the bed – an indication that the expansion may not be uniform within the bed and that the bed was mostly still at static condition. The bed expansion corresponds to the condition where the updraft created as result of the airflow became equal to bed weight. However, this condition did not support bed mixing and particle suspension in the gas stream. Further increase in the velocity resulted in the whole bed been carried up in plug flow (Fig. 4.7 c). At this point, the goal was to limit the entrainment of bed inventory been carried out of the bed in plug flow. This process entailed, gentle knocking on the bed wall, or reducing the air velocity and at certain instances the air source were stopped

completely and the experiment restarted. Fig 4.7 d showed a bed in complete fluidization stage. The velocity at this stage was far greater than the velocity at U_{mf}. (Also, see Section 3.4.3.4).

<div align="center">(a)   (b)   (c)   (d)</div>
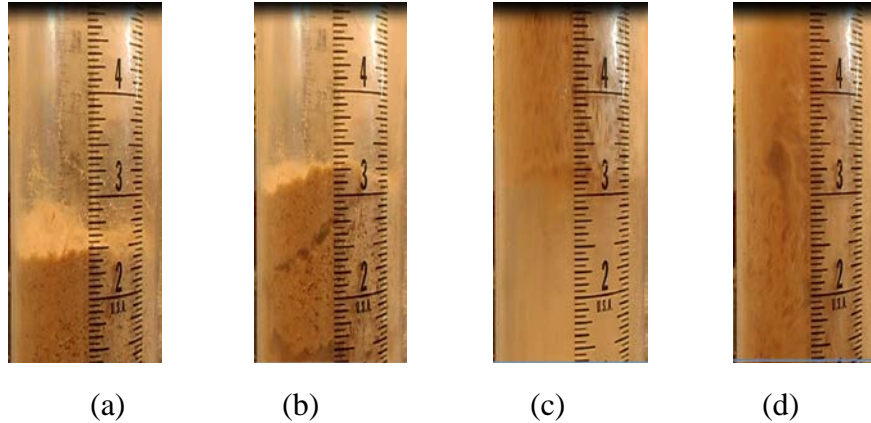
Figure 4.7: Fluidization behavior of 200 g unfractionated loblolly pine wood (8.46 %MC) with increasing gas velocity. (a) initial bed; (b) velocity at 0.30 m/s; (c) velocity at 0.45 m/s; (d) velocity at 0.60 m/s.

The bed behavior for 19.80 % wet basis is shown in Fig 4.8. The U_{mf} for this sample is 0.30 m/s and occurred between Fig 4.8 a and b. As the gas velocity increased, channeling, plug flow was observed before complete fluidization was achieved. For a fluidized bed system, a velocity whereby all particles within the bed are sufficiently fluidized needs be determined. In this study, it was found that loblolly pine wood grinds would completely fluidize at a velocity of 4×U_{mf}. Gauthier et al. (1999) reported 2×U_{mf} for a bed consisting of two different fraction of sizes of sand having a mean diameter of 0.28 and 1.8 mm. Also, using cylindrical shaped cotton stalk (5 mm) and sand particle (0.5 mm), Zhang et al. (2009) found that 5×U_{mf} promote bed mixing.

(a)	(b)	(c)	(d)	(e)
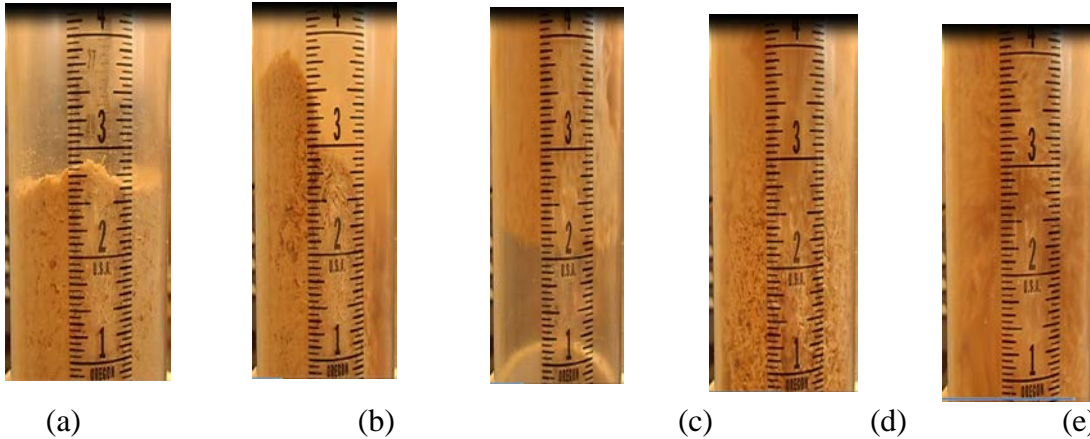
Fig 4.8: Fluidization behavior of unfractionated loblolly pine wood (19.8 %MC) with increasing gas velocity (a) initial bed; (b) velocity at 0.3 m/s; (c) velocity at 0.45 m/s; (d) velocity > 0.6 m/s.

When the fractionated samples were fluidized, the behavior observed was dependent upon if the particle size was greater or less than 1 mm nominal screen size. When particles being fluidized were greater than 1 mm nominal screen size (Fig. 4.9 a), channeling was the predominant phenomenon that was observed. Kunii and Levenspiel (1991) reported that beds of large uniformly sized particles often fluidized poorly because of the absence of fine particles that gives the lubricating effect needed for fluidization quality enhancement. We suspected that inter-connected pores within particles allowed easier passage of air without resistance. The pore channels quickly propagated into big channels (Figure 4.9 b) before complete fluidization were achieved. However, when particles being fluidized were less than 1 mm nominal screen size (Fig 4.9 c d and e), plug-low and channeling were prevalently observed in the bed. This is because, smaller particles have higher cohesive forces especially at the higher moisture levels. However, it was noticed that plug flow collapsed easily without aid (shaking or tapping the bed) unlike when bigger particles are fluidized. This suggests that particle interlocking effects were not significant when smaller particles are fluidized.
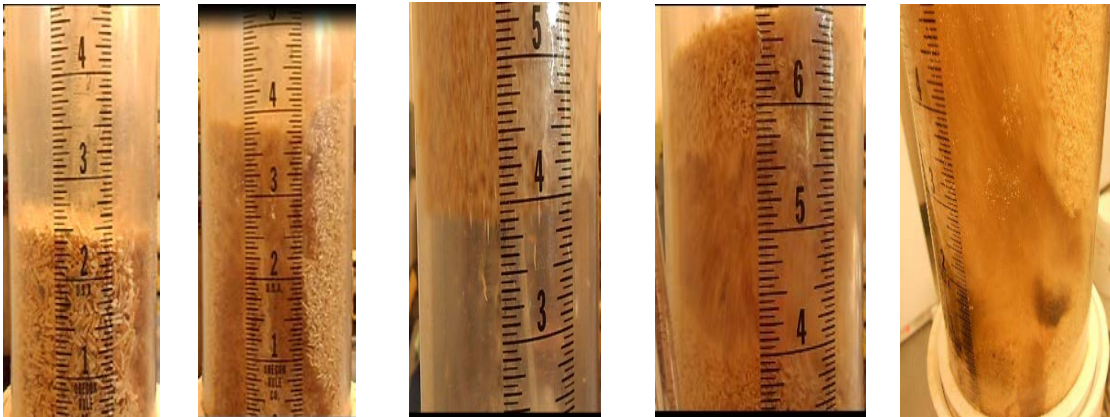
(a)	(b)	(c)	(d)	(e)

Figure 4.9: Effect of particle size by fractionation method at different moisture content on fluidization of bed
(a) 1.7 mm 8% MC; (b) 600 mm 8% MC; (c) 600 mm 15% MC;   (d) 600mm 19% MC; (d) 600mm 27.02% MC.
*diameters were reported as nominal screen size

In summary, the fluidization behavior of loblolly pine grinds is strongly linked to the physical properties of the grinds (moisture content, size, particle shape etc.). Fig. 4.10 schematically present sequence of various fluidization behavior that can be seen in a bed consisting of loblolly pine wood grinds. The typical behavior can occur in a seven-stage sequence with increasing airflow velocity. Stage 1 is the initial bed charge; Stage 2 shows bed rising in plug flow; Stage 3 shows bed collapse; Stage 4 shows bed segregation; Stage 5 shows bed channeling formation; Stage 6 shows a partial fluidized bed, and Stage 7 shows complete fluidized bed. Experimentally, U_{mf} occurs at stage 2 when the airflow velocity results in updraft sufficient to counterbalance the weight of the bed inventory. When sample moisture is sufficiently low, bed behavior may skip stages 2 and 3 because of density differences when grinds contains substantial amount of small particle that elutriate out of the bed. However, particle entrainment is always a constant phenomenon for stages above 4.

| 1 | 2 | 3 | 4 | 5 | 6 | 7 |
| Fixed bed | Plug flow | Collapsing Plug flow | Top fluidization | Bed channeling | Partial channeling | Complete fluidization |
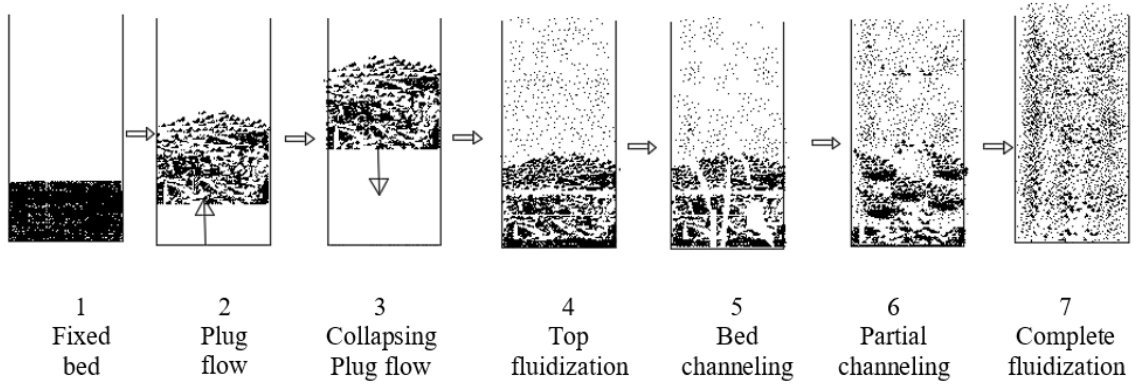
Fig 4.10: Schematic of fluidization behavior of ground loblolly pine wood grinds based on sequence of event

4.4.3.3 Correlation of minimum fluidization velocity

In this section, empirical correlation detailed in Chapter 2, (Section 2.9.2) presented two different approaches used in predicting minimum fluidization velocity (Eqn. 2.8 and 2.9). In chapter 3, equations evaluated are similar equation in Eqn. 2.8. Hence, in this section, the correlation to be used is based on Eqn. 2.9. This equation is re-expressed as shown in Eqn. 4.1.

$$U_{mf} = K \left[\frac{d_{eff}^2 (\rho_s - \rho_g) g}{\mu_g} \left(\frac{\rho_s}{\rho_g} \right)^{1.23} \right]^{\alpha} \tag{4.2}$$

For the effective diameter d_{eff} the relationship proposed by Anderson and Warburton (1949) (Eqn.4.3) was used.

$$d_{eff} = \overline{d} \left(1 + \gamma^2 \right) \tag{4.3}$$

Where d is the diameter from different diameter measurement schemes (Martins, Chord, Feret and surface-volume) and the coefficient of variation expressed as γ in decimal and is shown in Table 4.11.

146

Table 4.11: Particle characterization based on the coefficient of variation (COV) at the various moisture content levels

Screen size (mm)	MC (wet basis)	$\gamma = COV$
Unfractionated	8.40	0.90 (0.05)[a]
	14.86	0.65 (0.02)[b]
	19.80	0.58(0.04) [b]
	27.02	0.42 (0.02)[c]

The coefficient of variation were measured based on chord diameter scheme
Means with the different superscript (alphabet) in a column are significantly different (p<0.05)

In addition, moisture content term, ψ (in decimal) and particle sphericity terms, φ were

included in Eqn. 4.2 as follows

$$U_{mf} = K\left[\frac{d_{eff}^{2}\left(1+\gamma^{2}\right)^{2}\varphi^{2}\psi\left(\rho_{s}-\rho_{g}\right)g}{\mu_{g}}\left(\frac{\rho_{p}}{\rho_{g}}\right)^{1.23}\right]^{\alpha} \qquad (4.4)$$

Eqn. 4.4 can be simplified into

$$U_{mf} = KX^{\alpha} \qquad (4.5)$$

Where

$$X = \frac{d_{eff}^{2}\left(1+\gamma^{2}\right)^{2}\varphi^{2}\psi\left(\rho_{s}-\rho_{g}\right)g}{\mu_{g}}\left(\frac{\rho_{p}}{\rho_{g}}\right)^{1.23} \qquad (4.6)$$

U_{mf}	Minimum fluidization velocity (m/s)
MC, ψ	Moisture content (%)
$\overline{d}$	Mean diameter (m)
d_{sv}	Surface – volume diameter (m)
γ	Coefficient of variation
ρ_{s}	Solid density (kg/m^3)
S_{gw}	Geometric mean standard deviation (m)
d_{eff}	Effective diameter
μ_{g}	Dynamic viscosity (kg /ms)
K, α	Empirical constants
φ	Sphericity

Regression analysis was applied to the plot of the experimental values of the U_{mf} on y-axis against the parameters X (Eqn. 4.5) on x-axis. The particle diameter (size) used in estimating the parameter X were obtained from different diameter measurement schemes presented in Table 4.12. From the regression line in Fig. 4.11, the coefficient K and α presented in Table 4.13 were obtained using the trendline capability in MS Excel®. Also, Fig. 4.11 shows the significant effect of size measurement scheme on prediction of U_{mf}. The steepness reduced with increase in size with Feret and surface-volume diameter having the least and highest slope respectively. Table 4.12 showed that the measured values of α reduced in magnitude with reduction in actual size measured as follows i.e. Feret, Area, Chord, Martins, and surface-volume diameter. About 76% increase in the K value was estimated when the diameter changed from Ferret to surface-volume diameter, representing highest and least mean diameter respectively.

Table 4.12: Effect of moisture contents and diameter measurement schemes on mean size of unfractionated loblolly pine wood grinds

MC (% w.b)		Area	Chord	Ferret	Martin	Surface-vol.
				Diameter (mm)		
		2.87 [a, 2]	1.01 [a, 2,3]	4.90 [a,1]	1.59 [a, 3,4]	0.82 [b,4]
	8.40	(0.41)	(0.36)	(0.76)	(0.30)	(0.04)
		2.42 [a, 2]	1.43 [b c,3]	4.18 [a, 1]	1.18 [c b,4]	0.57 [c, 4]
	14.86	(0.12)	(0.26)	(0.11)	(0.01)	(0.03)
		1.89 [b, 2]	1.30 [c, 3]	3.10 [b, 1]	1.03 [c, 4]	0.71 [b c, 5]
Unfractionated	19.80	(0.03)	(0.03)	(0.06)	(0.02)	(0.02)
		2.48 [a, 2]	1.83 [b a, 3]	4.11 [a, 1]	1.37 [b, 2]	1.05 [a, 4]
	27.02	(0.27)	(0.26)	(0.48)	(0.15)	(0.19)

Values are means of three data points and numbers in parentheses are standard deviation,
Means with the different superscript (numeric) in a row are significantly different (p<0.05)
Means with the different superscript (alphabet) in a column are significantly different (p<0.05)
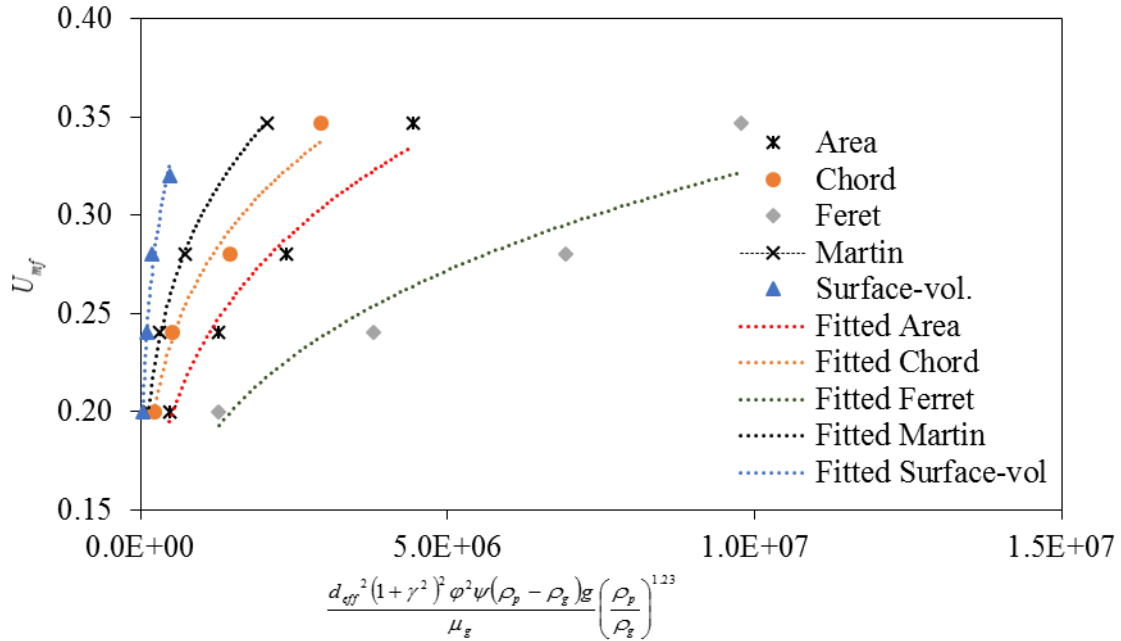
Figure 4.11. Determination of the U_{mf} correlation for unfractionated sample of loblolly pine wood grinds

Table 4.13: Coefficient estimation at various diameter types

Diameter measurement scheme	K	α	R^2
Ferret	0.0056	0.251	0.92
Area	0.0082	0.243	0.98
Chord	0.016	0.205	0.98
Martin	0.0183	0.203	0.99
Surface –volume	0.0234	0.201	0.99

4.4.3.4 Verification of the U_{mf} correlation.

To verify the suitability of equation 4.4, data presented in Chapter 3 were used. The

sample had moisture content of 9.40%, mean sphericity of 0.52, and coefficient of

variation of 0.65 (Please refer to Table 3.4 and 3.5). The U_{mf} of the sample was estimated

to be 0.25 (0.02) m/s (see Section 3.4.3.3). Using Eqn. 4.4 and the coefficients estimated

for various diameter schemes, the predicted values of the U_{mf} obtained for the samples

are given in Table 4.14.

Table 4.14: Predicting and validating the U_{mf} using Eqn. 4.4

Measurement scheme		Density (kg/m^3)			U_{mf} (m/s)		MRD (%)
Measured value (mm)	$d_{eff} \times 10^{-3}$ (m)	ρ_p	ρ_g	X	Predicted	Actual	
Ferret	4.07	3.01	1469.0	1.23	5008349.0	0.26		3.8
Chord	1.00	0.74	1469.0	1.23	303557.7	0.21	0.25	-7.4
Martin	0.83	0.61	1469.0	1.23	205785.0	0.22	(0.04)	-6.1
Sur.- vol.	0.79	0.58	1469.0	1.23	186313.8	0.27		3.6

Parameters of X calculated from calculated from Eqn. 4.4 and Table 4.11

Sur.-vol. means surface-volume diameter

MRD: mean relative deviation calculated from eqn. 4.2.

The mean relative deviations between experimental data and the predicted data using the

Feret, Chord, Martins, and surface-volume mean diameter scheme were 3.8, -7.4, -6.1,

and 3.6 % respectively. The error obtained were lower than to that of Zhong et al. (2008)

who obtained about 13.2 % error between predicted and experimental data using rice

husk and sawdust. Rao et al. (2001) obtained about 48% MRD from predicting the

experimental values of U_{mf} using sand and sawdust (15% fraction) mixture. Also, about

33.05 % MRD was obtained using sand and sawdust (28%) mixture (Aznar et al., 1992).

Therefore, since the percent deviation obtained using the measurement schemes are less

than 20% (Zhong et al., 2008), then all the equation performed satisfactorily. However,

surface –volume diameter produced the least MRD and it would be adjudged most

preferred. Also, most fluidization studies used surface –volume diameter for prediction

standard laboratory determination in absence of image analysis system has be developed.

In addition, this new correlation addressed the deficiencies of selected fluidization

equation shown in Table 3.9 and 3.10 principally inability to adapt to change of diameter measurement scheme and over prediction obtained with MRD greater than 15%.

4.5   Conclusion

Moisture content significantly affects the physical properties of biological material (bulk density, particle density, porosity, and particle size distribution) that are critical in determination of minimum fluidization velocity. We investigated the effect of moisture contents on properties that influences the determination of minimum fluidization velocity of ground loblolly pine wood. The result shows that as moisture content increased the bulk density, particle density, and porosity increased. However, with increase in moisture content, the particle size distribution reduced with coefficient of variation that ranges from 90 at 8.46% MC to 42 at 27.02 % MC. Also, as moisture content increased the minimum fluidization velocity values also increased. The minimum fluidization velocity (U_{mf}) of loblolly pine wood ground was found to be 0.20, 0.24, 0.28 and 0.32 m/s for moisture content of 8.45, 14.86, 19.86 and 27.02 % wet basis respectively. The grinds were found to be completely fluidized at $4U_{mf}$. The correlation developed predicted the experimental data with mean relative deviation less than 20%.

4.6   Reference

Abdullah, M. Z., Z. Husain, and S. L. Yin Pong. 2003. Analysis of cold flow fluidization test results for various biomass fuels. *Biomass and Bioenergy* 24(6):487-494.

Allen, T. 1997. *Particle Size Measurement: Volume 2: Surface Area and Pore Size Determination*. Springer.

Anderson, S., and F. Warburton. 1949. 46—The porous plug and fibre diameter measurement. Effect of fibre orientation and use of plugs of randomized fibres. *Journal of the Textile Institute Transactions* 40(11):T749-T758.

ASABE. 2006. ASAE S319. 3—method of determining and expressing fineness of feed materials by sieving, ASABE Standards, 602–605, American Society of Agricultural and Biological Engineers, St. *Joseph, MI.*

ASTM. 2006. Standard Test Method for Moisture Analysis of Particulate Wood Fuels," ASTM International, West Conshohocken, PA, 2006, DOI: 10.1520/E0870-82R06.

Aznar, M. P., F. A. Gracia-Gorria, and J. Corella. 1992. Minimum and maximum velocities for fluidization for mixtures of agricultural and forest residues with a second fluidized solid. II. Experimental results for different mixtures. *International chemical engineering* 32(1):103-113.

Clarke, K. L., T. Pugsley, and G. A. Hill. 2005. Fluidization of moist sawdust in binary particle systems in a gas solid fluidized bed. *Chemical Engineering Science* 60(24):6909-6918.

Cui, H., and J. R. Grace. 2007. Fluidization of biomass particles: A review of experimental multiphase flow aspects. *Chemical Engineering Science* 62(1):45-55.

Deshpande, S. D., S. Bal, and T. P. Ojha. 1993. Physical Properties of Soybean. *Journal of Agricultural Engineering Research* 56(2):89-98.

Downing, M., L. M. Eaton, R. L. Graham, M. H. Langholtz, R. D. Perlack, A. F. Turhollow Jr, B. Stokes, and C. C. Brandt. 2011. US Billion-Ton Update: Biomass supply for a bioenergy and bioproducts industry. Oak Ridge National Laboratory (ORNL).

Fasina, O. 2006. Flow and physical properties of switchgrass, peanut hull, and poultry litter. *Transactions of the ASABE* 49(3):721-728.

Fasina, O. O. 2008. Physical properties of peanut hull pellets. *Bioresource Technology* 99(5):1259-1266.

Gauthier, D., S. Zerguerras, and G. Flamant. 1999. Influence of the particle size distribution of powders on the velocities of minimum and complete fluidization. *Chemical Engineering Journal* 74(3):181-196.

Hughes, W. E., and E. D. Larson. 1997. Effect of fuel moisture content on biomass - IGCC performance In *International Gas Turbine and Aeroengine Congress and Exhibition*. ASME, ed: American Society of Mechanical Engineers.

Huntinton, C. 1924. The Idaho Forester. In *A preliminary study of shrinkage in Idaho confers*, 58. Moscow Idaho: university of Idaho.

Kenney, K. L., W. A. Smith, G. L. Gresham, and T. L. Westover. 2013. Understanding biomass feedstock variability. *Biofuels* 4(1):111-127.

Khanal, S. K. 2010. *Bioenergy and biofuel from biowastes and biomass*. ASCE Publications, Reston Virginia.

Kunii, D., and O. Levenspiel. 1991. *Fluidization engineering*. Butterworth-Heinemann Boston.

Lam, P., S. Sokhansanj, X. Bi, C. Lim, L. Naimi, M. Hoque, S. Mani, A. Womac, S. Narayan, and X. Ye. 2008. Bulk density of wet and dry wheat straw and switchgrass particles. *Applied Engineering in Agriculture* 24(3):351-358.

Mani, S., L. G. Tabil, and S. Sokhansanj. 2004. Grinding performance and physical properties of wheat and barley straws, corn stover and switchgrass. *Biomass and Bioenergy* 27(4):339-352.

Manickam, I. N., and S. Suresh. 2011. Effect of moisture content and particle size on bulk density, porosity, particle density and coefficient of friction of coir pith. *International Journal of Engineering Science* 3.

Mattsson, J. E., and P. D. Kofman. 2002. Method and apparatus for measuring the tendency of solid biofuels to bridge over openings. *Biomass and Bioenergy* 22(3):179-185.

Mujumdar, A. S. 2006. *Handbook of industrial drying*. 3rd ed. CRC Press, Florida US. Nemec, D., and J. Levec. 2005. Flow through packed bed reactors: 1. Single-phase flow. *Chemical Engineering Science* 60(24):6947-6957.

Oginni, O. J. 2014. Contribution of particle size and moisture content to flowability of fractionated ground loblolly pine. M.S thesis. Auburn University, Biosystems Engineering Department, Auburn Alabama.

Oliveira, T. J. P., C. R. Cardoso, and C. H. Ataíde. 2013. Bubbling fluidization of biomass and sand binary mixtures: Minimum fluidization velocity and particle

segregation. *Chemical Engineering and Processing: Process Intensification* 72(0):113-121.

Probst, K., A. Kingsly, R. Pinto, R. Bali, P. Krishnakumar, and K. Ileleji. 2013. The effect of moisture content on the grinding performance of corn and corncobs by hammermilling. *Transactions of the ASABE* 56(3):10251-11033.

Raigar, R., and H. Mishra. 2015. Effect of Moisture Content and Particle Sizes on Physical and Thermal Properties of Roasted Bengal Gram Flour. *Journal of Food Processing and Preservation*.

Rao, R., T. Ram, and J. V. Bheemarasetti. 2001. Minimum fluidization velocities of mixtures of biomass and sands. *Energy* 26(6):633-644.

Rhén, C., R. Gref, M. Sjöström, and I. Wästerlund. 2005. Effects of raw material moisture content, densification pressure and temperature on some properties of Norway spruce pellets. *Fuel Processing Technology* 87(1):11-16.

Rhodes, M. 2008. *Introduction to particle technology*. Wiley.

Rousset, P., T. Petithuguenin, T. Rodrigues, and A.-C. Azevedo. 2012. The fluidization behaviour of torrefied biomass in a cold model. *Fuel* 102(0):256-263.

SAS. 2011. *The SAS system for Windows.* Ver. Release 9.2. Cary, NC.: SAS Institute. Smith, W. B., P. D. Miles, C. H. Perry, and S. A. Pugh. 2009. Forest resources of the United States, 2007: a technical document supporting the forest service 2010 RPA Assessment. *General Technical Report-USDA Forest Service*(WO-78).

Srivastava, A., and S. Sundaresan. 2002. Role of wall friction in fluidization and standpipe flow. *Powder Technology* 124(1):45-54.

Tsinontides, S., and R. Jackson. 1993. The mechanics of gas fluidized beds with an interval of stable fluidization. *Journal of Fluid Mechanics* 255:237-274.

Wear, D., and J. Gries. 2011. The Southern Forest Futures Project. Technical Report. USDA Forest Service, General Technical Report SRS, Asheville, North Carolina.

Wilkinson, D. 1995. Determination of minimum fluidization velocity by pressure fluctuation measurement. *The Canadian Journal of Chemical Engineering* 73(4):562-565.

Woodcock, C., and J. Mason. 1988. *Bulk solids handling: an introduction to the practice and technology*. Springer.

Wormsbecker, M., and T. Pugsley. 2008. The influence of moisture on the fluidization behaviour of porous pharmaceutical granule. *Chemical Engineering Science* 63(16):4063-4069.

Wright, C. T., P. A. Pryfogle, N. A. Stevens, J. R. Hess, and C. W. Radtke. 2006. *Value of distributed preprocessing of biomass feedstocks to a bioenergy industry*. Idaho National Laboratory.

Yu, A., and N. Standish. 1993. Characterisation of non-spherical particles from their packing behaviour. *Powder Technology* 74(3):205-213.

Zhang, Y., B. Jin, and W. Zhong. 2009. Experimental investigation on mixing and segregation behavior of biomass particle in fluidized bed. *Chemical Engineering and Processing: Process Intensification* 48(3):745-754.

Zhong, W., B. Jin, Y. Zhang, X. Wang, and R. Xiao. 2008. Fluidization of Biomass Particles in a Gas−Solid Fluidized Bed. *Energy & Fuels* 22(6):4170-4176.

Zhou, B., K. Ileleji, and G. Ejeta. 2008. Physical property relationships of bulk corn stover particles. *Transactions of the ASABE* 51(2):581-590.

Chapter 5: Air Flow through Packed Columns of Ground Loblolly Pine Wood: Revised Ergun Expression

5.1 Abstract

Existing model equations that may be used for predicting pressure drop as a result of fluid flow through beds of granular materials non-uniform particle size are limited because the void correlation used were developed using uniformly sized particles. Also, the equation do not have terms to account for the influence of size distribution on air flow and penetration through the bed. In this study, Ergun equation was modified by revising the viscous and kinetic energy losses correlations and incorporating a term for coefficient of variation of particles of ground loblolly pine wood. In addition, a new frictional factor relating Reynold number to kinetic and viscous energy losses were proposed and tested. Furthermore, a revised Ergun's equation was proposed, tested and validated using ground loblolly pine wood, and data from other published work. The coefficient K_1 and K_2 was determined by methods of least square to be 201 and 2.7 respectively. The overall relative mean deviation obtained between the predicted and experimental pressure drop using ground loblolly pine wood and the equation developed in this study and the Ergun equation were -17.48 % and 63.5 % respectively.

5.2 Introduction

Fluidization is a process by which a bed of solids is transformed into a condition similar to fluid flow by suspending the solids in a stream of fluid. The goal is to enhance contact between fluid and solids, by increasing the surface area of solids exposed to the fluid – a desire feature in applications such as drying, adsorption, combustion, carbonation, and gasification. Depending on the objectives of the application, the solids may consist of multicomponent particles that have differing behavior to gas/liquid fluidization (Formisani *et al.,* 2011). Examples of fluidizing behaviors that have been observed for multicomponent particles include entrainment (Hrenya and Sinclair, 1997), segregation, channeling, pressure fluctuation and un-controllable bed expansion due to the formation of bubbles, slugging, plug flow and poor bed mixing (Das et al., 2008; Hoffmann et al., 1993; Hrenya and Sinclair, 1997; Liu et al., 2008; Seu-Kim and Arastoopour, 1995; Zhang et al., 2008, 2009). These undesirable behaviors have limited the ability of scientists and engineers to predict the state of bed during fluidization. As a result, advantages associated with proper mixing such as uniform thermal concentration gradient cannot be adequately exploited.

Fluidization of bed that consist of multicomponent particles have received attention of several researchers in the past (Abrahamsen and Geldart, 1980; Ergun, 1952; Geldart, 1972; Kumar and SenGupta, 1974; Obata et al., 1982; Reina et al., 2000; Rowe and Nienow, 1975; Wen and Yu, 1966). These researchers reported the influence of fluid flow velocity on pressure losses and particle-fluid behaviors. These studies used the fluid properties and averaged properties of solids (e.g. average density and average particle

157

size) to develop analytical/empirical expressions for predicting the pressure drop and velocity of a fluidized bed system.

One of the most widely used analytical expression for representing the relationship between pressure drop at different fluid flow in packed bed is Ergun's expression (henceforth refers to Ergun) (Wang, 2014). Ergun equation was developed with the recognition of additive effect of the viscous and kinetic energy losses in a packed bed and smooth transition from a viscous dominated to kinetic dominated effects as fluid flow rate increased in a bed. Starting from Eqn. 5.1, which states that pressure drop across a granular bed, is proportional to the fluid velocity at low flow rate and to the square of the velocity at high flow rates. Ergun plotted $\Delta P/LU$ against ρU, using a bed of crushed coke packed to different fractional void volume. Assuming a continuous function for the relationship between pressure drop and fluid flow rate. The author added Poiseuilles's expression and his earlier developed void fraction correlations (viscous and kinetic) (Ergun, 1951). A fit of experimental data to the Ergun's expression for crushed coke resulted in Ergun constants $K_1 = 150$ and $K_2 = 1.75$. The first term on the right-hand side of Eqn. 5.2 represents viscous energy at low fluid flow rate while the second term on the right hand side represent kinetic energy loss due to high fluid flow rate.

$$\frac{\Delta P}{L} = a\mu U + b\rho U^2 \tag{5.1}$$

$$\frac{\Delta P}{L} = K_1 \frac{(1-\varepsilon)^2}{\varepsilon^3} \frac{\mu U_m}{d_p^2} + K_2 \frac{1-\varepsilon}{\varepsilon^3} \frac{\rho_f U_m^2}{d_p} \tag{5.2}$$

where, $\Delta P/L$= pressure gradient across channel (Pa/m),
U_m = superficial velocity (m/s),

μ = fluid viscosity (Pa.s),

ρ_f = fluid density (kg/m^3),

ε = porosity, and

d_p = particle diameter (m).

Ergun identified the rate of fluid flow, viscosity and density of fluid, closeness and orientation, size, shape, surface area and bed void fraction as factors that influence the relationship between pressure drop and fluid flow velocity. When a bed consists of particle with uniform shape and size distribution, Ergun's expression has been proven to perform satisfactorily in predicting pressure drop data at different gas flow rates. For instance, using a bed consisting of spherical shaped alumina and glass beads, Nemec et al. (2001) and Mawatari et al. (2003) obtained 4.2% and 5% error deviation between experimental and predicted pressure drop data. Similar conclusion were made by Cloete et al. (2015), Jing et al. (2000), Dolejs and Machac (1995) and Lippens and Mulder (1993).

For a bed that consist of non-spherical particles with non-uniform particle size distribution typical of biomass grinds, there is a need to modify Ergun's equation before a good prediction can be made. For instance, Dolejs and Machac (1995) obtained 72.6 and 24.9 % mean relative deviation for a bed consisting of polyhedral and cubes respectively. Using a bed of Zeolite having a mean particle size of 6 mm and shape factor of 0.8, Çarpinlioğlu and Özahi (2008) obtained a 28% deviation of experimental data from predicted pressure drop. When bed is composed of cylindrical particles, the pressure drop obtained was 35% higher than the experimental (Gunarathne et al., 2014). Luckos and Bunt (2011) predicted the pressure drop in individual reaction zones in a commercial Sasol-Lurgi gasifier. The author obtained about 70% error in the predicted and

experimental pressure drop in the combustion and gasification zones and the author attributed the high deviation to voidage and Ergun equation inability to capture the effect of particle size distribution within the zones. Kim and Han (2006) obtained 50% deviation between predicted and experiment U_{mf}. The author attributed the discrepancy to high cohesive force between fine particles in phosphor which Ergun equation expression was unable to capture. Hence, it can be concluded that Ergun equation in its original form cannot be reliably used to predict pressure drop in beds that consist of non-spherical particles.

 In order to modify Ergun equation, the focus should not only be on changing Ergun's constants but also estimating appropriate void fraction at different flow velocity (laminar or turbulent). This is because, as fluid velocity passed through the bed increase, small particles are entrain, while larger and heavier particles are yet to be fluidized. In addition, size and shape of non-spherical particle depends on several factors such as particle orientation, measuring technology, and moisture content (Bouwman et al., 2004). These issues have resulted in limited success in improving Ergun equation for non-spherical and non-uniform particles size bed (Dolejs and Machac, 1995; Gunarathne et al., 2014; Innocentini et al., 1999).

Some authors have attempted to refit Ergun's equation and obtain new value for constant (K_1 and K_2) but retain Ergun's equation structure. Cloete et al. (2015) proposed $K_1 = 250$ and $K_2 = 2.5$ respectively for cylindrical particle of γ-Al_2O_3 Quinn (2014) proposed 267 for K_1 while K_2 is dependent on type of material. For leadshot, glass beads and white sand, the K_2 values were obtained to be 2.14, 2.51, 4.02 respectively. Also, Ozahi et al. (2008) proposed a constant of $K_1 = 160$ and $K_2 = 1.61$ for zeolite and chickpeas. In all

these studies, no attempt was made at changing or modifying the void fraction

correlation. In addition, these authors used spherical particles having uniform particle

size with void fraction that was less than 0.5. These conditions were sometimes imposed

on particles so as to satisfy Ergun assumptions (see section 2.9.1). Hence, the studies

were simply validating Ergun equation for other materials. However, for biomass grinds,

having high void fraction usually up to 0.8, lognormal size distribution, and non-spherical

particle shapes. Ergun's structures and assumption has to be reexamined before good

prediction can be obtained.

In light of the limitations highlighted, the overall goal of this study is to propose and

validate a revised Ergun's equation suitable for non-spherical materials with non-uniform

particle size distribution such as biomass grinds. First, a suitable void fraction correlation

will be derived for predicting kinetic and viscous fractional void correlation. Second,

Ergun's equation will be revised using the void fraction correlation obtained and adapted

to loblolly pine wood grinds by accounting for the shape, porosity, and particle size

distribution using the coefficient of variation.

5.3   Methodology

5.3.1   Material preparation

Clean loblolly pine wood chips were obtained from a forest plantation in Alabama, U.S.

The moisture content was determined to be 8.45 % using ASTM standard E871-82

ASTM (2007). The chips were ground through hammer mill (Model No. 10HBLPK,

Sheldon Manufacturing, Tiffin, OH) fitted with screen size of 22.23 mm (7/8 inches),

19.05 mm (3/4 inches), 15.88 mm (5/8 inches), 12.7 mm, (1/2 inches), 9.53 mm (3/8

inches), 6.35 mm (1.4 inches), or 3.18 mm (1/8 inches). This resulted in seven samples

with different bulk densities. The physical properties of each sample were determined as described below.

5.3.2 Particle size

Particle size distribution of each sample was determined using a particle size analyzer (Camsizer®, Retsch Technology, Haan, Germany). For this analysis, about 100g of each of the sample was poured into the hopper from where it was conveyed through the vibratory feeder to the measurement chamber of the system. In the chamber, images of the falling particles were taken using two cameras located at the measurement field. The software attached to the instrument then use the images recorded and the result was used to plot the size distribution. In addition, Ferret, Martins, area, surface to volume and chord diameter measurement schemes were recorded from the software. The surface to volume diameter measurement scheme was estimated from the specific surface data (Rhodes, 2008). The sphericity (φ) values of the particles were obtained from the software using ISO 9276-6 standard procedure (ISO/9276-6, 2008). For each particle size distribution data, particle characteristic needed (X_{84}, X_{16}, X_{50}) to compute the coefficient of variation (COV) (Eqn. 5.3) were recorded from the software.

$$COV = 50 \frac{X_{84} - X_{16}}{X_{50}} \qquad (5.3)$$

where;

X_{85} is particle diameter at 84% probability (mm)

X_{16} is particle diameter at 16% probability (mm)

X_{50} is particle diameter at 50% probability (mm)

5.3.3 Particle density

The particle density of sample were determined using a gas pycnometer (Accupyc 1330, Micromeritics Instrument Corp., Norcross, Ga.). The gas pycnometer, uses helium to estimate the pressure difference between a reference cell and a cell containing the sample. The pressure difference was used by the pycnometer to estimate the volume of a known mass of sample. A digital weighing scale (Model AR3130, Ohaus Corp, Pinebrook, NJ) was used to measure the sample mass. Particle density was estimated as the ratio of the mass of the sample in the cell and the volume estimated by the pycnometer.

5.3.4 Bulk density

Bulk density was determined using an apparatus that consists of a funnel through which the sample freely falls onto 1137 mm^3 cup. The ratio of the mass of the sample in the container to the volume of the container was used to compute the estimated bulk density.

5.3.5 Porosity

The inter – granular porosity (ε) of the ground wood sample was calculated from the measured values of bulk density and particle density as follows;

$$\varepsilon = 1 - \frac{\rho_b}{\rho_p} \tag{5.4}$$

where ρ_b is bulk density (kg/m^3) and ρ_p is particle density (kg/m^3).

5.3.6 Pressure drop and flow rate measurement test

A description of this experimental setup can be found in section 3.3.6.

5.3.7   Void fraction correlation modification: concept

Understanding Ergun's argument would aid improving the void fraction correlation in

Eqn. 5.2. In a packed bed, the solid and void fractions are related using Eqn. 5.5, 5.6, and

5.7.

$$\varepsilon_{void} = \frac{V_{air}}{V_{air} + V_{solid}} \tag{5.5}$$

$$V_{air}(1 - \varepsilon_{void}) = \varepsilon_{void} V_{solid} \tag{5.6}$$

$$V_{solid} = \frac{1 - \varepsilon_{void}}{\varepsilon_{void}} V_{air} \tag{5.7}$$

where,

ε_{void} is the void faction

V_{air} is the volume occupied by air (m^3)

V_{solid} volume occupied by solid (m^3)

Earlier researchers (Hatch, 1943; Leva et al., 1951) suggested a non-linear expression of

the void fraction $\left[\dfrac{(1-\varepsilon)^m}{\varepsilon^n}\right]$ as a function of fluid velocity, where m and n are positive

integer with values 1 (lamina) and 3 (turbulent) for bed with uniform particles sizes.

Using this concept, Ergun stated that the entropy in a bed at low (viscous) and high

(kinetic) fluid flow rate should be different and be proportional to the coefficients a and b

in Eqn. 5.1 respectively. In other word, coefficients a and b should be directly

proportional to $\dfrac{(1-\varepsilon)^m}{\varepsilon^n}$ at certain combinations of values of m and n for viscous and

turbulent flow for the theory to be valid. Then changing the value of m and n until such a

point that the value of R^2 is maximum would result in the appropriate void correlation. Hence, this approach would be used in this study to modify the void fraction correlations of Ergun equation for loblolly pine wood grinds.

5.3.8 Data analysis

All experiments were conducted in triplicates and results are presented in the relevant sections as mean values and standard deviation. Test of significance of the variables (screen size, porosity, particle and bulk density, particle size, sphericity and coefficient of variation) were conducted using the analysis of variance (ANOVA) procedures (SAS, 2011). Tukey multiple range test (using the same software) was used to compare means of each properties. Differences were considered to be statistically significant when $p < 0.05$. Statistical Mean Relative Deviation (MRD) (Eqn. 5.8) was used as statistical indicator to compare the predictive ability of the equations (Original Ergun and modified Ergun (Nemec and Levec, 2005).

$$MRD(\%) = \frac{1}{N} 100 \sum_{i=1}^{N} \frac{\left| \lambda_{i.calc} - \lambda_{i.\exp} \right|}{\lambda_{i.\exp}} \tag{5.8}$$

$\lambda_{i.\exp}$ is experimental values

$\lambda_{i.cal}$ is calculated/predicted

N is number of data points

5.4   Experimental result and model derivation

5.4.1   Particle size and coefficient of variation

The particle size distributions obtained by grinding the sample through different screen size are shown in Fig. 5.1. Similar to particle size of ground biological material, the distribution show positive skewness which indicates that the tail on the right side is longer than the left side. The estimated geometric mean diameter for each of the sample is given in Table 5.1. The values obtained for the sample coefficient of variations was greater than 60%, which further demonstrated that the particle size within the sample varied widely. However, screen size did not significantly affect the coefficient of variation of particle ($p < 0.05$).
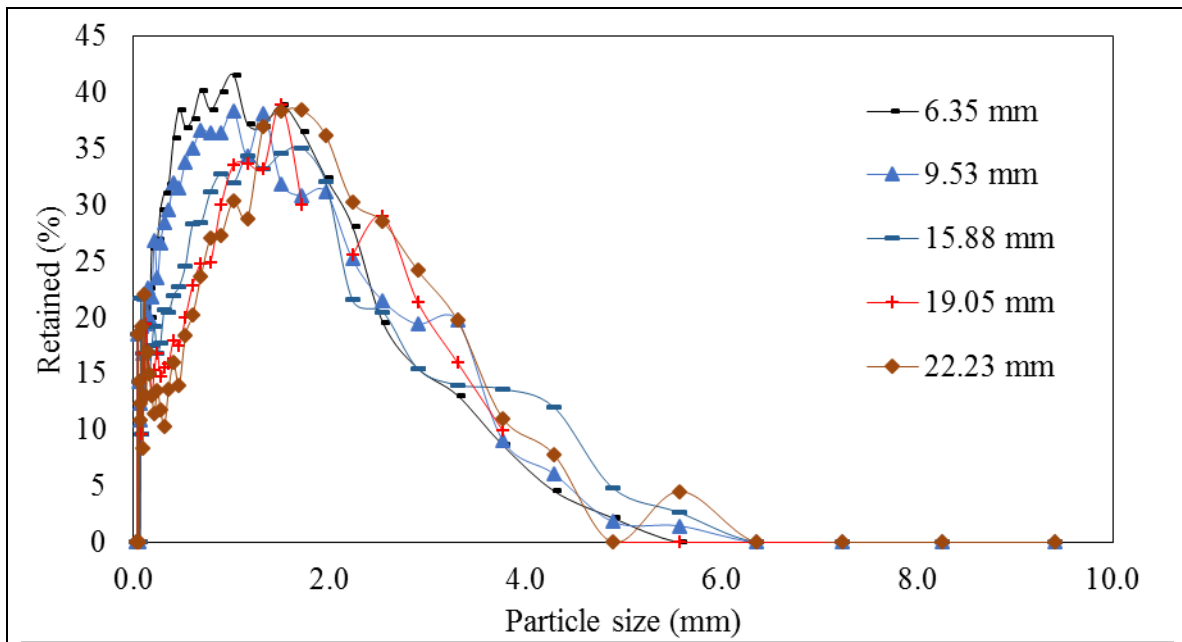
Figure 5.1: Particle size distribution for loblolly pine wood grinds obtained from hammer mill at different screen sizes.

Table 5.1: Physical properties of loblolly pine wood grinds ground through different screen sizes.

Screen Size (mm)	Diameter Sur.-vol. (mm)	Sphericity	Bulk density (kg/m^3)	Particle density (kg/m^3)	Porosity	COV
6.35	0.79 [c] (0.10)	0.37[c] (0.10)	250.89 [b] (2.40)	1453.30 [ab] (44.10)	0.83[b] (0.01)	72.60 [bc] (0.01)
9.53	0.91 [ba] (0.10)	0.37 [a] (0.10)	252.80 [b] (2.80)	1420.40[b] (12.10)	0.84[ab] (0.01)	72.80 [c] (0.1)
15.88	0.98[a] (0.10)	0.39 [b] (0.10)	229.93[d] (1.60)	1448.20[ab] (3.03)	0.84[ab] (0.01)	72.50 [abc] (0.1)
19.05	0.94[a] (0.03)	0.42 [a] (0.10)	228.27[d] (2.90)	1424.90[b] (12.15)	0.84[ab] (0.01)	67.90[c] (0.06)
22.23	0.98[a] (0.03)	0.41 [a] (0.01)	222.72[e] (3.30)	1438.80[ab] (11.70)	0.85[a] (0.01)	64.00 [c] (0.02)

Values are means of triplicates experimental runs
Numbers in parentheses are standard deviation
Means with the different superscript (alphabet) in a column are significantly different ($p<0.05$)
COV means coefficient of variations (calculated using Eqn. 5.3)
Sauter means surface to volume mean diameter (calculated using 6/specific surface obtained from CamSizer®)

5.4.2   Bulk and particle densities

The result showed that the bulk densities decreased ($p <0.05$) as particle size increased (Table 5.1). This has been attributed to reduction in voids between the particles as particle size decreased (see values of porosity in Table 5.1) (Gil *et al.,* 2013; Ryu *et al.,* 2006). Lam et al. (2008) also reported that bulk density of wet and dry wheat straw and switchgrass particles reduced with increase in nominal screen size. It is also important to point out that the bulk density result is opposite of Table 4.7. The sample in the present study composed of different particle sizes and smaller size particles occupy spaces between the bigger particles. Therefore, reduction in particle size produced more smaller size fraction resulting in increase in bulk density. However, particle density did not significantly vary with increase in particle size ($p < 0.05$). This could be that the exposure

of pores spaces as a result of size reduction process within the screen size ranged in this aspect of the study were not significant.

5.4.3   Porosity and sphericity

Table 5.1 shows that the reduction in porosity was less than 5 % as mean diameter reduced from 2.10 to 1.19 mm and this reduction was not statistically significant ($p < 0.05$). Marginal reduction in porosity value can be attributed to the particle distribution and the particle shape. As bigger particles reduced in size, the smaller particles in the sample increase and occupy some of the void in between the larger particles. In addition, particle shape (Table 5.1) influence the packing density as an irregularly shaped particle having a pin-like structure can bend and interlock with other particles within the sample, blocking available spaces and creating a more dense bed. The results also showed that the mean sphericity of particles increased by 20 % as particle size increased.

5.4.4   Pressure drop and flow rate measurement test

The plots of ratio of pressure gradient to velocity against air mass flow rate (Eqn. 5.1) are shown in Fig 5.2 for loblolly pine wood grinds that were prepared with different screen sizes are linear. This plot is similar to what Ergun obtained using crushed coke (Ergun, 1952). Also, it can be deduced from the plot that reduction in particle size resulted in higher pressure losses because air was forced through the packed bed. This could be attributed to the fact that as particle size reduced, void fraction reduced thereby reducing the airflow and increasing pressure gradient.
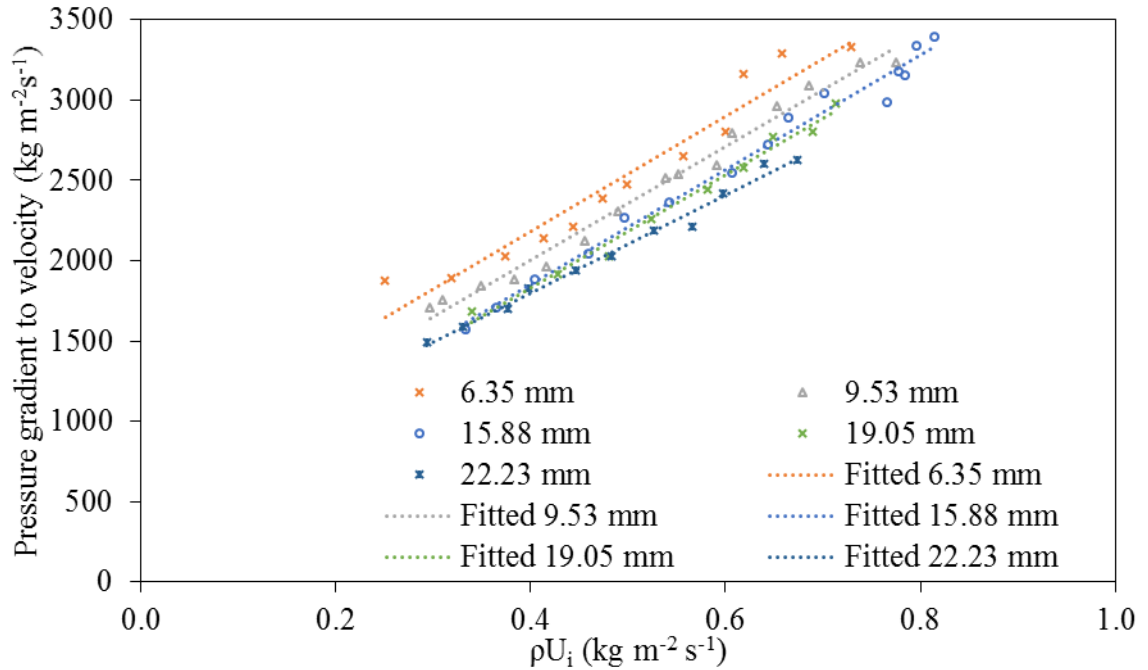
Figure 5.2: Linear form of pressure–drop equation (Eqn.5.1) using loblolly pine wood grinds having different size and void fractions.

The slopes, intercepts and the corresponding R^2 value of each plots in Fig 5.2 is summarized in Table 5.2. When the nominal screen size reduced by 89.8%, the slope and intercept increased by 67.7 and 38.2 % respectively. Since the intercept and slopes are related to viscous and kinetic energy losses respectively (Ergun, 1952), increases in the value of intercept or slope indicate that resistance of the bed material to stress-shear deformation at viscous level and bed entropy (particle-particle collision per unit area due to kinetic energy) increased with reduction in size.

Table 5.2: Estimation of slope and intercept parameters for loblolly pine wood at different particle sizes.

Screen size (mm)		$^+$Slope	$^+$Intercept	$^+R^2$	^{1}Viscous	^{2}Kinetic
6.35 mm	1/4 inches	3346.2	883.2	0.90	0.053	0.31
9.53 mm	3/8 inches	3248.3	811.1	0.95	0.046	0.28
15.88 mm	5/8 inches	3053.4	687.7	0.93	0.042	0.27
19.05 mm	3/4 inches	3071.1	670.5	0.98	0.041	0.26
22.23 mm	7/8 inches	2999.8	633.1	0.97	0.039	0.25

$^+$Values obtained from Fig. 4

^{1}values estimated from porosity data Table 5.2 and viscous void fraction correlation $(1-\varepsilon)^2/\varepsilon^3$

^{2}values estimated from porosity data Table 5.2 and kinetic void fraction correlation $(1-\varepsilon)/\varepsilon^3$

5.4.5   Void fraction correlation development: Ergun's correlation

Fig. 6.3 and 6.4 show the plot of slope and intercept (from Table 6.2) against viscous, $(1-\varepsilon)^2/\varepsilon^3$ and kinetic fractional correlation, $(1-\varepsilon)/\varepsilon^3$ used by Ergun respectively. It can be seen that the R^2 values from viscous energy void correlation is 0.9528 while that of kinetic energy correlation 0.611. Hence, the Ergun's kinetic energy correlation does not appear to be adequate for loblolly pine wood grinds.
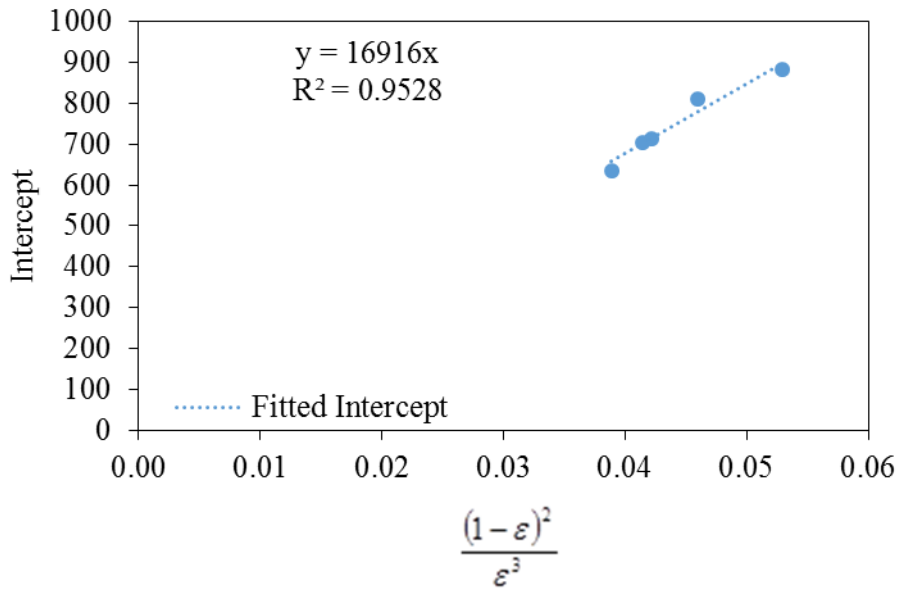
Figure 5.3: Dependence of viscous energy losses on fractional void volume correlation used in Ergun's equation.
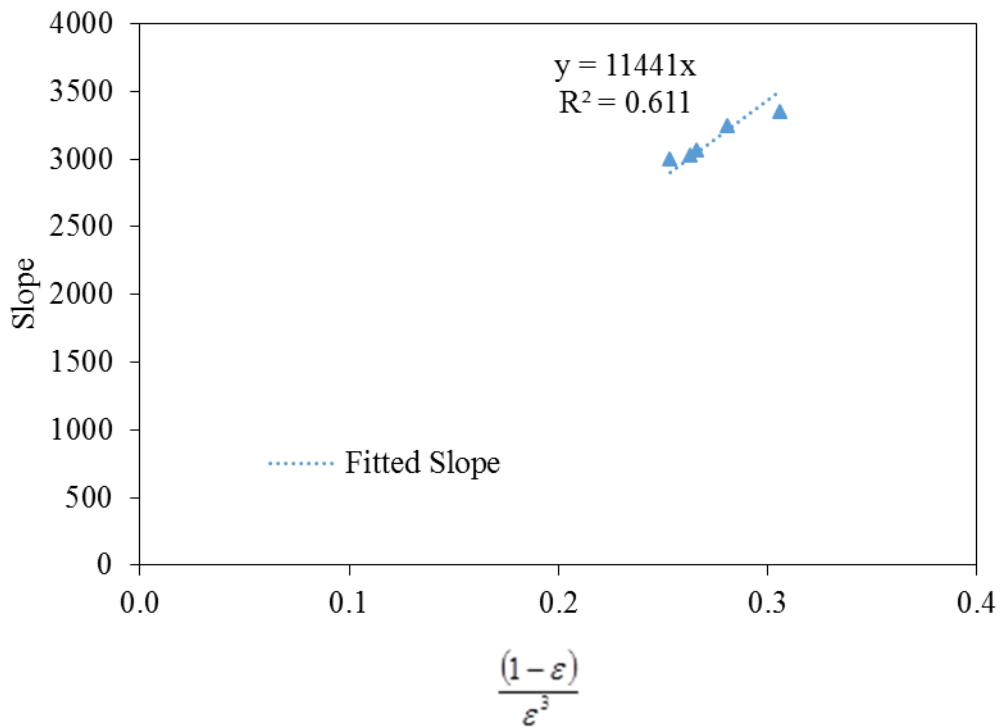
Figure 5.4: Dependence of kinetic energy losses on fractional void volume correlation used in Ergun's equation

5.4.6 Modification of void fraction correlation

In order to refit the void fraction correlations for kinetic energy losses, the Microsoft Excel® nonlinear solver was employed to minimize the error sum of square between predicted (void correlation data) and the corresponding actual data (slope data). While iterating, the solver simultaneously change the parameters of m and n until a solution in which all-internal solver constraint and optimality conditions are satisfied (in this case the solver minimized the error sum of square). At this point, the value of m and n was then chosen as the modified correlation as shown in Eqn. 5.9. Fig 6.5 show the plot of slope values (Table 6.2) against the new kinetic fractional void correlation obtained. It can be seen that the modified kinetic (R^2=0.94) fractional correlation resulted in 35 % improvement over R^2 obtained from Ergun's kinetic fractional void correlation (Fig. 6.4).

$$kinetic = \frac{(1-\varepsilon)^{0.3}}{\varepsilon^{3.4}} \qquad (R^2 = 0.94) \qquad (5.9)$$
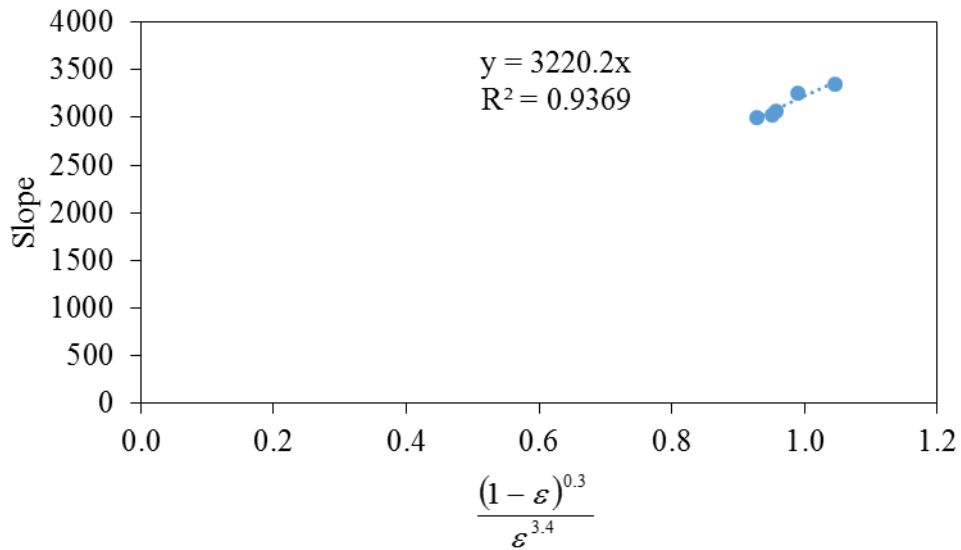
Figure 5.5: Dependence of kinetic energy losses on modified fractional void volume correlation used in Ergun's equation (Eqn. 1)

172

5.4.7 Model presentation

In this section the particle size, shape, particle distribution using coefficient of variation would now be included in the model.

Combining Eqn. 5.1 and the derived void fractional correlations (Fig. 5.3 and 5.5)

$$\frac{\Delta P}{L} = a^i \frac{(1-\varepsilon)^2}{\varepsilon^3} \mu U + b^i \frac{(1-\varepsilon)^{0.3}}{\varepsilon^{3.4}} \rho U^2 \tag{5.10}$$

Also, comparing Eqn. 5..10 with Eqn. 5.2

$$\frac{\Delta P}{L} = K_1 \frac{(1-\varepsilon)^2}{\varepsilon^3 d^2} \mu U + K_2 \frac{(1-\varepsilon)^{0.3}}{\varepsilon^{3.4} d} \rho_f U^2 \tag{5.11}$$

The relationship proposed by Anderson and Warburton (1949) was adopted for the coefficient of variation term as shown in Eqn. 5.12

$$d = \overline{d}\left(1 + cv^2\right) \tag{5.12}$$

Where d is the mean diameter (m) and cv is the coefficient of variation (in decimal)

Inserting Eqn. 5.12 and sphericity term into Eqn. 5.11

$$\frac{\Delta P}{L} = K_1 \frac{(1-\varepsilon)^2}{\varepsilon^3 \left(d\left(1+cv^2\right)\right)^2} \mu U + K_2 \frac{(1-\varepsilon)^{0.3}}{\varepsilon^{3.4} d\left(1+cv^2\right)} \rho_f U^2 \tag{5.13}$$

In order to incorporate the effect of shape of the particle, several researchers multiply the diameter with the sphericity factor (Zhong et al., 2015).

$$\frac{\Delta P}{L} = K_1 \frac{(1-\varepsilon)^2}{\varepsilon^3 \left(d\varphi\left(1+cv^2\right)\right)^2} \mu U + K_2 \frac{(1-\varepsilon)^{0.3}}{\varepsilon^{3.4} d\varphi\left(1+cv^2\right)} \rho_f U^2 \tag{5.14}$$

where φ is the sphericity of the particle

Converting Eqn. 5.14 into a linear form result in

$$\frac{\Delta P}{LU} \frac{\varepsilon^3 d^2 \varphi^2 \left(1+cv^2\right)^2}{\mu(1-\varepsilon)^2} = K_1 + K_2 \frac{\rho_f U d\varphi\left(1+cv^2\right)}{\varepsilon^{0.4}(1-\varepsilon)^{1.7} \mu} \tag{5.15}$$

173

where,

$$N_{Re} = \frac{\rho U d}{\mu}$$

and $d = \bar{d}\left(1 + cv^2\right)$

then, Eqn. 17 can be re-expressed as

$$\frac{\Delta P}{LU} \frac{\varepsilon^3 d^2}{\mu(1-\varepsilon)^2} = K_1 + K_2 \frac{N_{Re}}{\varepsilon^{0.4}(1-\varepsilon)^{1.7}} \quad (5.16)$$

Since the viscous term was used in the denominator of Eqn. 5.16, the left hand side of

Eqn. 5.16 can then be defined as the ratio of pressure drop to the viscous energy term and

will be designated by f_v

$$f_v = \frac{\Delta P}{LU} \frac{\varepsilon^3 d^2}{\mu(1-\varepsilon)^2} \quad (5.17)$$

$$f_v = K_1 + K_2 \frac{N_{Re}}{\varepsilon^{0.4}(1-\varepsilon)^{1.7}} \quad (5.18)$$

According to Eqn. 5.18, a linear relationship exist between f_v and $\dfrac{N_{Re}}{\varepsilon^{0.4}(1-\varepsilon)^{1.7}}$

Similar to Eqn. 5.18, the Ergun version of the expression of ratio of pressure drop to the

viscous energy term is expressed as follows

$$f_{v-Ergun} = K_1 + K_2 \frac{N_{Re}}{1-\varepsilon} \quad (5.19)$$

It can be seen that Eqns. 5.18 and 5.19 are comparable because they are both related to

void fraction. Furthermore, when kinetic term was used in denominator of Eqn. 5.20, and

the left hand side can then be defined as the ratio of pressure drop to the viscous energy

term and will be designated by f_k

$$\frac{\Delta P}{LU} \frac{\varepsilon^{3.4} d\left(1 + cv^2\right)}{\rho_f U^2 (1-\varepsilon)^{0.3}} = K_1 \frac{(1-\varepsilon)^{1.7} \varepsilon^{0.4} \mu}{d\varphi(1+cv)\rho_f U} K_1 + K_2 \quad (5.20)$$

$$f_k = \frac{\Delta P}{LU} \frac{\varepsilon^{3.4} d\left(1 + cv^2\right)}{\rho_f U^2 \left(1 - \varepsilon\right)^{0.3}} \tag{5.21}$$

$$f_k = \frac{\varepsilon^{0.4} \left(1 - \varepsilon\right)^{1.7}}{N_{Re}} K_1 + K_2 \tag{5.22}$$

Similar to Eqn. 5.19, the Ergun version of the expression of ratio of pressure drop to the

kinetic energy term, f_k is expressed as follows

$$f_{k-Ergun} = K_1 \frac{1 - \varepsilon}{N_{Re}} + K_2 \tag{5.23}$$

Based on Eqn. 5.19, Ergun stated that a linear relationship existed between $f_{v\text{-Ergun}}$ and

$$\frac{N_{Re}}{1 - \varepsilon}$$

Therefore, a plot of all the data in Fig. 5.2 using Eqn. 5.19 should result in a single value

with intercept K_1 and slope K_2. Using Ergun's methodology, we plotted f_v against

$\dfrac{\rho U}{1 - \varepsilon}$ and this resulted in the plot shown in Fig 5.6. A fit of a linear equation to the data

presented in Fig 5.6 resulted in a negative intercept of -67.8. Ergun first assumption was

to recognize the additive effect of the viscous and kinetic energy losses in a packed bed

and the smooth transition from a viscous dominated to kinetic dominated effects as fluid

flow rate increased. In addition, it can be seen that the data fall on different lines with

respect to their screen sizes. Similar observation was made by Quinn (2014) who

attributed the inability to align all data on a single line using Ergun's procedure to the

imbalance created as a result of absence of diameter and viscosity terms as expected in

Eqn. 5.19.
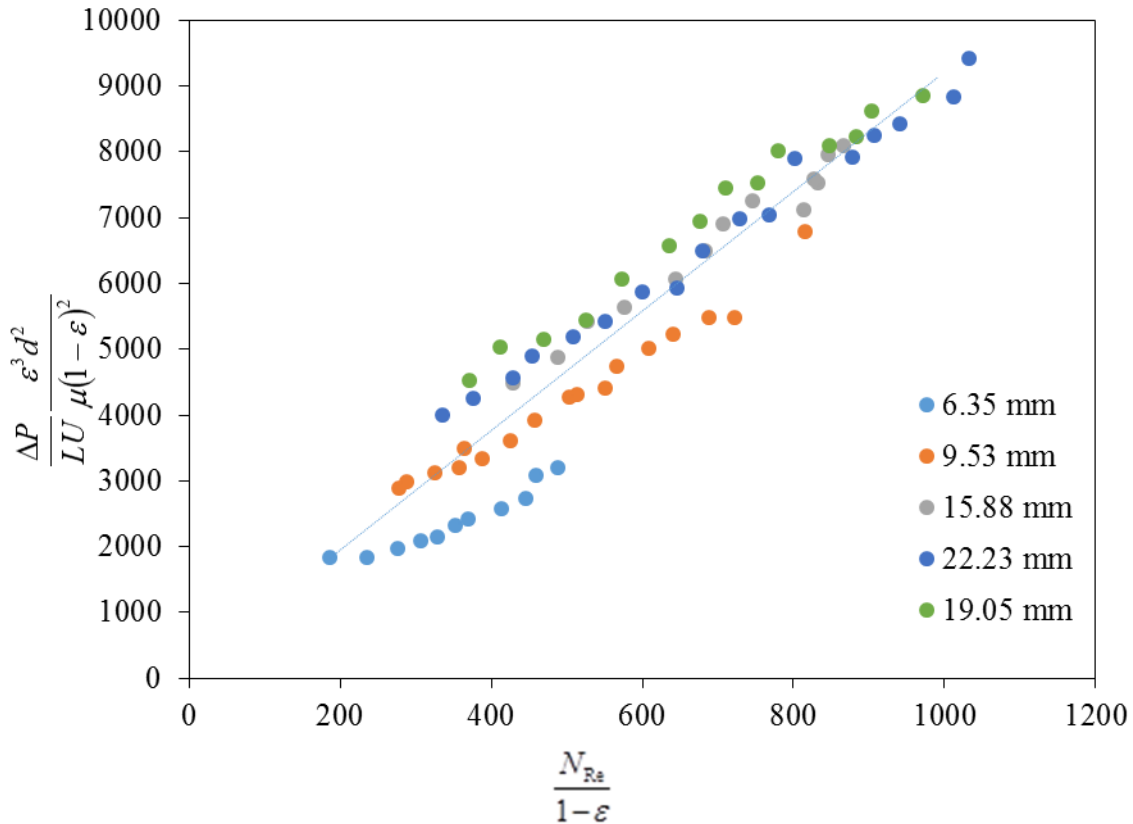
Figure 5.6: A general plot for a single system having different void fraction using Ergun's concept using chord diameter scheme.

When f_v was plotted against $\dfrac{N_{Re}}{\varepsilon^{0.4}(1-\varepsilon)^{1.7}}$ (Eqn. 5.18), Fig. 5.7 shows that all data

essentially fell on a straight line with R^2 value of 0.95 when chord diameter measurement

scheme was used. The plots for other diameter measurement scheme are presented in

appendix 5. From Fig 5.7, the estimated values $K_1 = 201.6$ and $K_2 = 2.7$. These K_1 and K_2

values are comparable to the values obtained by other author who had earlier remodified

Ergun equation reported (Table 5.3). Inserting the coefficient values into Eqn. 5.14

results in eqn. 5.24.

$$\frac{\Delta P}{L} = 201 \frac{(1-\varepsilon)^2}{\varepsilon^3 (d\varphi(1+cv^2))^2} \mu U + 2.7 \frac{(1-\varepsilon)^{0.3}}{\varepsilon^{3.4} d\varphi(1+cv^2)} \rho_f U^2 \qquad (5.24)$$
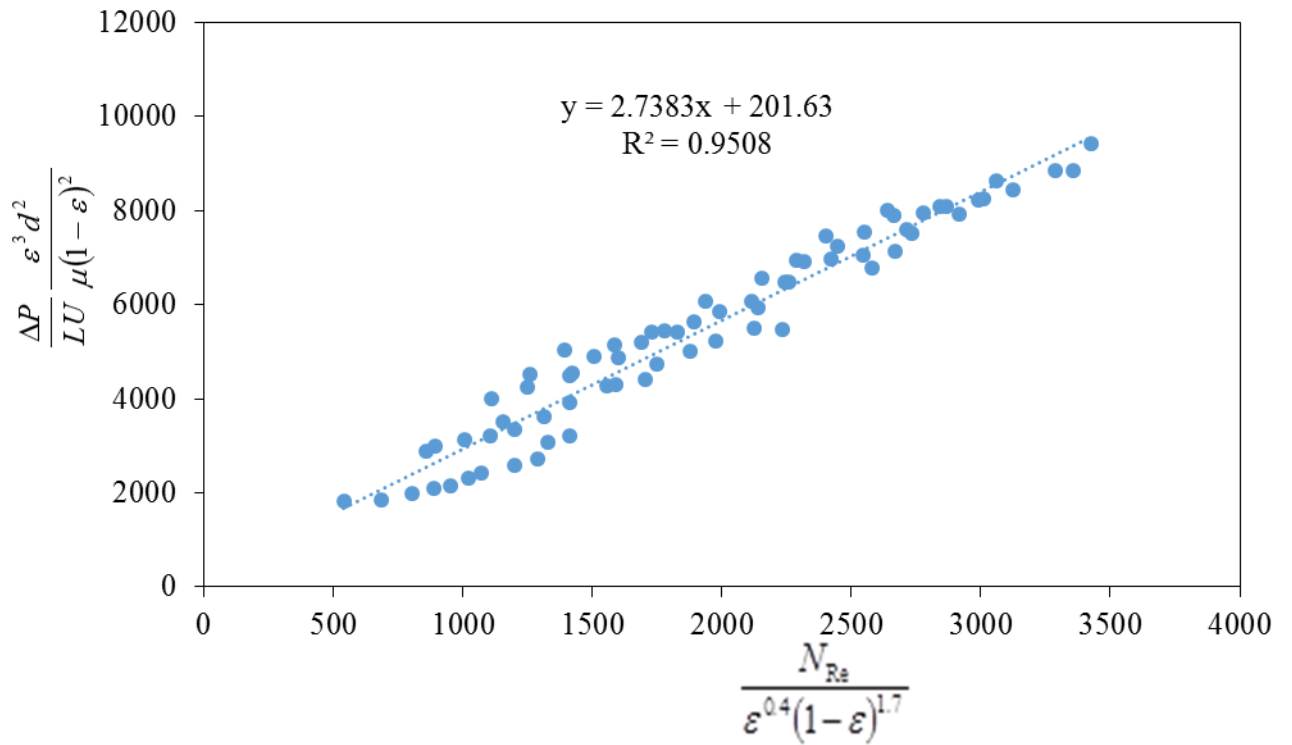
Figure 5.7: A general plot for a single system having different void fraction using chord diameter measurement scheme.

The chart shows $y = 2.7383x + 201.63$ with $R^2 = 0.9508$, with the y-axis labeled $\frac{\Delta P}{LU} \frac{\varepsilon^3 d^2}{\mu(1-\varepsilon)^2}$ and the x-axis labeled $\frac{N_{Re}}{\varepsilon^{0.4}(1-\varepsilon)^{1.7}}$.

Table 5.3: Comparison of K_1 and K_2 values with literature data

K_1	K_2		Reference
201.6	2.7	Ground loblolly pine wood	In this study
250	2.5	Polylobed particles	(Nemec and Levec, 2005)
160	1.61	Glass beads	(Ozahi et al., 2008)
160.4	2.8	Coal char	(Koekemoer and Luckos, 2015)
180	1.8	Literature data	(Macdonald et al., 1979)
250	2.5	γ-Al2O	Cloete et al. (2015)
267	2.14,	Leadshot, Glass beads and white	Quinn (2014)
	2.51,	sand	
	4.02		

From Eqn. 5.18, following Ergun's procedure the normalized viscous energy losses f_v can be expressed as

$$f_v = 201 + 2.7 \frac{N_{\mathrm{Re}}}{\varepsilon^{0.4}(1-\varepsilon)^{1.7}} \tag{5.25}$$

Similarly, the normalized kinetic energy losses f_k is shown in Eqn. 5.22 can now be re-expressed as

$$f_k = 201 \frac{\varepsilon^{0.4}(1-\varepsilon)^{1.7}}{N_{\mathrm{Re}}} + 2.7 \tag{5.26}$$

5.5   Model validation

5.5.1   Performance of equation by experimental pressure drop data

Validation of modified equation (Eqn. 5.26) was carried out by comparing the prediction obtained with Ergun equation expressed in Eqn. 5.27.

$$\frac{\Delta P}{L} = K_1 \frac{(1-\varepsilon)^2}{\varepsilon^3} \frac{\mu U_m}{\varphi^2 d_p^2} + K_2 \frac{1-\varepsilon}{\varepsilon^3} \frac{\rho_f U_m^2}{\varphi d_p} \qquad (5.27)$$

where, $\Delta P/L$ = pressure gradient across channel (Pa/m),

U_m = superficial velocity (m/s),

μ = fluid viscosity (Pa.s),

ρ_f = fluid density (kg/m^3),

ε = porosity,

d_p = particle diameter (m), and

φ = sphericity factor

A new set of loblolly pine wood chips were acquired with the initial moisture content were determined to be 9.45 % using ASTM standard E871-82 ASTM (2007). The chips were ground through hammer mill (Model No. 10HBLPK, Sheldon Manufacturing, Tiffin, OH) fitted with screen sizes 15.88 mm (5/8 inches), 12.7 mm, (1/2 inches), 9.53 (3/8 inches), 6.35 mm (1/4 inches), or 3.18 (1/8 inches). The physical properties of each these samples were determined as described Section 5.3 and the result of the physical properties is presented as follows;

Table 5.4: Physical properties of loblolly pine wood grinds used for validation

Screen size	Diameter (mm) Sur-vol.	Density kg/m^3 Particle	Bulk	Porosity	Sphericity	COV
15.8 mm	2.28[a]	1437.70[a]	275.38[c]	0.81[a]	0.45[a]	60.03[a]
(5/8 inches)	(0.30)	(4.97)	(2.62)		(0.003)	(4.49)
12.7 mm	2.04[a]	1436.40[a]	282.36[c]	0.80[a]	0.46[a]	60.52[a]
(½ inches)	(0.20)	(9.08)	(4.25)		(0.01)	(2.77)
9.53 mm	1.37[b]	1433.20[a]	297.85[b]	0.79[b]	0.46[a]	63.72[a]
(3/8 inches)	(0.16)	(10.33)	(10.43)		(0.01)	(4.37)
6.35 mm	0.79c	1422.30[ba]	311.14[ab]	0.78[c]	0.38[cb]	65.48[a]
(¼ inches)	(0.03)	(2.45)	(1.57)		(0.01)	(11.94)
3.18 mm	0.68 c	1426.83a	312.19[a]	0.78[c]	0.43[cb]	61.87[a]
(1/8 inches)	(0.01)	(4.93)	(0.88)		(0.01)	(2.42)

Values are means of triplicates experimental runs
Numbers in parentheses are standard deviation
Means with the different superscript (alphabet) in a column are significantly different (p<0.05)
Sauter means surface to volume mean diameter (calculated using 6/specific surface obtained from CamSizer®)
COV means coefficient of variations (calculated using Eqn. 5.3)

Fig 5.8 shows pressure drop per unit length against airflow velocity. The pressure drop increased as airflow velocity increased. Similar profile was obtained by Mayerhofer et al. (2011) who investigated pressure drop across a packed bed of irregular shaped wood particles and Li et al. (2015) who used sand bed materials. Fig 5.8 – 5.10, shows comparison between the experimental data and the predictions of pressure drop at various airflow velocities obtained from Ergun equation (Eqn. 5.2) (the Ergun expression used has sphericity term) and the equation developed in this study (Eqn. 5.24). Figure 5.9 shows that the prediction obtained when the loblolly pine wood was ground through 5/8 inches screen size was used. It can be seen that the predicting equations (Ergun and modified) under predicted the pressure drop at any air velocity. However, modified equation predictions were closer to experimental data. Similar profile was obtained from sample ground through ¼ inch screen size (Fig 5.9). However, in Fig. 5.11, modified equation over predicted the experimental data.
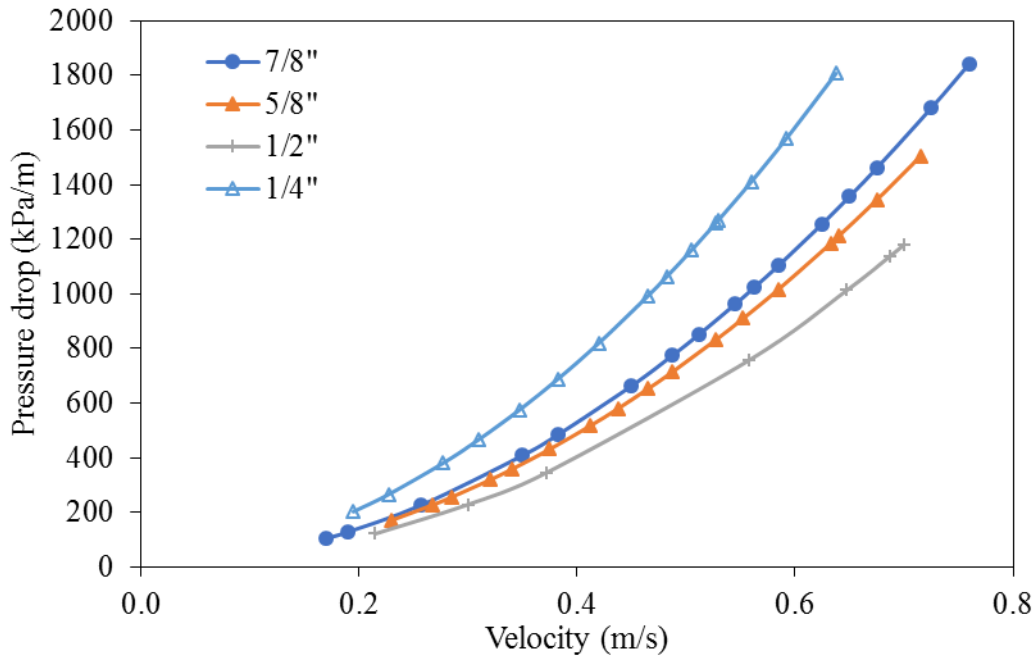
Figure 5.8: Pressure drop versus superficial velocity for loblolly pine wood grind.
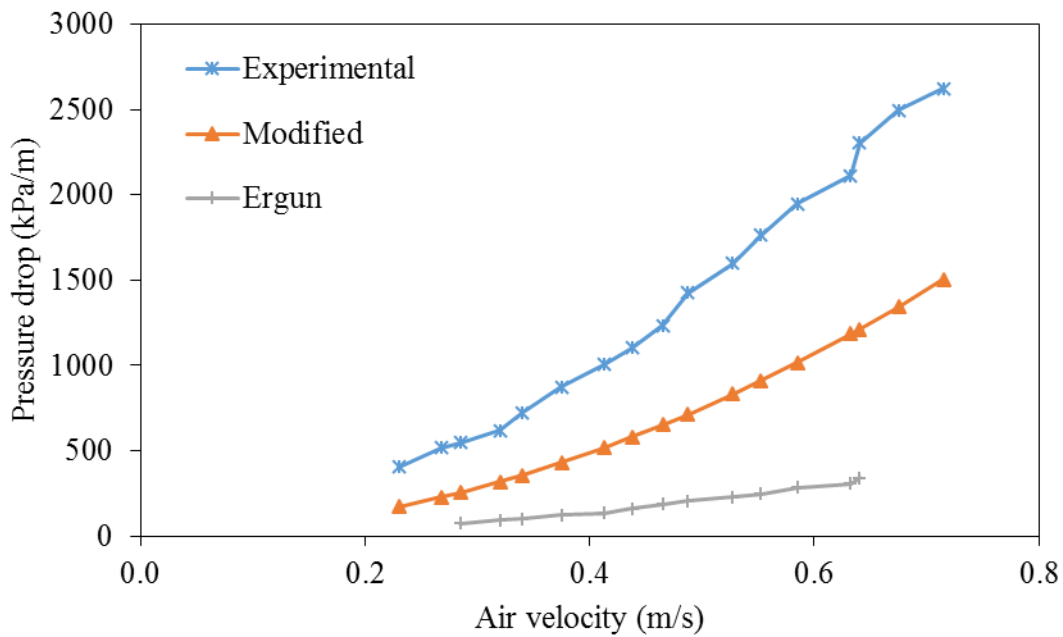
Figure 5.9: Performance comparison of Eqn. 5.1, 5.24 and experimental pressure drop data using ground loblolly pine wood ground through 5/8 inches screen size. Particle size 2.28×10^{-3}m, coefficient of variation of 0.65, sphericity factor of 0.45, and porosity of 0.81.
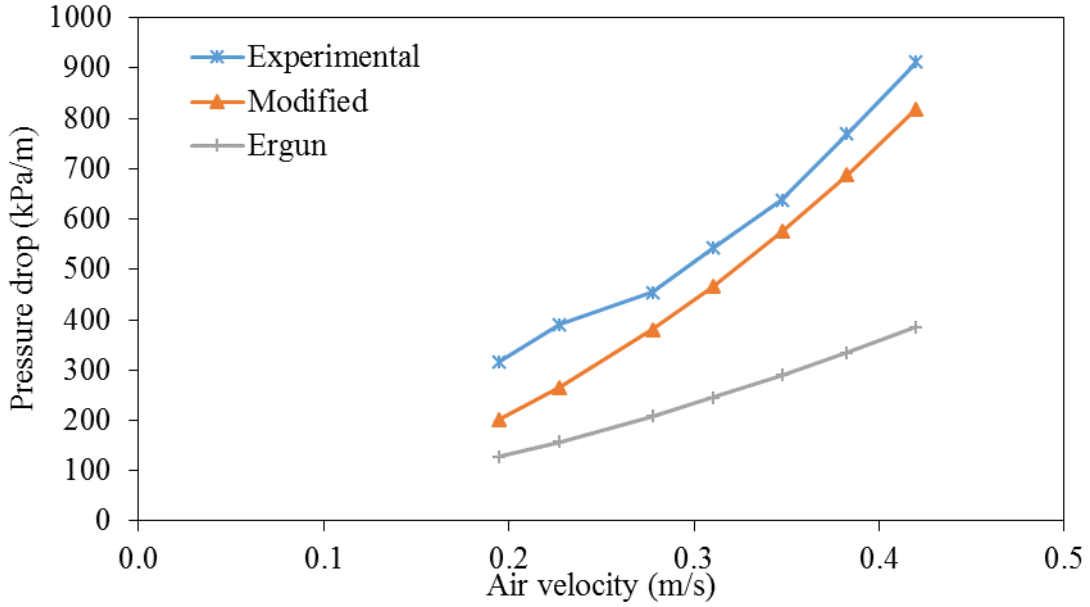
Figure 5.10: Performance comparison of Eqn. 5.1, 5.24 and experimental pressure drop data using equations with ground loblolly pine wood ground through 1/4 inches screen size. Particle size 1.4×10^{-3}m, coefficient of variation of 0.73, sphericity factor of 0.47, and porosity of 0.81
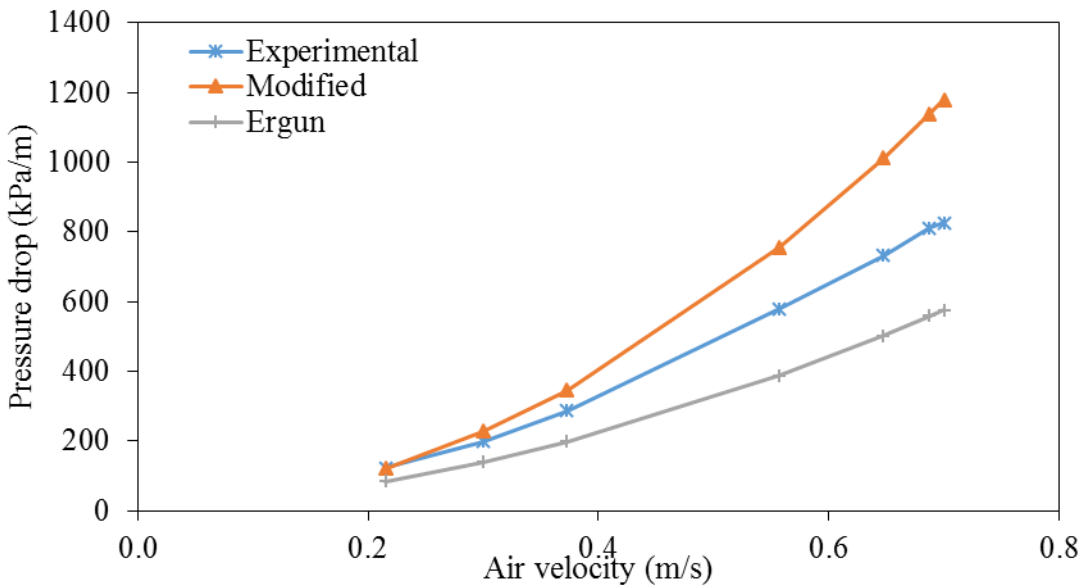
Figure 5.11: Performance comparison of Eqn. 5.1, 5.24, and experimental pressure drop data using ground loblolly pine wood ground through 1/2 inches screen size. Particle size 0.76×10^{-3} m, coefficient of variation of 0.60, sphericity factor of 0.46, and porosity of 0.80.

Table 5.5 showed the comparison between the predicted pressure drop and the experimental data set. Only the prediction obtained from grinding loblolly pine wood through ¼-inch screen size produced a MRD less than 20%. Hence, there is a need to tune up the modified equation for better prediction. However, comparing the relative mean deviation, from Table 5.5, the equation developed in this study improved capability to predict pressure drop of loblolly pine wood using Ergun equation concept. Although the MRD obtained were high (up to 50%), some authors also recorded similar high deviation between experimental and predicted pressure drop after refitting Ergun's equation for a particular material. For instance Nemec and Levec (2005) used neutral network approach to modify Ergun using material shaped into various geometry sphere (size ranged between 1.66 – 3.50 mm, porosity 0.4 – 0.44), cylinder (size ranged between 2.62 – 3.50 , porosity 0.32 – 0.68) and Quadralobes (size 2.13 porosity 0.47 – 0.50) and obtained MRD of 42.2, 20.6 and 60.0%. The author attributed it to sensitivity of the correlations for the Ergun on absolute particle size and bed porosities. Harrison et al. (2013) refitted Ergun's expression and obtained 119.8 for K_1 and K_2 to be 4.63 and author validated the equation over a wide range of Reynold numbers and tube-diameter to particle diameter ratio. The author reported an absolute mean relative deviation of up to 50.7 %.

Table 5.5: Comparison of the overall relative mean deviation between predicted and the experimental data

Screen size (inches)	Present study (%) Eqn. 5.24	Ergun Equation (%), Eqn. 5.27
1/4"	-18.4	-56.7
7/8"	-32.8	-76.9
3/4"	-31.2	-76.6
1/2"	44.1	-25.5
5/8"	-49.1	-81.8

5.5.2   Performance of equation for determination of minimum fluidization velocity

To verify the ability of equation 5.24 to predict U_{mf}, data presented in chapter 4 were used. The sample had varying initial moisture contents (see Table 4.1), particle sizes (Table 4.11), coefficient of variations (Table 4.10) sphericities (Table 4.5), bulk densities (Table 4.7), and particle densities (Table 4.8). The experimental data was used to estimate the U_{mf} of the samples 0.20, 0.24, 0.28 and 0.32 m/s for 8.40, 14.86, 19.80, 27.02 % MC wet basis. The predicted data is in appendix 5. The percent error between experimental and predicted U_{mf} obtained from Eqn. 5.24, Eqn. 5.2, and Eqn. 5.27 is presented in Table 5.6.

Table 5.6: Comparison of Eqn. 5.2, 5.24 and 5.27 for predicting the U_{mf}

Diameter measurement scheme	Experimental U_{mf} (m/s)	MRD (%)		
		Present study	Ergun	Ergun+
		Eqn. 5.24	Eqn. 5.2	Eqn. 5.27
Area	0.20	64.3	283.6	135.9
	0.24	31.5	197.2	104.1
	0.28	8.3	131.6	65.2
	0.32	18.0	131.7	60.0
Chord	0.20	50.1	242.3	54.8
	0.24	10.3	133.4	40.3
	0.28	-3.2	96.2	8.2
	0.32	7.8	103.6	5.0
Ferret	0.20	101.4	391.5	121.6
	0.24	59.0	280.3	133.4
	0.28	26.4	187.5	54.9
	0.32	38.5	187.3	41.8
Martin	0.20	32.2	190.1	29.5
	0.24	3.5	113.1	26.5
	0.28	-9.6	76.4	-2.5
	0.32	-0.8	79.9	-6.2
Surface-volume	0.20	3.4	106.7	-11.4
	0.24	-19.0	45.8	-17.6
	0.28	-19.0	47.5	-18.0
	0.32	-8.0	60.1	-15.8

+ Ergun equation with sphericity value

Generally, Ergun equation 5.2 (without sphericity factor) gave the highest MRD when

Area, chord, Ferret, and Martins diameter measurement scheme were used in the

equations. This confirms the inability of Ergun equation to predict minimum fluidization

velocity of non-spherical unless an adjustment is made. Furthermore, it can be seen that

using area, chord, Feret and Martins diameter measurement scheme in Eqn. 5.24 gave the

least overall mean relative deviation. Hence, the newly developed equation in this study improved the prediction of U_{mf}.

5.5.3 Conclusion

Ergun's equation has attracted the attention of several researchers since it was first developed. Some of the authors showed that the equation is best suited for uniformly sized particles while others concluded that the void fraction correlation, the coefficients (K_1 and K_2) and a term of introducing the effect of size distribution need to be carefully determined before Ergun's equation can be used for a bed consisting of non-uniform particles having non-spherical shape. In this study, we introduced a new concept of determining the void fraction correlation suitable for non-uniform particle size distribution. We also incorporated coefficient of variation to capture the effect of particle distribution. Accordingly, we estimated a new coefficient K_1 and K_2 to be 201.6 and 2.7 respectively. We also proposed new frictional loss equation using ground loblolly pine wood. The result showed that the new equation resulted in lower overall mean relative deviation of pressure drop data compared with original Ergun equation. Also, when predicting the minimum fluidization velocity, lower mean relative deviation were obtained varied with the diameter measurement scheme used.

5.6 Reference

Abrahamsen, A., and D. Geldart. 1980. Behaviour of gas-fluidized beds of fine powders part I. Homogeneous expansion. *Powder Technology* 26(1):35-46.

Anderson, S., and F. Warburton. 1949. 46—The porous plug and fibre diameter measurement. Effect of fibre orientation and use of plugs of randomized fibres. *Journal of the Textile Institute Transactions* 40(11):T749-T758.

ASTM. 2007. Standard test methods for direct moisture content measurement of wood and wood-base materials. American Society for Testing Materials. ASTM International West Conshohocken, PA.

Bouwman, A. M., J. C. Bosma, P. Vonk, J. A. Wesselingh, and H. W. Frijlink. 2004. Which shape factor(s) best describe granules? *Powder Technology* 146(1–2):66-72.
Çarpinlioğlu, M. Ö., and E. Özahi. 2008. A simplified correlation for fixed bed pressure drop. *Powder Technology* 187(1):94-101.

Cloete, S., S. T. Johansen, and S. Amini. 2015. Grid independence behaviour of fluidized bed reactor simulations using the Two Fluid Model: Effect of particle size. *Powder Technology* 269(0):153-165.

Das, M., B. C. Meikap, and R. K. Saha. 2008. Characteristics of axial and radial segregation of single and mixed particle system based on terminal settling velocity in the riser of a circulating fluidized bed. *Chemical Engineering Journal* 145(1):32-43.

Dolejs, V., and I. Machac. 1995. Pressure drop during the flow of a Newtonian fluid through a fixed bed of particles. *Chemical Engineering and Processing: Process Intensification* 34(1):1-8.

Ergun, S. 1951. Determination of Particle Density of Crushed Porous Solids. *Analytical Chemistry* 23(1):151-156.

Ergun, S. 1952. Fluid flow through packed columns. *Chem. Eng. Prog.* 48:89-94.
Formisani, B., R. Girimonte, and V. Vivacqua. 2011. Fluidization of mixtures of two solids differing in density or size. *AIChE Journal* 57(9):2325-2333.

Geldart, D. 1972. The effect of particle size and size distribution on the behaviour of gas-fluidised beds. *Powder Technology* 6(4):201-215.

Gil, M., D. Schott, I. Arauzo, and E. Teruel. 2013. Handling behavior of two milled biomass: SRF poplar and corn stover. *Fuel Processing Technology* 112(0):76-85.

Gunarathne, D. S., J. K. Chmielewski, and W. Yang. 2014. Pressure drop prediction of a gasifier bed with cylindrical biomass pellets. *Applied Energy* 113(0):258-266.

Harrison, L. D., K. M. Brunner, and W. C. Hecker. 2013. A Combined Packed-Bed Friction Factor Equation: Extension to Higher Reynolds Number with Wall Effects. *AIChE Journal* 59(3):703-706.

Hatch, L. P. 1943. Flow of fluids through granular material: Filtration, expansion, and hindered settling. *Eos, Transactions American Geophysical Union* 24(2):536-547.

Hoffmann, A., L. Janssen, and J. Prins. 1993. Particle segregation in fluidised binary mixtures. *Chemical Engineering Science* 48(9):1583-1592.

Hrenya, C. M., and J. L. Sinclair. 1997. Effects of particle-phase turbulence in gas-solid flows. *AIChE Journal* 43(4):853-869.

Innocentini, M. D., V. R. Salvini, A. Macedo, and V. C. Pandolfelli. 1999. Prediction of ceramic foams permeability using Ergun's equation. *Materials Research* 2(4):283-289. ISO/9276-6.2008.9276-6: Representation of results of particle size analysis -- Part 6: Descriptive and quantitative representation of particle shape and morphology. Geneva: International Organization for Standardization.

Jing, S., Q. Hu, J. Wang, and Y. Jin. 2000. Fluidization of coarse particles in gas–solid conical beds. *Chemical Engineering and Processing: Process Intensification* 39(4):379-387.

Kim, J., and G. Y. Han. 2006. Effect of agitation on fluidization characteristics of fine particles in a fluidized bed. *Powder Technology* 166(3):113-122.

Koekemoer, A., and A. Luckos. 2015. Effect of material type and particle size distribution on pressure drop in packed beds of large particles: Extending the Ergun equation. *Fuel* 158(0):232-238.

Kumar, A., and P. SenGupta. 1974. Prediction of minimum fluidization velocity for multicomponent mixtures. 225-227. Council Scientific Industrial Research Publ & Info Directorate, New Delhi 110012, India.

Lam, P., S. Sokhansanj, X. Bi, C. Lim, T. JayaShankar, G. Rezaie, and L. Naimi. 2008. The Effect of Particle Size and Shape on Physical Properties of Biomass Grinds. In *An ASABE Meeting Presentation. Paper*.

Leva, M., M. Weintraub, M. Grummer, M. Pollchik, and H. Storch. 1951. *Fluid flow through packed and fluidized systems*. US Government Printing Office.

Li, L., X. Zou, J. Lou, H. Li, and X. Lei. 2015. Pressure drops of single/two-phase flows through porous beds with multi-sizes spheres and sands particles. *Annals of Nuclear Energy* 85(0):290-295.

Lippens, B. C., and J. Mulder. 1993. Prediction of the minimum fluidization velocity. *Powder Technology* 75(1):67-78.

Liu, X., G. Xu, and S. Gao. 2008. Fluidization of extremely large and widely sized coal particles as well as its application in an advanced chain grate boiler. *Powder Technology* 188(1):23-29.

Luckos, A., and J. R. Bunt. 2011. Pressure-drop predictions in a fixed-bed coal gasifier. *Fuel* 90(3):917-921.

Macdonald, I., M. El-Sayed, K. Mow, and F. Dullien. 1979. Flow through porous media-the Ergun equation revisited. *Industrial & Engineering Chemistry Fundamentals* 18(3):199-208.

Mawatari, Y., Y. Tatemoto, and K. Noda. 2003. Prediction of minimum fluidization velocity for vibrated fluidized bed. *Powder Technology* 131(1):66-70.

Mayerhofer, M., J. Govaerts, N. Parmentier, H. Jeanmart, and L. Helsen. 2011. Experimental investigation of pressure drop in packed beds of irregular shaped wood particles. *Powder Technology* 205(1):30-35.

Nemec, D., G. Berčič, and J. Levec. 2001. The hydrodynamics of trickling flow in packed beds operating at high pressures. The relative permeability concept. *Chemical Engineering Science* 56(21–22):5955-5962.

Nemec, D., and J. Levec. 2005. Flow through packed bed reactors: 1. Single-phase flow. *Chemical Engineering Science* 60(24):6947-6957.

Obata, E., H. Watanabe, and N. Endo. 1982. Measurement of size and size distribution of particles by fluidization. *Journal of Chemical Engineering of Japan* 15(1):23-28.

Ozahi, E., M. Y. Gundogdu, and M. Ö. Carpinlioglu. 2008. A Modification on Ergun's Correlation for Use in Cylindrical Packed Beds With Non-spherical Particles. *Advanced Powder Technology* 19(4):369-381.

Quinn, H. M. 2014. A Reconciliation of Packed Column Permeability Data: Deconvoluting the Ergun Papers. *Journal of Materials* 2014.

Reina, J., E. Velo, and L. Puigjaner. 2000. Predicting the minimum fluidization velocity of polydisperse mixtures of scrap-wood particles. *Powder Technology* 111(3):245-251.
Rhodes, M. 2008. *Introduction to particle technology*. Wiley.

Rowe, P. N., and A. W. Nienow. 1975. Minimum fluidisation velocity of multi-component particle mixtures. *Chemical Engineering Science* 30(11):1365-1369.

Ryu, C., Y. B. Yang, A. Khor, N. E. Yates, V. N. Sharifi, and J. Swithenbank. 2006. Effect of fuel properties on biomass combustion: Part I. Experiments—fuel type, equivalence ratio and particle size. *Fuel* 85(7–8):1039-1046.

SAS. 2011. *The SAS system for Windows.* Ver. Release 9.2. Cary, NC.: SAS Institute.

Seu-Kim, H., and H. Arastoopour. 1995. Simulation of FCC particles flow behavior in a CFB using modified kinetic theory. *The Canadian Journal of Chemical Engineering* 73(5):603-611.

Wang, L. 2014. *Sustainable bioenergy production*. CRC Press.

Wen, C. Y., and Y. H. Yu. 1966. A generalized method for predicting the minimum fluidization velocity. *AIChE Journal* 12(3):610-612.

Zhang, Y., B. Jin, and W. Zhong. 2008. Fluidization, mixing and segregation of a biomass-sand mixture in a fluidized bed. *International Journal of Chemical Reactor Engineering* 6(1).

Zhang, Y., B. Jin, and W. Zhong. 2009. Experimental investigation on mixing and segregation behavior of biomass particle in fluidized bed. *Chemical Engineering and Processing: Process Intensification* 48(3):745-754.

Zhong, W., X. Li, G. Tao, and T. Kagawa. 2015. Measurement and Determination of Friction Characteristic of Air Flow through Porous Media. *Metals* 5(1):336-349.

Chapter 6: CFD modeling of ground Loblolly Pine Wood fluidization

6.1   Abstract

This study, the CFD modeling of solid –gas fluidized bed was performed using Eulerian –Lagrangian frame work with Dense Discrete Phase Model. The simulation was carried out using CFD commercial software package, Fluent ANSYS. The validation was carried out using a bench scaled fluidized bed set up of 0.101 m internal diameter and 1.5 m height. The interface exchange drag laws (Gidaspow, Syamlal-Obrien, Wen & Yu and non-spherical) was evaluated for a bed consisting of particles similar to ground loblolly pine wood that was ground using hammer mill fitted with 3.2 mm screen size. The modeling was carried out at velocities ranging between 0.04 m/s to 1.2 m/s which covers the velocity ranges at which biomass grinds have the minimum and complete fluidization. For a particular case, pressure drop across the bed against time and void fraction against time were plotted. The result showed that non-spherical drag law predicted the minimum fluidization velocity. There was a need to modify other drag law before a good prediction of U_{mf} can be obtained. The body force correlation applied improved the non-spherical drag law while other drag law showed little impact. It was also observed that bed entrainment occurred for all drag law at 2 sec simulation time. Review of several simulations case revealed differences between experimental and predicted, which further proved that the drag laws must be modified before it can be used for ground biomass.

Nomenclature

C_D	Drag coefficient
ε_s	Void fraction of solid in dense phase
ε_g	Void fraction of gas in dense phase
ρ_g	Gas/ fluid density (kg m^{-3})
ρ_s	Solid density (kg m^{-3})
d_s	Particle diameter (m)
$\vec{v}_g$	Superficial fluid velocity (m/s)
$\vec{v}_s$	Superficial solid velocity (m/s)
f	Drag function
Re_s	Reynold number based on solid fraction
k_{sg}, β	Momentum exchange coefficient (kg m^{-3}s^{-1})
μ_g	Viscosity of gas (Pa s)
$v_{r,s}$	Terminal velocity of solid (m/s)
Re_{sph}	Reynold computed with the diameter of a sphere having the same volume.
m	Mass of particle (kg)
dt	Time step (s)
$\overline{F}_{drag}$	Drag force (N)
$\overline{F}_{pressure}$	Pressure force (N)
$\overline{F}_{virtual\_mass}, \vec{F}_{vm,g}$	Virtual mass force (N)
$\overline{F}_{gravitation}, \vec{F}_{lift,g}$	Gravitational force (N)
$\vec{F}_{td,g}$	Turbulent dispersion force based on fluid phase (N)
$\overline{F}_{others}$	Other force e.g. body force (N)
$F_{friction}$	Frictional force (N)
F_{normal}	Normal force (N)
S_g	Fluid phase source term
S_s	Solid phase source term
∇p	Pressure shared by all phases (N m^{-2})
$\overline{\tau}_g$	Fluid phase stress-strain tensor (N m^{-2})
τ_s	Particle relaxation time (s)
$\vec{g}$	Gravitational acceleration (9.81 m s^{-2})
$\vec{F}_s$	Solid phase drag force
∇p_s	Solid pressure (N/ m^{-2})
$\vec{a}_s$	Particle acceleration (m/s)
subscripts	
g, s	Gas & solid phase

6.2 Introduction

Despite the popularity of fluidized bed technology, detailed understanding of particle flow behavior during fluidized bed gasification has been limited. This can be attributed to the harsh operating environments of a typical fluidization system (e.g. high pressure, high temperature, and dusty environment) that make physical and quick examination of the state of the bed very challenging, expensive and complicated (Cloete et al., 2015). Another reason is the biomass feedstock with particles that are non-uniform and non-spherical. With advances in technology, computer models such as computational fluid dynamics (CFD) can be used to explore and optimize the behavior of these particles in a fluidized state thereby minimizing the requirement for elaborate experimental setup (Li et al., 2014; Zhang et al., 2008).

Biomass grinds typically have non-uniform size distribution and the shapes of the grinds are not spherical as illustrated in Chapters 3, 4 and 5. The grinds are obtained feedstock that come from diverse sources having varying moisture contents (Chapter 4). These properties have dramatic effect on the overall behavior of particulate flow thereby makes modeling process very challenging (Rao et al., 2011; Wang et al., 2014). Unfortunately, researchers have disregarded these unique properties of biomass grinds, and computationally modeled a fluidizing bed as one consisting of particles that are uniform and spherical, even though particle – particle collision, particle – fluid interaction and particle to wall collision of spherical and uniformly sized particles are significantly different to that of non-spherical and non-uniformly sized particles.

Drag equations are typically used to study and simulate solid-solid and solid-fluid interactions. For instance Louge et al. (1991) investigated the interaction within particles

of uniform diameter in a solid-gas system and develop a numerical scheme for exchange

of momentum when particles collide with one another and between the particle and the

wall. Similarly, Hrenya and Sinclair (1997) investigated the interaction between particles

and interaction associated with collective motion of particles in a dense gas-solid flow

using two models. In the first model, the governing equations (force, momentum, and

continuity) were used to quantify the effect of particle phase on bed turbulence. In the

second model, the kinetic theory equations were used. The author found that laminar flow

contribution to solid-phase pressure was greater than turbulent flow contribution. This

effect was attributed to excessive sensitivity of particle phase to inelastic particle –

particle collisions in which a single-phase turbulent constant was used to describe the

phenomena of particle phase turbulence. In addition, the author concluded that first

model failed to adequately describe the behavior of gas-solid flows, while the second

predicted particle segregation and other salient features associated with such flows.

Owing to these limitations, several researchers have summarized that governing

equations alone cannot be used to describe particle- particle-fluid interaction (Pei et al.,

2012; Van Wachem et al., 2001; Yasuna et al., 1995).

Generally, the drag force acting on a particle in a fluid-solid system can be represented by

the product of a momentum transfer coefficient (β) and the slip velocity between the fluid

and solid phases $\vec{v}_g - \vec{v}_s$ (Eqn.1):

$$F_{drag} = \beta\left(\vec{v}_g - \vec{v}_s\right) \tag{6.1}$$

$$\beta = \frac{3}{4}C_D \frac{\varepsilon_s \rho_g}{d_s}\left|\vec{v}_g - \vec{v}_s\right| f\left(\varepsilon_g\right)\left(\vec{v}_g - \vec{v}_s\right) \tag{6.2}$$

However, experimental determinations of relative velocity between two phases are difficult to measure in a laboratory setting (Fig. 6.1). Hence, researchers rely on empirically correlations of drag force in computing particle-particle and particle wall interactions. When a bed consist of a single particles (Fig. 6.1a), high tech velocimetry imaging technology can be used to study particle location as function of time in a known fluid velocity. Also, when particle consist of many uniformly sized particles, an average displacement can also be used to quantify the displacement at a given velocity and time (Kumar et al., 2011). However, for a non-uniform size distribution particles, determining particle location as a function to time in a fluid flow is problematic (Fig 6.1b) because particle displacement are significantly affected by particle size and density.
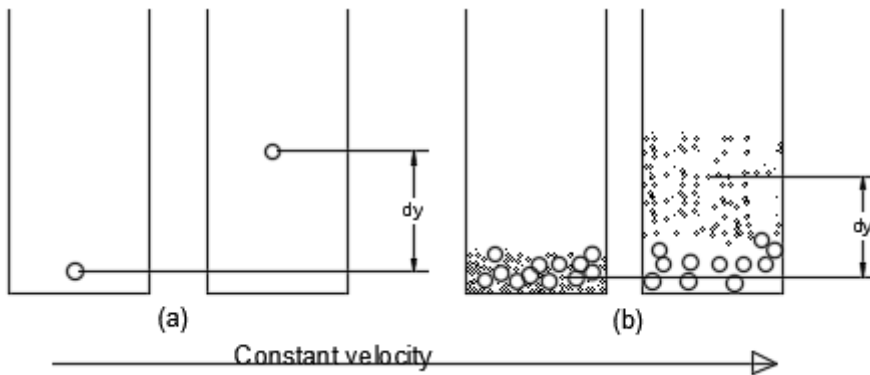
Figure 6.1: Effect of particle size distribution on solid velocity measurement

Vejahati et al. (2009) developed correlations for β by using two types of experimental data and verifying them using multi-fluid model in Fluent. The first type developed for packed bed with high solid volume fractions, uses the packed-bed pressure drop data to derive a drag function. This is similar to Ergun (1952) expression. In the second set of data, the terminal velocity of the particle in fluidized bed was employed to derive the

drag function similar to the model of Richardson and Zaki (1954). For both models, drag, β, obtained was a function of void fraction[3].

One of the most widely used drag correlation in CFD simulation of gas-solid fluidized beds is the Ergun-Wen-Yu model (Gidaspow, 1986) popularly called Gidaspow model (Benzarti et al., 2012; Pei et al., 2012; Ye et al., 2005). This is the combination of two equations but used at different simulation conditions. The Wen and Yu[4] correlations (Wen and Yu, 1966) is used to calculate the drag when the porosities are higher than 0.8 (Eqn. 6.3) and the well-known Ergun equation (Ergun, 1952) is employed for porosities less than 0.8 (Eqn. 6.5)

$$\beta = \frac{3\varepsilon_s \varepsilon_g \rho_g}{4d_s} C_D \left| \vec{v}_s - \vec{v}_g \right| \varepsilon_g^{-2.65}, \qquad \varepsilon_g > 0.8 \tag{6.3}$$

$$C_D = \frac{24}{\varepsilon_g \operatorname{Re}_s} \left[1 + 0.15 \left(\varepsilon_g \operatorname{Re}_s \right)^{0.687} \right] \tag{6.4}$$

$$\beta = 150 \frac{\varepsilon_s \left(1 - \varepsilon_g \right) \mu_g}{\varepsilon_g d_s^2} + 1.75 \frac{\rho_g \varepsilon_s \left| \vec{v}_s - \vec{v}_g \right|}{d_s}, \quad \varepsilon_g \leq 0.8 \tag{6.5}$$

Where

$$\operatorname{Re}_s = \frac{\varepsilon_g \rho_g d_p \left| v_p - v_g \right|}{\mu_g} \tag{6.6}$$

Furthermore, Syamlal and O'Brien (1988) developed a drag correlation based on a single spherical particle in a fluid, and with modified relative velocity (*f*), which is the terminal settling velocity of a particle in a system divided by the terminal settling velocity of a single sphere given by Garside and Al-Dibouni (1977). The author assumed that the

---

[3] Most of the available drag functions are related to void fraction of the bed.

[4] Definition of the parameters in this equation and other equation are presented in the table of nomenclature

Archimedes number in a single particle and multi-particle system are the same and can be represented by

$$f = \frac{C_D \, \text{Re}_s \, \varepsilon_g}{24 v_{r,s}^2} \tag{6.7}$$

$$C_D = \left[0.63 + \frac{4.7}{\sqrt{\text{Re}_s / v_{r,s}}} \right]^2 \tag{6.8}$$

$$\beta = \frac{3 \varepsilon_s \varepsilon_g \rho_g}{4 v_{r,s}^2 d_s} C_D \left(\frac{\text{Re}_s}{v_{r,s}} \right) \left| \vec{v}_s - \vec{v}_g \right| \tag{6.9}$$

$$v_{r,s} = 0.5 \left(A - 0.06 \,\text{Re}_s + \sqrt{\left((0.06 \,\text{Re}_s)^2 + 0.12 \,\text{Re}_s (2B - A) + A^2 \right)} \right) \tag{6.10}$$

$$\text{Where,} \, \text{Re}_s = \frac{\rho_g d_s \left| \vec{v}_s - \vec{v}_g \right|}{\mu_g}$$

$$A = \varepsilon_g^{4.14}$$

$$B = 0.8 \varepsilon_g^{1.28} \qquad \varepsilon_g \leq 0.85$$

$$B = \varepsilon_g^{2.65} \qquad \varepsilon_g > 0.85$$

In the three previously discussed drag laws correlation, it is clear that particle shape and particle size distribution were not taken into consideration. For instance, non-spherical particles rotation is different from spherical particle during transport (Chen et al., 2012) Non-spherical drag equation such as that given by Haider and Levenspiel (1989) can be employed for particles with irregular shapes.

$$C_D = \frac{24}{Re_{sph}}\left(1 + b_1 \, Re_{sph}^{b_2}\right) + \frac{b_3 \, Re_{sph}}{b_4 + Re_{sph}}$$ (6.11)

where, $b_1 = \exp\left(2.3288 - 6.4581\varphi + 2.4486\varphi^2\right)$

$b_2 = 0.0964 - 0.5565\varphi$,

$b_3 = \exp\left(4.905 - 13.8944\varphi + 18.4222\varphi^2 - 10.2599\varphi^3\right)$,

$b_3 = \exp\left(1.4681 - 12.2584\varphi + 20.7322\varphi^2 - 15.8855\varphi^3\right)$

The shape factor φ, is defined as

$$\varphi = \frac{s}{S}$$

where,

s, the surface area of a sphere having the same volume as the particle
S is the actual surface area of the particle.
Re_{sph} is the Reynolds number computed with the diameter of a sphere having the same volume.

Despite the abundance of various kinds of drag model in literature (Clift et al., 1978; Huilin and Gidaspow, 2003; Morsi and Alexander, 1972; Syamlal and O'Brien, 1989; Takamasa and Tomiyama, 1999), Vejahati et al. (2009) reported that care must be taken in selecting a drag model for fluidized bed simulation. In fact, almost all available studies dealt with Eulerian –Eulerian model that is incapable of handling particle with wide size distribution and incapable of estimating the trajectories/collision of particles at a given time. In addition, comparative studies of the appropriateness of various drag laws on CFD modeling fluidize bed consisting of non-uniform particle size distribution with irregular particle shapes using Eulerian – Lagrangian with DDPM framework is lacking in literature. The objective of this work is to determine the appropriateness of drag laws

198

that are available in FLUENT 14.5 (FLUENT, 2012) for a 3-D bed consisting of non-spherical particles having particle sizes that are log-normal distribution such as the typical distribution for biomass grinds. In addition, the study proposed a body force correlation that can be incorporated into the existing drag law model to improve prediction and simulation of gas –solid fluidization of biomass grinds.

6.3   Simulation steps and procedure

6.3.1   Simulation condition

The multiphase flow (solid – gas) in a fluidized bed is classified as turbulent, 3D system in which the gas/fluid phase is considered continuous (primary) and solid phase is regarded as secondary (FLUENT, 2012). This simulation was modelled after a bench scale fluidized system with internal diameter of 101.6 mm and height of 1400 mm. The system consists of velocity inlet, pressure outlets, and the stationary wall. At the inlet, the distributor serves as the solid support boundary in which the solid cannot cross this boundary. The whole system was modeled as a plane cylindrical block having the bed height along the z- axis (Fig. 6.2). The ground particles was injected into the bed chamber (Fig. 6.2 a), where there is an airflow modeled as a laminar or turbulent depending on the velocity. In addition, the fluidized bed was not modeled as having a central axis (symmetric flow) because the particles may be forced to obey the centerline axis and affect particle flow and behavior. As the particles fluidize, when velocity is sufficiently high to entrain a particle out of the bed and reach the outlet boundary, then the particle is allowed to be discharged.
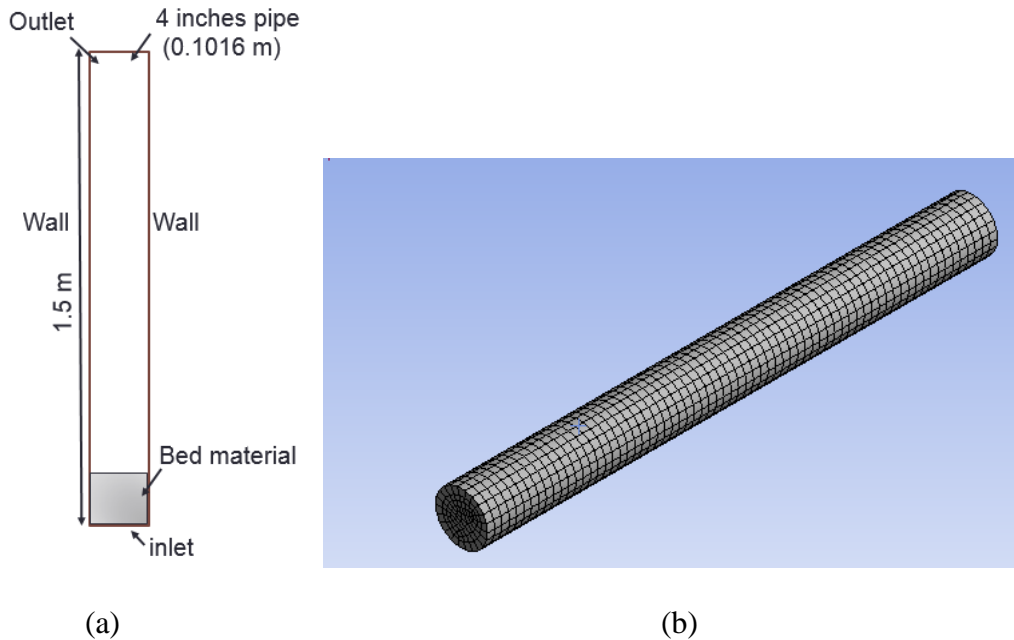
Figure 6.2: Schematic diagram of the fluidized bed and 3-D mesh (Cells (33728), Faces (103608), and Nodes (36305)) used for simulation.

In order to perform a simulation for a particular case, multiphase Eulerian model was first selected, then Dense Discrete Phase Model was activated as the Eulerian parameters while the segregated implicit unsteady solver was selected (Wei et al., 2007) for volume fraction parameter. After this, k- ε turbulent equation from the viscous model was selected using Fluent default parameters (C1-Epsilon 1.44, C2-Epsilon 1.92, and C-viscous 0.09). At this time, the Discrete Phase (DPM) model was automatically turned on. Inside the DPM panel, the number of continuous phase iteration per DPM iteration is set to 200 (FLUENT, 2012). The unsteady particle tracking at particle treatment was activated and particle injection was set at flow fluid time step of 0.002 ms and the default collision coefficient values for fluidized bed were used (Table 6.1) (FLUENT, 2012). These procedures explained are FLUENT ANSYS DPPM + DEM standard steps.

Table 6.1: Discrete event collision setting parameter

Contact law	Constants
Spring-dashpot, k	100
Friction dashpot	0.5
μ_{sticks}	0.5
μ_{glide}	0.2
μ_{limit}	0.1

Where

μ_{sticks} is the sticking friction coefficient

μ_{glide} is the gliding friction coefficient

μ_{glide} is the gliding velocity

6.3.2   Particle size determination and particle injection file

Loblolly pine wood chips were obtained from a forest plantation in Alabama, U.S. The

chips were ground using a hammer mill (Model 358, New Holland, Pa.) fitted with 3.18

mm diameter round holes screen. After grinding, the moisture content of the sample was

determined, using ASTM standard E871-82 ASTM (2007) procedure, to be 8.45 % wet

basis. A particle size analyzer (Fig 6.3a) (Camsizer®, Retsch Technology, Haan,

Germany) was used to obtain particle size (based on chord diameter measurement

scheme) distribution in the form of cumulative particle size distribution plot (Fig 6.3 b).

In addition, the mean sphericity of the particles was extracted from the software of the

system. The cumulative distribution plot was subsequently converted to an injection file

using a python program (the python code is proprietary program provided by ANSYS

Fluent support). Table 6.2 shows the summary distribution characteristics of injected

particles.

(a) Camsizer: Particle size analyzer. (b) Cumulative distribution of particles
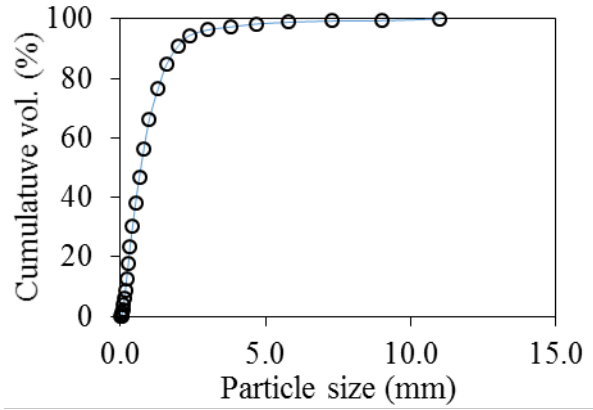
Figure 6.3: Particle size analysis and cumulative distribution plot of ground loblolly pine wood.

Table 6.2: Distribution characteristics of injected particle obtained from FLUENT®

Particle characteristics	Values
Total number of parcels	40824
Total number of particles	1.3e+08
Total mass	200 g
Overall RR Spread Parameter	1.1
Maximum Error in RR fit	0.041
Overall RR diameter (D_RR)	0.00091 mm
Maximum RMS distance from injector	0.23 mm
Maximum particle diameter	0.11 mm
Minimum particle diameter	0.000048 mm
Overall mean diameter (D_{10})	0.00011 mm
Overall mean surface area (D_{20})	0.00015 mm
Overall mean volume (D_{30})	0.00022 mm
Overall surface diameter(D_{21})	0.00020 mm
Overall volume diameter(D_{31})	0.00031 mm
Overall Sauter diameter(D_{32})	0.00048 mm
Overall De Brouckere diameter (D_{43})	0.0011 mm

202

6.3.3 Governing equations and mathematical model

The Eulerian-Lagrangian with Dense Discreet Phase model was used to simulate and analyze the flow in the fluidized solid- air system. This was achieved by solving the set of governing momentum and continuity equations for each phase (solid and fluid) and coupling the two phases through pressure and interphase exchange coefficients. The solid gas-solid interphase exchange coefficient was declared as a function of drag force. In addition, optional body forces are coupled to the drag force in Fluent. The body forces are localized forces on individual particles which the standard drag did not consider e.g. virtual mass and lift (FLUENT, 2012). In order to consider virtual mass as a body force, the density of the fluid must approach or exceed the density of the particles. In this case, the ratio of solid density to fluid density was greater than 1000. Therefore the virtual mass effect is insignificant (FLUENT, 2012; Rajeswari et al., 2011). Lift force is used for submicron particles and often cause significant convergence problems (FLUENT, 2012), thus inclusion of lift force was neglected. Body forces are typically applied to particle with initial void fractions less than 0.6 with the assumption that particles with high void fraction (void > 0.8) are not expected to have body forces application in Fluent. Therefore, in order to obtain a reliable solution from simulation of biomass grinds with void fraction that approximate to 0.8, this study present a void body force correlation. The procedure used to capture the effect of body force using biomass grinds is discussed in the next section. The body force developed was integrated into the Eulerian-Lagrangian DDPM model for gas- solid (Eqn. 6.11– 20 Table 6.3). These equations were chosen from the FLUENT CFD software, based on the aforementioned assumptions, as they are found most suitable for modeling multiphase flow which consists of a primary

continuous phase (air) and a secondary phase (solid biomass) dispersed within the

continuous phase.

Table 6.3: Governing equations and constitutive law of Eulerian Lagrangian, DDPM
model for gas-solid flow

Governing equation	Detail		Eqn. #
$$m\frac{d\bar{v}}{dt} = \overline{F}_{drag} + \overline{F}_{pressure} + \overline{F}_{virtual\_mass} + \overline{F}_{gravitation} + \overline{F}_{others}$$ $$\frac{dx}{dt} = \bar{v}, \ \overline{F}_{others} = \overline{F}_{friction}, \ \overline{F}_{body}$$	Particle motion		6.12
$F_{friction} = \mu F_{normal}$ $\mu = \mu_{stick}$ = sticking friction coefficient $\mu = \mu_{glide}$, gliding friction coefficient $\mu = \mu_{\lim it}$, high velocity limit friction coefficient Friction coefficient plot is showed in Appendix 5	Frictional collision law		6.13
$\varepsilon_g + \varepsilon_s = 1$	Volume fraction of the phases		6.14
$$\frac{\partial \rho}{\partial t}\left(\varepsilon_g \rho_g\right) + \nabla \cdot \left(\varepsilon_g \rho_g \vec{v}_g\right) = \sum_{p=1}^{n}\left(\dot{m}_{sg} - \dot{m}_{gs}\right) + S_g$$	Continuity equation for gas		6.15
$$\frac{\partial \rho}{\partial t}\left(\varepsilon_s \rho_s\right) + \nabla \cdot \left(\varepsilon_s \rho_s \vec{v}_s\right) = \sum_{p=1}^{n}\left(\dot{m}_{gs} - \right.$$	Continuity equation for solid		6.16
	Momentum equation for gas		6.17
$$\frac{\partial \rho}{\partial t}\left(\varepsilon_g \rho_g \vec{v}_g\right) + \nabla \cdot \left(\varepsilon_g \rho_g \vec{v}_g \vec{v}_g\right) = -\varepsilon_g \nabla p + \nabla \cdot \overline{\tau}_g + \varepsilon_g \rho_g \vec{g} + \sum_{g=1}^{n}\left(K_{sg}\left(\vec{v}_s - \vec{v}_g\right) + \dot{m}_{sg}\vec{v}_{sg} - \dot{m}_{gs}\vec{v}\right)$$ $$+ \left(\vec{F}_g + \vec{F}_{lift,g} + \vec{F}_{vm,g} + \vec{F}_{td,g}\right)$$			
	Momentum equation for solid phase		6.18
$$\frac{\partial \rho}{\partial t}\left(\varepsilon_s \rho_s \vec{v}_s\right) + \nabla \cdot \left(\varepsilon_s \rho_s \vec{v}_s \vec{v}_s\right) = -\varepsilon_s \nabla p_s - \nabla p_s + \nabla \cdot \overline{\tau}_s + \varepsilon_s \rho_s \vec{g} + \sum_{l=1}^{N}\left(K_{gs}\left(\vec{v}_g - \vec{v}_s\right) + \dot{m}_{gs}\vec{v}_{gs} - m_{sg}v_{sg}\right)$$ $$+ \left(\vec{F}_s + \vec{F}_{lift,s} + \vec{F}_{vm,s} + \vec{F}_{td,s}\right)$$			
$$K_{sg} = \frac{\varepsilon_s \rho_s f}{\tau_s},$$	Solid-gas exchange coefficient		6.19
$$\tau_s = \frac{\rho_s d_s^2}{18\mu_f}$$	Relaxation time		6.20

Syamlal-Obrien	$k_{sl} = \dfrac{3\alpha_s\alpha_l\rho_l}{4v_{r,s}^2 d_s} C_D\left(\dfrac{\text{Re}_s}{v_{r,s}}\right)\left|\vec{v}-\vec{v}\right|$ $\qquad C_D = \left[0.63 + \dfrac{4.7}{\sqrt{\text{Re}_s/v_{r,s}}}\right]^2$	6.21
Wen & Yu	$k_{sl} = \dfrac{3\alpha_s\alpha_l\rho_l}{4d_s} C_D\left|\vec{v}_s-\vec{v}_l\right|\alpha_l^{-2.65}$ $C_D = \dfrac{24}{\alpha_l \text{Re}_s}\left(1+0.15(\alpha_l \text{Re}_s)^{0.687}\right)$	6.22
Gidaspow	$k_{sl} = 150\dfrac{\alpha_s(1-\alpha_l)\mu_l}{\alpha_l d_s^2} + 1.75\dfrac{\rho_l\alpha_s\left|\vec{v}_s-\vec{v}_l\right|}{d_s}$ $C_D = \dfrac{24}{\alpha_l \text{Re}_s}\left(1+0.15(\alpha_l \text{Re}_s)^{0.687}\right)$	6.23
Non-spherical	$k_{sl} = \dfrac{3\alpha_s\alpha_l\rho_l}{4d_s} C_D\left|\vec{v}_s-\vec{v}_l\right|\alpha_l^{-2.65}$ $C_D = \dfrac{24}{\text{Re}_{sph}}\left(1+b_1 \text{Re}_{sph} b_2\right)+\dfrac{b_3 \text{Re}_{sph}}{b_4 + \text{Re}_{sph}}$	6.24

6.3.4   Formulation of body force correlation

In the formulation scheme for particle motion (Eqn. 6.12), body force is an optional force embedded under the $\overline{F}_{others}$. The contact force are due to particle to particle interaction, whereas the body forces are any external force fields acting on the particles (Sen et al., 2014). For fluent to implement a body force (bforce), an acceleration term must be developed in the form of eqn. 6.21.

$$bforce = \frac{force}{mass} \qquad (6.25)$$

Relating void fraction to the particle and fluid occupying a control volume

$$\varepsilon = \frac{V_{air}}{V_{air} + V_{solid}} \qquad (6.26)$$

$$V_{air} = \frac{\varepsilon}{1-\varepsilon} V_{solid} \tag{6.27}$$

Expanding the force in relation to fluid volume and density

$$bforce = \frac{force}{mass} = \frac{\rho_{air} V_{air} a}{\rho_s V_s} \tag{6.28}$$

$$bforce = \frac{force}{mass} = \frac{\rho_{air} \dfrac{\varepsilon}{1-\varepsilon} V_{solid} \vec{a}_s}{\rho_s V_{solid}} \tag{6.29}$$

Thus, the body force acting on a bed of material can be related to the porosity of air, density of air, and particle.

$$bforce = \frac{force}{mass} = \frac{\rho_{air}}{\rho_s} \frac{\varepsilon}{1-\varepsilon} \vec{a} \tag{6.30}$$

6.3.5   Boundary and initial condition

In order to obtain a well-posed system of equations, reasonable boundary condition for the computational domain was implemented. At the inlet boundary, is a uniform air velocity inlet while the outlet boundary is the pressure boundary condition set at zero gauge pressure to model the opening of the system to the atmosphere. Also, mixture boundary was also activated for the outlet boundary. Here, the discrete phase boundary condition was set at escape boundary. This means that the particles that crossed the boundary is eliminated. For the wall, boundary conditions were set at no-slip conditions for gas phase and discrete event collision for the solid phase. At the initial condition, 0.2 kg of loblolly pine grinds with the following characteristics was injected: void fraction of 0.7 for ground loblolly pine wood, and sphericity of 0.45. For all simulations, the time step, maximum iterations/time, and reporting interval were set at 1E-3 s, 20 sec, and 5 (frequency) respectively.

6.3.6 Solver related details

The Eulerian-Lagrangian with Dense Discrete Phase Model(DDPM) equations were implemented in FLUENT 14.5.7 solver employing finite volume solution method and Phase Coupled SIMPLE (FLUENT, 2012) algorithm to solve the pressure–velocity coupled equations in a discretization scheme. The unsteady state formulation employed QUICK scheme solver for momentum and volume fraction for discretization. The solution was initialized from solid inlet and air inlets and the convergence was monitored approximately up to 10,000 iterations with residual convergence fixed between 1×10^{-3} and 1×10^{-6}.

6.3.7 User defined function implementations

To compute the bed voidage, it was mandatory to computationally designate which cells belonged to the bed region (the region where particles reside). In order to discount the very dilute suspension in the freeboard, only cells with > 0.01 solid volume fraction (ε_s) were designated as belonging to the bed. This study used the Fluent UDF macro written in the C programming language called DEFINE_EXECUTE_AT_END. This is a general-purpose macro that is executed at the end of an iteration in a steady state run, or at the end of a time step in a transient run (FLUENT, 2012). In addition, body force correlation implementation used UDF macro DEFINE_DPM_BODY_FORCE. The UDF is used to identify body force other than a gravitational or drag force on the particles. The macro return the real value of the acceleration due to the body force (in m/s^2) to the ANSYS FLUENT solver. The UDFs for bed voidage and body force are presented in Appendix 5.

6.4   Result and discussion

6.4.1   Mesh convergence/ independent study

Mesh independent study are usually first conducted to reduce the error in CFD calculations due to the usage of an incorrect mesh sizes (Rundle et al., 2011). Solutions over a range of significantly different grid resolutions have to be presented to demonstrate grid-independent or grid-convergent results. For mesh independent study, five different mesh sizes that varies from 4000 to 65000 numbers of element were considered (Table 6.4). When a particular mesh size is selected, about 200 g particles were injected into the bed and airflow of 0.2 m/s was applied. Using a simulation time step of 2000 corresponding to 2 seconds simulation time, the pressure drop, bed voidage at each time step were extracted using the FLUENT programming user define function (UDF) described in 7.2.7.

Table 6.4: Meshing method and sizes obtained for mesh independent study

Mesh type	Program controlled				
Sizing method	Proximity and curvature				
Mesh number	1	2	3	4	5
Numbers of node	4558	4730	33728	49248	67725
Numbers of Element	3570	3740	36304	45390	63510

It can be seen from Fig. 6.4 that the pressure drop profile at various mesh sizes behaved similarly and reach steady state by 2-seconds of simulation time. For comparison purposes, the theoretical pressure drop obtained that was calculated by dividing bed weight by the cross-sectional area of the bed was 268 Pa. The percentage errors between the theoretical pressure drop and predicted pressure drop for the number of elements 3570, 3740, 33728, 45390, and 63510 were 12.51 %, 15.8 %, 8.6 %, 9.2%, and 8.6% respectively. Similarly, the plot of bed voidage with time showed similar profile for all the mesh size. In addition, the bed voidage converged at 2-second simulation time.
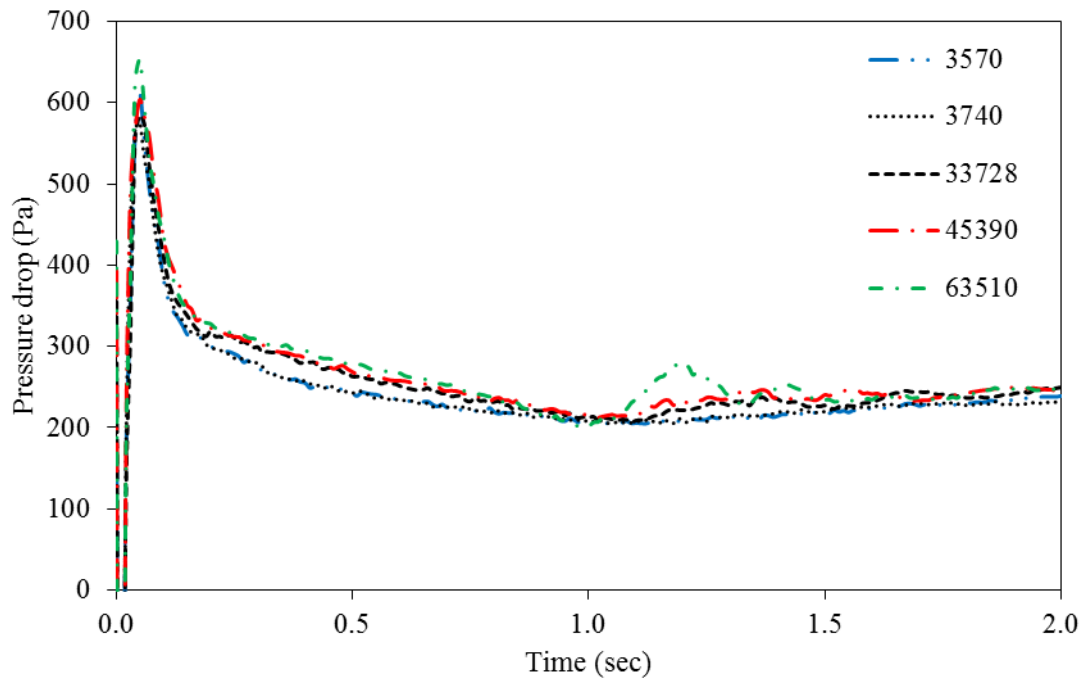
Figure 6.4: Effect of using different mesh sizes on pressure drop across the bed with simulation time
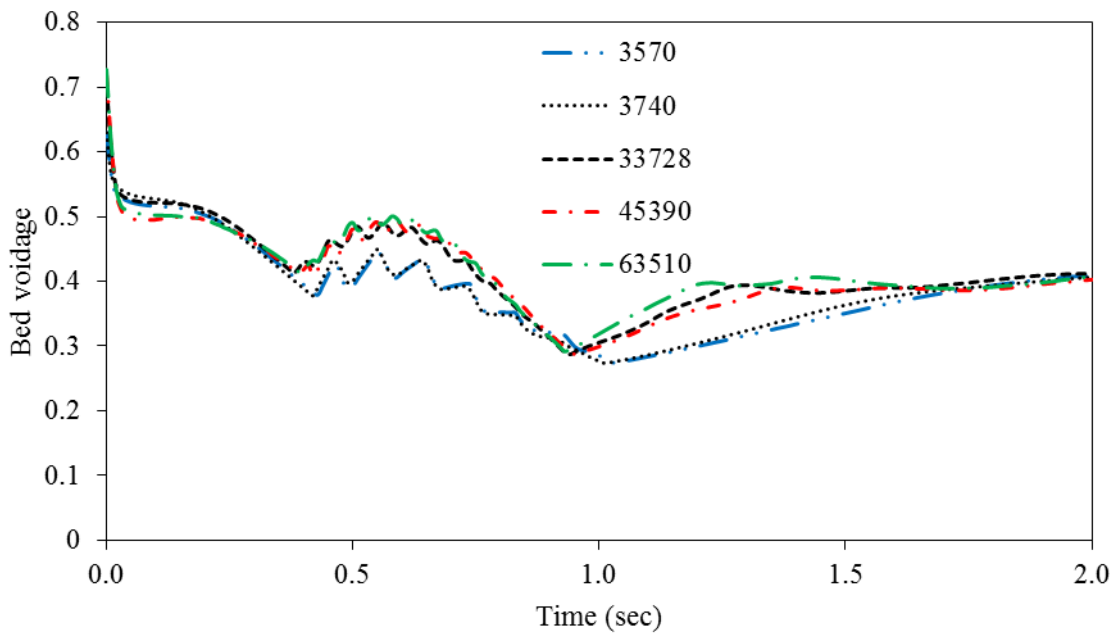
Figure 6.5: Effect of using different mesh sizes on bed voidage with simulation time

In general, the smaller the mesh size, the closer the simulation results were to the theoretical pressure drop. When mesh size reduced, the total number of the control volume increased (mesh total number). This also increased the number of governing equations that must be solved for each mesh and hence the solution becomes more precise (Pin et al., 2014). However, increase in number of mesh also increase the computational effort (time and resources) needed for convergence and for producing result. About 100 hours is required to complete a simulation case. However additional 2 hours existed between cases (based mesh size variation) using High-performance computing cluster (HPCC) that consist of 512 cores @ 2.80 GHz X5560, 1.536TB shared memory, and 20.48TB raw internal storage. HPCC Theoretical Performance calculated @ 5.735 teraflops with memory bandwidth up to 90 GB/s. Therefore, with low deviation in pressure drop and insignificant computational time compared to other mesh sizes, mesh size of 33728 was chosen as the optimum mesh size. Subsequent simulations were therefore carried out using this mesh size. Fig 6.6 shows the flow chart used to simulate the solid-gas fluidized bed system that comprised of non-uniform and non-spherical particles such as particles from loblolly pine grinds.
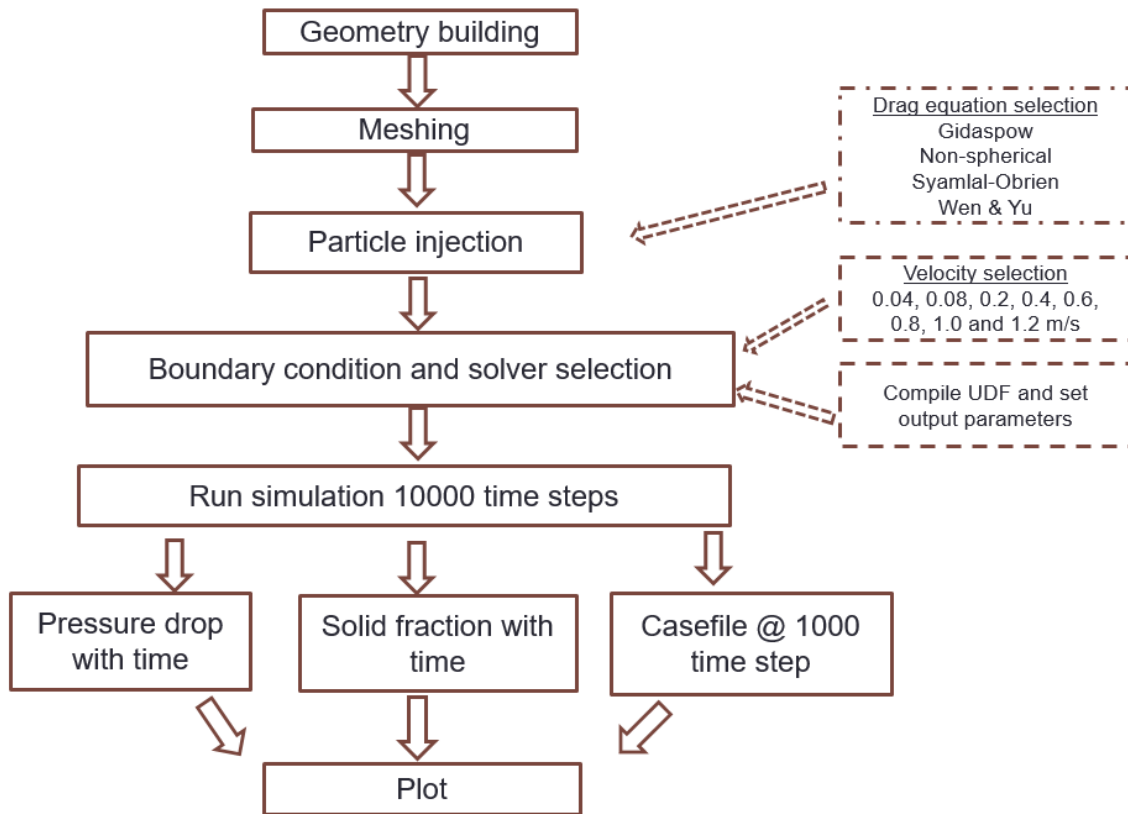
Figure 6.6: Flowchart showing scheme used for solving equations for multi-phase CFD model

6.4.2 Effect of drag model on transient bed voidage profile

Fig. 6.7 a – d illustrates transient bed voidage profile for velocities in the range of 0.08 –

1.2 m/s using Gidaspow, non-spherical, Syamlal-Obrien, and Wen & Yu drag model

respectively (FLUENT, 2012). For our system, velocity of interest is between 0.25 -1.0

m/s because the minimum and complete fluidization velocities respectively falls within

this range (Chapter 4 and 5). However, the choice simulating wider velocity range (0.08 –

1.2 m/s) was to enable the plotting of pressure drop-velocity profile for the sample.
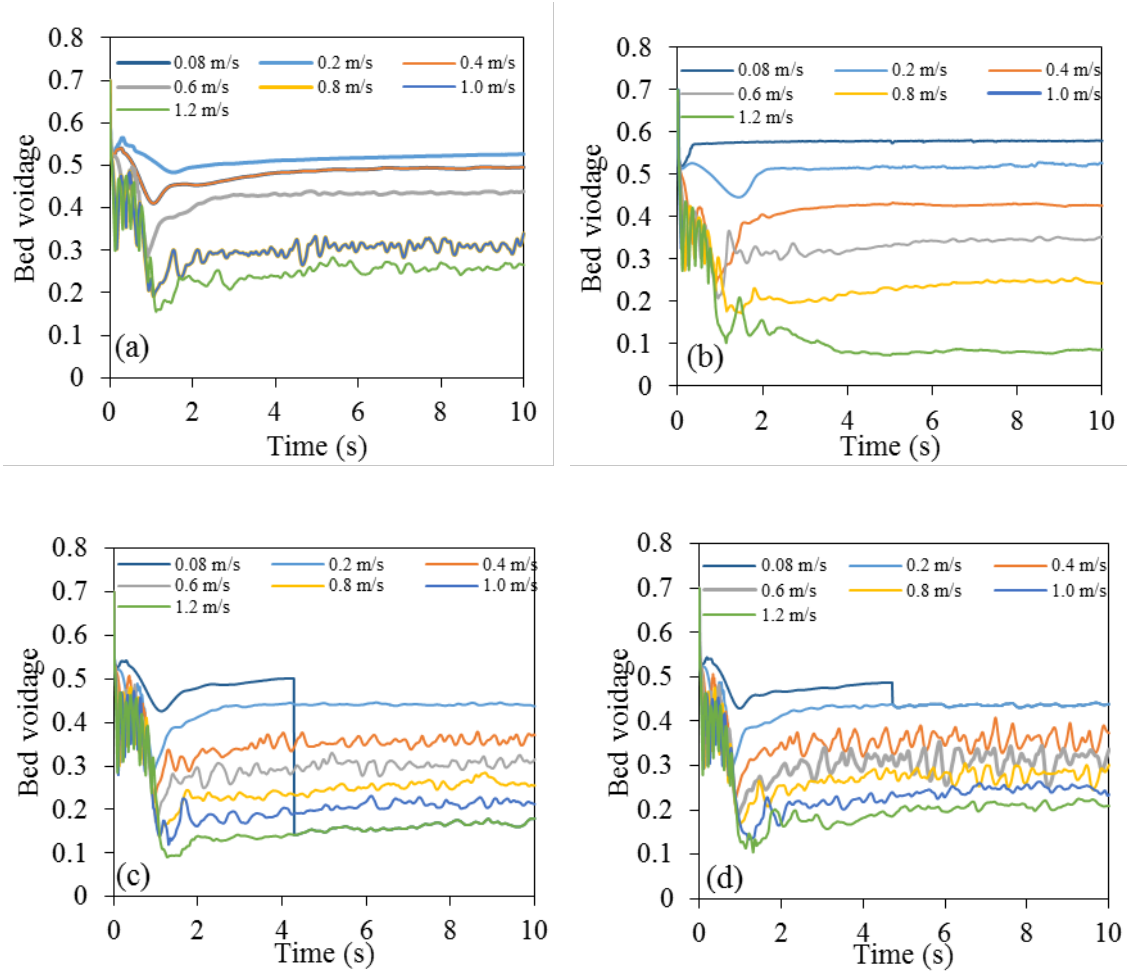
Figure 6.7: Transient bed voidage profiles for velocities in the range of 0.08 -1.2 m/s for different drag law: (a) Gidaspow; (b) Non-spherical; (c) Syamlal-Obrien, and (d) Wen & Yu

The bed voidage profile using different drag equations and at different velocities showed similar profile. Firstly, the initial bed was unstable until simulation time of 2.0. We attribute this behavior to shock at bed startup (Chialvo et al., 2012; Sande and Ray, 2014). Initially when air is introduced into the packed bed, the air attempts to flow through the void spaces within the bed: However, since the voids are not directly connected, the tortuous movement of air and the flow velocity create a situation where the air create its own path resulting in bed realignment intense mixing. As the air establishes its own flow path, the void settles down (time at 2 sec to 10 seconds). Figure

213

6.8 a –d shows the snapshots of the contour plot of the transient solid volume fraction at

2.0 m/s air flow using the different drag equations.

(a)   0 sec   1 sec   2 sec   4 sec   6 sec   8 sec   10 sec

(b)   0 sec   1 sec   2 sec   4 sec   6 sec   8 sec   10 sec

(c)   0 sec   1 sec   2 sec   4 sec   6 sec   8 sec   10 sec

(d)   0 sec   1 sec   2 sec   4 sec   6 sec   8 sec   10 sec
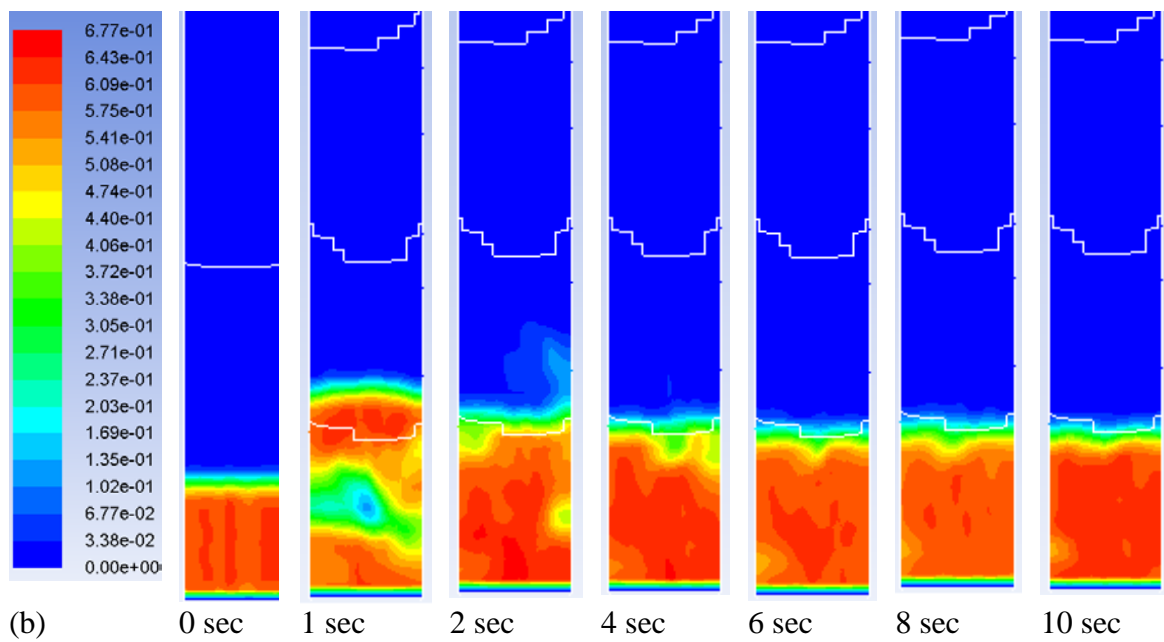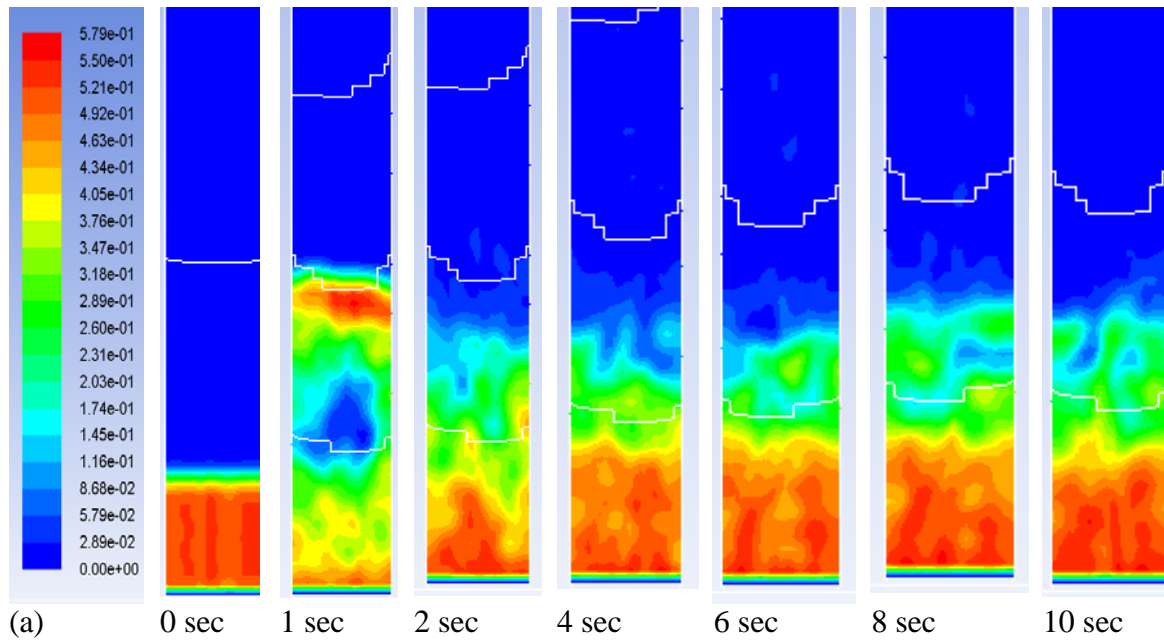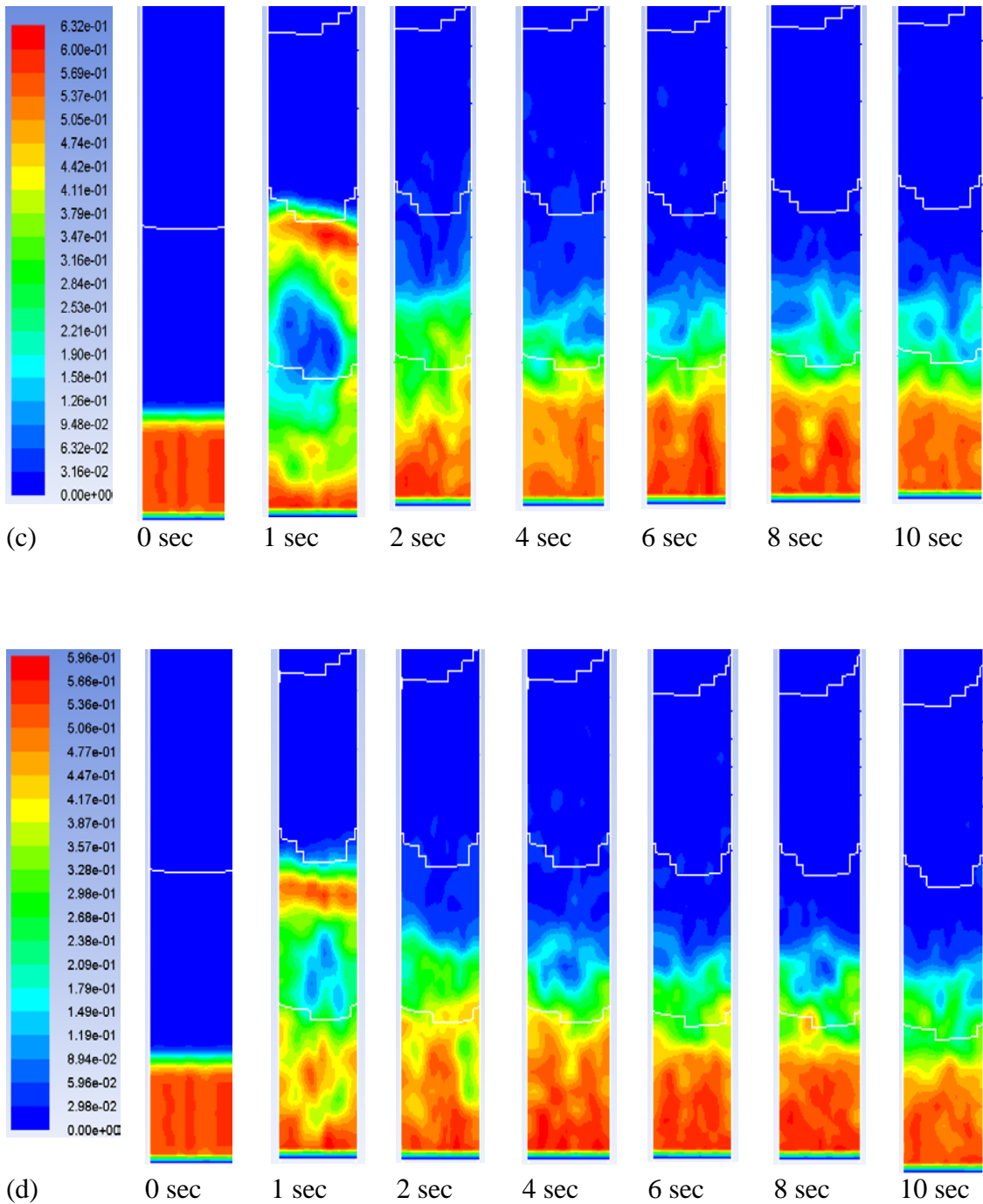
Figure 6.8: Snapshots of transient solid volume fraction contours of the fluidized bed at 2.0 m/s: (a) Gidaspow: (b) Non-spherical; (c) Syamlal-Obrien: (d) Wen & Yu drag law

A careful look at the snapshot (Fig. 6.8) revealed a plug flow at simulation time of 1 sec. This corroborated the initial resistance of the bed to air penetration as air attempt to establish its path in the bed. It can be seen that the bed initially bubble sizes are almost

215

equal to the diameter of the bed which could be likened to a plug flow. Immediately after this initial bed resistance, the bed resettled.

The bed perturbation was least when non-spherical drag law was used, while the rest showed an extensive bed mixing. This observation was different from what was observed by Sande and Ray (2014) and Zhang et al. (2008). These authors using a bed consisting of uniformly sized particles and the simulation were carried out using Eulerian - Eulerian simulation schemes. These authors reported that after the initial bed disturbance, the whole bed return to the homogenous fluidization state. However, when a bed consists of non-uniform particle size, small particles trapped between big particles could initially offer resistance to fluid flow through the bed. Thus, part of the bed move in a plug flow. Immediately afterwards, the bed collapses resulting in escape of small particle trapped between the bigger particles. In addition, air flow causes structural realignment of the bed, small particles that are light in weight are entrained out of their position to a new place or some are entrained in the air. This movement of particles creates void/ channels and various routes for air passage through the bed. We suspect that the entrainment of the smaller particles out of the bed, makes the bed to consist more of bigger particles. An increase in air velocity is then required before fluidization can occur. Thus an initial perturbed bed simply resettled after some time. This behavior was experimentally observed and details presented in Chapter 3.

0.0 mm					Wen & Yu
Initial state		1 sec	4 sec	10 sec	Drag law
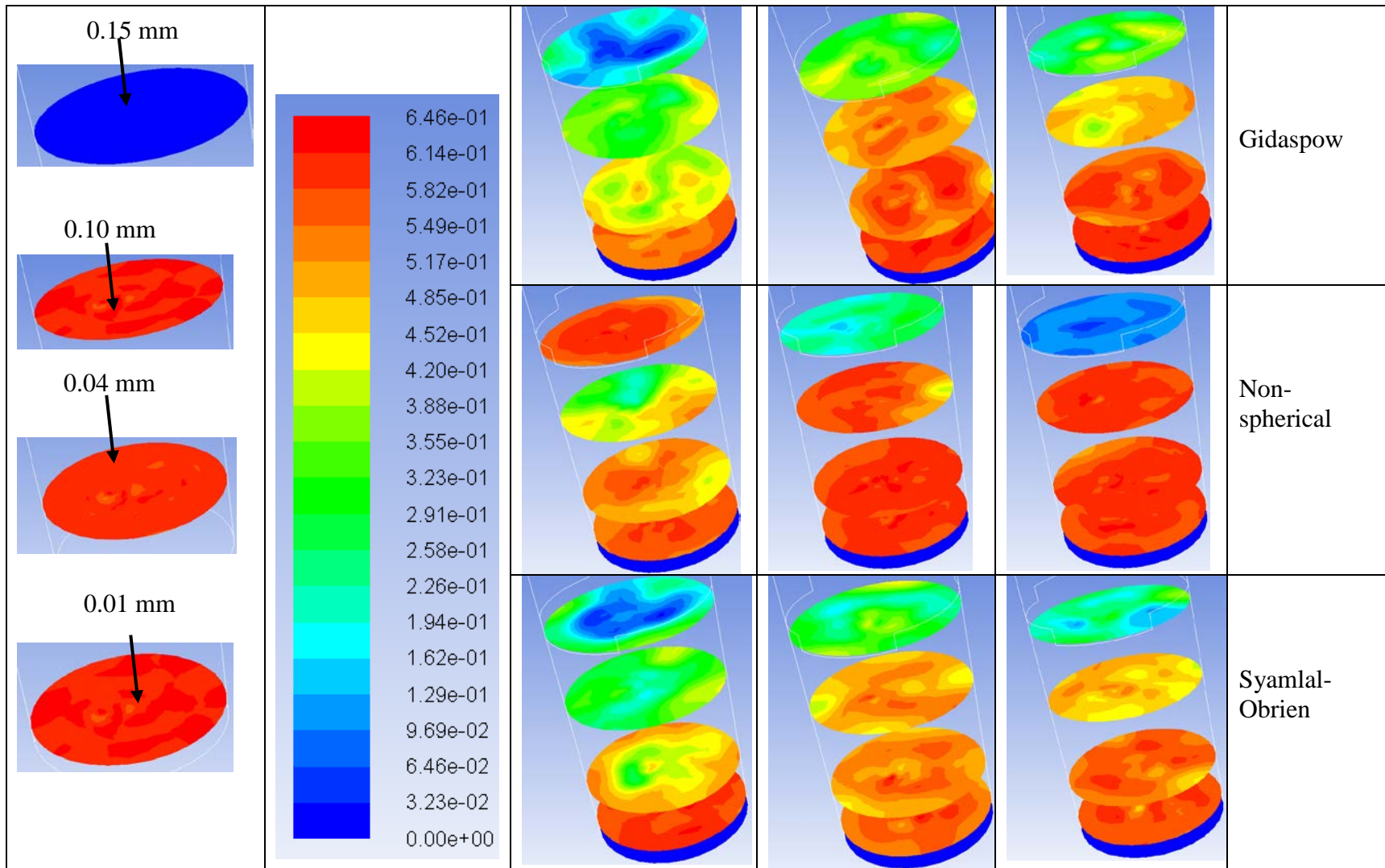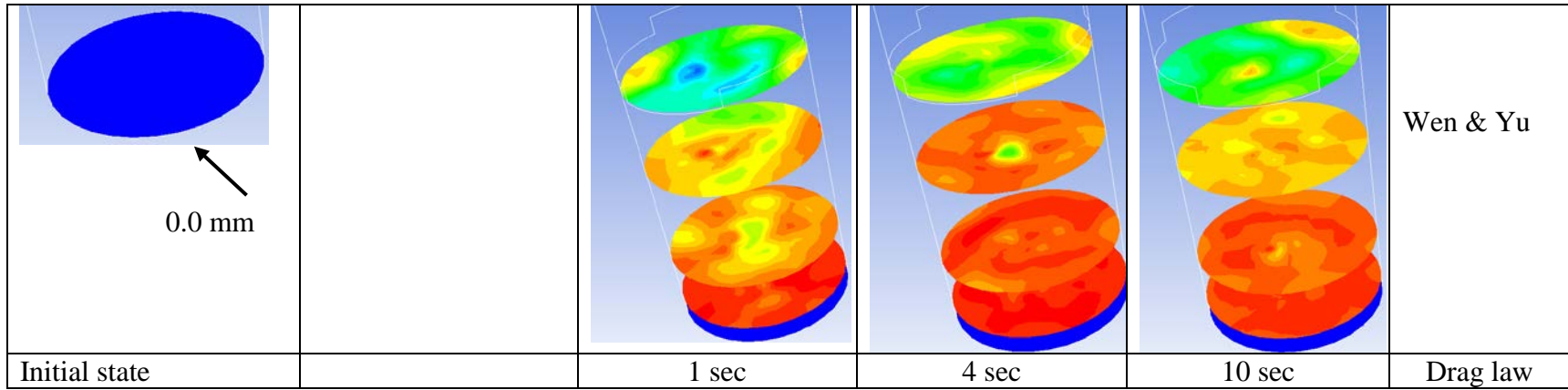
Figure 6.9: Contour plot of volume fraction of solid on z-coordinate at 0.0, 0.01, 0.04, 0.10, and 0.15 mm at 0.2 m/s air velocity

Similarly, Fig. 6.9 shows the contour plot of volume fraction of solid at 0.0, 0.01, 0.04, 0.10 and 0.15 mm and 0.2 m/s velocity (using different drag laws). Dark red represent high concentration of material at the particular location while yellow signifies void spaces. It can be seen that virtually all the model showed various size of channels and particle realignments. As the simulation time increase, particle concentration at the base of the bed increased for Gidaspow, non-spherical, and Wen & Yu models. This may be attributed to structure of Syamlal drag law in which terminal velocity is used as particle velocity in drag function.

6.4.3   Effect of drag model on pressure drop profile

Pressure drop across the bed is an important parameter to determine for proper scaling up and reactor design. Traditionally, the pressure drop in a fluidized bed has always been described by the buoyant weight (i.e. weight per unit cross-sectional area of bed) of the suspension (Brandani and Zhang, 2006; Shi et al., 2010). Figure 6.10 shows the bed pressure drop profile as a function of the flow time at various fluidizing velocity (using Gidaspow drag law). Similar profiles were obtained for Syamlal-Obrien, Wen & Yu and non-spherical drag laws (Appendix 5).
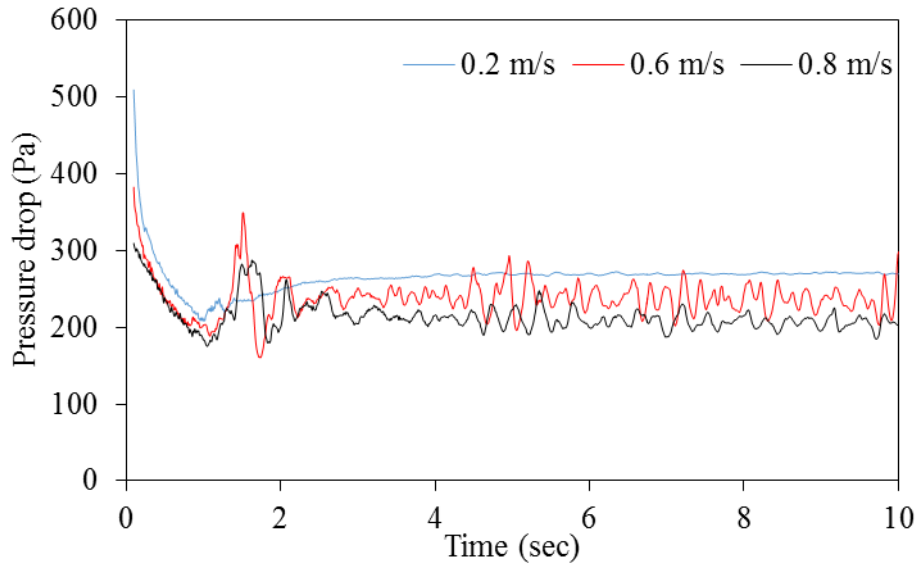
Figure 6.10: Evolution of pressure with simulation time at different velocity using Gidaspow drag law

Moreover, according to Figure 6.10, it is worth noting that four typical regions could be identified (Shi et al., 2010). The startup stage is the initial pressure of the bed (at time 0 second). Slow drop stage (0 s < time < 1.5 s), vibration stage (1.5 s time < 4.0 s), and stable fluidization stage (time > 4 s). The maximum bed pressure drop occurred at the start-up point/ stage and the pressure is far greater than any other three stages because of the inter-particle locking and bed cohesive forces that must be overcome. Afterward, the bed pressure drop decreased slowly because of formation of the gas-phase flow field and the looseness of the solid phase following the flow proceeding in the period of 0-1.5 s. In the period of 1.5-4.0 s, air bubble formation was predominantly found that developed with time; causing the bed pressure drop to fluctuate greatly. After the vibration stage, the bed pressure drop fluctuates with time around a mean value corresponding to the gas flow as shown in Figure 6.10, namely, the stable fluidization stage.

Since the bed achieve stable fluidization at later stage of the fluidization, the mean pressure drop was obtained using the 10 sec time step simulation case file.

6.4.4 Comparison of CFD simulation and experimental result

Figure 6.11 showed the pressure drop against the airflow velocity of both experimental and simulated data. The pressure profile behavior can be categorized into two different behaviors based on the velocity, namely, before (0- 0.2 m/s) and after (0.2-1.0 m/s).
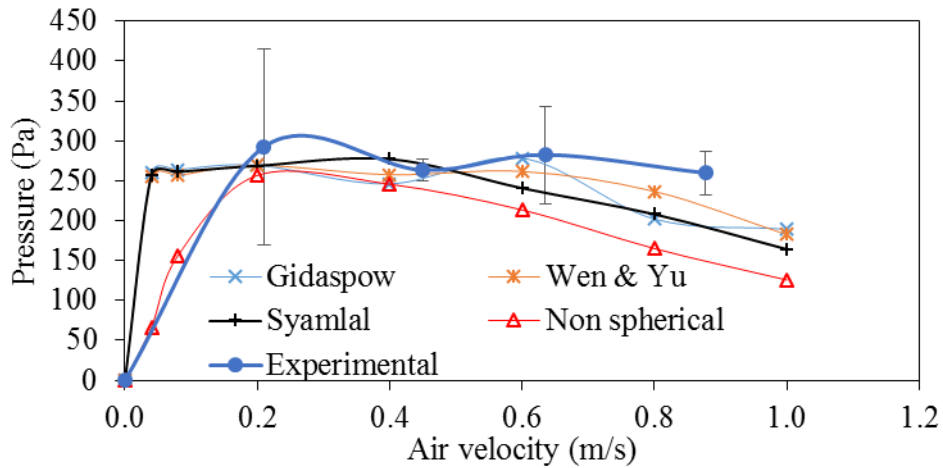
Figure 6.11: Determination of U_{mf} using the plot of pressure drop against the airflow velocity

Between 0– 0.2 m/s, air velocity and pressure increased progressively, and only non-spherical drag matches the experimental data. When the velocity was greater than 0.2 m/s, the experimental pressure drop became constant, while the predicting drags law started to decline progressively. The decline in pressure drop with increase velocity above 0.2 m/s was traced to bed material entrainment and loss of inventory. This situation is further investigated in subsequent section. In experimental situation at ~0.2 m/s, particle distribution and particle forming network / interlocked offered additional resistance to fluid flow apart from buoyant weight of the suspension. Thus, intra and inter-particle bridging contributed to pressure addition hence the slight increase in pressure drop (Zhuang et al., 2014). Furthermore, Table 6.5 showed the mean relative deviation (MRD) between the predicted and the experimental pressure drop data. It can

be seen that all the drag laws under predicted the experimental data and the deviation

increased with increase in velocity.

Table 6.5: Mean relative deviation between predicted pressure drop using different drag
equation and experimental data.

Velocity (m/s)	Mean Relative deviation (%)			
	Gidaspow	Wen & Yu	Syamlal-Obrien	Non-spherical
0.2	-3.9	-3.9	-4.1	-6.1
0.4	-3.3	-1.1	2.6	-3.3
0.6	-0.8	-3.7	-7.4	-12.2
0.8	-11.1	-4.4	-9.9	-18.2

This could be attributed to the bed channeling and particles entrainment out of the bed.

Eqn. 6.31 was used to calculate the bed entrainment after 10 seconds simulation time.

$$entrainment = \frac{M_i - M_f}{t} \times 60$$ 6.31

where

entrainment is (g/min)

M_i is the initial mass (g)

M_f is the final mass (g) at 10 sec (t) simulation time step.

Fig. 6.12 shows the comparison of predicted and experimental entrained bed material. At

0.2 m/s both experimental and predicted showed there were no bed material entrainments.

However, at 0.24 m/s, predicted and experimental bed material entrainments were

comparable. However, at 0.6 and 0.8 m/s the drag law significantly over-predicted the

bed entrainment. This can be attributed to inability of the drag laws to capture the

particles interaction because Fluent software see the particles as spherical and the

interlocking effect coupled with particle to particle friction of non-spherical particles

were not properly captured by the drag laws. Hence, the need to revise existing

equation/laws in order to effectively predict the bed expansion and material entrainment. When the bed inventory reduced because of entrainment, the total weight of the bed reduces with the corresponding reduction in pressure drop. Bed entrainment also caused similar drop in pressure during the simulation as velocity increased. The detail is presented in next section.
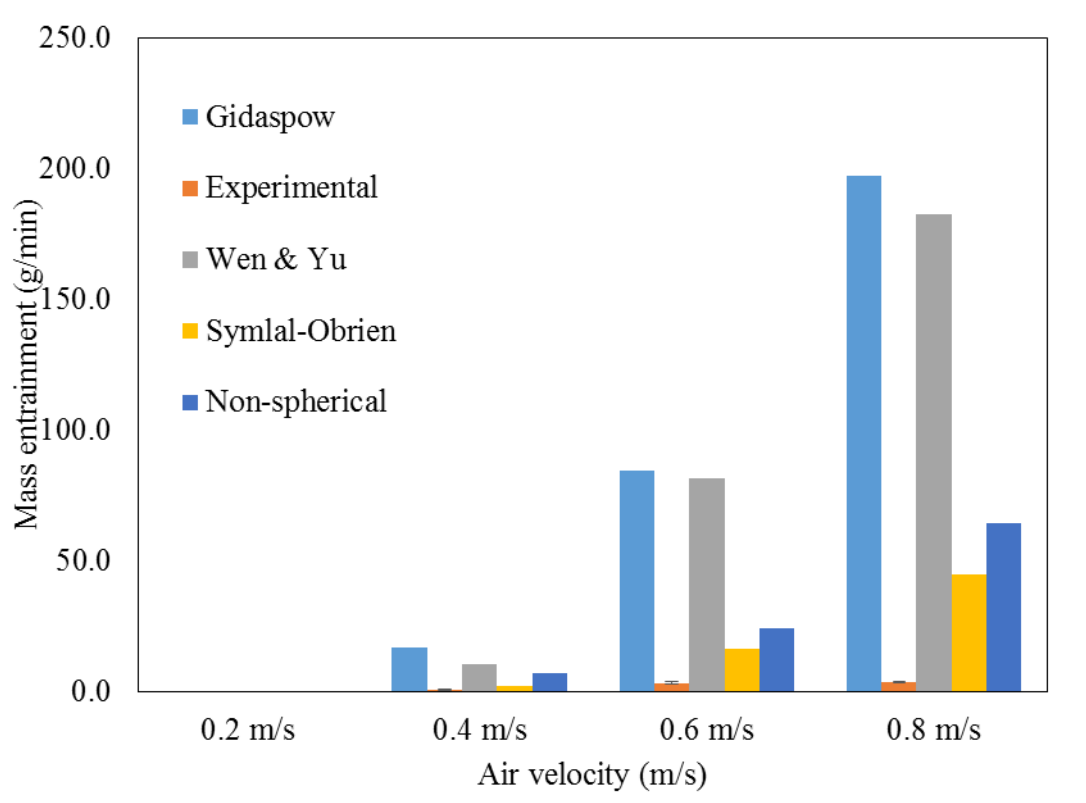
Figure 6.12: Comparison of predicted and experimental bed material entrainment as velocity increased.

6.4.5   Prediction of minimum fluidization velocity

The minimum fluidization velocity was identified as the velocity at which increasing trend in bed pressure of the packed bed terminates in the plot of pressure drop against the airflow rate. This approach was used in chapter 4 and 5. From Figure 6.13, the minimum fluidization velocity of the bed varied according to the drag law used. The experimental U_{mf} was 0.2 m/s while non-spherical and other drag laws predicted 0.2 m/s and less than

0.1 m/s respectively. Hence, the non-spherical seems to have successfully predicted the experimental U_{mf}.
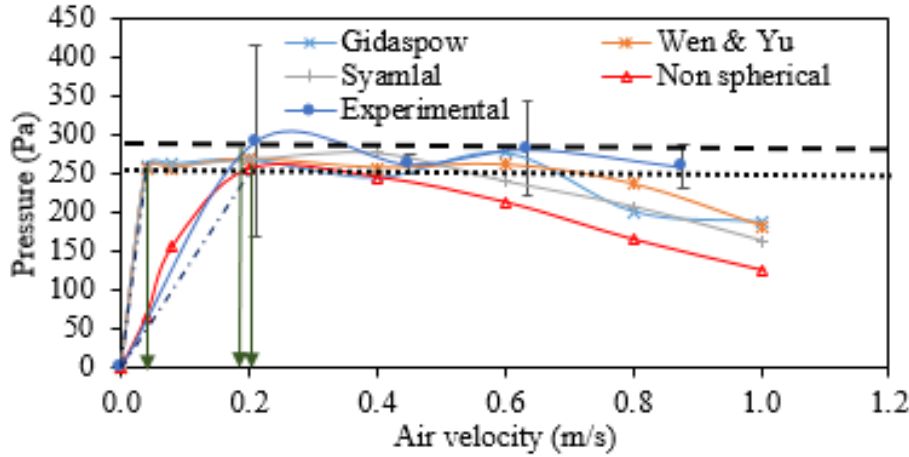
Dash line represents the theoretical pressure drop defined as bed weight per unit cross-sectional area

Figure 6.13: Pressure drop against velocity for determination of minimum fluidization velocity.

In order to understand particle behavior at fluidization, it is important that we examine the state of bed at velocity before (0.2 m/s) and after (0.4 m/s) the minimum fluidization velocity. Fig 6.14 particle traces colored by particle velocity magnitude using non-spherical drag law at 0.2 m/s. It can be seen that the bed was still in static position as larger percentage of the bed was still in fixed bed. However, smaller particles were increasingly entrained out of the bed area as simulation proceeds from 2 sec to 10 second. Similarly, Figure 6.15 shows particle traces colored by particle velocity magnitude using non-spherical drag law at 0.4 m/s. It can be seen that particle entrainment out of the bed began after 2-second simulation time. Similar particle entrainments were observed while using Gidaspow, Wen & Yu, and Syamlal-Obrien. (Appendix 7). In addition, from scale in Fig 6.15, the smallest and the highest solid velocity was 1.1e-7 m/s, and 1.28 m/s

224

respectively. This wide difference in solid velocity is attributed to the wide variation in the size and densities of particles in the bed. When particle size varied largely, bigger particle settles while smaller particle entrained. This is important because residence time for ground biomass is approximately 3 seconds (Capareda, 2013). Thus, operating the fluidize bed at a velocity above U_{mf} would result in particle carryover. Even as particle entrained out of the bed, a large part of the solid was still on the distributor.
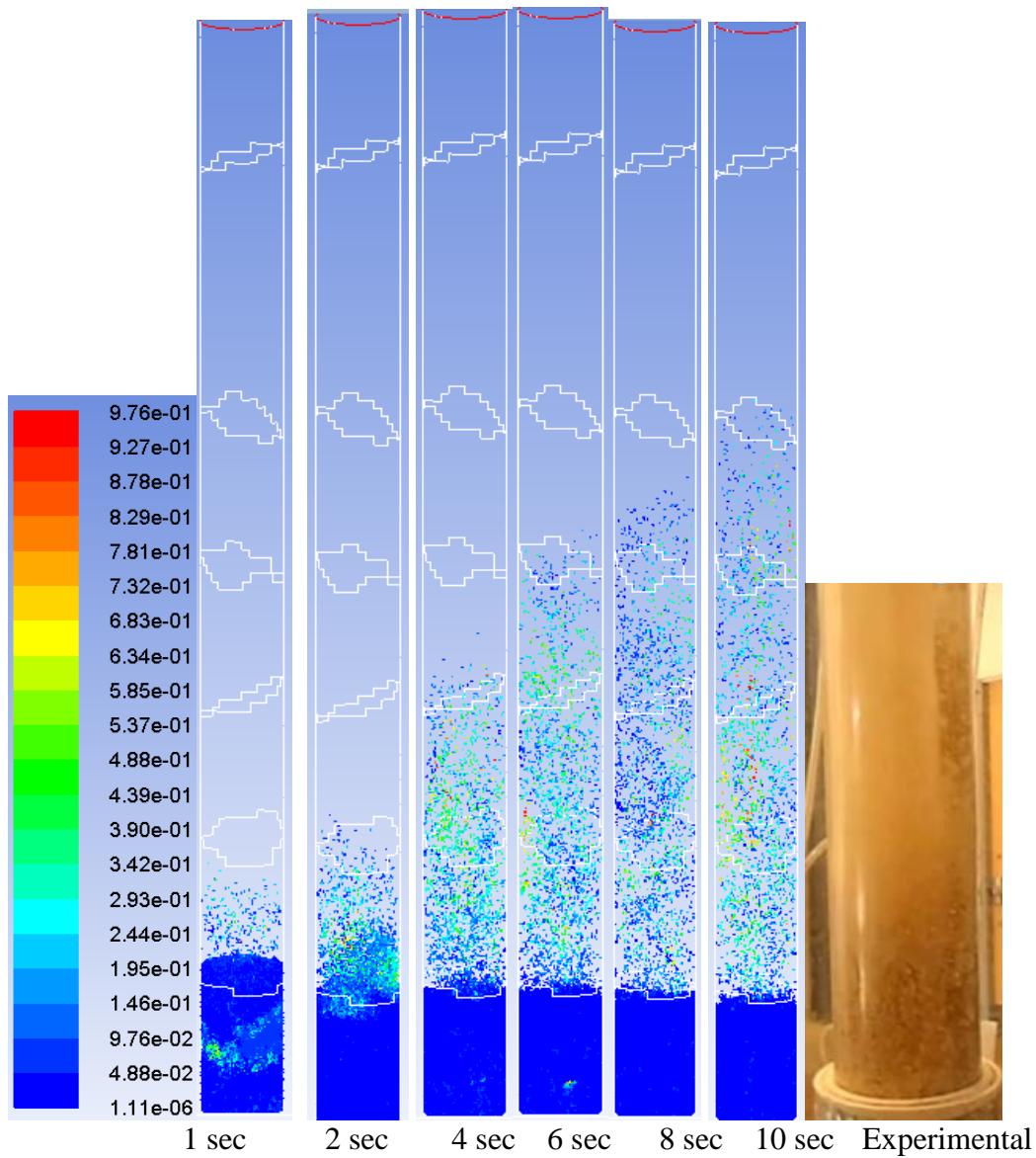
Figure 6.14: Particle traces colored by particle velocity magnitude using non-spherical drag law at 0.2 m/s

225
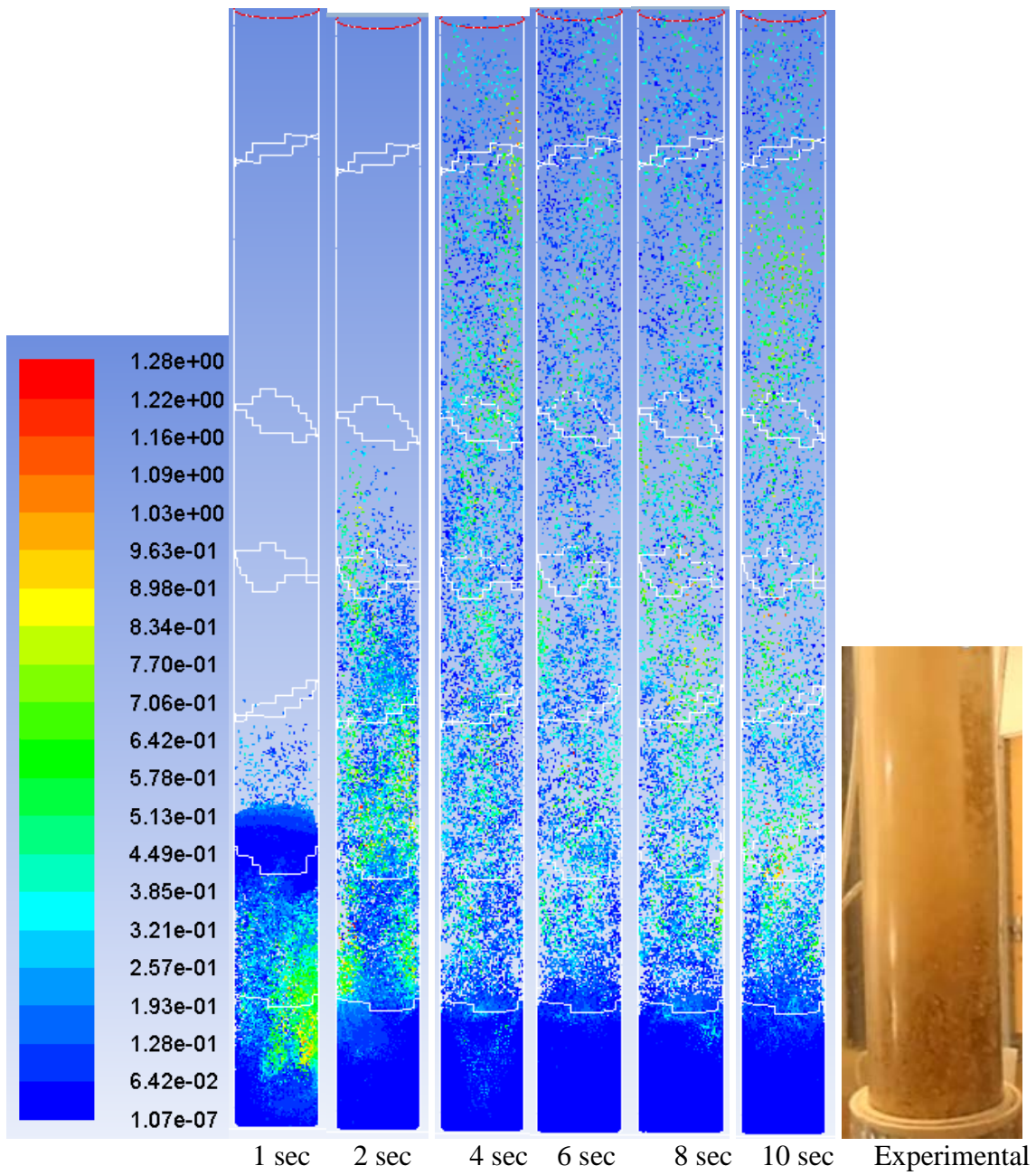
Figure 6.15 Particle traces colored by particle velocity magnitude using non-spherical
drag law at 0.4 m/s

6.4.6 Effect of void body force application on pressure drop profile

Table 6.16 shows the pressure drop at different air velocities after application of the body force correlation. It can be seen that pressure drop first increased until velocity reached 0.2 m/s then reduced for all drag law considered. This relationship obtained between pressure drop and velocity is similar to the relationship obtained when body force was not applied (section 6.4.4). The reduction in pressure drop with increase in velocity was earlier attributed to loss of bed material inventory. Also, it was observed that the least pressure drop considering all the velocities was obtained when non-spherical drag was used. For instance, about 46% difference were recorded between Gidaspow and non-spherical at 0.04 m/s velocity.

Table 6.6: Pressure drop obtained at different velocities after application of body force correlation.
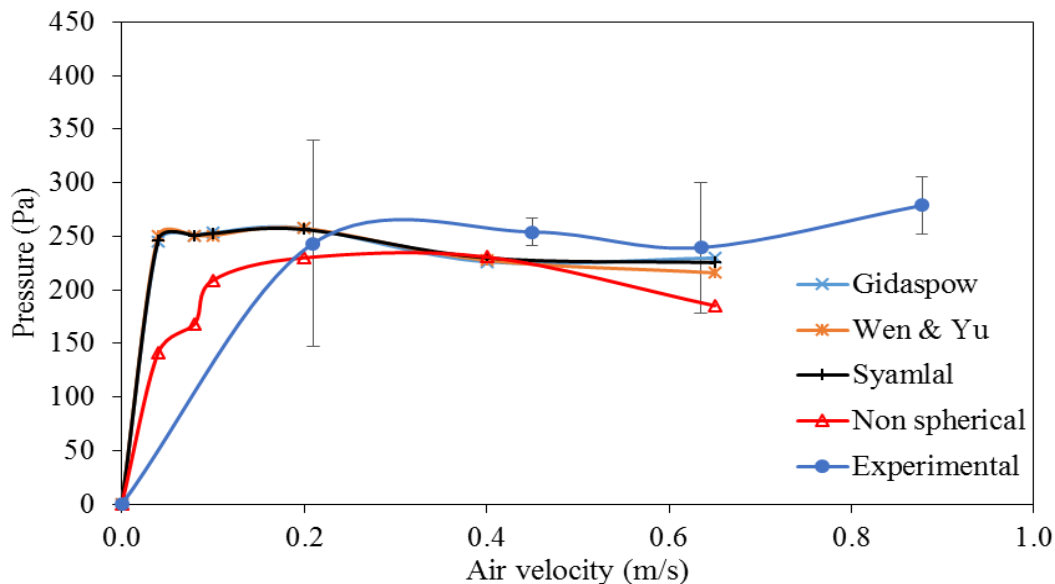
Figure 6.16: Pressure drop obtained at different velocities after application of body force correlation.

Furthermore, Table 6.7 shows the mean relative deviation between experimental and predicted pressure drop. A large mean relative deviation at lower velocity (0.2 m/s). We attributed this to updraft generated from airflow is not sufficient to lift the bed, air penetration largely depends on the ability of the air to navigate through the available void fraction. However, when the velocity was greater than was greater than 0.2 m/s, deviation between predicted and the experimental pressure drop reduced.

Table 6.7: Mean relative deviation between experimental and predicted pressure drop at different velocity and drag models.

| | Mean relative deviation (%) | | | |
| | Drag model | | | |
Velocity (m/s)	Gidaspow	Wen & Yu	Syamlal	Non spherical
0.2	12.5	12.5	12.3	5.8
0.4	4.9	5.3	5.8	6.0
0.6	5.8	2.4	4.8	-5.0

Fig. 6.17 shows the comparison between the pressure drop obtained when body force was not applied and pressure drop obtained after the application of void body force at different drag laws. The pressure drops investigated were obtained when air velocity was at 0.1 and 0.4 m/s. This velocity range was chosen in order to cover the velocity before and after the minimum fluidization velocity. It can be concluded that before U_{mf} was achieved, (0.1 m/s velocity), prediction obtained when void body force was applied was better than when the body force was not incorporated. However, at 0.4 m/s, the model with no application of body force predicted better (Fig. 6.18) because at 0.4 m/s the air penetration through the bed was sufficiently high to suspend larger percent of the bed.
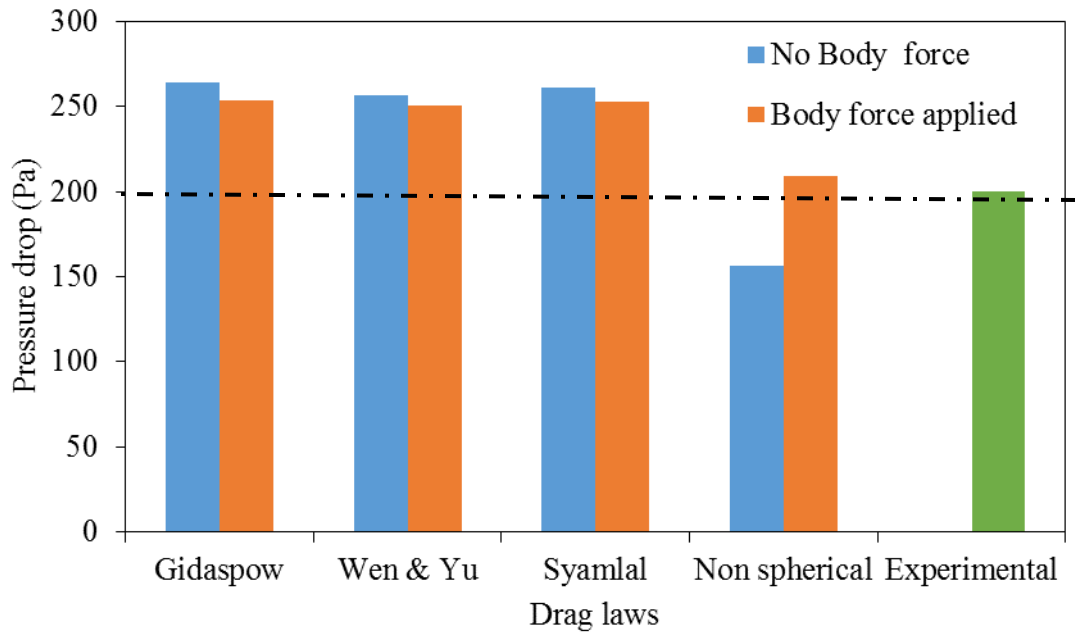
Figure 6.17: Comparison of pressure drop obtained from modeling with and without application of body force at different drag law and velocity of 0.1 m/s air velocity.
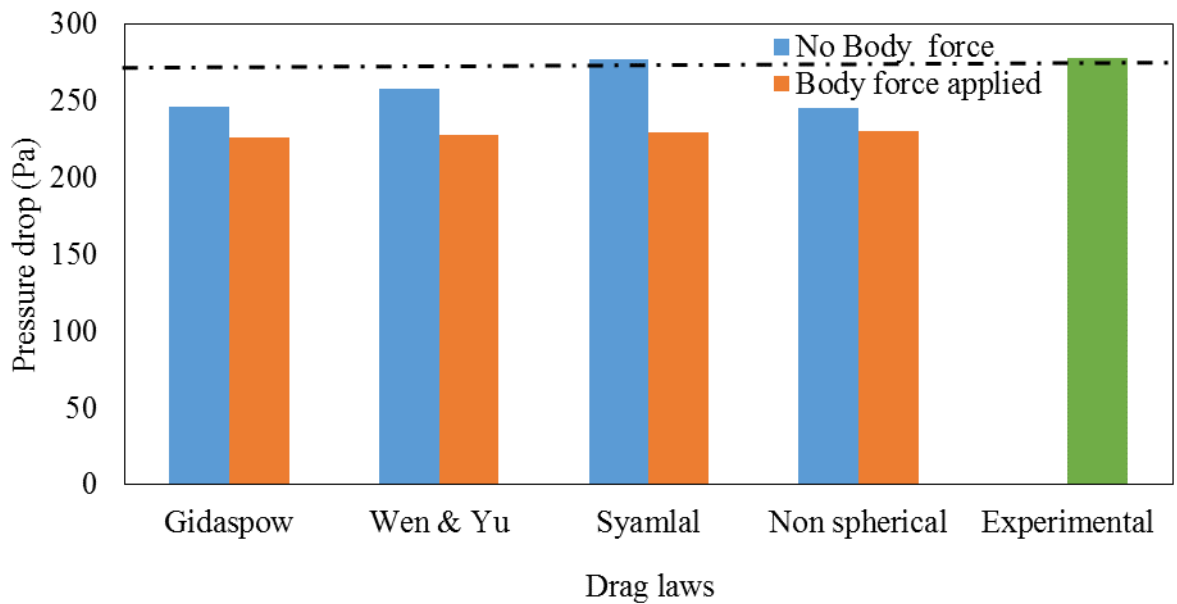
Figure 6.18 Comparison of pressure drop obtained from modeling with and without application of body force at different drag law and velocity of 0.4 m/s air velocity.

However, the bed entrainments were not significantly affected by application of body force. It can be seen from Fig 6.19 that the mass entrainment increased with increase in velocity. Particle entrainment increased under application of body force (Fig 6.19) compared with when body force was not applied (Fig 6.12).
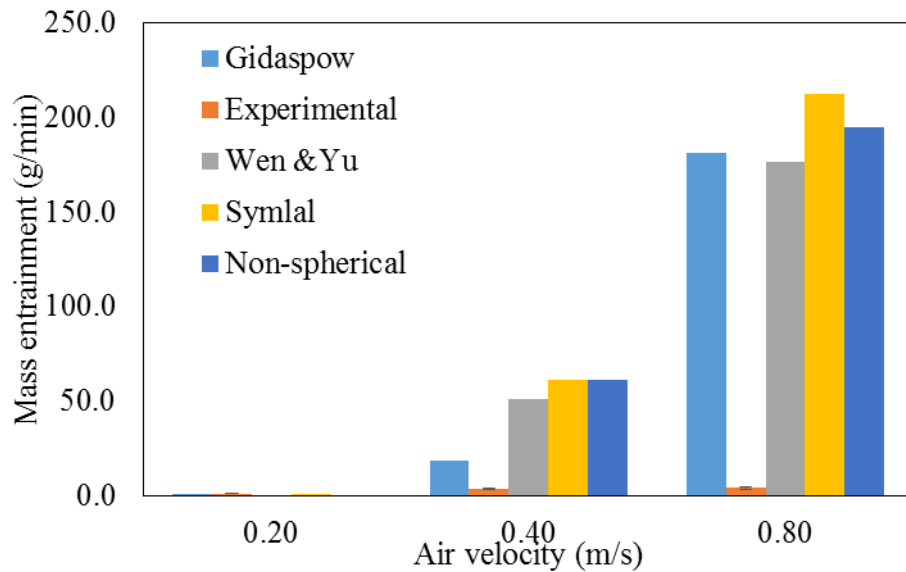
Figure 6.19: Comparison of predicted and experimental bed material entrainment as velocity increased under application of body force.

6.4.7   Prediction of minimum fluidization velocity

The minimum fluidization velocity was identified by following the methods used in section 6.4.5. The experimental U_{mf} was found to be 0.2 m/s. while non-spherical drag law predicted 0.1 m/s all other drag law under predicted the experimental data with more than 50% error (Fig 6.20). In addition, the result of minimum fluidization velocity is similar to the result obtained when body force was not applied (Fig. 6.13). The inability of the drag laws to predict the U_{mf} of loblolly pine wood confirms the need to modify existing equations for loblolly pine wood grinds.
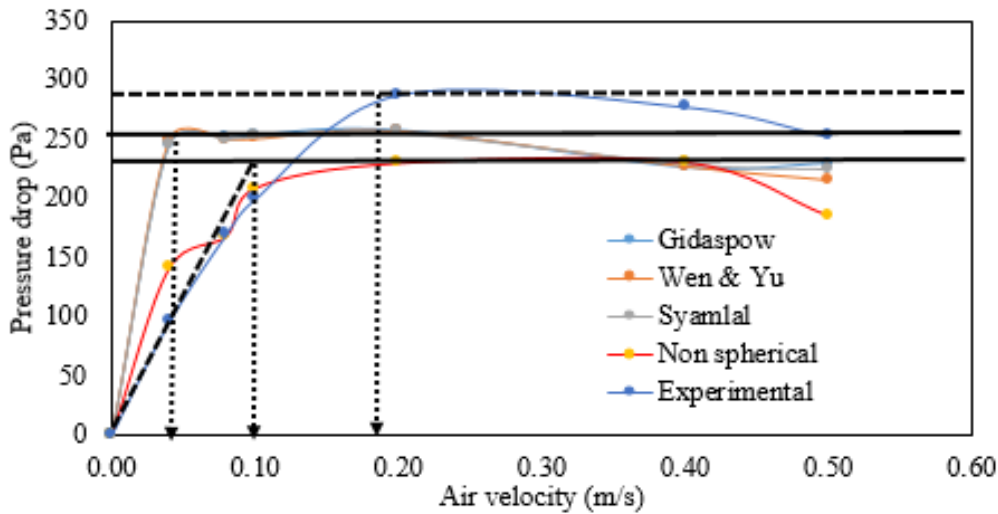
Figure 6.20: Pressure drop against velocity for determination of minimum fluidization velocity of bed having body force applied.

6.5   Conclusion

The first part of the study investigated the effect of mesh size on predictive capability of Eulerian-Lagrangian coupled with Dense Discreet Phase Model (DDPM) in a solid gas flow fluidized bed consisting of particles having lognormal distribution. The computational domain was of laboratory scale size and even numbers of mesh sizes simulation ranging from 400 to 60000 were simulated and presented. The results of the simulation were analyzed using pressure drop prediction and the ability of the voidage to reach a stable profile with increase in simulation time. For pressure drop, the percentage errors for each mesh were 12.51 %, 15.8 %, 8.6 %, 9.2%, and 8.6% for the 3570, 3740, 33728, 45390, and 63510 numbers of meshes respectively. Similarly, the plot of bed voidage with time showed similar profile for all the mesh considered. In addition, the bed voidage converged at 2-second simulation time. The percentage errors for each different mesh size were 28.7 %, 15.3 %, 15.6 %, 15.3%, and 15.3 % for 3570, 3740, 33728, 45390, and 63510. However, for bed voidage, all equation converged nicely at 2 seconds

231

simulation time. Hence, due to least percent error in pressure drop prediction, 33728-mesh size was used for subsequent study.

Simulation results showed that the drag models generally under predicted the pressure drop with maximum mean relative deviation (MRD) obtained from non-spherical drag law. In addition, the Gidaspow, Wen & Yu and Syamlal-Obrien failed to predict the minimum fluidization velocity. When body force correlation was applied, we could not resolve the convergence problem at 0.2 m/s. However, the body force application resulted in reduction of MRD of the non-spherical drag law but no significant influence on other drag equation in pressure drop prediction were observed. In addition, the body force application did not improve the prediction of U_{mf} of the all drag equations except the non-spherical drag model. We also observed that particle entrainment occurred after simulations time of 2 second and this was experimentally validated. It can be safely concluded that there is a need to modify drag law equations if they are to be used to simulate the fluidization of particles with lognormal particle size distribution.

6.6   Reference

ASTM. 2007. Standard test methods for direct moisture content measurement of wood and wood-base materials. American Society for Testing Materials. ASTM International West Conshohocken, PA.

Benzarti, S., H. Mhiri, and H. Bournot. 2012. Drag models for Simulation Gas-Solid Flow in the Bubbling Fluidized Bed of FCC particles. *World Academy of Science, Engineering and Technology* 61.

Brandani, S., and K. Zhang. 2006. A new model for the prediction of the behaviour of fluidized beds. *Powder Technology* 163(1):80-87.

Capareda, S. 2013. *Introduction to biomass energy conversions*. CRC Press.

Chen, X., W. Zhong, X. Zhou, B. Jin, and B. Sun. 2012. CFD–DEM simulation of particle transport and deposition in pulmonary airway. *Powder Technology* 228(0):309-318.

Chialvo, S., J. Sun, and S. Sundaresan. 2012. Bridging the rheology of granular flows in three regimes. *Physical Review E* 85(2):021305.

Clift, R., J. R. Grace, and M. E. Weber. 1978. Bubbles, drops, and particles. Accademic Press.

Cloete, S., S. T. Johansen, and S. Amini. 2015. Grid independence behaviour of fluidized bed reactor simulations using the Two Fluid Model: Effect of particle size. *Powder Technology* 269(0):153-165.

Ergun, S. 1952. Fluid flow through packed columns. *Chem. Eng. Prog.* 48:89-94.

FLUENT, M. 2012. ANSYS Release Version 14.5, ANSYS Inc. Documentation.

Garside, J., and M. R. Al-Dibouni. 1977. Velocity-voidage relationships for fluidization and sedimentation in solid-liquid systems. *Industrial & Engineering Chemistry Process Design and Development* 16(2):206-214.

Gidaspow, D. 1986. Hydrodynamics of fiuidizatlon and heat transfer: Supercomputer modeling. *Applied Mechanics Reviews* 39(1):1-23.

Haider, A., and O. Levenspiel. 1989. Drag coefficient and terminal velocity of spherical and nonspherical particles. *Powder Technology* 58(1):63-70.

Hrenya, C. M., and J. L. Sinclair. 1997. Effects of particle-phase turbulence in gas-solid flows. *AIChE Journal* 43(4):853-869.

Huilin, L., and D. Gidaspow. 2003. Hydrodynamics of binary fluidization in a riser: CFD simulation using two granular temperatures. *Chemical Engineering Science* 58(16):3777-3792.

Kumar, N., S. Ramaswamy, and A. Sood. 2011. Symmetry properties of the large-deviation function of the velocity of a self-propelled polar particle. *Physical Review Letters* 106(11):118001.

Li, T., A. Gel, S. Pannala, M. Shahnam, and M. Syamlal. 2014. Reprint of "CFD simulations of circulating fluidized bed risers, part I: Grid study". *Powder Technology*.

Louge, M., E. Mastorakos, and J. Jenkins. 1991. The role of particle collisions in pneumatic transport. *Journal of Fluid Mechanics* 231:345-359.

Morsi, S., and A. Alexander. 1972. An investigation of particle trajectories in two-phase flow systems. *Journal of Fluid Mechanics* 55(02):193-208.

Pei, P., K. Zhang, and D. Wen. 2012. Comparative analysis of CFD models for jetting fluidized beds: The effect of inter-phase drag force. *Powder Technology* 221(0):114-122.

Pin, S., W. Rashmi, M. Khalid, C. Chong, M. Woo, and L. Tee. 2014. Simulation of spray drying on Piper betle Linn extracts using Computational Fluid Dynamics. *International Food Research Journal* 21(3):1053-1060.

Rajeswari, M. S. R., K. Azizli, S. Hashim, M. Abdullah, M. A. Mujeebu, and M. Abdullah. 2011. CFD simulation and experimental analysis of flow dynamics and grinding performance of opposed fluidized bed air jet mill. *International Journal of Mineral Processing* 98(1):94-105.

Rao, A., J. S. Curtis, B. C. Hancock, and C. Wassgren. 2011. Classifying the fluidization and segregation behavior of binary mixtures using particle size and density ratios. *AIChE Journal* 57(6):1446-1458.

Richardson, J. F., and W. N. Zaki. 1954. Sedimentation and fluidization (Part 1). *Trans. Inst. Chem. Eng,.* 32:35 -52.

Rundle, C., M. Lightstone, P. Oosthuizen, P. Karava, and E. Mouriki. 2011. Validation of computational fluid dynamics simulations for atria geometries. *Building and Environment* 46(7):1343-1353.

Sande, P., and S. Ray. 2014. Mesh size effect on CFD simulation of gas-fluidized Geldart A particles. *Powder Technology* 264:43-53.

Sen, M., D. Barrasso, R. Singh, and R. Ramachandran. 2014. A multi-scale hybrid CFD-DEM-PBM description of a fluid-bed granulation process. *Processes* 2(1):89-111.

Shi, D.-P., Z.-H. Luo, and A.-Y. Guo. 2010. Numerical simulation of the gas− solid flow in fluidized-bed polymerization reactors. *Industrial & engineering chemistry research* 49(9):4070-4079.

Syamlal, M., and T. O'Brien. 1988. Simulation of granular layer inversion in liquid fluidized beds. *International Journal of Multiphase Flow* 14(4):473-481.

Syamlal, M., and T. J. O'Brien. 1989. Computer simulation of bubbles in a fluidized bed. In *AIChE Symp. Ser.*

Takamasa, T., and A. Tomiyama. 1999. Three-dimensional gas–liquid two-phase bubbly flow in a C-shaped tube. In *Proceedings of the 1999 NURETH-9 Conference.*

Van Wachem, B., J. Schouten, C. Van den Bleek, R. Krishna, and J. Sinclair. 2001. CFD modeling of gas-fluidized beds with a bimodal particle mixture. *AIChE Journal* 47(6):1292-1302.

Vejahati, F., N. Mahinpey, N. Ellis, and M. B. Nikoo. 2009. CFD simulation of gas–solid bubbling fluidized bed: A new method for adjusting drag law. *The Canadian Journal of Chemical Engineering* 87(1):19-30.

Wang, Q., T. Niemi, J. Peltola, S. Kallio, H. Yang, J. Lu, and L. Wei. 2014. Particle size distribution in CPFD modeling of gas–solid flows in a CFB riser. *Particuology*(0).

Wei, X., X. Meng, X. Ma, J. Zhang, and X. He. 2007. Design and Optimization of Fluid-bed Reactor of Biomass Pyrolysis System. In *Challenges of Power Engineering and Environment*, 1134-1138. K. Cen, Y. Chi, and F. Wang, eds: Springer Berlin Heidelberg.

Wen, C. Y., and Y. H. Yu. 1966. A generalized method for predicting the minimum fluidization velocity. *AIChE Journal* 12(3):610-612.

Yasuna, J. A., H. R. Moyer, S. Elliott, and J. L. Sinclair. 1995. Quantitative predictions of gas-particle flow in a vertical pipe with particle-particle interactions. *Powder Technology* 84(1):23-34.

Ye, M., M. Van der Hoef, and J. Kuipers. 2005. The effects of particle and gas properties on the fluidization of Geldart A particles. *Chemical Engineering Science* 60(16):4567-4580.

Zhang, K., S. Brandani, J. Bi, and J. Jiang. 2008. CFD simulation of fluidization quality in the three-dimensional fluidized bed. *Progress in Natural Science* 18(6):729-733.

Zhuang, Y.-Q., X.-M. Chen, Z.-H. Luo, and J. Xiao. 2014. CFD–DEM modeling of gas–solid flow and catalytic MTO reaction in a fluidized bed reactor. *Computers & Chemical Engineering* 60(0):1-16.

Chapter 7: Conclusion and Recommendation

7.1   Conclusions

Importance of particle size in fluidization dynamics of ground loblolly pine wood and switchgrass has been researched in this dissertation. In this regard, some light has been shed on the fluidization parameter which are of importance to the design, operation and control of fluidized bed systems. In chapter 3, it was shown that the use of mean particle diameter in fluidization equation would result in wrong parameter estimation because the particles of the material considered in this study are non-spherical and the distributions are not normal. This was illustrated by experimental determination of U_{mf} of ground loblolly pine wood then employed some fluidization equation to predict the experimental data. The result showed that Geldart model should be cautiously applied for biomass material. Also, the fluidization equation used must be modified before a good prediction can be obtained. Chapter 4 addressed the fluidization challenges faced with ground switchgrass. Switchgrass shapes are extremely spiky, thin, and flexible. Several authors have previously reported their inability to fluidize switchgrass. So we look at different fluidization behavior of switchgrass grind at different airflow by using the principle of pressure drop again superficial gas flow velocity. Swichgrass was ground multiple times in order to see if there will be improvement in switchgrass size particles, however, the result showed that size reduction by multiple grinding has no significant effect on switchgrass physical properties. Furthermore, the U_{mf} of switchgrass was found to be 0.3 m/s but fluidizing switchgrass at this velocity resulted in an un-fluidized bed.

Furthermore, the study examined the effect of particle size based on sieve fractions on the determination of the U_{mf} and found about 100 percent differences in U_{mf} of the smallest sized fraction compared to biggest sized fraction. Further still, this chapter examined the behavior of fluidizing switchgrass with sand material addition at different proportion of switchgrass. The U_{mf} of the mixture and the sand component were equal. Whereas there was a difference between the U_{mf} of the switchgrass ground only and the switchgrass-sand mixture. However, as switchgrass fraction increased, the pressure –velocity graph start to exhibit some differences in profile. The issue of moisture content of ground loblolly pine wood was on fluidization of biomass was the major focus of Chapter 5. The result of the physical properties show that as moisture content increased the bulk density and particle density increases. Also the value of porosity was found to increase from 0.81 to 0.91with an increase in moisture content. However, with an increase in moisture content, the particle size distribution reduced with coefficient of variation value ranges from 90 at 8.45% MC to 40 at 25% MC. The minimum fluidization velocity (U_{mf}) was found to be 0.2 m/s for 8% MC, 0.24 for 14.86% MC, 0.28 m/s for19.86 % MC and 0.32 m/s for 27.02% MC. Generally, as moisture content increase the minimum fluidization velocity values also increases. Using a popular fluidization model scheme, model fitting using different diameter types was performed, the correlations developed predicted the experimental data with mean relative deviation that were less than 21%. In chapter 6, since the correlation developed in chapter 5 were material specific and they are excellent under the fitting condition, we developed a pressure drop velocity relationship using Ergun's equation as a springboard. In this study, a new void fraction correlation was developed and model fitting was carried out by including terms for coefficient of

variation, and particle shape that was originally lacking in Ergun's equation. The

behavior of ground loblolly pine wood particle were investigated using computational

fluid dynamics through the commercial code FLUENT ANSYS sopftware using

Eulerian-Lagraningian approach in Chapter 6. The proposed CFD model used particle

size distribution data obtained from Camsizer software® to generate an injection file that

served as input file. The study evaluate different drag laws in fluent for ground biomass

fluidized bed simulation specifically, the pressure drop at different air velocity were

estimated. The result showed that the drag laws in Fluent ansys need to be adjusted

before a reasonable prediction of minimum fluidization velocity could be obtained. The

result also showed that particle entrainment out of the bed occurs within by 2 seconds

simulation time.

7.2   Original contributions

The novel aspects of this study are as follows:

    a) Detailed study of moisture effect and size distribution on clod flow fluidization properties and behavior of non-uniform and non-spherical particles.

    b) Develop an understanding of influence of diameter measurement scheme on ability of models to predict fluidization properties of non-uniform and non-spherical particles.

    c) Developing a pressure – velocity model by modifying Ergun's equation. This also includes redeveloping void fraction correlation of ground loblolly pine wood

    d) Developing an Eulerian-Lagrangian (E-L) model for the numerical simulation of ground loblolly pine wood fluidized bed and validating the simulation results by experimental data. The impact of airflow velocity on bed inventory trajectories and mixing behavior of the fluidized bed was also scrutinized.

7.3 Future work and recommendation

This research shed light on the impact of the irregular particles on the typical characteristics of fluidized beds. In addition to the insight gained about the characteristics, at different flow velocities, segregation and channeling now makes it more clearer some of the aspects that calls for a more in-depth study

7.3.1 Determining the hydrodynamics of the biomass under real hot condition

It is well known that at a high temperature the volatiles loss and individual particle mass reduction due to thermal decomposition will affect particle buoyancy, segregation and some other fluidized bed behavior studied in this work. It is therefore important to understand particle trajectory, bubble formation, particle entrainment, and segregation at elevated temperatures and different fluidizing velocities.

7.3.2 Determining the effect of bed distributor to velocity distribution and pressure drop

During the development of the cold flow fluidized bed, the choice of distributors vis-à-vis pressure drop because of airflow were not considered. This eventually caused the pump to overheat at high velocity. There are no published work that made attempt at optimizing optimize particle size with the permeability of distributor in relation to the pressure drop.

7.3.3 Effect of bed width on fluidization

It was observed in this study that at certain bed mass (30 g) particle fluidization becomes erratically unpredictable for instance bed material sometime settles at a particular size in the bed and an already fluidized bed could be considered as defluidized. I suppose that

when the bed width was too wide for the sample causing fluidization behavior to change. Hence looking at bed width may help in determining the critical load of biomass

7.3.4 Estimating the void fraction of ground biomass

There is a need to better understand how the bulk density and particle density of ground biomass relates to it void fraction. This study has shown that the void fraction is high (0.8). However, at 0.8 void fraction, it suggests that, 80% of every one unit volume constitute the air space /void. In reality, this is not true. Hence the need to redefine the void fraction of ground biomass.

Appendix 1: Additional data for Chapter 1

Table 2.2: Properties of powders in Geldart's classification (Ajbar et al., 2002; Fan and
Zhu, 2005; Geldart, 1973; Geldart and Cranfield, 1972)

Geldart's Grouping	Particle size (µm)	Particle density (kg/m^3)	Bed expansion behavior	Bubbling formation
		Properties and behavior of particles during fluidization		
A	20 and 100	< 1400	Bed expand considerably before bubbling commences and collapse slowly at the rate of 0.3 – 0.6 cm/s when gas supply is suddenly cut off.	In freely bubbling beds, the velocity of small bubbles (< 4 cm) appears to be about 30 – 40 cm/s regardless of bubble size.
B	40 < dp <500	1400 – 4000	Small bed expansion and rapid collapse of bed when gas supply is cut off.	Bubble size increases linearly with both bed height and excess gas velocity (U - Uo).
C	dp < 20	200 - 1200	Powder lifts as a plug in a small diameter tube or formation of channel extending from distributor to the bed surface. Bed collapses slowly when gas supply is cut off.	Inter-particle forces are generally higher than forces exerted by fluid on the particle due to small particle size, strong electrostatic charges and or wet or sticky material, making bubbling formation difficult.
D	dp > 1000	> 400	Bed expansion is low and it is characterized by combination of steady slug motion and intense irregular particles motion. Bed collapse rapidly when gas supply is cut off.	Instead of bubbling, spouted bed can easily form

Appendix 2.1: Aperture sizes for test sieves

ISO 3310-1 Supplementary Sizes R40/3	US Sieve No.	US Sieve Opening		Tyler Designation
mm		mm	in.	
4.75	4	4.76	0.187	4
3.35	6	3.36	0.132	6
2.36	8	2.38	0.0937	8
1.70	12	1.68	0.0661	10
1.18	16	1.19	0.0469	14
µm		µm		
850	20	841	0.0331	20
600	30	595	0.0234	28
425	40	420	0.0165	35
300	50	297	0.0117	48
212	70	210	0.0083	65
150	100	149	0.0059	100
106	140	105	0.0041	150
75	200	74	0.0029	200
53	270	53	0.0021	270
Pan				

Appendix 2: Additional data for Chapter 3
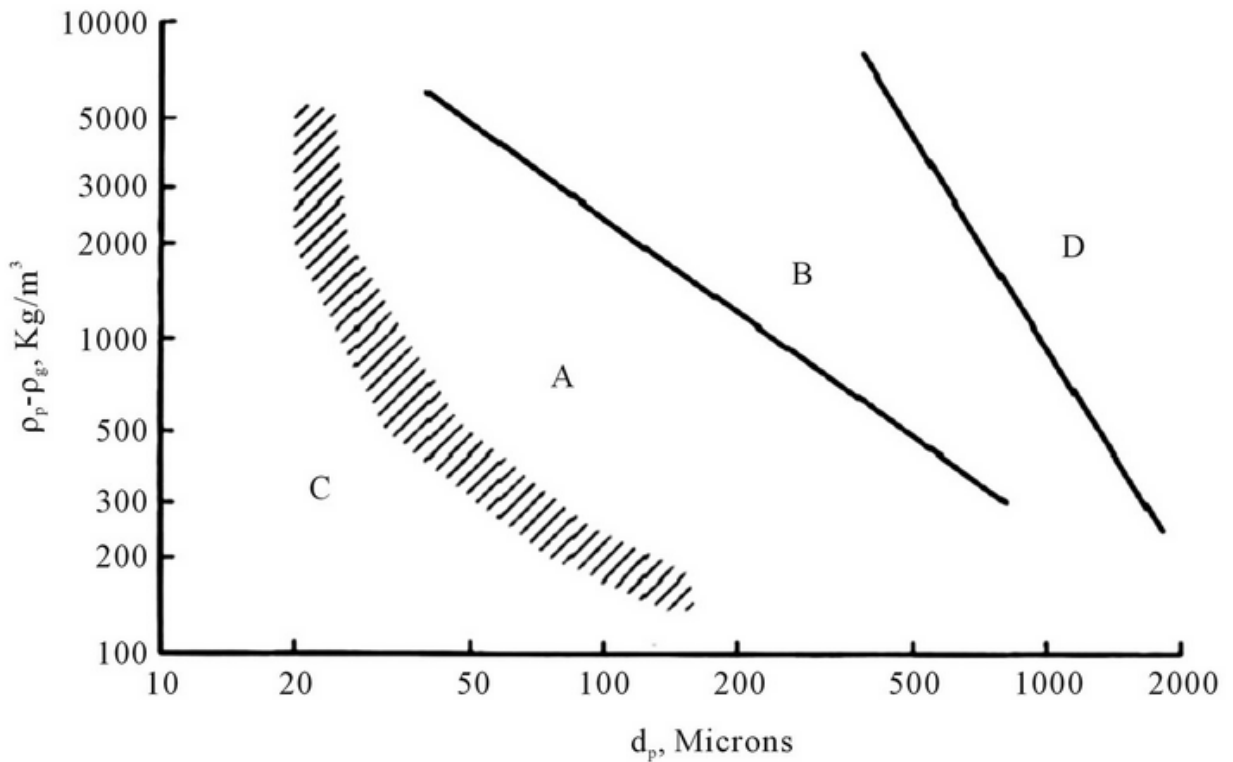
Figure 1: Geldart's classification

Table : Range specification for FM Metal Vane anemometer, model 407113, Nashua, NH 03063

Air Velocity Measurements	Range	Resolution	Accuracy (%rdg)
m/s (meters per second)	0.50 - 35.00 m/s	0.01 m/s	± (2% + 0.2m/s)
km/h (kilometers per hour)	1.8 – 126.0 km/h	0.1 km/h	± (2% + 0.8km/h)
ft/min (feet per minute)	100 – 6890 ft/min	1 ft/min	± (2% + 40ft/min)
mph (miles per hour)	1.1 – 78.3 mph	0.1 mph	± (2% + 0.4m/h)
knots (nautical miles per hour)	1.0 to 68 knots	0.1 knots	± (2% + 0.4knots)
Air Flow Measurements	Range	Resolution	Area
CMM (cubic meters per minute)	0-999,900 m³/min	0.001 to 100	0 to 9,999m²
CFM (cubic feet per minute)	0-999,900 ft³/min	0.001 to 100	0 to 9,999ft²
Air Temperature	Range	Resolution	Accuracy
	32 to 175°F (0 to 80°C)	0.1° F/C	1.5°F (0.8°C)

243

Actual minimum fluidization velocity for unfractionated and fractionated loblolly pine wood grids and effect of diameter measurement schem.

		Ergun	Mod-Ergun	Leva	Geldart	Miller
		mininum Fluidization velocity (m/s)				
	Dimater scheme	0.96	1.52	0.37	0.30	0.50
Sample A	Martins	1.11	1.71	0.53	0.43	0.73
	Chord	1.16	1.77	0.59	0.48	0.82
	MFD	0.92	1.47	0.34	0.28	0.45
	Surf-vol.	0.96	1.52	0.37	0.30	0.50
	Geometric					
Sample B1	Martins	2.28	3.02	1.64	1.26	2.50
	Chord	2.46	3.24	2.12	1.63	3.33
	MFD	2.54	3.34	2.37	1.82	3.75
	Surf-vol.	2.28	3.02	1.64	1.26	2.50
	Geometric	2.47	3.25	2.14	1.65	3.36
Sample B2	Martins	1.99	2.63	1.03	0.80	1.50
	Chord	2.16	2.86	1.39	1.08	2.10
	MFD	2.24	2.96	1.58	1.22	2.41
	Surf-vol.	2.02	2.68	1.09	0.85	1.60
	Geometric	2.29	3.03	1.73	1.34	2.65
Sample B3	Martins	1.57	2.12	0.63	0.51	0.88
	Chord	1.77	2.38	0.97	0.77	1.41
	MFD	1.83	2.47	1.10	0.87	1.62
	Surf-vol.	1.63	2.20	0.73	0.58	1.04
	Geometric	1.86	2.51	1.17	0.93	1.73
Sample B4	Martins	1.18	1.65	0.35	0.28	0.46
	Chord	1.35	1.89	0.57	0.46	0.78
	MFD	1.40	1.97	0.66	0.53	0.92
	Surf-vol.	1.21	1.70	0.38	0.31	0.51
	Geometric	1.40	1.96	0.65	0.52	0.91
Sample B5	Martins	0.77	1.20	0.12	0.10	0.15
	Chord	0.91	1.42	0.23	0.19	0.29

	MFD	0.95	1.49	0.27	0.22	0.34
	Surf-vol.	0.77	1.20	0.12	0.10	0.15
	Geometric	0.98	1.53	0.30	0.24	0.39
Sample B6	Martins	0.65	1.37	0.16	0.13	0.20
	Chord	0.67	1.41	0.18	0.15	0.22
	MFD	0.69	1.46	0.20	0.17	0.25
	Surf-vol.	0.43	0.93	0.04	0.03	0.04
	Geometric	0.53	1.12	0.08	0.07	0.09
	Martins	0.84	1.14	0.08	0.07	0.09
	Chord	1.00	1.36	0.15	0.13	0.19
	MFD	1.02	1.40	0.17	0.15	0.21
Sample B7	Surf-vol.	0.72	0.99	0.05	0.04	0.05
	Geometric	0.85	1.16	0.09	0.07	0.10

Picture of the fluidized bed used in this study

Sas code for analysis of variance on particle size measurement method

```
data chapter3data;
input size$ chord     Ferret Martins Surface-volume Geometric;
datalines;
whol   0.821   0.821   0.821   0.821   0.821
whol   0.953   0.953   0.953   0.953   0.953
whol   0.83    0.83    0.83    0.83    0.83
17     2.101   2.231   1.812   1.833   2.125
17     2.086   2.214   1.815   1.81    2.122
17     2.152   2.287   1.847   1.854   2.133
14     1.691   1.807   1.428   1.475   1.805
14     1.686   1.801   1.417   1.46    1.805
14     1.676   1.789   1.415   1.466   2.061
1      1.381   1.486   1.029   1.188   1.561
1      1.392   1.5     1.134   1.191   1.548
1      1.389   1.494   1.142   1.195   1.512
0.6    1.045   1.138   0.796   0.84    1.104
0.6    1.06    1.151   0.804   0.845   1.13
0.6    1.013   1.098   0.788   0.822   1.145
0.3    0.632   0.689   0.448   0.444   0.824
0.3    0.648   0.706   0.454   0.452   0.661
0.3    0.608   0.665   0.436   0.4397  0.728
0.15   0.284   0.315   0.634   0.245   0.34
0.15   0.571   0.605   0.386   0.233   0.362
0.15   0.508   0.85    0.551   0.23    .
0.53   0.526   0.562   0.373   0.242   0.17
0.53   0.397   0.428   0.268   0.243   0.16
0.53   0.593   0.625   0.44    0.312   0.17

;
run;
proc glm data = chapter3data;
class size;
model Xc Femin martin surface geom= size;
means size/ duncan;
run;
```

Analysis of variance with dependent Variable: Chord diameter

Source	DF	Sum of Squares	Mean Square	F Value	Pr > F

Source	DF	Sum of Squares	Mean Square	F Value	Pr > F
Model	7	7.49385063	1.07055009	212.07	<.0001
Error	16	0.08077000	0.00504812		
Corrected Total	23	7.57462062			

R-Square	Coeff Var	Root MSE	Chord Mean
0.989337	6.547647	0.071050	1.085125

Analysis of variance with dependent Variable: Femin

Source	DF	Sum of Squares	Mean Square	F Value	Pr > F
Model	7	8.14662996	1.16380428	103.37	<.0001
Error	16	0.18013200	0.01125825		
Corrected Total	23	8.32676196			

R-Square	Coeff Var	Root MSE	Femin Mean
0.978367	9.080113	0.106105	1.168542

Analysis of variance with dependent Variable:: martin

Source	DF	Sum of Squares	Mean Square	F Value	Pr > F
Model	7	5.44331729	0.77761676	186.03	<.0001
Error	16	0.06688267	0.00418017		
Corrected Total	23	5.51019996			

R-Square	Coeff Var	Root MSE	martin Mean
0.987862	7.046460	0.064654	0.917542

Analysis of variance with dependent Variable: Surface-volume diameter

Source	DF	Sum of Squares	Mean Square	F Value	Pr > F
Model	7	6.99128443	0.99875492	1017.67	<.0001

Source	DF	Sum of Squares	Mean Square	F Value	Pr > F
Error	16	0.01570259	0.00098141		
Corrected Total	23	7.00698702			

R-Square	Coeff Var	Root MSE	surface Mean
0.997759	3.509478	0.031327	0.892654

Sas code for analysis of variance on densities

```
data chapter3data;
input size$ Bulk particle porosity;
datalines;
1.7     277     1474   0.812075984
1.7     278     1470.7 0.810974366
1.7     279     1470.3 0.810242808
1.4     280     1457.6 0.807903403
1.4     276     1469.5 0.812181014
1.4     277     1471.3 0.811731122
1       323     1484.7 0.782447633
1       320     1461.7 0.781076828
1       319     1465.7 0.782356553
0.6     297     1464.4 0.797186561
0.6     282     1464.3 0.807416513
0.6     292     1475.9 0.802154618
0.3     234     1482.5 0.842158516
0.3     236     1478.3 0.840357167
0.3     233     1500.1 0.844677022
0.15    169     1493.4 0.886835409
0.15    172     1516.8 0.886603376
0.15    167     1528.1 0.890713959
0.053   165     1510.6 0.890771879
0.053   167     1515.9 0.889834422
0.053   167     1546.5 0.892014226
whole   326.81 1448.3 0.774349237
whole   316.013        1447.7 0.781713753
whole   311.4   1449.6 0.785182119
;
run;
proc glm data = chapter3data;
class size;
model Bulk particle porosity= size;
means size/ duncan;
run;
```

Analysis of variance with dependent Variable: Bulk

Source	DF	Sum of Squares	Mean Square	F Value	Pr > F
Model	7	78546.62817	11220.94688	638.67	<.0001
Error	16	281.10769	17.56923		
Corrected Total	23	78827.73586			

R-Square	Coeff Var	Root MSE	Bulk Mean
0.996434	1.631959	4.191567	256.8426

Dependent Variable: particle

Source	DF	Sum of Squares	Mean Square	F Value	Pr > F
Model	7	13663.29625	1951.89946	14.48	<.0001
Error	16	2157.00000	134.81250		
Corrected Total	23	15820.29625			

R-Square	Coeff Var	Root MSE	particle Mean
0.863656	0.783903	11.61088	1481.163

Source	DF	Sum of Squares	Mean Square	F Value	Pr > F
Model	7	0.04010476	0.00572925	611.34	<.0001
Error	16	0.00014995	0.00000937		
Corrected Total	23	0.04025471			

R-Square	Coeff Var	Root MSE	porosity Mean
0.996275	0.370639	0.003061	0.825957

Sas code for analysis of variance on shapes

```
data chapter3data;
input size$ sphe aspect Symmetry;
datalines;
1.7     0.599  0.403  0.853
1.7     0.599  0.402  0.852
1.7     0.599  0.403  0.853
1.4     0.572  0.389  0.843
1.4     0.572  0.388  0.845
1.4     0.573  0.39   0.854
1       0.548  0.381  0.828
1       0.547  0.38   0.827
1       0.554  0.384  0.833
0.6     0.519  0.4    0.796
0.6     0.515  0.411  0.797
0.6     0.539  0.393  0.814
0.3     0.409  0.465  0.686
0.3     0.414  0.448  0.688
0.3     0.455  0.483  0.745
0.15    0.239  0.496  0.659
0.15    0.244  0.493  0.656
0.15    0.235  0.486  0.684
0.053   0.43   0.602  0.705
0.053   0.47   0.596  0.704
0.053   0.436  0.606  0.724
whole   0.518  .      0.81
whole   0.502  .      0.795
whole   0.497  .      0.796
;
run;
proc glm data = chapter3data;
class size;
model sphe    aspect  Symmetry= size;
means size/ duncan;
run;
```

Analysis of variance with dependent Variable: Sphericity

Source	DF	Sum of Squares	Mean Square	F Value	Pr > F
Model	7	0.27604394	0.03943485	211.91	<.0001
Error	14	0.00260533	0.00018610		
Corrected Total	21	0.27864927			

R-Square	Coeff Var	Root MSE	sphe Mean
0.990650	2.835035	0.013642	0.481182

Appendix 3: Additional data for Chapter 4
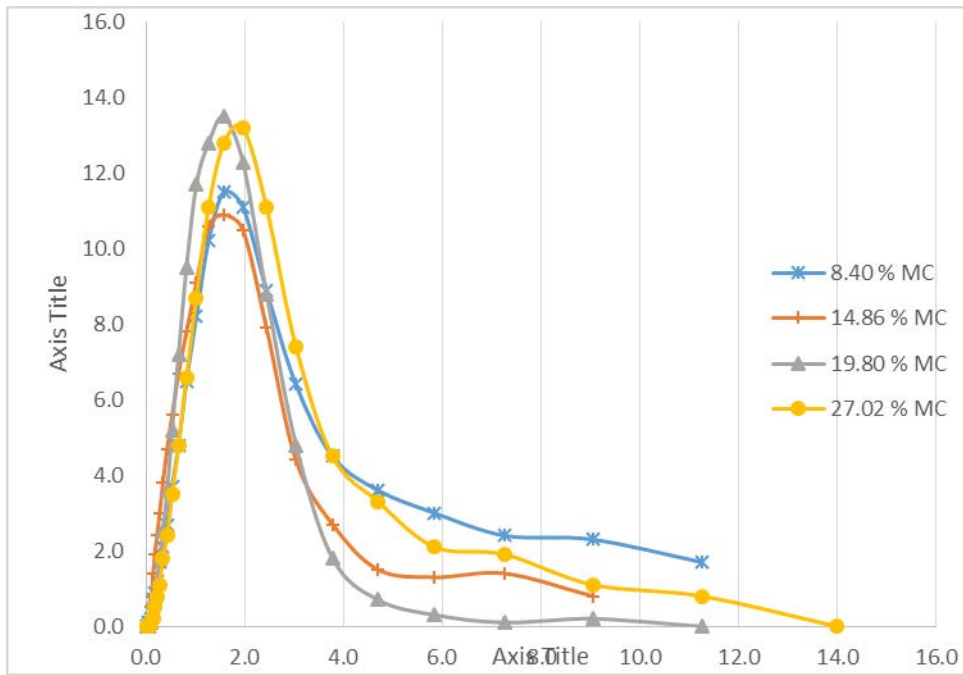
Chord diameter
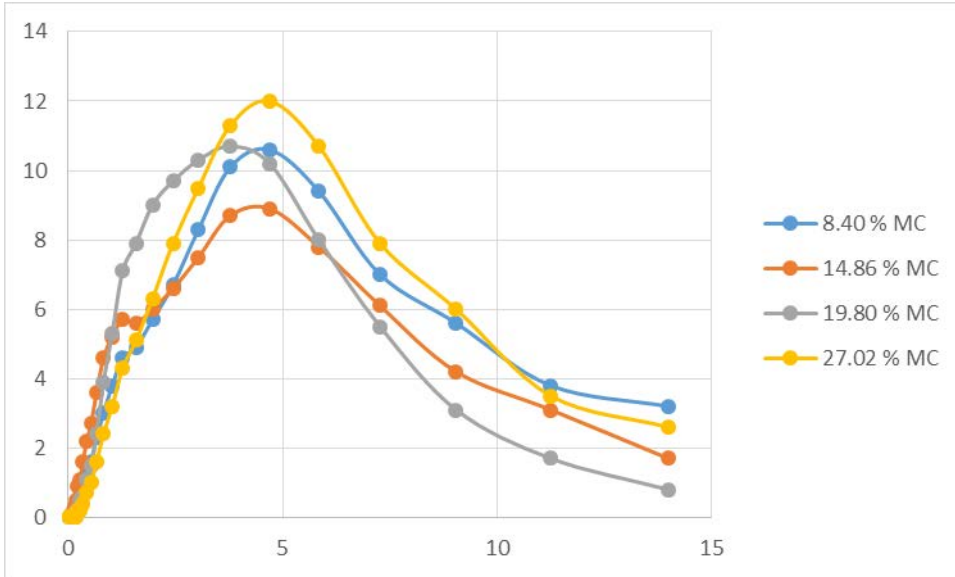
Ferret diameter
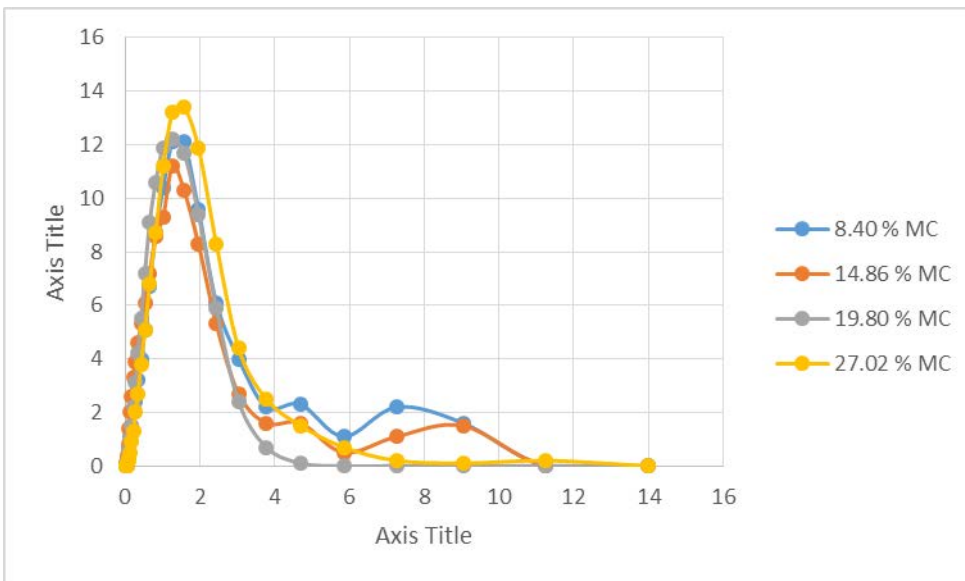
Martins diameter
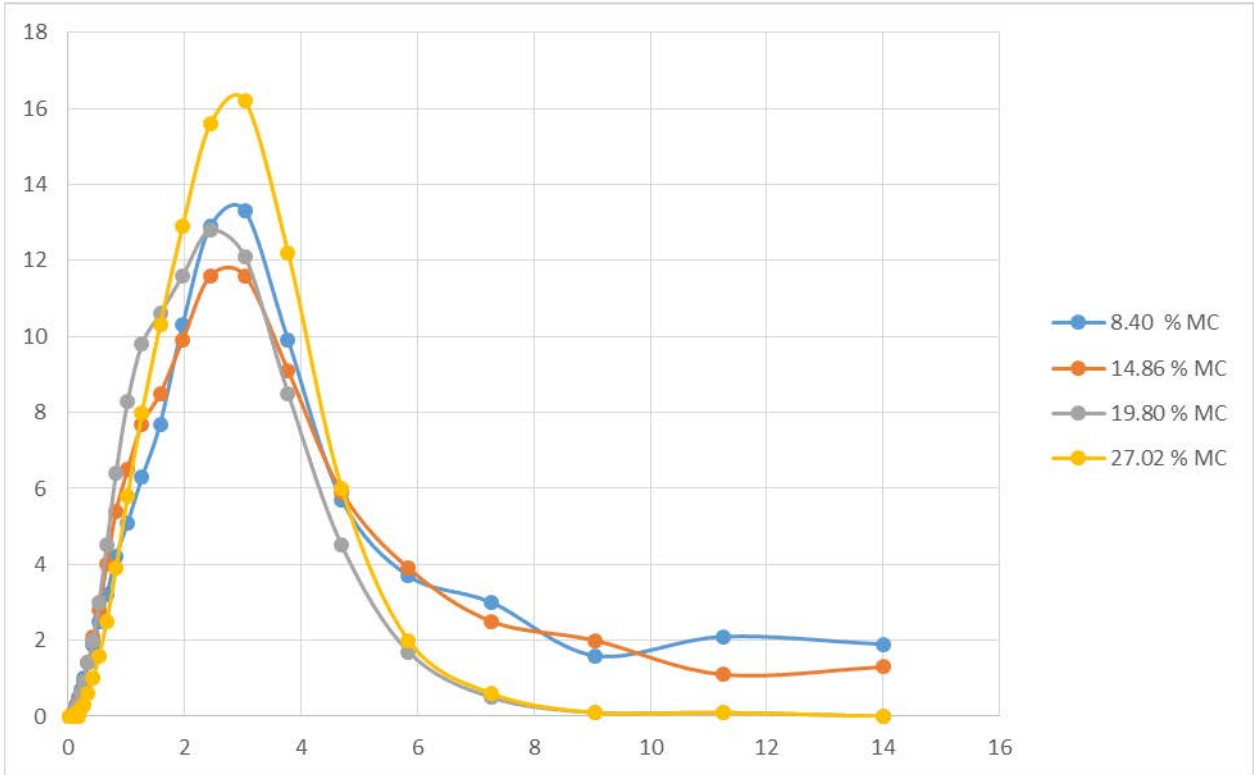
Area diameter

```
data chapter5data;
input size$ M8M14    M20    M25;
datalines;
WHOLE        0.376 0.441 0.475 0.415
WHOLE        0.379 0.445 0.467 0.458
WHOLE        0.343 0.452 0.481 0.396
1.7    0.553 0.546 0.582 0.58
1.7    0.579 0.547 0.578 0.588
1.7    0.572 0.534 0.592 0.59
1.4    0.52  0.482 0.556 0.555
1.4    0.537 0.513 0.557 0.554
1.4    0.531 0.52  0.557 0.56
1      0.489 0.486 0.538 0.518
1      0.488 0.482 0.534 0.53
1      0.505 0.51  0.533 0.532
0.6    0.46  0.482 0.546 .
0.6    0.466 0.479 0.547 .
0.6    0.464 0.473 0.535 .
0.3    0.282 0.339 0.4   .
0.3    0.282 0.335 0.401 .
0.3    0     0.326 0.398 .
;
run;
proc glm data = chapter5data;
```

254

```
class size;
model M8      M14    M20    M25= size;
means size/ duncan;
run;
```

Dependent Variable: M8

Source	DF	Sum of Squares	Mean Square	F Value	Pr > F
Model	5	0.28992378	0.05798476	12.76	0.0002
Error	12	0.05452533	0.00454378		
Corrected Total	17	0.34444911			

R-Square	Coeff Var	Root MSE	M8 Mean
0.841703	15.50391	0.067408	0.434778

Dependent Variable: M14

Source	DF	Sum of Squares	Mean Square	F Value	Pr > F
Model	5	0.07860911	0.01572182	119.86	<.0001
Error	12	0.00157400	0.00013117		
Corrected Total	17	0.08018311			

R-Square	Coeff Var	Root MSE	M14 Mean
0.980370	2.456511	0.011453	0.466222

Dependent Variable: M20

Source	DF	Sum of Squares	Mean Square	F Value	Pr > F
Model	5	0.06785161	0.01357032	524.18	<.0001
Error	12	0.00031067	0.00002589		
Corrected Total	17	0.06816228			

R-Square	Coeff Var	Root MSE	M20 Mean
0.995442	0.987238	0.005088	0.515389

Dependent Variable: M25

Source	DF	Sum of Squares	Mean Square	F Value	Pr > F
Model	3	0.04528067	0.01509356	54.65	<.0001
Error	8	0.00220933	0.00027617		

Source	DF	Sum of Squares	Mean Square	F Value	Pr > F
Corrected Total	11	0.04749000			

R-Square	Coeff Var	Root MSE	M25 Mean
0.953478	3.177488	0.016618	0.523000

```
data chapter5data;
input mc$ whol S1_7 S1_4 S1     S0_6 S0_3;
datalines;
M8     0.376  0.553  0.52   0.489  0.46   0.282
M8     0.379  0.579  0.537  0.488  0.466  0.282
M8     0.343  0.572  0.531  0.505  0.464  .
M14    0.441  0.546  0.482  0.486  0.482  0.339
M14    0.445  0.547  0.513  0.482  0.479  0.335
M14    0.452  0.534  0.52   0.51   0.473  0.326
M20    0.475  0.582  0.556  0.538  0.546  0.4
M20    0.467  0.578  0.557  0.534  0.547  0.401
M20    0.481  0.592  0.557  0.533  0.535  0.398
M25    0.415  0.58   0.555  0.518  .      .
M25    0.458  0.588  0.554  0.53   .      .
M25    0.396  0.59   0.56   0.532  .      .
;
run;
proc glm data = chapter5data;
class MC;
model whol S1_7     S1_4 S1      S0_6   S0_3= mc;
means mc/ duncan;
run;
```

Dependent Variable: whol

Source	DF	Sum of Squares	Mean Square	F Value	Pr > F
Model	3	0.01901400	0.00633800	17.03	0.0008
Error	8	0.00297667	0.00037208		
Corrected Total	11	0.02199067			

R-Square	Coeff Var	Root MSE	whol Mean
0.864640	4.513915	0.019289	0.427333

Dependent Variable: S1_7

Source	DF	Sum of Squares	Mean Square	F Value	Pr > F
Model	3	0.00366425	0.00122142	15.59	0.0011
Error	8	0.00062667	0.00007833		
Corrected Total	11	0.00429092			

R-Square	Coeff Var	Root MSE	S1_7 Mean
0.853955	1.552512	0.008851	0.570083

Dependent Variable: S1_4

Source	DF	Sum of Squares	Mean Square	F Value	Pr > F
Model	3	0.00552967	0.00184322	14.92	0.0012
Error	8	0.00098800	0.00012350		
Corrected Total	11	0.00651767			

R-Square	Coeff Var	Root MSE	S1_4 Mean
0.848412	2.070113	0.011113	0.536833

Dependent Variable: S1

Source	DF	Sum of Squares	Mean Square	F Value	Pr > F
Model	3	0.00432558	0.00144186	14.99	0.0012
Error	8	0.00076933	0.00009617		
Corrected Total	11	0.00509492			

R-Square	Coeff Var	Root MSE	S1 Mean
0.849000	1.915013	0.009806	0.512083

Dependent Variable: S0_6

Source	DF	Sum of Squares	Mean Square	F Value	Pr > F
Model	2	0.01069067	0.00534533	214.77	<.0001
Error	6	0.00014933	0.00002489		
Corrected Total	8	0.01084000			

R-Square	Coeff Var	Root MSE	S0_6 Mean
0.986224	1.008533	0.004989	0.494667

Dependent Variable: S0_3

Source	DF	Sum of Squares	Mean Square	F Value	Pr > F
Model	2	0.01731054	0.00865527	463.68	<.0001
Error	5	0.00009333	0.00001867		
Corrected Total	7	0.01740388			

R-Square	Coeff Var	Root MSE	S0_3 Mean
0.994637	1.250957	0.004320	0.345375

Table 5.2: Particle characterization based on the coefficient of variation (COV)

Screen size (mm)		MC (wet basis)	D_{16}	D_{50}	D_{84}	COV
Control		8.40	0.58 (0.02)	1.44 (0.10)	3.76 (0.1)	90.33[a]
		14.86	0.39 (0.02)	1.08 (0.05)	2.31 (0.2)	65.56[b]
		19.80	0.54 (0.01)	1.14 (0.03)	2.03 (0.05)	58.60[b]
		27.02	0.87 (0.14)	1.58 (0.23)	3.17 (0.80)	42.20[c]
Fractionated sample						
US Sieve #						
Pass through	Retained on					
-	12	8.40	1.49 (0.01)	1.95 (0.02)	2.80 (0.02)	33.70[a]
		14.86	1.52 (0.01)	2.02 (0.2)	2.88 (0.1)	33.60[a]
		19.80	1.54 (0.01)	2.00 (0.01)	2.67 (0.03)	32.20[a]
		27.02	1.45 (0.01)	1.94 (0.01)	2.70 (0.02)	28.20[b]
12	14	8.40	1.15 (0.1)	1.54 (0.01)	2.32 (0.01)	37.99[a]
		14.86	1.14 (0.02)	1.51 (0.02)	2.33 (0.1)	39.54[a]
		19.80	1.17 (0.01)	1.49 (0.01)	1.89 (0.02)	24.33[b]
		27.02	1.08 (0.01)	1.39 (0.01)	1.80 (0.03)	25.82[b]
14	18	8.40	0.83 (0.1)	1.25 (0.10)	1.95 (0.10)	44.90[ba]
		14.86	0.88 (0.01)	1.21 (0.01)	2.07 (0.10)	49.20[a]
		19.80	0.88 (0.01)	1.17 (0.01)	1.62 (0.03)	31.73[b]
		27.02	0.77 (0.01)	1.07 (0.01)	1.58 (0.06)	37.77[ba]
18	30	8.40	0.63 (0.01)	0.94 (0.01)	1.82 (0.01)	64.03[ba]
		14.86	0.60 (0.01)	0.88 (0.01)	1.61 (0.03)	57.10[b]
		19.80	0.57 (0.01)	0.80 (0.01)	1.20 (0.02)	39.60[c]
		27.02	1.07 (0.2)	2.53 (0.3)	4.56 (0.32)	74.05[a]
30	50	8.40	0.34 (0.01)	0.70 (0.1)	1.72 (0.01)	98.6[a]
		14.86	0.33 (0.01)	0.63 (0.01)	1.24 (0.04)	73.03[b]
		19.80	0.27 (0.01)	0.47 (0.01)	0.76 (0.01)	53.46c
		27.02	0.75 (0.01)	1.97 (0.01)	4.25 (0.01)	70.80[b]
50	100	8.40	0.80 (0.1)	1.95 (0.01)	4.89 (0.02)	78.20[a]
		14.86	0.52 (0.01)	1.16 (0.02)	1.96 (0.01)	61.60[b]
		19.80	0.43 (0.2)	1.28 (0.3)	2.84 (1.8)	81.75[a]
		27.02	na	na	na	

na particle cohesiveness caused flow problem during measurement, thus data not available
Data in parenthesis are standard deviation from means of triplicates
COV means coefficient of variation
Data in COV columns within the same screen size classification having the same alphabet are not significantly different

259

Table 4: Effect of moisture contents and diameter types on fractions from ground

Screen size	MC (% w.b)	Diameter types (mm)				
		Area	Chord	Ferret	Martin	Surface-vol.
Whole	8.40	$2.87^{\,a,\,2}(0.41)$	$1.01^{\,a,2\,3}(0.36)$	$4.90^{\,a,1}(0.76)$	$1.59^{\,a,\,3,4}(0.30)$	$0.82^{\,b,4}(0.04)$
	14.86	$2.42^{\,a,\,2}(0.12)$	$1.43^{\,b\,c,3}(0.26)$	$4.18^{\,a,\,1}(0.11)$	$1.18^{\,c\,b,4}(0.01)$	$0.57^{\,c,\,4}(0.03)$
	19.80	$1.89^{\,b,\,2}(0.03)$	$1.30^{\,c,\,3}(0.03)$	$3.10^{\,b,\,1}(0.06)$	$1.03^{\,c,\,4}(0.02)$	$0.71^{\,b\,c,\,5}(0.02)$
	27.02	$2.48^{\,a,\,2}(0.27)$	$1.83^{\,b\,a,\,3}(0.26)$	$4.11^{\,a,\,1}(0.48)$	$1.37^{\,b,\,2}(0.15)$	$1.05^{\,a,\,4}(0.19)$
2.3 > dp < 1.7	8.40	$3.53^{\,b,\,2}(0.1)$	$2.17^{\,b,\,3}(0.10)$	$6.15^{b,\,1}(0.24)$	$1.83^{\,a,\,5}(0.03)$	$1.86^{\,b,\,4}(0.01)$
	14.86	$3.75^{b,\,2}(0.1)$	$2.31^{\,a,\,3}(0.10)$	$6.72^{\,a,\,1}(0.04)$	$1.88^{\,a,\,5}(0.16)$	$1.92^{\,a,\,4}(0.02)$
	19.80	$3.54^{\,a,\,2}(0.1)$	$2.16^{\,b,\,3}(0.04)$	$6.09^{\,c,\,1}(0.15)$	$1.89^{\,a,\,5}(0.02)$	$1.89^{\,b,\,4}(0.01)$
	27.02	$3.37^{\,c,\,2}(0.1)$	$2.1^{\,b,\,3}(0.01)$	$5.72^{\,d,\,1}(0.04)$	$1.88^{\,a,\,4}(0.01)$	$1.83^{\,c,\,5}(0.01)$
1.7 > dp < 1.40	8.40	$2.75^{\,a,\,2}(0.03)$	$1.75^{\,b,3}(0.02)$	$4.87^{\,b,\,1}(0.10)$	$1.37^{\,a,\,5}(0.01)$	$1.46^{\,a,\,4}(0.01)$
	14.86	$2.8^{\,a,2}(0.01)$	$1.79^{\,a,\,3}(0.02)$	$5.07^{\,a,\,1}(0.03)$	$1.37^{\,a,\,5}(0.15)$	$1.44^{b\,a,\,4}(0.03)$
	19.80	$2.63^{\,b,\,2}(0.01)$	$1.61^{\,c,\,3}(0.01)$	$4.53^{\,c,\,1}(0.10)$	$1.36^{\,a,\,4}(0.01)$	$1.42^{\,b,\,4}(0.01)$
	27.02	$2.42^{c,\,2}(0.02)$	$1.48^{d,\,3}(0.02)$	$4.22^{d,\,1}(0.04)$	$1.28^{\,b,\,4}(0.01)$	$1.31^{\,c,\,4}(0.01)$
1.4 > dp < 1.00	8.40	$2.63^{\,a,\,2}(0.25)$	$1.54^{\,a,\,3}(0.05)$	$4.13^{\,b,\,1}(0.14)$	$1.13^{a,\,4}(0.02)$	$1.18^{\,a,\,4}(0.01)$
	14.86	$2.25^{\,b,\,2}(0.07)$	$1.48^{\,a,\,3}(0.04)$	$4.09^{\,a,\,1}(0.01)$	$1.09^{\,b,\,4}(0.02)$	$1.14^{\,b\,a,\,4}(0.01)$
	19.80	$2.06^{\,b,\,2}(0.01)$	$1.29^{\,b,\,3}(0.01)$	$3.65^{\,c,\,1}(0.02)$	$1.05^{b,\,5}(0.01)$	$1.11^{b,\,4}(0.04)$
	27.02	$1.8^{c,\,2}(0.03)$	$1.19^{\,c,\,3}(0.03)$	$3.17^{\,d,\,1}(0.10)$	$0.94^{\,b,\,4}(0.01)$	$0.96^{\,c,\,4}(0.01)$
1.0 > dp < 0.60	8.40	$1.91^{b,\,2}(0.38)$	$1.20^{\,b,\,3}(0.02)$	$3.41^{b,\,1}(0.68)$	$0.9^{\,2,\,3c}(0.20)$	$0.84^{\,b,\,3}(0.01)$
	14.86	$1.57^{b\,c,\,2}(0.02)$	$1.10^{\,b\,c,\,3}(0.02)$	$2.77^{\,c,\,1}(0.45)$	$1.03^{\,b,\,3}(0.03)$	$0.79^{\,c,\,3}(0.02)$
	19.80	$1.34^{\,c,\,2}(0.01)$	$0.89^{\,d,\,3}(0.01)$	$2.3^{\,c,\,1}(0.03)$	$0.69^{\,c,\,4}(0.01)$	$0.71^{d,\,4}(0.01)$
	27.02	$2.99^{\,a,\,2}(0.02)$	$2.59^{\,a,\,3}(0.02)$	$4.69^{\,a,\,1}(0.02)$	$1.89^{\,a,\,4}(0.03)$	$1.35^{\,a,\,5}(0.01)$
0.6 > dp < 0.30	8.40	$1.36^{\,a,\,2}(0.94)$	$1.38^{\,a,\,2}(0.47)$	$2.96^{\,a,\,1}(1.03)$	$0.88^{\,b,\,2}(0.32)$	$0.53^{\,a,\,2}(0.04)$
	14.86	$1.10^{b,\,2}(0.10)$	$0.85^{b,\,3}(0.06)$	$1.87^{b,1}(0.05)$	$0.55^{a,\,3}(0.11)$	$0.47^{\,b,\,4}(0.01)$
	19.80	$0.71^{b,\,2}(0.01)$	$0.51^{b,\,3}(0.02)$	$1.16^{\,b,\,1}(0.01)$	$0.36^{\,c,\,5}(0.02)$	$0.36^{\,c,\,4}(0.02)$
	27.02	n/a	n/a	n/a	n/a	n/a
0.3 > dp < 0.015	8.40	$2.84^{\,a,\,1}(0.02)$	$2.25^{a,\,2\,1}(0.03)$	$2.31^{a,\,2\,1}(0.10)$	$1.56^{\,a,\,2.3}(0.23)$	$0.93^{\,a,\,3}(0.22)$
	14.86	$1.52^{\,a,\,2}(0.02)$	$1.25^{\,a,\,3}(0.02)$	$2.25^{\,a,\,1}(0.01)$	$2.25^{\,a,\,1}(0.01)$	$0.66^{\,a,\,4}(0.06)$
	19.80	$2.00^{\,a,\,1}(0.08)$	$1.62^{\,a,\,1}(0.89)$	$2.77^{a,\,1}(0.02)$	$1.11^{a,\,1}(0.61)$	$0.64^{a,\,1}(0.21)$
	27.02	n/a	n/a	n/a	n/a	n/a

* Values are means of three data points and numbers in parentheses are standard deviation,
*values within a screen size in a column, having the same superscript (alphabet) are statistically not significant (p < 0.05)
*values within a screen size in a row, with the same superscript (numeric) are statistically not significant (p < 0.05)
*N/A means: readings at those point were not available on Camsizer

Appendix 4: Additional data for Chapter 6

Particle diameter		0.00182	m					
Coefficient of variation		0.8						
	sphericity	0.38						
	porosity	0.84						
	viscosity	0.000015	Pa.s					
	Screen size	1/2"						
Pressure (Inches of H_2O)	Flow (m/s)	Pressure (Pa)		Present (Pa/m)	RMD (%)		Ergun (Pa/m)	RMD (%)
1.56	0.15	366.05		113.7	-68.9		48.8	-86.7
2.15	0.24	498.96		271.0	-45.7		94.1	-81.1
2.56	0.27	595.93		346.5	-41.8		114.1	-80.9
2.82	0.29	657.06		404.2	-38.5		129.0	-80.4
3.16	0.31	738.60		459.3	-37.8		142.9	-80.7
3.85	0.35	905.42		556.1	-38.6		166.8	-81.6
4.9	0.41	1156.38		777.6	-32.7		219.9	-81.0
5.33	0.42	1261.64		824.5	-34.6		230.9	-81.7
6.23	0.47	1477.55		1025.5	-30.6		277.5	-81.2
6.9	0.49	1641.38		1112.0	-32.2		297.2	-81.9
7.56	0.50	1804.53		1156.6	-35.9		307.3	-83.0
8.5	0.55	2031.62		1355.9	-33.3		352.2	-82.7
9.48	0.59	2268.12		1584.1	-30.2		402.8	-82.2
9.99	0.60	2393.24		1650.7	-31.0		417.5	-82.6
10.85	0.64	2601.05		1858.5	-28.5		463.0	-82.2
11.4	0.67	2732.24		2048.6	-25.0		504.3	-81.5
			Overall RMD		-36.6			-82.0

Particle diameter			0.00202	m			
Coefficient of variation			0.68				
sphericity			0.38				
porosity			0.84				
viscosity			0.000015	Pa.s			
Screen size			3/4"				
Pressure (Inches of H$_2$O)	Flow (m/s)	Pressure (Pa)		Present (Pa/m)	RMD (%)	Ergun (Pa/m)	RMD (%)
1.83	0.22	421.50		217.0	-48.5	63.8	-84.9
2.31	0.27	534.29		303.5	-43.2	83.7	-84.3
2.88	0.31	669.04		410.9	-38.6	107.4	-83.9
3.29	0.34	766.74		484.5	-36.8	123.3	-83.9
3.81	0.37	891.02		579.3	-35.0	143.3	-83.9
4.61	0.43	1081.19		759.0	-29.8	180.6	-83.3
5.22	0.45	1230.07		830.4	-32.5	195.2	-84.1
6.23	0.49	1474.34		1002.7	-32.0	229.9	-84.4
7.1	0.53	1685.36		1147.8	-31.9	258.9	-84.6
8	0.58	1900.97		1372.3	-27.8	303.2	-84.1
8.7	0.60	2071.22		1492.0	-28.0	326.6	-84.2
9.4	0.63	2241.44		1616.7	-27.9	350.8	-84.3
10.01	0.64	2392.01		1668.0	-30.3	360.8	-84.9
10.82	0.69	2584.31		1950.4	-24.5	415.2	-83.9
11.8	0.71	2824.89		2078.2	-26.4	439.7	-84.4
12.9	0.73	3096.92		2165.6	-30.1	456.4	-85.3
					-32.7		-84.3

262

Particle diameter		0.00209						
Coefficient of variation		0.73						
	0.39	0.42						
	0.84	0.84						
	0.000015	0.000015						
	Screen size	5/8"						
Pressure (Inches of H_2O)	Flow (m/s)	Pressure (Pa)		Present (Pa/m)	RMD (%)		Ergun (Pa/m)	RMD (%)
1.76	0.23	402.73		229.4	-43.0		71.2	-82.3
2.24	0.27	516.36		306.7	-40.6		89.9	-82.6
2.38	0.29	548.36		346.6	-36.8		99.4	-81.9
2.68	0.32	617.30		433.7	-29.7		119.5	-80.6
3.12	0.34	723.80		487.9	-32.6		131.8	-81.8
3.74	0.38	872.63		590.3	-32.4		154.7	-82.3
4.3	0.41	1005.94		710.8	-29.3		181.1	-82.0
4.71	0.44	1103.93		797.4	-27.8		199.9	-81.9
5.26	0.47	1236.42		898.3	-27.3		221.5	-82.1
6.04	0.49	1427.30		985.4	-31.0		240.0	-83.2
6.76	0.53	1599.89		1150.1	-28.1		274.7	-82.8
7.43	0.55	1762.71		1259.6	-28.5		297.5	-83.1
8.2	0.59	1949.07		1409.2	-27.7		328.5	-83.1
8.89	0.63	2112.49		1643.1	-22.2		376.5	-82.2
9.67	0.64	2306.05		1681.7	-27.1		384.4	-83.3
10.46	0.68	2496.75		1867.6	-25.2		422.2	-83.1
11.01	0.72	2626.40		2091.9	-20.3		467.5	-82.2
					-30.0			-82.4

Table Comparison of Eqn. 5.2, 5.24 and 5.27 for predicting the U_{mf}

Diameter measurement scheme	Experimental U_{mf} (m/s)	Present study (%) Eqn. 5.24	Ergun (%) Eqn. 5.2	Ergun (%) Eqn. 5.27
Area	0.20	0.46	1.33	0.74
	0.24	0.39	1.19	0.74
	0.28	0.33	1.02	0.65
	0.32	0.44	1.16	0.70
Chord	0.30	0.40	1.17	0.63
	0.28	0.29	0.88	0.51
	0.42	0.26	0.82	0.49
	0.52	0.37	0.98	0.57
Ferret	0.30	0.61	1.77	1.03
	0.28	0.52	1.59	1.03
	0.42	0.43	1.33	0.88
	0.52	0.57	1.52	0.96
martin	0.30	0.33	0.96	0.48
	0.28	0.26	0.78	0.43
	0.42	0.23	0.71	0.40
	0.52	0.32	0.83	0.46
Surface-volume	0.30	0.21	0.63	0.23
	0.28	0.15	0.46	0.18
	0.42	0.17	0.55	0.27
	0.52	0.27	0.70	0.36

Friction Coefficient μ(v_rt)

$$\mu_{stick}=0.5$$
$$\mu_{glide}=0.2$$
$$\mu_{limit}=0.1$$
$$v_{glide}=1 \text{ m/s}$$
$$v_{limit}=10 \text{ m/s}$$
$$slope_{limit}=100 \text{ m/s}$$
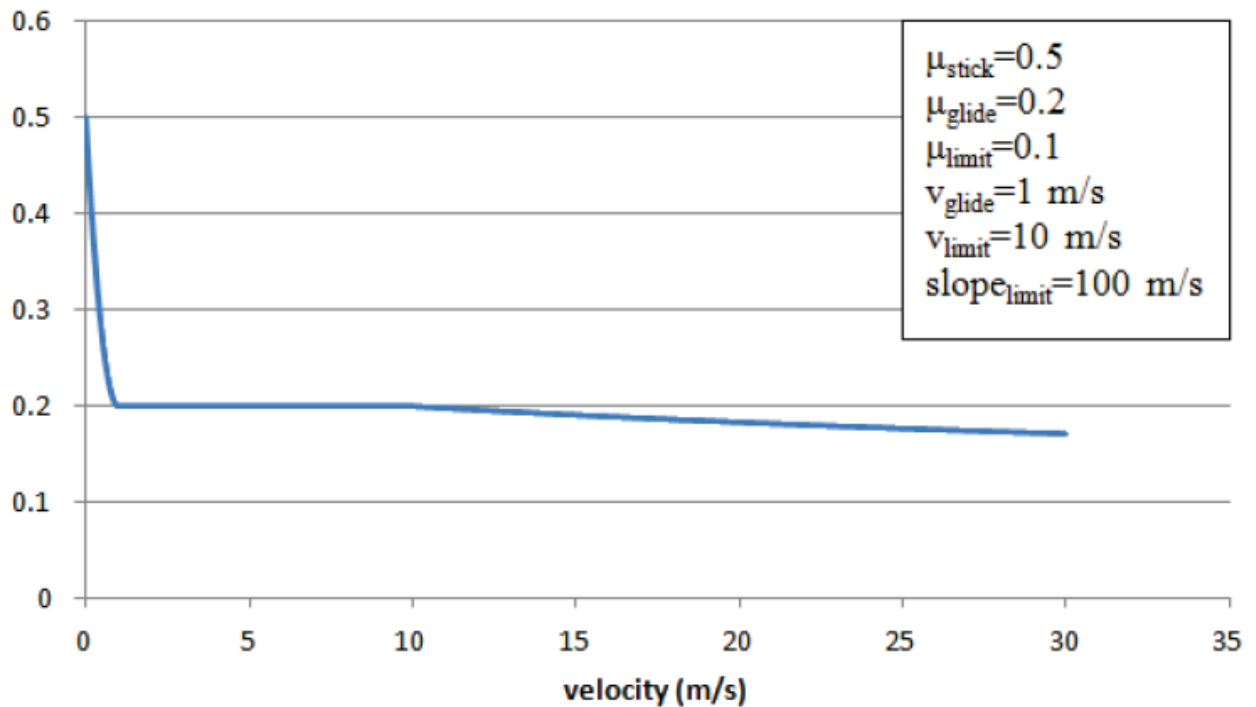
UDF for bed voidage

```
#include "udf.h"
real vof;
DEFINE_EXECUTE_AT_END(excecute_at_end)
{

        Domain *d;
        Thread *t;
        Thread **pt;
        cell_t c;

        real bed_voidage =0.;
        real sum_v_s =0.;
        real sum_v_cell =0.;
        real current_time;
        current_time = RP_Get_Real("flow-time");
```

```
        d = Get_Domain(1);
        mp_thread_loop_c(t, d, pt)
        {
                    begin_c_loop_int(c, t)
                    {
                            if (C_VOF(c,pt[1])> 0.01)
                                    {
                                            sum_v_s += C_VOF(c,pt[1]) *
C_VOLUME(c, t);

                                            sum_v_cell += C_VOLUME(c, t);
                                            pres_sum += C_P(c,t) *
C_VOLUME(c,t);
                                    }
                    }
                    end_c_loop(c,t)
        }
                    bed_voidage = sum_v_s/sum_v_cell;

        mp_thread_loop_c(t, d, pt)
        {
                    begin_c_loop_int(c, t)
                    {
                            C_UDMI(c,t,0) = bed_voidage;
                    }
                    end_c_loop(c,t)
        }

}

```

UDF for body force
```
DEFINE_DPM_BODY_FORCE(particle_body_force,p,i)
{
        Domain *d;
        Thread *t=P_CELL_THREAD(p);
        cell_t c=P_CELL(p);

        Thread **pt = THREAD_SUB_THREADS(t);
        Thread *tp = pt[0];     /* initialize fluid phase (primary phase) */
        Thread *tsk= pt[1]; /* initialize mixture phase for particle (secondary phase) */

        real bforce;

        bforce= ( C_R(c,tp)/ C_R(c,tsk))*(C_VOF(c,tp)/(1.0 -
C_VOF(c,tp)))*((P_VEL(p)[0]-P_VEL(p)[1])/CURRENT_TIMESTEP);
        return bforce;
```
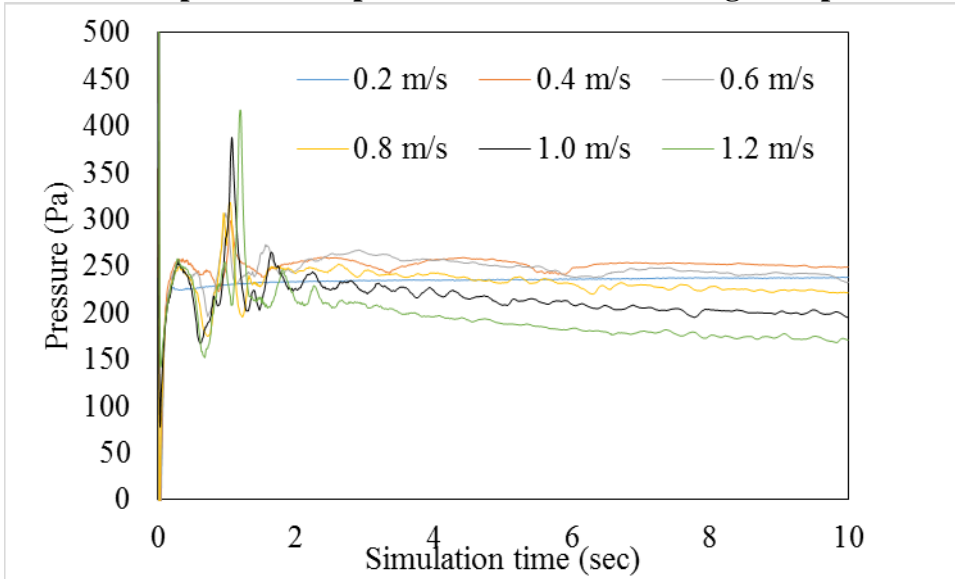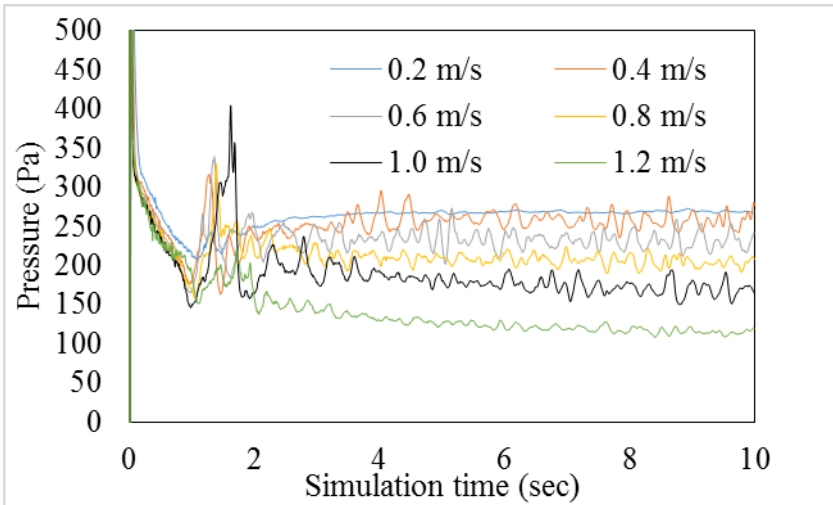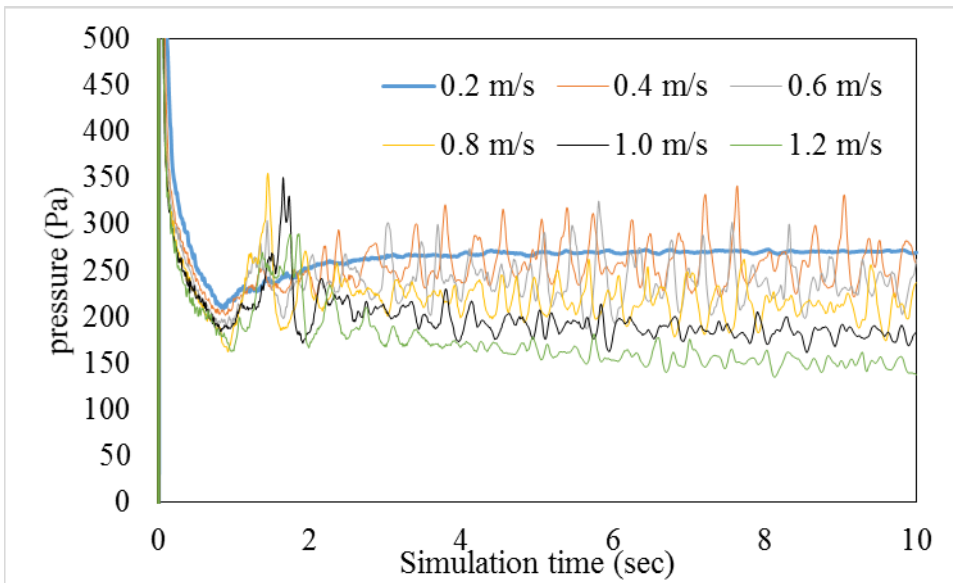
}
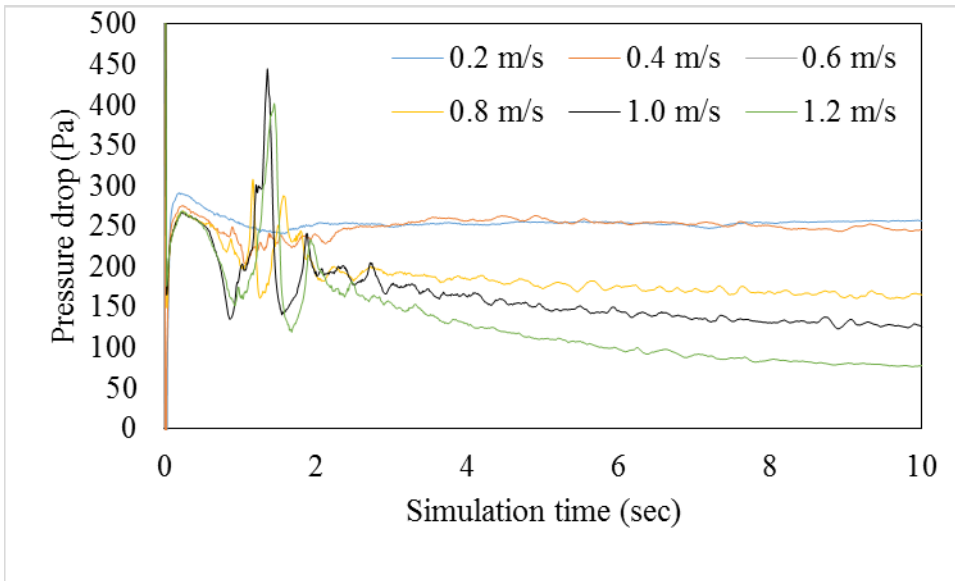
Evolution of pressure drop with simulation time using non spherical drag law

Evolution of pressure drop with simulation time using spherical drag law

Evolution of pressure drop with simulation time using Syamlal - Obrien drag law

Evolution of pressure drop with simulation time using Wen & Yu drag law

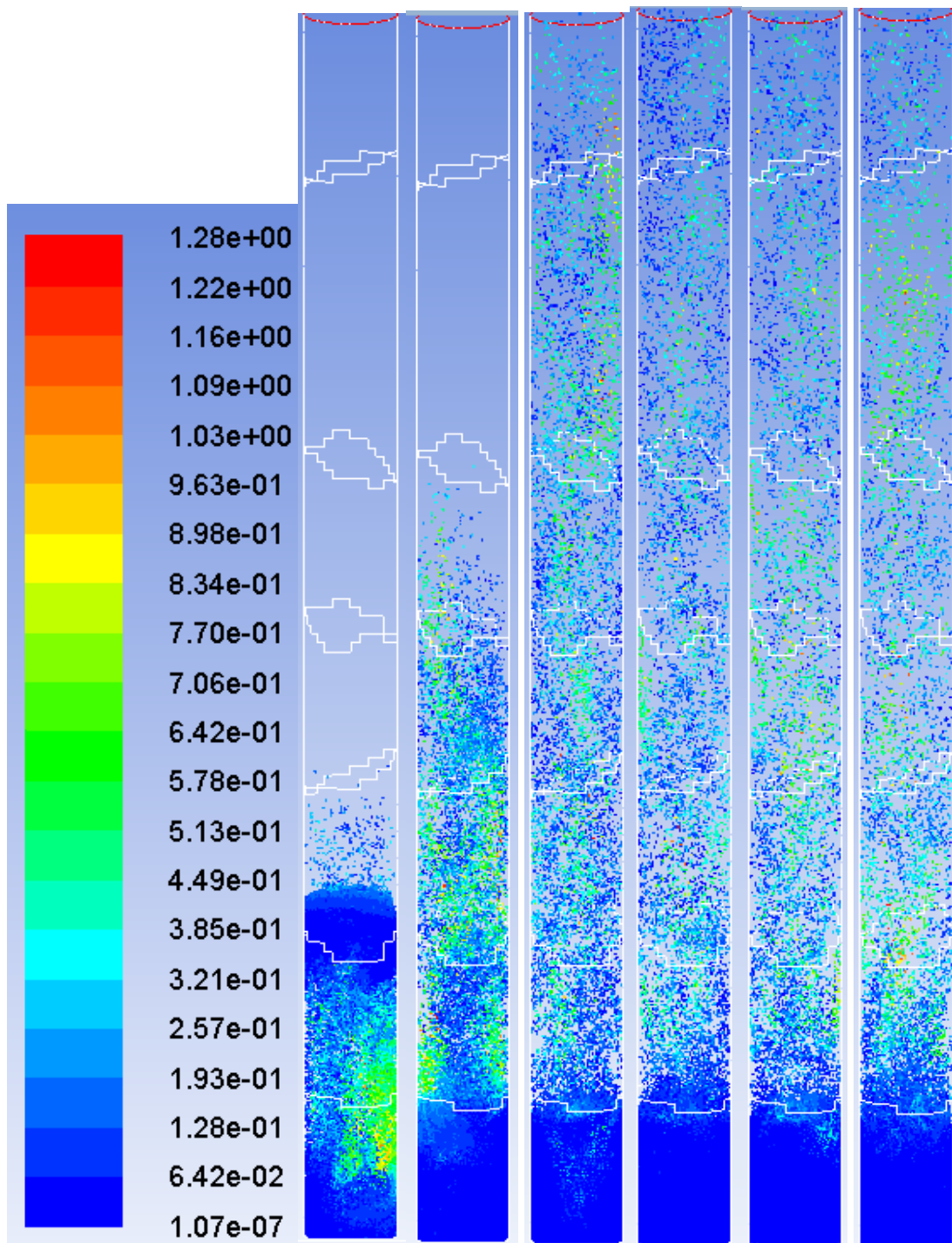**Additional data at predicting minimum fluidization velocitysection**

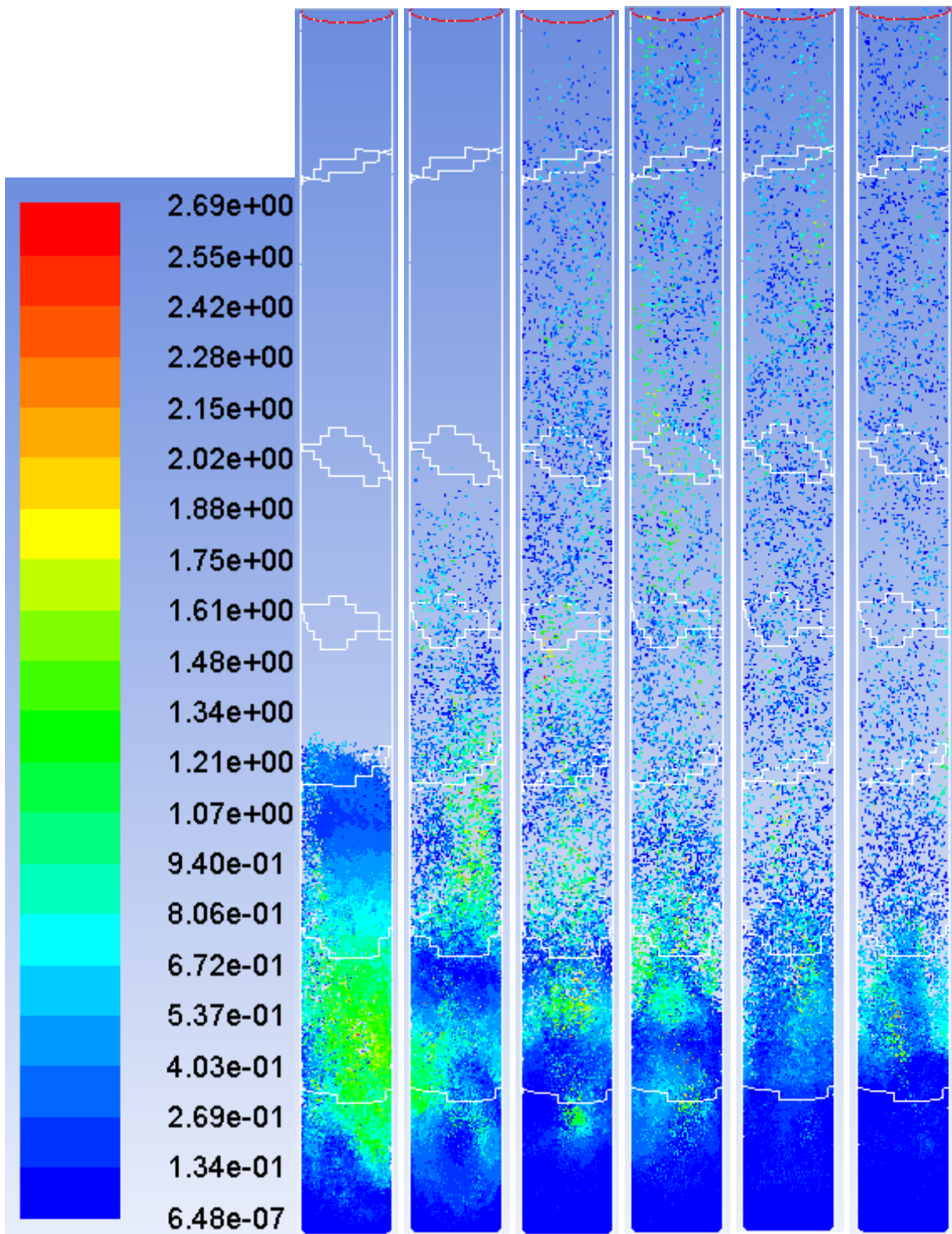Figure 7.13: Particle traces colored by particle velocity magnitude using non-spherical drag law at 0.4 m/s

Figure 7.13: Particle traces colored by particle velocity magnitude using Syamla-Obrien drag law at 0.4 m/s
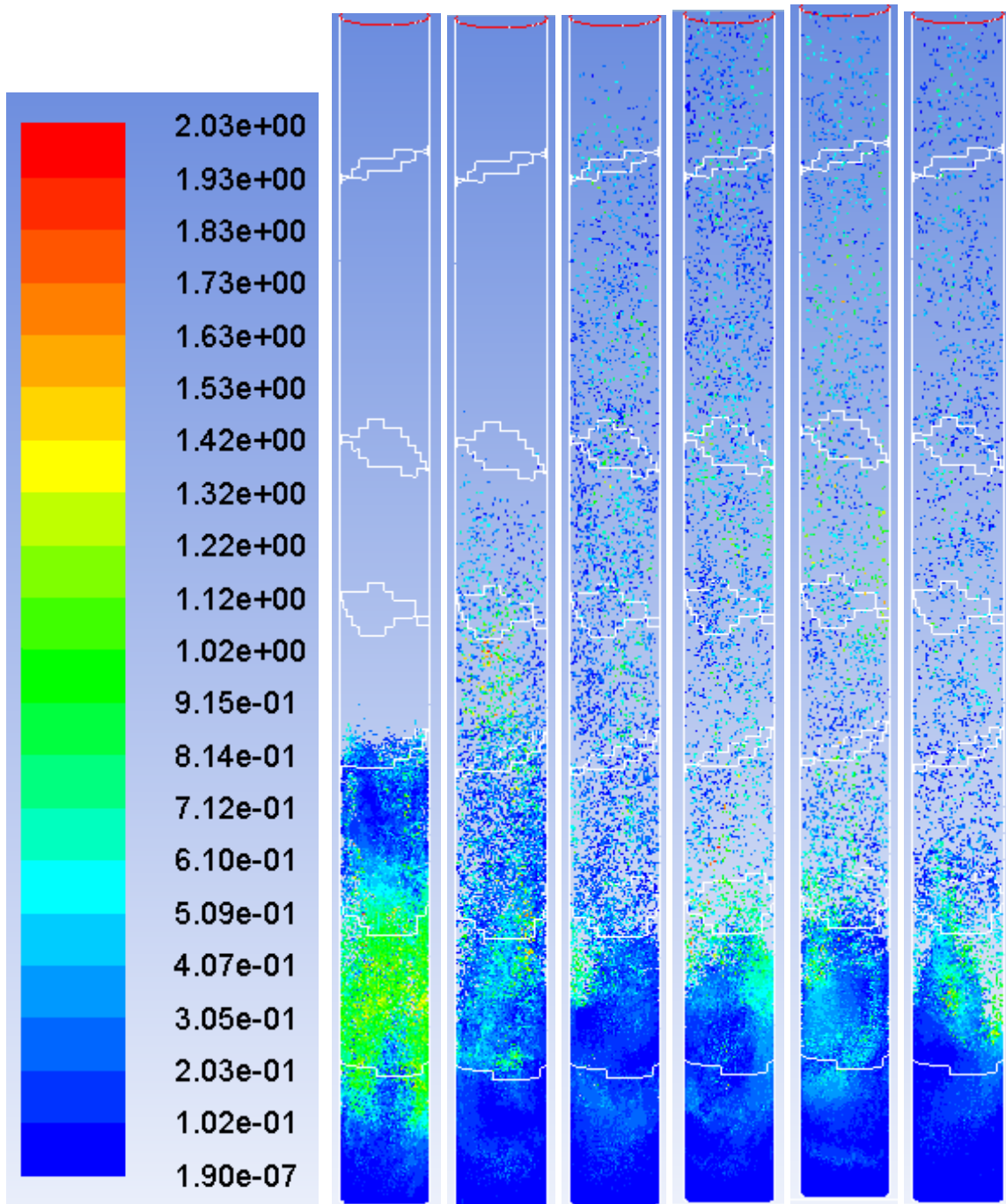
Figure 7.13: Particle traces colored by particle velocity magnitude using Wen & Yu drag law at 0.4 m/s